

Boston College
The Graduate School of Arts and Sciences
Department of Physics

**Emergent Phenomena in twisted
Van der Waals Materials**

a dissertation

by

Xiaodong Hu

submitted in partial fulfillment of the requirements

for the degree of

Doctor of Philosophy

May 2024

©Copyright by Xiaodong Hu

2024

Abstract

Twisted two-dimensional (2D) van der Waals (vdW) materials have become a fertile ground for discovering novel quantum phenomena. The stacking of layers and twisting angles serve as independent tuning parameters, expanding the search space for quantum phases of matter for both experimentalist and theorists. Additionally, the formation of moiré superlattices, as a unique property of twisted vdW materials, is able to cover a wide range of energy and length scales controlled by the twisting angles. This makes such platform an efficient playground for exploring exotic quantum phases. This thesis is divided into two parts based on whether moiré physics is involved.

In the first part, we focus on the fractional Chern insulators (FCI) realized on the moiré miniband of twisted transition metal dichalcogenides. FCI were proposed theoretically about a decade ago. These exotic states of matter are fractional quantum Hall states realized when a nearly flat Chern band is partially filled, even in the absence of an external magnetic field. Recently, exciting experimental signatures of such states have been reported in twisted MoTe₂ bilayer systems. Motivated by these experimental and theoretical progresses, in this paper, we develop a projective construction for the composite fermion states (either the Jain's sequence or the composite Fermi liquid) in a partially filled Chern band with Chern number $C = \pm 1$, which is capable of capturing the microscopics, e.g., symmetry fractionalization patterns and magnetoroton excitations. On the mean-field level, the ground states' and excited states' composite fermion wavefunctions are found self-consistently in an enlarged Hilbert space. Beyond the mean-field, these wavefunctions can be projected back to the physical Hilbert space to construct the electronic wavefunctions, allowing direct comparison with FCI states from exact diagonalization on finite lattices. We find that the projected electronic wavefunction corresponds to the *combinatorial hyperdeterminant* of a tensor. When applied to the traditional Galilean invariant Landau level context, the present construction exactly reproduces Jain's composite fermion wavefunctions. We apply this projective construction to the twisted bilayer MoTe₂ system. Experimentally relevant properties are computed, such as the magnetoroton band structures and quantum numbers.

In the second part, we focus on the platform of twisted 2D superconductors where moiré physics is absent. We first consider the twisted Ising superconductors like NbSe₂ and TaS₂. These materials have demonstrated Ising superconductivity down to atomically thin layers. Due to the spin-orbit coupling, these superconductors have the in-plane upper critical magnetic field far beyond the Pauli limit. We theoretically demonstrate that, twisted bilayer Ising superconductors separated by a ferromagnetic buffer layer can naturally host chiral topological superconductivity with Chern numbers, which can be realized in heterostructures like NbSe₂/CrCl₃/NbSe₂. Under appropriate experimental conditions the topological superconducting gap

can reach > 0.1 meV, leading to readily observable signatures such as the quantized thermal Hall transport at low temperatures. Then we take twisted 2D superconductors as a general platform for transport measurement study. 2D superconductors have been realized in various atomically thin films such as the twisted bilayer graphene, some of which are anticipated to involve unconventional pairing mechanism. Due to their low dimensionality, experimental probes of the exact nature of superconductivity in these systems have been limited. We propose, by applying a *vertical* supercurrent to a bilayer superconductor where the mirror symmetry is naturally broken by the twisting, there will be anomalous thermal Hall effect induced by the supercurrent that can serve as a sharp probe for the *in-plane* anisotropy of the superconducting gap function. This effect occurs in the *absence* of an external magnetic field and spontaneous breaking of the time-reversal symmetry in the ground state. We derive explicit formulas for the induced thermal Hall conductivity and show them to be significant in the examples of twisted cuprates and twisted FeSe where monolayer superconductivity have already been observed. Though technical challenges still exist, we propose this to be a generic probe of the gap anisotropy in a twisted bilayer superconductor.

Publication/Preprint List

- **Xiaodong Hu**, Di Xiao, Ying Ran, *Hyperdeterminants and Composite fermion States in Fractional Chern Insulators*, [arXiv:2312.00636v2](https://arxiv.org/abs/2312.00636v2).
- **Xiaodong Hu**, Jung Hoon Han, Ying Ran, *Supercurrent-induced anomalous thermal Hall effect as a new probe to superconducting gap anisotropy*, [Phys. Rev. B **108** \(4\), L041106](https://doi.org/10.1103/PhysRevB.108.L041106).
- **Xiaodong Hu**, Ying Ran, *Engineering chiral topological superconductivity in twisted Ising superconductors*, [Phys. Rev. B **106** \(12\), 125136](https://doi.org/10.1103/PhysRevB.106.125136).
- Faranak Bahrami, **Xiaodong Hu**, Yonghua Du, Oleg I Lebedev, Chennan Wang, Hubertus Luetkens, Gilberto Fabbris, Michael J Graf, Daniel Haskel, Ying Ran, Fazel Tafti, *First demonstration of tuning between the Kitaev and Ising limits in a honeycomb lattice*, [Sci. Adv. **8**, eabl5671 \(2022\)](https://doi.org/10.1126/sciadv.adl5671).

Acknowledge

The time in Boston College passed so fast. My google photo constantly reminds me of the life details six year ago, when I entered the US, purchasing furnitures in IKEA, moving around Boston with one day nowhere to go due to the empty day on the rental lease, settling down in Brighton, and starting my PhD journey at Boston College. As the graduation approaches, I have an intense feeling that there is a growing force pulling me back to the beginning of the journey. Similar to the instanton effects in a compact spacetime, fragments of memories flood in my mind, getting interfferenced and becoming increasingly vivid. Now, standing at the end of the journey, I would like to take this opportunity to express my sincer gratitude to all the people who have helped me along the way.

I would like to express my deepest gratitude and respect to my advisor, Prof. Ying Ran. The open and extensive discussions in his office are the most joyful moments during my PhD life. Ying's style of research, asking right questions, and never taking unexamined points for granted, has largely shaped my academic personality. As an academic role model, Ying also led by example, teaching me important lessons on how to become an independent theorist. He always emphasized the importance of being honest with oneself: to be crystal clear on the physical picture, to slow down and think deeply and correctly. I would also emphasize Ying's kindness and gentleness. Ying was always welcoming of so-called "stupid" questions, yet he also encouraged me to think independently. Whenever I feel drained and frustrated, the talk with him would recharge and motivate me again. Ying also taught me many stills to be a physicist, not only computational techniques but also skills outside of physics. I still remember the day before my presentation on the the March Meeting, Ying spent the entire afternoon going through my slides, page by page, teaching me how to present in an engaging and attractive way. I am deeply grateful for Ying's guidance and extremely luck to be his student.

I would like to thank the the rest of my thesis committee: Prof. Kenneth Burch, Prof. Xiao Chen, and Prof. Qiong Ma. I thank Prof. Burch for many assistance during the early years, on both course selection and course exemption. That helps me to save time learning advanced courses. I thank Prof. Xiao Chen for being a friend bouldering at Central Rock Gym during the pandemic and for sharing his research in the field of quantum information. I appreciate Prof. Qiong Ma for introducing Moiré physics to our department, which directed my attention to this fascinating field.

I am deeply thankful to Prof. Jung Hoon Han, for the collaboration on SATHE projection and inspiring discussion during his sabbatical visit at Boston College, also for his help on my postdoc applications. I would like to thank Prof. Fazel Tafti for sharing his expertise in solid state physics during our collaborations on Kitaev materials and for his patience with my delayed calculations. I am also grateful to Prof. Liang Kong,

for his hospitality during my visit to his group at SUSTech. Additionally, I extend my gratitude to the faculty members of the Physics Department, including Prof. Ziqiang Wang, Prof. Ilijia Zeljkovic, Prof. David Broido, and Prof. P. Bakshi, for great experience with them as both a student and as a teaching assistant. My sincere thanks also go to the department staff, especially Jane Carter, Scott Bortolotto, and Nancy Chevry, whose kindness made my stay at Boston College a pleasant experience.

I also want to thank my colleagues and collaborators, both at Boston College and elsewhere. In particular, I would like to thank our senior group member Xu Yang. The condensed matter theory journal club we held for two years, with just the two of us as speakers, was highly beneficial. I gained much from his sharing and the questions he posed during my talks. I would also like to thank my roommates and close friends, Hong Li and Hanchen Liu. The countless discussions over delicious food in Allston, ranging from scanning tunneling microscope details to measurement-induced phase transitions, and from physics to politics, have broadened my perspective and reshaped my understanding of the world. I extend my gratitude to my academic friends, Zhihao Zhang, Yongxin Zeng, Jiaqi Cai, Junkai Dong, Chong Wang, and Prof. Yinghai Wu. The online discussions through Q&A websites and WeChat have been incredibly helpful and inspiring for my research. I am also thankful to Prof. Subir Sachdev, Prof. Xiaogang Wen, and Prof. John McGreevy, for their open-access notes and slides, covering high-level knowledge to frontier research. For friends at BC, I would like to thank Yiping Wang and He Zhao for organizing numerous hiking and food exploration around Boston, refreshing my mind everytime I got frustrated. I would also like to thank Yiqiu Han, Owen Yang, Sylvia Chen, Boxi Song, Rule Yi, Xiaohan Yao, Shrinkhala Sharma, and my officemate Vikram Ravindranoth, Jayakrishnan M.P. Nair, Vincent Plisson, Kewen Huang, and Wenya Liu. The happy moments spent with them prevented me from getting “permanent head damage” (PhD).

To my parents

Contents

1	Introduction	1
1.1	Motivation for Twisted van der Waals Materials	1
1.1.1	On Dimensionality	2
1.1.2	On Moiré Physics	4
1.1.3	As a New Experimental Knob	5
1.1.4	As a Platform for Quantum Simulations	6
1.2	Structure of the Thesis	9
2	Background	10
2.1	Twisted Moiré Physics	10
2.1.1	Transition Metal Dichalcogenides	10
2.1.2	Moiré Continuum Hamiltonian	13
2.2	Fractional Quantum Hall Effect	17
2.2.1	Jain's Composite Fermion	17
2.2.2	Murthy-Shankar's Algebraic Description of Composite Fermion	18
2.2.3	Remarks of FCI	19
3	Projective Construction of Composite Fermion States in Fractional Chern Insulators	21
3.1	Introduction	21
3.2	A brief review of related previous works	24
3.2.1	Jain's composite-fermion construction	24
3.2.2	Murthy-Shankar's Hamiltonian theory	25
3.2.3	Pasquier-Haldane-Read construction for the bosonic $\nu = 1$ composite fermion liquid .	27
3.3	The projective construction on a finite-size system	28
3.3.1	Mapping a Chern band to the lowest Landau level	28
3.3.2	Composite fermion substitution	35
3.3.3	Gauge redundancy and projective symmetries	39
3.3.4	Hartree-Fock and time-dependent Hartree-Fock	42
3.3.5	Projection to physical states: Hyperdeterminant	45
3.3.6	Connections with Jain's wavefunctions	46
3.3.7	Connections with parton states for FCI systems	50

3.4	Benchmark results	52
3.4.1	Models	52
3.4.1.1	Mixed Landau level (MLL) model	52
3.4.1.2	TMD moiré (tMoTe₂) model	53
3.4.2	Exact diagonalization, Hartree-Fock and time-dependent Hartree-Fock	54
3.4.2.1	CF mean-field ground states	54
3.4.2.2	Overlap between projected wavefunctions and ED ground states	55
3.4.2.3	Magnetoroton spectra and quantum numbers	56
3.5	Discussion and Conclusions	60
3.A	The rotation transformations of LLL bloch states and the CB-LLL mapping	61
3.B	Composite fermion substitution for the case of $\nu = \frac{1}{2s}$ composite Fermi liquid	64
3.C	Density operator expectation values in Laughlin states on the torus	65
3.D	Time-dependent Hartree-Fock approximation in the presence of constraints	66
3.E	Derivation of Eq.(3.93) and Eq.(3.98)	71
3.F	Continuous coherent state and the projective construction for Laughlin's states on the torus	74
3.G	Extended Data	74
4	Supercurrent-induced Anomalous Thermal Hall Effect as a New Probe to Superconducting Gap Anisotropy	76
4.1	Introduction	76
4.2	Main Results	78
4.3	The \hat{L} operator and Doppler shift	78
4.4	Derivation of Eq. (4.1)	79
4.5	Interband pairing and nodal superconductivity	80
4.6	Applications to FeSe and cuprates	81
4.7	Conclusion and Discussion	83
4.A	The Doppler shift and the gauge transformation due to the supercurrent	84
4.B	Details on the Derivation of the Main Result	86
4.B.1	Supercurrent-indcued Berry Curvature for Intraband Pairing	86
4.B.2	Fermi Surface Integral	88
4.C	Supercurrent-indcued Berry Curvature for Interband Pairing	89
4.D	Fermi Surface Reconstruction for Twisted Bilayer FeSe	93
5	Engineering Chiral Topological Superconductivity in Twisted Ising Superconductors	96
5.1	Introduction	96
5.2	Main results	98
5.3	Model	101
5.4	Discussion and conclusions	107
5.A	Domain-wall chiral modes	108

5.B	A mean-field treatment for the ferromagnetic buffer layer	110
5.C	Details of the phase diagram calculations and discussions on the stacking-dependence	111
5.D	Details of analytical perturbative calculations	113
5.D.1	Perturbative theory for $\sqrt{(v_{\text{Ising}} k_F \theta)^2 + 4t_\perp^2} \gg \Delta$: $C = 12$ Topological Phases	113
5.D.1.1	Construction of Hamiltonian	113
5.D.1.2	Low-energy Effective Theory in Nambu Space	116
5.D.1.3	Topological Nodes C and D	117
5.D.1.4	Trivial Nodes F and G	119
5.D.2	A different perturbative regime: $C = 6$ Topological Phases	120
5.E	Two-center approximation	120
Bibliography		122

List of Figures

1.1	Fractional Quantum Hall Effect extracted from [1]. Fractional plateaus of transverse resistance ρ_{xy} observed in GaAs/AlGaAs heterostructures at low temperatures and high magnetic fields, quantized to fractional values of h/e^2 at various filling factors $\nu = 1/3, 2/5, 3/7$, etc. Note: $\nu = 1/2$ is metallic — there is no plateau at all.	3
1.2	Illustration of Short-range Entangled and Long-range Entangled States adapted from Ref. [2]. (a) . Possible phase diagram for a Hamiltonian $H(g_1, g_2)$ without any symmetry. (b) . Possible phase diagram for a Hamiltonian $H(g_1, g_2)$ with some symmetries. All shaded regions in (a) and (b) represent the phases with short range entanglement (i.e. those ground states can be transformed into a direct product state via a generic LU transformations that do not have any symmetry).	4
1.3	UV-IR Energy Scales in High Energy and Condensed Matter Physics	5
1.4	High-Temperature Topological Superconductors in Twisted Cuprates extracted from Ref. [3]. (a) at small twisting angle $\theta < \theta_c$ the free energy is minimized when the interlayer phase differences $\varphi = 0$, resulting in a split Dirac cone with TRS. (b) at large twisting angle $\theta > \theta_c$ the free energy is minimized when $\varphi \neq 0$, resulting in a spontaneous TRS breaking with a fully gapped cone. (d) Phase diagram based on Ginzburg-Landau free-energy analysis.	6
1.5	Node Movement for Twisted Nodal Superconductors adapted from Ref. [4].	6
1.6	Phase Diagram for the Unconventional Superconductivity extracted from Ref. [5] and Ref. [6]. The superconducting domes adjacent to mott insulating phase is similar in cuprates phase diagram (left) and tBLG phase diagram (right).	7
1.7	Fractional Chern Insulators in tBLG adapted from Ref.[7]. Streda formula $C = \frac{\partial n}{\partial B}$ can be used to extract the states. Here ν is the number of electrons per moiré unit cell, and the FCI states are those that possess both fractional slopes and fractional interceptions.	8
1.8	Experimental Observation of Fractional Quantum Anomalous Hall Effects in tMoTe₂ extracted from Ref. [8] (left) and Ref. [9] (right).	8

2.1	Structure and electronic properties of TMDs adapted from Ref. [10]. (a) Atomic structure of single layers of TMD in their <i>trigonal prismatic</i> (2H), <i>distorted octahedral</i> (1T) and <i>dimerized</i> (1T') phases. (b) “Periodic table” of known layered TMDs, organized based on the transition metal elements, their existing structural phases (2H, 1T and 1T'), and the observed electronic phases (see the right panel). (c) Evolution of the band structure of 2H-MoS ₂ from bulk material down to monolayers. Clearly a indirect gap to direct gap transition occurs for monolayer material only. (d) Schematic band structure of 2H-MoS ₂ , showing the spin splitting (orange and blue colors) at K and K' points.)	11
2.2	MoS₂ Crystal Structure and Band Structure adapted from Ref. [11]. (a) The unit cell of bulk 2H-MoS ₂ . (b) Top view of MoS ₂ monolayer. (c) Schematic drawing of the band structure at the band edges located at the K points.	12
2.3	DFT Band Structures for Several MX₂ Monolayer Materials (extracted from [12]).	13
2.4	Twisted BZ with K-valley Target Regions, mBZ, and Q_l Grids. (a) . Green arrows are three target-region crystal momentum differences {q ₁ , q ₂ , q ₃ }. (b) . Iterative addition of the momentum differences forms two pair of triangular lattice $Q_l = m_{1,l}\mathbf{b}_{M1} + m_{2,l}\mathbf{b}_{M2}$ spanned by the moiré reciprocal vectors (red dots and blue dots).	17
2.5	Jain’s Composite Fermion Theory adapted from Ref. [13].	18
3.1	Illustration for the possible change of Wen-Zee shift due to the CF band inversion when tuning the parameter λ , so that the CF states at $\lambda = 0$ and $\lambda = 1$ belongs to different SET phases.	22
3.2	Geometry Setup of the LLL Bloch Basis: The torus sample, equivalent to a parallelogram, is parameterized by a real length L_1 and a modular parameter τ . The $N_{1,e} \cdot N_{2,e}$ zeros $\{z_\nu\}$ (red hexagons) of the Haldane-Rezayi wave function are equally distributed on the torus sample by construction, see Eq.(3.32). There are also $N_{1,e} \cdot N_{2,e}$ independent groups of $\{k, z_{sum}\}$ satisfying the boundary condition Eq.(3.28), i.e. $N_{1,e} \cdot N_{2,e}$ independent basis parameterized by different values of $z_{1,0}$, which also forms a $N_{2,e} \cdot N_{1,e}$ grids as green triangles, see Eq.(3.33).	32
3.3	Filled CF band dispersion obtained using the Hartree-Forck approximation. The calculation is done for MLL model (a) with parameter $V_{10} = 0.12$ units of $\frac{e^2}{\epsilon\ell_e}$ and MoTe ₂ model (b) with parameter $\lambda = 0.6$ on a 9×9 lattice. These Hartree-Fock CF bands turn out to be <i>nearly flat</i> . As is shown in Eq.(3.79), a three-fold periodicity of CF band dispersion emerges as a manifestation of the translation-symmetry fractionalization, as is seen in both subfigures on the right. Note that we have used the <i>electron’s Brillouin Zone</i> (BZ) to plot the CF dispersion for better visualization of the symmetry fractionalization (in the tMoTe ₂ model the electron’s BZ is the moiré BZ.). The CF’s BZ should be 1/3 of the electron’s BZ due to the enlarged real-space unit cell along the a_1 direction.	55
3.4	Selected many-body spectrum obtained from exact diagonalization on 6×4 unit cells. (a),(b) for MLL model and (c),(d) for tMoTe ₂ model. (a) and (c) are close to the flat band limit, while (b) and (d) have much smaller many-body gaps. The three nearly degenerate topological ground states are highlighted in dark purple.	57

3.5	(a1)-(a3) and (c1)-(c3) exhibit the overlaps between our electronic hyperdeterminant states and the ED ground states (red line), and the the overlaps between Laughlin's states and the ED ground states (blue line) for both MLL model and tMoTe ₂ model. Here, the overlap is defined as $ \langle \psi_{\text{ED}} \psi_{\text{Proj}} \rangle $ where the two wavefunctions are obtained from ED and the projective construction respectively. There exists three sectors of ground states carrying center-of-mass momentum Γ , $\frac{1}{3}\mathbf{G}_{1,e}$, and $\frac{2}{3}\mathbf{G}_{1,e}$ (the dark purple points in FIG.3.4). The ribbon around each overlap curve represents the error bar due to variational Monte Carlo samplings. The many-body gap (i.e., the energy difference between the ground state manifold and the first excited state.) as a function of the tuning parameter is plotted in (b) and (d).	58
3.6	Magnetoroton bands for samples of 9×9 unit cells obtained using the TDHF approximation. (a), (b) are for the MLL model with the parameter $V_{10} = 0.04$ units of $e^2/\epsilon l_e$, and (c), (d) are for the tMoTe ₂ model with the parameter $\lambda = 0.2$. (a) and (c) are the fitted 2D surface contour of the lowest magnetoroton band (band-1), while (b) and (d) exhibit the full magnetoroton spectra, where scattering points represent the raw data along the path, and the higher horizontal crosses are from the particle-hole (PH) continuum. See Fig.3.3 for the definitions of the high-symmetry points. Note: there is no raw data point along the X-M line in the MLL model due to the choice of 9×9 sample size. We provide the raw data for a smaller 6×6 MLL sample in the Appendix. 3.G for comparison. We do not perform band fitting for the magnetoroton band-3 and band-4 for the MLL model due to the limited number of points outside the PH continuum. The appearance of the nearly zero-energy modes (red dots in all four figures) at the Γ -point is due to the \mathcal{R}_v gauge degrees of freedom discussed in the main text near the end of Sec.3.3.4.	59
3.7	Magnetoroton bands for the 6×6 MLL model.	75
4.1	(a) SATHE for bilayer-SC. The vertical supercurrent J_S , or equivalently, a pairing phase twist φ between the two layers of, either a vertical JJ or an intrinsic bilayer superconductor, would induce an in-plane thermal Hall effect in a bilayer superconductor. In the former case, an insulating buffer layer may be present (not shown). (b) an illustration for the dimensionless function $\xi(x)$ in Eq.(4.2).	77
4.2	(a): JJ formed by twisted bilayer FeSe. (b) and (c): the topological non-trivial and trivial phases induced by the supercurrent in JJ formed by twisted bilayer cuprates. The twisted Fermi surfaces are shown on the left panels. For FeSe the moiré zone folding effect plays an important role on the topology of reconstructed Fermi surfaces. The color scheme on each Fermi surface represents the strength of $\langle u_{\mathbf{k}} \hat{L} u_{\mathbf{k}} \rangle \in [-1, 1]$, serving as the indicator of the layer-component of states. For all three cases, κ_{xy} is computed in unit of the thermal conductance quantum g_0 as a function of temperature, and a simple mean-field temperature-dependence of $\Delta_{\mathbf{k}}(T) = \Delta_{\mathbf{k}}(T=0)\sqrt{1-T/T_c}$ is implemented. For the topologically nontrivial case (b), gaps ~ 0.2 meV are generated around superconducting nodes, leading to a Chern number $C = 8$ topological superconductivity, while for the topological trivial case (c) the net Chern number is zero.	83

4.3	The schematic plot of the phase φ involved in the gauge transformation to describe a finite supercurrent state. The two curves represent the case of a Josephson junction (JJ) and an intrinsic bilayer superconductor(Intrinsic) respectively.	86
4.4	(a) Rotated top layer (green) and bottom layer (orange). The interference of all different hopping processes capture the spatial variation of interlayer tunnelings, which determines the moiré Brillouin zone (gray square). Up to the lowest truncation on such moiré k-shell, there are just two vertical hopping vectors δq^t and δq^b involved in the reconstruction of the left/right M -pockets (ditto for the top/bottom ones under a C_4 -rotation). (b) Illustration for the moire-pattern-involved Fermi surface reconstruction. Taking the top layer elliptic Fermi surface (green dashed lines) as the reference, both the rotated bottom layer (down orange dashed lines) and the copied M -pockets due to G_x (up orange dashed lines) involve in the reconstruction of the Fermi surfaces (red solid lines).	94
5.1	Setups: Proposals of twisted β -bilayer TMD heterostructures with an insulating middle buffer layer. (a,b1): The vertical cyan arrow represents the super-current J_S tuning the Josephson phase between top and bottom layers of TMD, and θ is a small twisting angle. The middle buffer layer with an <i>in-plane</i> ferromagnetic moment (red arrows) introduces an exchange Zeeman field $H_{\text{exch.}}$ for TMD layers through magnetic proximity effect, realizing the chiral topological superconducting phase. Outside the trilayer overlapping region, trivial superconductivity is realized. The gapless chiral edge modes are localized (yellow curves and arrows) at the boundary of the overlapping region. (b2,b3): Two additional proposals in the same spirits allowing more tunabilities for the parameters t_\perp , $t_{s,\perp}$ and $H_{\text{exch.}}$: FM (NM) means a ferromagnetic (nonmagnetic) buffer layer.	98
5.2	t_\perp-(H/H_p) Phase Diagram: The superconducting gap (gap minimum in the momentum space) and Chern numbers for proposed heterostructures involving TaS_2 (a) and NbSe_2 (b) based on numerical calculations. Here the Josephson phase is fixed to be $\varphi = \pi/2$ and the parameter ξ (see Eq.(5.1) for its definition) is fixed to be $\xi^{\text{TaS}_2} = 0.9$ and $\xi^{\text{NbSe}_2} = 1.1$. H_p in the vertical axis is the Pauli limit field strength. t_\perp and the corresponding twisting angle are displayed on the horizontal axis. For both materials the phase diagrams corresponding to case-(i) and case-(ii) in Eq.(5.2) are calculated. The black dashed lines exhibit the predicted topological/trivial phase boundary from analytical perturbative calculations (see Eq.(5.12)).	100
5.3	θ-φ Phase Diagram: The superconducting gap (gap mininum in the momentum space) and Chern numbers by varying the twisting angle θ and the Josephson phase φ for proposed heterostructures involving TaS_2 and NbSe_2 . Here in each figure we fix the Zeeman field to be four times the Pauli limit $H_{\text{exch.}} = 4H_p$ and fix the spin-independent tunneling t_\perp . Red arrows are to indicate the trivial-topological phase transitions by tuning φ in a single device. Note that the regime $\varphi \leq \pi/2$ corresponds to the stable branch of the Josephson junction.	102

5.4 Monolayer Fermi Surfaces and Band Structures: Γ -pocket and K -pocket of monolayer NbSe ₂ and TaS ₂ are shown. Point P is the intersection of Γ - M line and the the Γ -pocket, where Ising SOC vanishes and two nodes (cross symbols) emerge when an in-plane Zeeman field H_{exch} exceeds the superconducting gap. Magenta and blue colors indicate the different S_z -spin components.	103
5.5 Monolayer Band Structures.	104
5.6 Schematic Plot of Four Fermi Surface Intersection Points in a Twisted Bilayer Near Point-P: When $\varphi = 0$, each intersection point will give rise to two pairing nodes after H_{exch} is tuned up. When $\varphi \neq 0$, these nodes open up energy gaps: The four nodes near points F and G along the Γ - M line have total Chern number zero. The four nodes near points C and D have total Chern number 4.	105

List of Tables

3.1	Counting of the electronic guiding-center degrees of freedom \mathcal{R}_e , vortice's guiding-center degrees of freedom \mathcal{R}_v , and composite-fermion's both guiding-center \mathcal{R} and cyclotron η degrees of freedom on a finite-size sample for Jain's sequences $\nu = \frac{p}{2sp+1}$	37
3.2	Rotation eigenvalues for high-symmetry points of TDHF bands. For MLL model, unlike Γ or M points, the rotation eigenvalue for X and Y points are defined for C_2 rotation instead of C_4 . For tMoTe ₂ model, all high symmetry points are defined for C_3 rotation, and the magnetorotons at K and K' points are related by the $C_{2y}\mathcal{T}$ symmetry [14] and thus have identical eigenvalues. Note: when the magnetoroton band merges into the particle-hole(PH) continuum, the corresponding rotation eigenvalue is not presented since one cannot separate the magnetoroton state from the PH continuum. See Fig.3.6 for details.	58
3.3	$\mathbf{A}(n_1 = 1, n_2 = 0)$ (see Eq.(3.142)) for Laughlin's $\nu = 1/2$ state, with the sample shape parameter $\tau = i$ and $\tau = e^{i\frac{2\pi}{3}}$, and boundary condition $\varphi_{1,e} = \varphi_{2,e} = 0$ (see Eq.(3.26)).	66
5.1	The parameters in the $k \cdot p$ model.	101

Chapter 1

Introduction

1.1 Motivation for Twisted van der Waals Materials

The main topic of condensed matter physics are about phases and phase transitions. In this thesis, we focus on the study of zero-temeprature phases and transitions, i.e., the *quantum* phases of matter and *quantum* phase transistions.

From the perspective of experiments, these two topics roughly corresponds the two main strategies in search of exotic quantum phases of matter:

- one way is to directly step into the quantum phases by growing new materials;
- the other one is to drive phase tansitions from existing materials by tune external parameters.

Traditionally the former way is more popular due to the variaty and maturity of the material growth techniques and experimental apparatus. For example, iron-based superconductors FeSe thin films are grown with MBE (Molecular Beam Epitaxy) [15], the cuprates like $\text{YBa}_2\text{Cu}_3\text{O}_{7-x}$ are grown with PLD (Pulsed Laser Deposition) [16], and the Kitaev candidate $\alpha\text{-RuCl}_3$ are grown with CVT (Chermial Vapor Transport) [17]. However, the drawback of the material-growth strategy is that it is hard to connect the lattice-level information, including the lattice constants, bond angles, the dopings with the material properties to the mesoscopic physical properties of the grown materials, and the growth procedure itself is always a time-consuming, expensive, and labor-intensive process. As for the other way, there are plenty of external parameters that can be tuned, like doping, pressure, magnetic field, gating field, and so on. The advantage over the material-growth route is its tunability and controllability. For example, fractional quantum Hall effect (FQHE) is disordered by turning on a large magnetic fields in very clean GaAs/AlGaAs heterostructures [18, 19, 1], and the high-pressure room-temeprature superconductors are obtained by tunning the pressure up to 200 GPa [20]. However, there are still drawback for the parameter-tuning strategy: usually the entire phase diagram is unknown to us, and there can be many competing phases close to the target phase. More seriously, to reach some exotic phases, the parameter has been tuned to some extreme value that is really hard to achieve for most experimental groups, and we may fall back to the old problem of the high expenses.

So a natural problem is to ask that how to *effectively* search and explore the exotic quantum phase of matters, or more precisely can we find a platform combining both experimental routes' advantages but avoid their drawbacks? Here “effective” can be understood as many aspects: the cost, the time consumption, the labor, the predictability, the controllability, and so on. It turns out that, the rapidly growing fields of *twisted physics*, or *twistronics*, provides an answer to this question.

In study of twisted physics, at least two layers of building blocks are stacked together, stabilizing with weak interlayer van der Waals interactions (so are also called *van der Waals (vdW) materials*) with the presence of some twisting angles. It has been commonly agreed that most of these 2D materials are cheap for exfoliation and fabrication (and can be easier in comparison with material growth approach). The familiar tuning parameters like magnetic fields/gating fields can still be used here. The advantage of twisted physics is that, the number of stacking layers, as well as the twist angle between each two layers, can be recognized as a new experimental knob to tune the electronic properties of the system, which is also fully controllable and tunable.

1.1.1 On Dimensionality

The building blocks in twisted physics are mainly graphene, transition metal dichalcogenides (TMD), and other two-dimensional (2D) materials including monolayer cuprates and monolayer iron-based superconductor FeSe. Reducing the dimensionality of a system is believed to be associated with enhancement of the quantum effects. In fact, before the discovery of monolayer graphene in 2004 by Geim and Novoselov [21], people even wrongly use the entropy argument, or Mermin-Wagner theorem to argue the non-existence of 2D materials, and even Lev Landau made mistakes here¹. But nowadays, we know that a vast family of 2D materials has been grown, including metals like NbSe₂ [22], semi-conductor like most TMD materials [10], insulators like hexagonal Boron nitride (hBN), and even 2D magnets like CrI₃ [23, 24]. The broadening of the 2D materials family opened up the possibility to stack different 2D crystals on top of each other thus building new types of heterostructures. This allowed researchers to explore novel collective phenomena [25].

On the theoretical aspect, although symmetry-protected topological ordered (SPT) states are widely studied in one-dimensional (1D) models, for example the famous Haldane gap in integer-spin Heisenberg antiferromagnets [26, 27] and the following AKLT model [28], from the viewpoint of modern classification theory on quantum phases [29, 30], it was proved that there cannot be topological ordered (TO) states for 1D gapped systems [31]. Thus, a 2D system is the minimal dimensional requirement for the existence of TO states, at least for gapped phases, which possesses long-range entanglement [32, 33, 34], fractional excitations and ground-state degeneracy [35]. The fractional quantum Hall effect (FQHE), first realized in GaAs/AlGaAs heterostructures (see Fig.1.1), is the most famous example of a TO state, featuring fractionally charged electrons and a ground state degeneracy on the torus [35, 36]. In fact, it is the study of FQHE that first brought in the concept of topological orders to the condensed matter physics community, opening an era of topology in condensed matter physics that extends beyond the traditional Landau paradigm of spontaneous symmetry breaking [37] (as well as renormalization group analysis) and Landau Fermi liquid theory [38]. As an intrinsic 2D systems, twisted

¹Landau claim the non-existence based on the experimental facts that no divergence has been observed under a disorder to order (like liquid to crystal) phase transition. But most arguments are wrong here due to the presence of lattice structure and the absence of divergence.

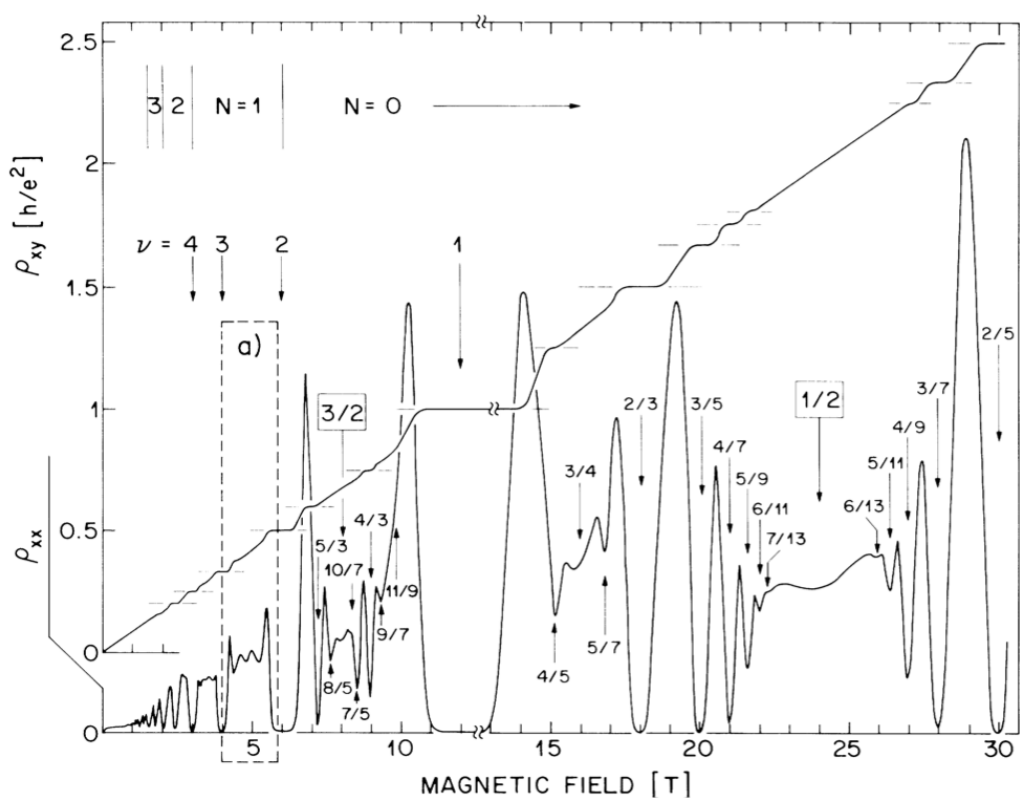


Figure 1.1: **Fractional Quantum Hall Effect** extracted from [1]. Fractional plateaus of transverse resistance ρ_{xy} observed in GaAs/AlGaAs heterostructures at low temperatures and high magnetic fields, quantized to fractional values of h/e^2 at various filling factors $\nu = 1/3, 2/5, 3/7$, etc. Note: $\nu = 1/2$ is metallic — there is no plateau at all.

vdW materials is much more complicated than the *isotropic* electronic liquids in GaAs/AlGaAs heterostructures² due to the presence of crystalline symmetries. The coexistence of symmetries and topological orders may enrich the phase diagrams, leading us to a more exotic regime of *symmetry-enriched topological orders* (SET) [39, 32], see in Fig. 1.2.

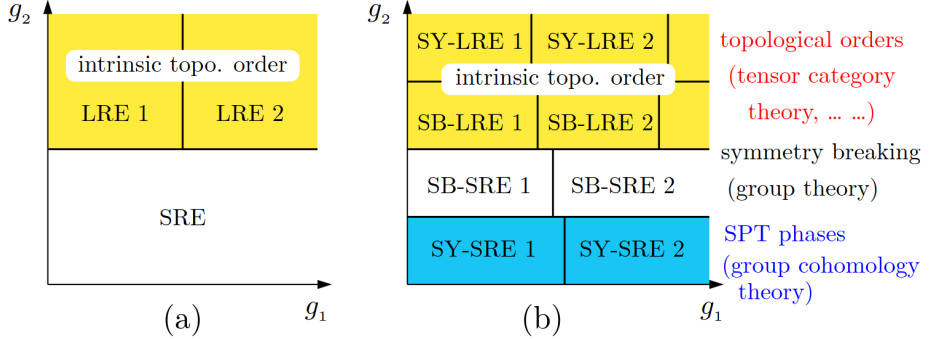


Figure 1.2: **Illustration of Short-range Entangled and Long-range Entangled States** adapted from Ref. [2]. **(a)**. Possible phase diagram for a Hamiltonian $H(g_1, g_2)$ without any symmetry. **(b)**. Possible phase diagram for a Hamiltonian $H(g_1, g_2)$ with some symmetries. All shaded regions in (a) and (b) represent the phases with short range entanglement (i.e. those ground states can be transformed into a direct product state via a generic LU transformations that do not have any symmetry).

Generally speaking, twisted vdW materials stands as new platform to explore the interplay between crystalline symmetries and TO, in particular in illustration of SET states. For instance, as a significant part of this thesis, we study fractional Chern insulators (FCI), the lattice analogue of FQHE, as the interplay of intrinsic topological orders and crystalline symmetries, which is recently realized in twisted vdW materials [8, 9, 40, 41, 42].

1.1.2 On Moiré Physics

The highlights of twisted physics is the possible formation of moiré patterns with the presence of twisting angles, which brings another long-range length scale or low-energy scale physics to the electronic system (we coin it as the *moiré physics*). Theoretically, the effective field theory, along with Anderson's pioneering work on the declaration of independence for condensed matter physics [43], has recognize the existence of infrared (IR) and ultra-violet (UV) scales in each field of physics. In contrast to high-energy physics, where IR corresponds to the energy scale of the Large Hadron Collider (LHC) and UV corresponds to the unreachable Planck length related to cosmic inflation and grand unification, condensed matter physics naturally has its own IR and UV limits — the lattice constants (short-range and high-energy) and the sample sizes (long-range and low-energy), see Fig. 1.3.

Experimentally, a natural advantage of condensed matter physics is that we can employ various kinds of probes across all energy scales. At the UV scale, we can image the electronic density of states using a scanning tunneling microscope (STM). Slightly larger than the atomic length scale, we have optical and ARPES measurements. Close to the IR limit, across the entire sample, we have transport measurements. These probes

²In GaAs/AlGaAs heterostructures, there is always a Galilean invariance for the electronic liquids.

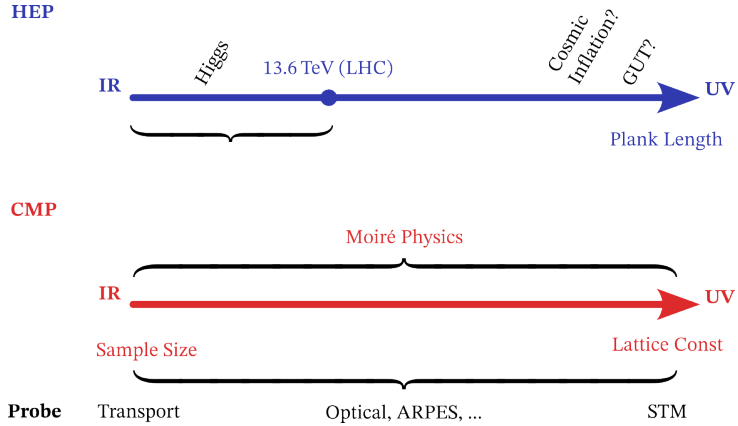


Figure 1.3: **UV-IR Energy Scales in High Energy and Condensed Matter Physics.**

have been traditionally applied to different materials and systems. However, in twisted vdW materials, where moiré physics comes into play, although the UV details is not altered, the physical length scale can be significantly tuned with the twisting angle. This provides a unified platform for all these experimental probes to work together. The most famous example would be the significant flatten of the Dirac dispersions in twisted bilayer graphene [44, 45]. As a result, the extended tunability and the unified experimental approach provide the primary reasons why twisted physics has garnered so much attention in recent years.

1.1.3 As a New Experimental Knob

Even without moiré physics, twisting angle itself can still serve as an extra tuning parameters along with the existing ones, including magnetic fields, gating fields, and strains. If there is a phase space of all tuning parameters, then consider twisted vdW materials is equivalent to introduce another dimension, which must be helpful for search of quantum phases, in particular for the situation when tuning other existing parameters cannot reach the target exotic phases.

For example, when considering twisted cuprates, theoretically it is proposed to have a spontaneous time-reversal symmetry (TRS) breaking when the twisting angle is close to $\theta \approx 45^\circ$, giving rise to the presence of topological superconductors (TSC) phases, which is rarely realized in conventional materials, as is shown in Fig.1.4.

In a similar proposal of twisted cuprates, another group of Rutgers analyzes the node movement for small twisting angles regimes, unveil the existence of “magic angle” not due to moiré physics at all, but from the appearance of *quadratic band touch point* (QBT), from which plenty of topological phase transitions can be tuned. In particular, when a vertical supercurrent is inserted, Chern number transfer would happen, leading to the realization of chiral topological superconductivity [4, 46]. The appearance of QBT can be summarized as following:

1. Two overlapped fermi surfaces, with two superconducting nodes live on them, get separated due to the interlayer tunneling t_{\perp} ;
2. The nodes get close after twisting, leading to QBT appears at some magin angle θ_{MA} .

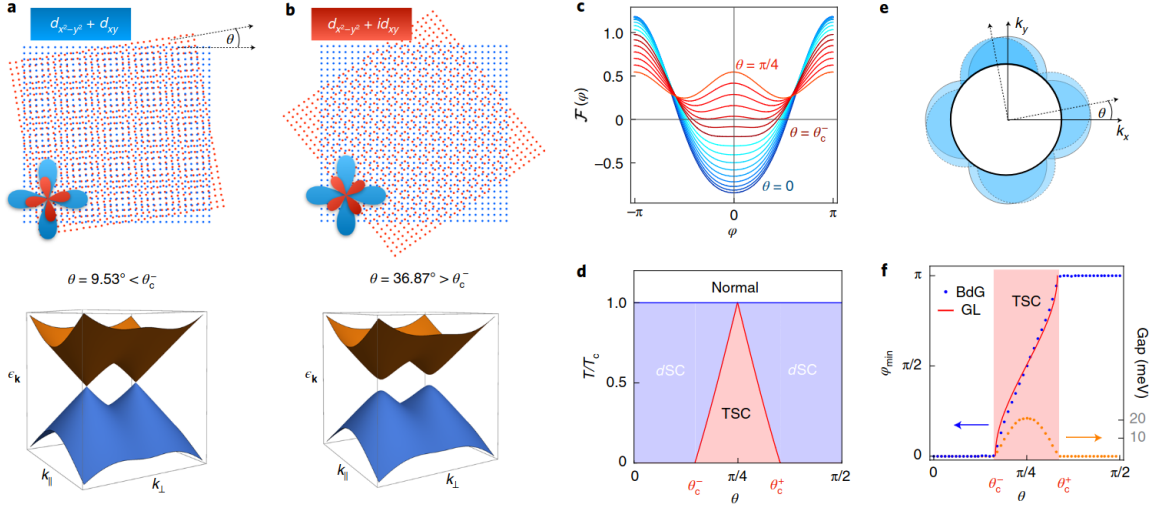


Figure 1.4: High-Temperature Topological Superconductors in Twisted Cuprates extracted from Ref. [3]. **(a)** at small twisting angle $\theta < \theta_c^-$ the free energy is minimized when the interlayer phase differences $\varphi = 0$, resulting in a split Dirac cone with TRS. **(b)** at large twisting angle $\theta > \theta_c^+$ the free energy is minimized when $\varphi \neq 0$, resulting in a spontaneous TRS breaking with a fully gapped cone. **(d)** Phase diagram based on Ginzburg-Landau free-energy analysis.

as is illustrated Fig.1.5.

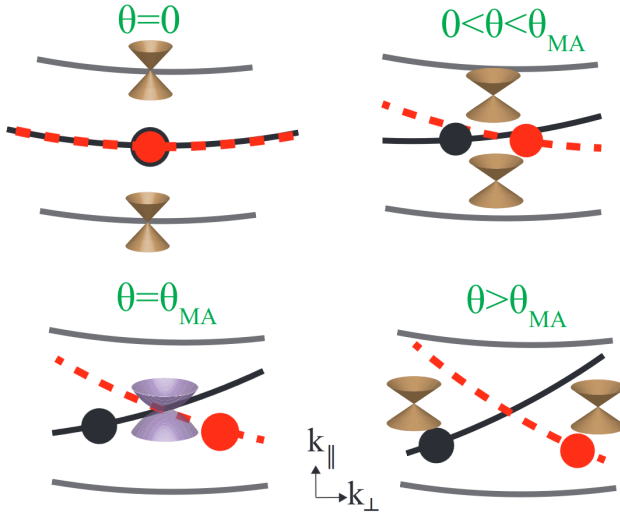


Figure 1.5: Node Movement for Twisted Nodal Superconductors adapted from Ref. [4].

1.1.4 As a Platform for Quantum Simulations

As is discussed before, the unique feature for the platform of twisted vdW materials is the possible presence of the moiré physics. The size of Moiré patterns are tightly connected with the twisting angles, so can be used to cover a wide range of physical length/energy scales, which can be useful for searching of more exotic phases.

The most famous example, as a declaration on the born of twisted physics (or twistronics), is the discovery of correlated insulating phases and unconventional superconductivity in twisted bilayer graphene (tBLG) [45, 6], as is shown in Fig.1.6. Although the superconducting transition temperature seems to be low in tBLG, it indeed falls into the strongly-correlated regime³ because of its much lower carrier density in the moiré superlattice (around $1.0 \times 10^{12} \text{ cm}^{-2}$ compared to the cuprates around $1.0 \times 10^{14} \text{ cm}^{-2}$). Thereafter, extensive work

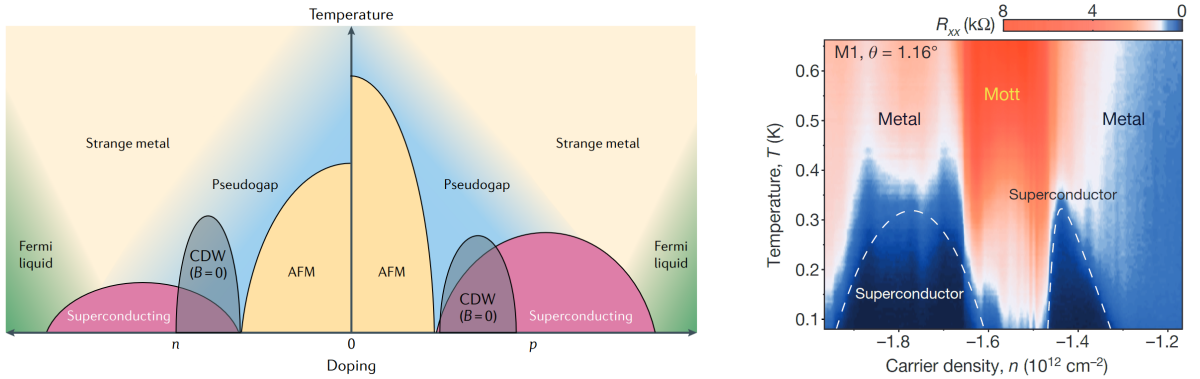


Figure 1.6: **Phase Diagram for the Unconventional Superconductivity** extracted from Ref. [5] and Ref. [6]. The superconducting domes adjacent to mott insulating phase is similar in cuprates phase diagram (left) and tBLG phase diagram (right).

of correlated physics around the superconducting phases has been studied in tBLG, including the competing orders like nematicity [47], and the linear- T resistivity in strange metals [48]. Outside of superconductivity, there are other correlated phenomena, including the ferromagnetism [49], quantum anomalous Hall effect [50], and even the fractional chern insulators [7] (still with small external magnetic fields, though) has been found in tBGL, see Fig.1.7.

Apart from graphene, the huge family of transition metal dichalcogenides (TMDs) also provide other choices for the building blocks of twisted 2D vdW materials. Correlated phases like mott insulators can still be realized [51, 52] in twisted TMD, as flat bands are also reproducible either due to moiré physics or lattice relaxation [53, 54]. But more importantly, due to the more complicated electronic band structures [10] and extra controllable knobs like valley/spin degrees of freedom [11], the twisted TMD platform can be expected to realize more exotic phases. The most convincing example would be the realization on the phase of fractional Chern insulators (FCI), which is numerically heavily studied one decade ago [55, 56, 57, 58], as a natural theoretical extension of FQHE on lattices, but has never be realized in experiments until last year (2023), when three independently groups in UW [8, 9], Cornell [41], and SJTU [42] claim the observation of fractional quantum anomalous Hall effect (FQAH) in twisted MoTe₂ (tMoTe₂), as is show in Fig. 1.8. As another interesting fact, fractional quanutum anomalous Hall effects are also realized in rhombohedral pentalayer graphene (RPG)-hBN moiré superlattice very recently in MIT group [40], exhibiting the power of both stacking and twisting engineerings.

³Actually tBLG is more strongly-correlated in comparison with cuprates.

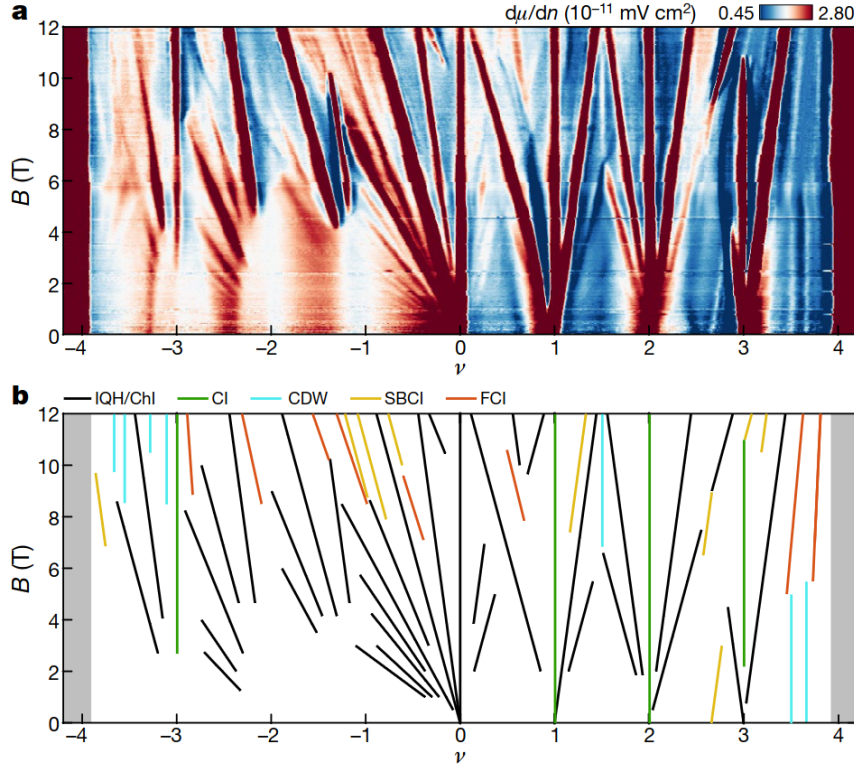


Figure 1.7: **Fractional Chern Insulators in tBLG** adapted from Ref.[7]. Streda formula $C = \frac{\partial n}{\partial B}$ can be used to extract the states. Here ν is the number of electrons per moiré unit cell, and the FCI states are those that possess both fractional slopes and fractional interceptions.

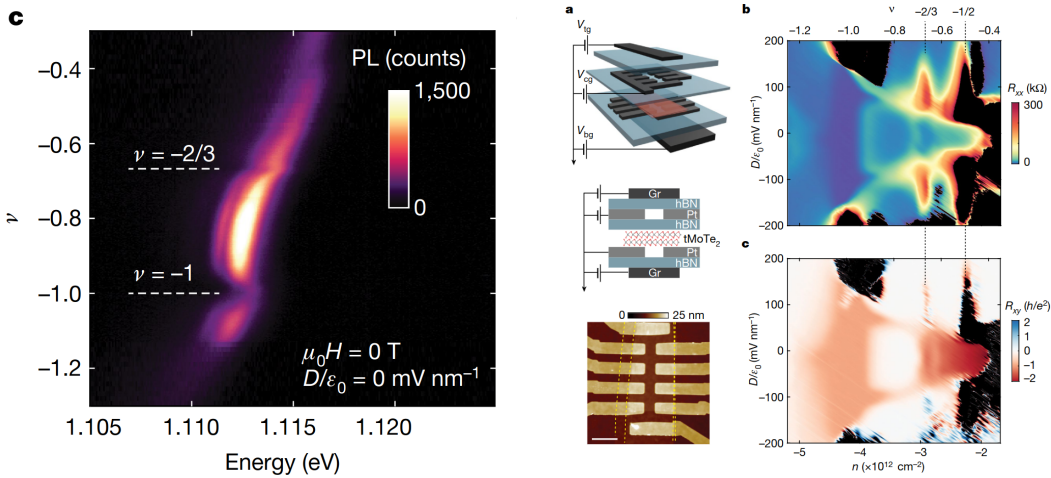


Figure 1.8: **Experimental Obversvation of Fractional Quantum Anomalous Hall Effects in tMoTe₂** extracted from Ref. [8] (left) and Ref. [9] (right).

1.2 Structure of the Thesis

In this thesis, I will focus on the study of the quantum phases of matter in two-dimensional space, particularly in the context of the twisted 2D vdW materials exhibiting complexities from the interplay of symmetry, topology (either free-fermion topology or in the sense of topological orders), and strong correlations. The thesis is organized as follows:

- In the first (this) chapter, I briefly discuss the motivation for studying the twisted 2D vdW materials, from the perspective of both experimental feasibility and theoretical complexity. Due to the unique features of moiré physics, twisted 2D vdW materials appears as the new platform for exploring exotic quantum phases of matter.
- In the second chapter, to make the thesis self-contained, I will introduce some necessary background, starting from simple $k \cdot p$ analysis of graphene and transition metal dichalcogenides (TMD) to a general derivation for the moiré continuum Hamiltonian. This chapter will also include the basic knowledge of fractional quantum Hall effect (FQHE), in particular the vortex-binding picture of composite fermions (CF), and some previous theoretical efforts on mapping fractional Chern insulators (FCI) states to the lowest Landau levels (LLL).
- As the main part of the thesis, I will list three of my works on twisted 2D vdW materials:
 - The first long and recent work is for fractional Chern insulators, the lattice analogue of FQHE, realized in recent experiments. To address many fundamental questions closely related to the microscopic understandings of FCI, we propose a projective construction based on Murthy-Shankar's CFs. The construction mainly splits into four steps: a Chern band to LLL mapping, the CF substitution on lattice, a CF mean-field state and computation of CF excitations (as magnetorotons), and the electronic projections. In construction of the framework, all factors of complexity mentioned above get intertwined, including moiré physics, strong correlations, and symmetry-enriched topological orders.
 - The last two works are about twisted 2D superconductors in small twisting angle regime. The first work is to extend the picture of topological phase transitions in twisted cuprates to twisted Ising superconductors like NbSe_2 and TaS_2 , to give another platform for realization of chiral topological superconductivity. The second work is to take the twisted 2D superconductors as a general platform for transport measurements breaking, where we propose the supercurrent-induced anomalous thermal Hall effects as a sharp probe to the superconducting gap anisotropy.

Chapter 2

Background

2.1 Twisted Moiré Physics

2.1.1 Transition Metal Dichalcogenides

Graphene, as the most famous 2D materials first discovered in 2004 by Geim and Novoselov [21], is well-known for the presence of Dirac points in its band structure.

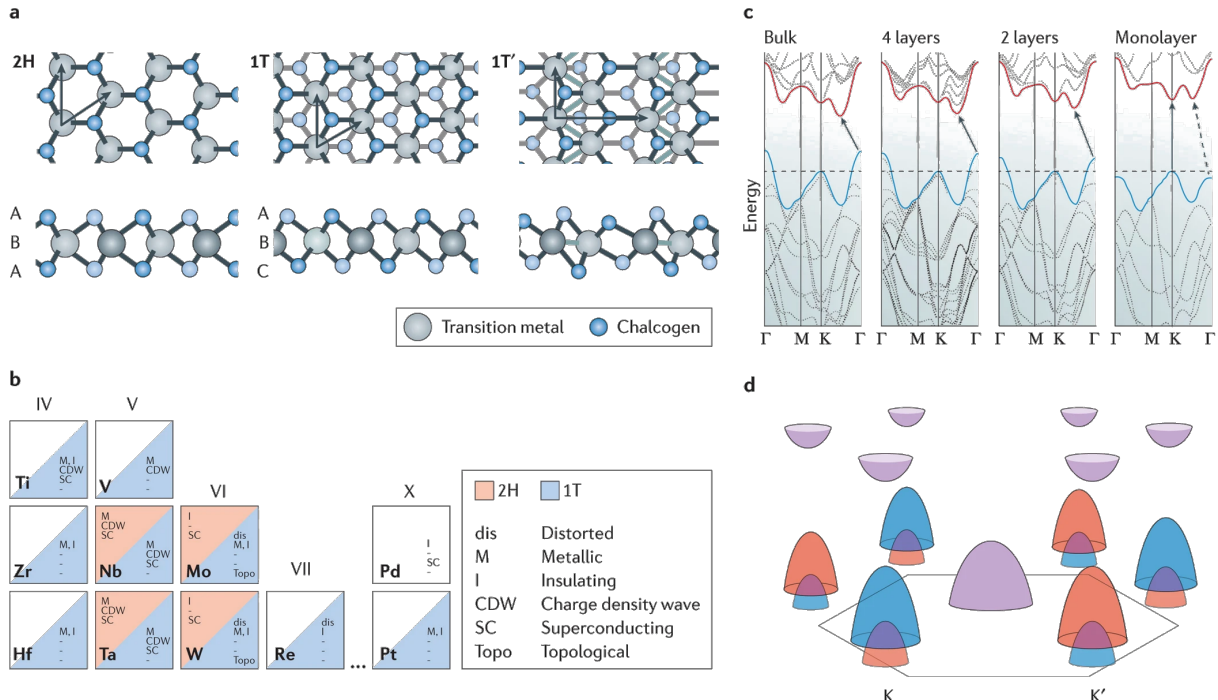
$$H_K(\mathbf{k}) = \hbar v_F \mathbf{k} \cdot \boldsymbol{\tau} \equiv \hbar v_F |\mathbf{k}| \begin{pmatrix} e^{-i\theta_k} \\ e^{i\theta_k} \end{pmatrix} \quad (2.1)$$

with the angle of the momentum $\theta_k \equiv \arctan \frac{k_y}{k_x}$.

Transition metal dichalcogenides (TMDs) of chemical formula MX_2 , on the other hand, has a more complicated structure comprising a plane having hexagonally-placed transition metal atoms M (group-IIIB to group-IIB) placed between two chalcogen atom-based hexagonal planes X (e.g., S, Se, Te). There are three monolayer structures: the *trigonal prismatic* 1H phase, the *distorted octahedral* 1T phase, and the *dimerized* 1T' phase, as are shown in Fig. 2.1. We will mostly focus on the group V and group VI transition metal elements, particularly those with 1T and 1T' phases shown to be unstable. So without loss of generalization, when we talk about monolayer TMDs in this thesis, we always refer to the 1H phase structure.

For monolayer TMDs of 1H phase, the corresponding bulk material are mostly of 2H stacking form, with *alternating* alignment of transition metal atoms and chalcogen atoms, as is shown in (a) in Fig. 2.2. Experimentally, there has been reports on the emergence of the peak in the optical spectroscopy study in Ref. [59] and photoluminescence (PL) signals in Ref. [60], which is ascribed as the manifestation on the evolution of the TMD band structure from bulk's indirect gap to monolayer's direct K - K' gaps, see (c) in Fig. 2.1.

Taking group-IV dichalcogenides MX_2 as the example, the 2H stacking bulk material has space group D_{6h} with inversion symmetry (see (a) in Fig. 2.2), but reduces to D_{3h} breaking the inversion symmetry down to monolayers. For monolayer MX_2 , DFT calculation tells that the relevant orbitals within the conduction and valence bands around K and K' points are mostly from d-orbitals [61]. From the character table of D_{3h} (see, for example, <http://symmetry.jacobs-university.de/cgi-bin/group.cgi?group=603&option=>



Nature Reviews | Materials

Figure 2.1: Structure and electronic properties of TMDs adapted from Ref. [10]. **(a)** Atomic structure of single layers of TMD in their *trigonal prismatic* (2H), *distorted octahedral* (1T) and *dimerized* (1T') phases. **(b)** “Periodic table” of known layered TMDs, organized based on the transition metal elements, their existing structural phases (2H, 1T and 1T'), and the observed electronic phases (see the right panel). **(c)** Evolution of the band structure of 2H-MoS₂ from bulk material down to monolayers. Clearly a indirect gap to direct gap transition occurs for monolayer material only. **(d)** Schematic band structure of 2H-MoS₂, showing the spin splitting (orange and blue colors) at K and K' points.)

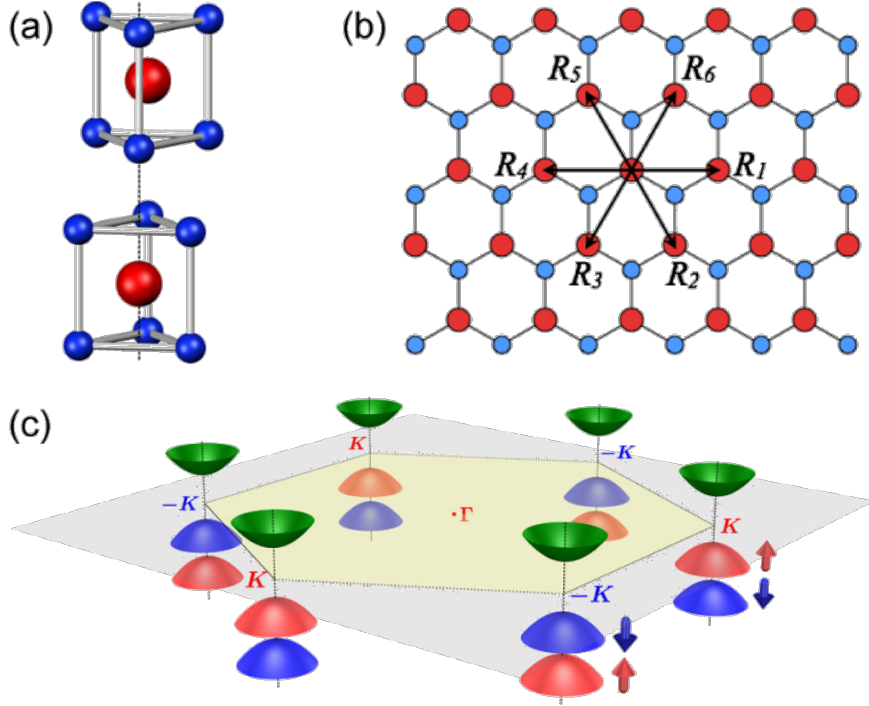


Figure 2.2: **MoS₂ Crystal Structure and Band Structure** adapted from Ref. [11]. **(a)** The unit cell of bulk 2H-MoS₂. **(b)** Top view of MoS₂ monolayer. **(c)** Schematic drawing of the band structure at the band edges located at the K points.

4), we know that the trigonal prismatic crystal field splits the d-orbitals of transition metal elements into three groups: $A'_1(d_{z^2})$, $E'(d_{xy}, d_{x^2-y^2})$, and $E''(d_{xz}, d_{yz})$, where the former two groups A'_1 and E' is even under the in-plane mirror symmetry $\sigma_h : z \rightarrow -z$, while the latter one E'' is odd under σ_h . Now that only two bands are concerned in our analysis: the conduction band and the valence band, we can simply take the irreps A'_1 and E' into account, resulting in a simple two-band model $H_\tau(\mathbf{k}) = \mathbf{d}(\mathbf{k}) \cdot \boldsymbol{\sigma}$ if the spin-orbit coupling is temporarily ignored.

To the lowest-order expansion, the constant part of the diagonal terms represent the K - K (or K' - K') direct band gap Δ . While for the off-diagonal term, we can either use the brute-force expansion and fix the expansion coefficients using C_3 rotation transformation as we did for graphene, or use the standard $\mathbf{k} \cdot \mathbf{p}$ analysis [62, 63, 64] by computing the matrix element $\langle \psi_a | \frac{\hbar}{m} \mathbf{k} \cdot \hat{\mathbf{p}} | \psi_b \rangle$ for $|\psi_{a,b}\rangle \in \{|\psi_{A'_1}\rangle, |\psi_{E'}\rangle\}$. Note: not all terms survives in such matrix element. In fact, because we have the rotation eigenvalues $C_3|\psi_{A'_1}\rangle = |\psi_{A'_1}\rangle$ and $C_3|\psi_{E'}\rangle = e^{i\frac{2\pi}{3}}|\psi_{E'}\rangle$ (for K -valley, for example), and for $\hat{p}_\pm \equiv \hat{p}_x \pm i\hat{p}_y$ we have $C_3\hat{p}_\pm C_3^\dagger = e^{i\mp\frac{2\pi}{3}}$, the C_3 rotation transformation forces either term within $H_{\mathbf{k} \cdot \mathbf{p}} \equiv \frac{\hbar}{2m} \mathbf{k} \cdot \hat{\mathbf{p}} \equiv \frac{\hbar}{2m} (k_+ \hat{p}_- + k_- \hat{p}_+)$ to be vanishing in the off-diagonal matrix element, leaving simply the massive Dirac Hamiltonian (with insertion of valley index)

$$H_{\text{eff}}^{\text{SOC off}} = H_0 + H_{\mathbf{k} \cdot \mathbf{p}} = \begin{pmatrix} \frac{\Delta}{2} & Ak_- \\ Bk_+ & -\frac{\Delta}{2} \end{pmatrix} \equiv \hbar v_F (\tau k_x \sigma_x + k_y \sigma_y) + \frac{\Delta}{2} \sigma_z. \quad (2.2)$$

Now let us include the spin-orbit couplings (SOC) in the $\mathbf{k} \cdot \mathbf{p}$ analysis

$$H_{\mathbf{k} \cdot \boldsymbol{\pi}} \equiv \frac{\hbar}{m} \mathbf{k} \cdot \left(\mathbf{p} + \frac{\hbar}{4mc^2} \mathbf{s} \times \nabla V \right).$$

The SOC Hamiltonian can also be written as $H_{\text{SOC}} = \lambda \mathbf{L} \cdot \mathbf{s} = \lambda(L_z s_z + L_+ s_- + L_- s_+)$. Noting that both L_+ and L_- are odd under in-plane mirror symmetry σ_h , while L_z is even, so the orbital-part of the matrix element satisfying $\langle \psi_a | L_\pm | \psi_b \rangle \equiv \langle \psi_a | s_h^{-1} s_h L_\pm s_h^{-1} s_h | \psi_b \rangle$ must connect states whose orbital contents behaves *differently* under σ_h . However, our chosen basis $|\psi_{A'_1}\rangle$ and $|\psi_{E'}\rangle$ are both even under σ_h , so we are left with simply the L_z term, resulting

$$H_{\text{eff}} = H_0 + H_{\mathbf{k} \cdot \boldsymbol{\pi}} = H_{\text{eff}}^{\text{SOC off}} \otimes s_0 + \begin{pmatrix} \Delta_{A'_1\text{-SOC}} & \\ & \Delta_{E'\text{-SOC}} \end{pmatrix} \otimes s_z \quad (2.3)$$

with $\Delta_{A'_1\text{-SOC}}$ and $\Delta_{E'\text{-SOC}}$ dictating the band splittings due to SOC. The energy scale of them can be read from the DFT results in Fig. 2.3, where $\Delta_{A'_1\text{-SOC}}$ always turns out to be almost vanishing so we just ignore it. The

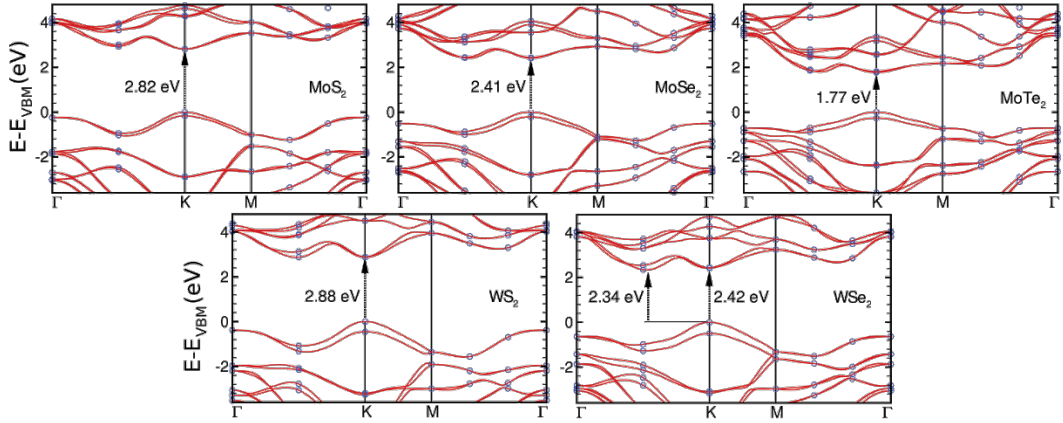


Figure 2.3: DFT Band Structures for Several MX_2 Monolayer Materials (extracted from [12]).

final form of the effective Hamiltonian (with insertion of valley index)

$$H_{\text{eff}} = \left(\hbar v_F (\tau k_x \sigma_x + k_y \sigma_y) + \frac{\Delta}{2} \sigma_z \right) \otimes s_0 - \lambda \tau \frac{\sigma_z - \mathbf{1}}{2} \otimes s_z. \quad (2.4)$$

2.1.2 Moiré Continuum Hamiltonian

Moiré patterns are known as the interference patterns generated when two or more periodic structures of the same scale (lattice constant a) are overlaid. The interference pattern exhibits a new large-scale (coin as *Moiré scale*) periodic structure on top of the original one (which can be different from the original ones), so that the original lattice information is smeared out, leaving physics occurring at such new Moiré scale.

The general bilayer system can be described with two set of grids spanned by $\{\mathbf{R}_{l,1}, \mathbf{R}_{l,2}\}$ with $l = 1, 2$ labeling the layers. We are interested in the physics when the two layers are related with some rotation \mathcal{R}_θ and some displacement \mathbf{d} . Namely the same cartesian coordinate within these two coordinates systems are

related with the linear transformation: $\mathbf{r}_{l',\alpha} = \mathcal{R}_\theta \mathbf{r}_{l,\alpha} + \mathbf{d}$. This leads to a useful identity for the inner product that

$$\mathbf{k}_{l'} \cdot \mathbf{r}_{l',\alpha} \equiv (\mathcal{R}_\theta \mathbf{k}_l) \cdot (\mathcal{R}_\theta \mathbf{r}_{l,\alpha} + \mathbf{d}) \equiv \mathbf{k}_l \cdot \mathbf{r}_{l,\alpha} + \mathbf{k}_l \cdot \mathbf{d}, \quad (2.5)$$

where we recognize $\mathbf{k}_l \equiv \mathcal{R}_\theta \mathbf{k}_{l'}$.

Each layer possesses its own Bloch states

$$|\mathbf{k}_l, \alpha\rangle = \frac{1}{\sqrt{N}} \sum_{\mathbf{R}_l} e^{i\mathbf{k}_l \cdot (\mathbf{R}_l + \boldsymbol{\tau}_{l,\alpha})} |\mathbf{R}_l + \boldsymbol{\tau}_{l,\alpha}\rangle,$$

so the general momentum-space Hamiltonian of the bilayer system can be obtained from the matrix element

$$\langle \mathbf{k}_l, \alpha | H | \mathbf{k}'_{l'}, \alpha' \rangle = \frac{1}{N} \sum_{\mathbf{R}_l, \mathbf{R}'_{l'}} e^{-i\mathbf{k}_l \cdot (\mathbf{R}_l + \boldsymbol{\tau}_{l,\alpha})} e^{i\mathbf{k}'_{l'} \cdot (\mathbf{R}'_{l'} + \boldsymbol{\tau}_{l',\alpha'})} \langle \mathbf{R}_l + \boldsymbol{\tau}_{l,\alpha} | H | \mathbf{R}'_{l'} + \boldsymbol{\tau}_{l',\alpha'} \rangle.$$

Since the Wannier center is highly localized in real-space, it is OK to take the real-space matrix element on the right hand side as a function of the distance of two Wannier centers only (and of course also labelled with the species of the Wannier orbitals), i.e.

$$\langle \mathbf{R}_l + \boldsymbol{\tau}_{l,\alpha} | H | \mathbf{R}'_{l'} + \boldsymbol{\tau}_{l',\alpha'} \rangle \simeq H_{l,\alpha; l', \alpha'}(\mathbf{R}_l + \boldsymbol{\tau}_{l,\alpha} - \mathbf{R}'_{l'} - \boldsymbol{\tau}_{l',\alpha'}),$$

which is known as the *two-center approximation* [44]. Scalar function $H(\mathbf{R}_l + \boldsymbol{\tau}_{l,\alpha} - \mathbf{R}'_{l'} - \boldsymbol{\tau}_{l',\alpha'})$ is still periodic. Switching to momentum space, and using the Poisson summation formula

$$\frac{1}{N} \sum_{\mathbf{R}} e^{i\mathbf{R} \cdot \mathbf{q}} = \sum_{\mathbf{G}} \mathcal{F}[e^{i\mathbf{R} \cdot \mathbf{q}}](\mathbf{G}) = \sum_{\mathbf{G}} \delta_{\mathbf{q}, \mathbf{G}}$$

we have

$$\begin{aligned} \langle \mathbf{k}_l, \alpha | H | \mathbf{k}'_{l'}, \alpha' \rangle &= \frac{1}{N} \sum_{\mathbf{R}_l, \mathbf{R}'_{l'}} e^{-i\mathbf{k}_l \cdot (\mathbf{R}_l + \boldsymbol{\tau}_{l,\alpha})} e^{i\mathbf{k}'_{l'} \cdot (\mathbf{R}'_{l'} + \boldsymbol{\tau}_{l',\alpha'})} \frac{1}{NA} \sum_{\mathbf{q}} e^{i\mathbf{q} \cdot (\mathbf{R}_l + \boldsymbol{\tau}_{l,\alpha} - \mathbf{R}'_{l'} - \boldsymbol{\tau}_{l',\alpha'})} H_{l,\alpha; l', \alpha'}(\mathbf{q}) \\ &= \frac{1}{A} \sum_{\mathbf{q}} \left(\frac{1}{N} \sum_{\mathbf{R}_l} e^{i\mathbf{R}_l \cdot (\mathbf{q} - \mathbf{k}_l)} \right) \left(\frac{1}{N} \sum_{\mathbf{R}'_{l'}} e^{i\mathbf{R}'_{l'} \cdot (\mathbf{q} - \mathbf{k}'_{l'})} \right) e^{i\boldsymbol{\tau}_{l,\alpha} \cdot (\mathbf{q} - \mathbf{k}_l)} e^{-i\boldsymbol{\tau}_{l',\alpha'} \cdot (\mathbf{q} - \mathbf{k}'_{l'})} H_{l,\alpha; l', \alpha'}(\mathbf{q}) \\ &= \frac{1}{A} \sum_{\mathbf{q}} \sum_{\mathbf{G}_l, \mathbf{G}_{l'}} \delta_{\mathbf{q} - \mathbf{k}_l, \mathbf{G}_l} \delta_{\mathbf{q} - \mathbf{k}'_{l'}, \mathbf{G}_{l'}} e^{i\boldsymbol{\tau}_{l,\alpha} \cdot (\mathbf{q} - \mathbf{k}_l)} e^{-i\boldsymbol{\tau}_{l',\alpha'} \cdot (\mathbf{q} - \mathbf{k}'_{l'})} H_{l,\alpha; l', \alpha'}(\mathbf{q}) \\ &= \frac{1}{A} \sum_{\mathbf{G}_l, \mathbf{G}_{l'}} \delta_{\mathbf{k}_l + \mathbf{G}_l, \mathbf{k}'_{l'} + \mathbf{G}_{l'}} e^{i\boldsymbol{\tau}_{l,\alpha} \cdot \mathbf{G}_l} e^{-i\boldsymbol{\tau}_{l',\alpha'} \cdot \mathbf{G}_{l'}} H_{l,\alpha; l', \alpha'}(\mathbf{k}_l + \mathbf{G}_l) \\ &= \frac{1}{A} \sum_{\mathbf{G}_l, \mathbf{G}_{l'}} \delta_{\mathbf{k}_l + \mathbf{G}_l, \mathbf{k}'_{l'} + \mathbf{G}_{l'}} e^{i\mathbf{G}_l \cdot (\boldsymbol{\tau}_{l,\alpha} - \boldsymbol{\tau}_{l',\alpha'})} e^{-i\mathbf{G}_l \cdot \mathbf{d}} H_{l,\alpha; l', \alpha'}(\mathbf{k}_l + \mathbf{G}_l), \end{aligned} \quad (2.6)$$

where we use the fact that the two layers share the same value of \mathbf{G} but differ by at most some rotations, and the linear transformation Eq.(2.5).

The momentum-space expression Eq. (2.6) is the general result of the two-center approximation. It is true for both intralayer hopping processes and interlayer tunneling processes. The Dirac delta function signatures

the momentum conservation of the hopping/tunneling processes within/across top and bottom layers. And the exponential $e^{-i\mathbf{G}_l \cdot \mathbf{d}}$ signatures the stacking dependence ($\mathbf{d} = 0$ for AA stacking). It turns out to be more helpful to explicitly split Eq.(2.6) into intralayer and interlayer parts:

$$\begin{aligned} \langle \mathbf{k}_l, \alpha | H | \mathbf{k}'_{l'}, \alpha' \rangle &= \delta_{l,l'} \frac{1}{A} \left[\sum_{\mathbf{G}_l} \delta_{\mathbf{k}_l, \mathbf{k}'_{l'}} H_{l,\alpha;l',\alpha'}(\mathbf{k}_l + \mathbf{G}_l) e^{-i\mathbf{G}_l \cdot \mathbf{d}} \right] \\ &\quad + (1 - \delta_{l,l'}) \frac{1}{A} \left[\sum_{\mathbf{G}_l, \mathbf{G}_{l'}} \delta_{\mathbf{k}_l + \mathbf{G}_l, \mathbf{k}'_{l'} + \mathbf{G}_{l'}} H_{l,\alpha;l',\alpha'}(\mathbf{k}_l + \mathbf{G}_l) e^{i\mathbf{G}_l \cdot (\tau_{l,\alpha} - \tau_{l',\alpha'})} e^{-i\mathbf{G}_l \cdot \mathbf{d}} \right] \\ &\equiv \delta_{l,l'} \delta_{\mathbf{k}_l, \mathbf{k}'_{l'}} \frac{1}{A} \left[H_{l,\alpha;l',\alpha'}(\mathbf{k}_l) + \sum_{\mathbf{G}_l \neq 0} H_{l,\alpha;l',\alpha'}(\mathbf{k}_l + \mathbf{G}_l) e^{-i\mathbf{G}_l \cdot \mathbf{d}} \right] \\ &\quad + (1 - \delta_{l,l'}) \frac{1}{A} \left[\sum_{\mathbf{G}_l, \mathbf{G}_{l'}} \delta_{\mathbf{k}_l + \mathbf{G}_l, \mathbf{k}'_{l'} + \mathbf{G}_{l'}} H_{l,\alpha;l',\alpha'}(\mathbf{k}_l + \mathbf{G}_l) e^{i\mathbf{G}_l \cdot (\tau_{l,\alpha} - \tau_{l',\alpha'})} e^{-i\mathbf{G}_l \cdot \mathbf{d}} \right], \quad (2.7) \end{aligned}$$

where we explicitly separate out the $\mathbf{G}_l = 0$ and $\mathbf{G}_l \neq 0$ term in Eq.(2.7), as is suggested in Ref. [65]. Clearly only the $\mathbf{G}_l = 0$ parts of the intralayer hoppings are diagonal in the original Bloch basis, while the $\mathbf{G}_l \neq 0$ part of both the intralayer hoppings and the interlayer tunnelings contribute to the off-diagonal terms. There are two kinds of summation in Eq.(2.7), $\sum_{\mathbf{G}_l}$ and $\sum_{\mathbf{G}_{l'}}$. Fortunately, both can be simplified from the following observations:

First of all, noting that we usually wish to derive the low-energy effective model for a small region of the BZ. For general discussion, let us denote such small region as \mathcal{K}_l , and consider the perturbation around that region $\mathbf{k}_l = \mathcal{K}_l + \delta\mathbf{k}_l$, then clearly we always have $|\delta\mathbf{k}_l - \delta\mathbf{k}_{l'}| \ll ||\mathcal{K}_l||$. On the other hand, the Dirac delta function in the interlayer tunneling term of Eq.(2.7) tells that the only non-vanishing contributions are those satisfying $\delta\mathbf{k}_l - \delta\mathbf{k}_{l'} = \mathcal{K}_l + \mathbf{G}_l - \mathcal{K}_{l'} - \mathbf{G}_{l'}$. But clearly **most of the differences between the two collections $\{\mathcal{K}_l + \mathbf{G}_l\}$ and $\{\mathcal{K}_{l'} - \mathbf{G}_{l'}\}$ are no less than $||\text{BZ}||$, except for those when they differ by just a rotation — this is reasonable because twisting angle θ appears as the only small parameter in our model setup.** As a consequence, the summation over $\mathbf{G}_{l'}$ is always associated with \mathbf{G}_l and gets highly suppressed for those terms satisfying $\mathbf{G}_{l'} = \mathbf{G}_l$, resulting in a simple summation over \mathbf{G}_l only.

Secondly, because the real-space profile $H_{l,\alpha;l',\alpha'}(\mathbf{R}_l + \tau_{l,\alpha} - \mathbf{R}_{l'} - \tau_{l',\alpha'})$ decays exponentially due to the locality of Wannier orbitals, the momentum-space profiles $H_{l,\alpha;l',\alpha'}(\mathbf{k}_l + \mathbf{G}_l)$ should also reflect such exponentially-decay behaviors. So **usually it is enough to keep only several low-order expansions for \mathbf{G}_l in $H_{l,\alpha;l',\alpha'}(\mathbf{k}_l + \mathbf{G}_l)$ respecting the crystal symmetries.**

Depending on the position of the target region \mathcal{K}_l , we are divided into two situations:

1. If the target region \mathcal{K}_l is indeed close to some high-symmetry points at the zone boundary, like the K -point (or K' -point) in twisted bilayer graphene or twisted MoTe₂, and the small M -pocket of twisted monolayer FeSe, the collection $\{\mathcal{K}_l + \mathbf{G}_l\}$ will introduce other high-symmetry points with different crystal momentum compatible with rotation symmetries.

If we denote $\mathbf{q}_1 \equiv \mathcal{K}_l - \mathcal{K}_{l'}$, and introduce the other rotation-related crystal momentum differences as a finite set $\{\mathbf{q}_i \equiv C_n^{i-1} \mathbf{q}_1\}$, then Any momentum shift differences satisfying $\delta_{\delta\mathbf{k}_l - \delta\mathbf{k}'_{l'}, \mathbf{q}_i}$ would contribute

to the interlayer tunnelings. Consequently, the momentum-space Hamiltonian becomes

$$\begin{aligned}
\langle \mathbf{k}_l, \alpha | H | \mathbf{k}'_{l'}, \alpha' \rangle &= \delta_{l,l'} \delta_{\mathbf{k}_l, \mathbf{k}'_{l'}} \frac{1}{A} \left[H_{l,\alpha;l',\alpha'} (\delta \mathbf{k}_l + \mathcal{K}_l) + \sum_{\mathbf{G}_l} H_{l,\alpha;l',\alpha'} (\delta \mathbf{k}_l + \mathcal{K}_l + \mathbf{G}_l) e^{-i \mathbf{G}_l \cdot \mathbf{d}} \right] \\
&\quad + (1 - \delta_{l,l'}) \frac{1}{A} \left[\sum_i \delta_{\delta \mathbf{k}_l - \delta \mathbf{k}'_{l'}, \mathbf{q}_i} H_{l,\alpha;l',\alpha'} (\delta \mathbf{k}_l + \mathcal{K}_l + \mathbf{G}_l) e^{i \mathbf{G}_l \cdot (\boldsymbol{\tau}_{l,\alpha} - \boldsymbol{\tau}_{l',\alpha'})} e^{-i \mathbf{G}_l \cdot \mathbf{d}} \right] \\
&\simeq \delta_{l,l'} \delta_{\mathbf{k}_l, \mathbf{k}'_{l'}} \left[h_{\alpha\alpha'}^l (|\mathcal{K}_l|) + \sum_{\mathbf{G}_l} V_{\alpha\alpha'}^l (|\mathcal{K}_l|) e^{-i \mathbf{G}_l \cdot \mathbf{d}} \right] \\
&\quad + (1 - \delta_{l,l'}) \left[\sum_i \delta_{\delta \mathbf{k}_l - \delta \mathbf{k}'_{l'}, \mathbf{q}_i} [T_i(\mathcal{K}_l)]_{\alpha,\alpha'} \right], \tag{2.8}
\end{aligned}$$

where we recognize $H_{l,\alpha;l',\alpha'} (\delta \mathbf{k}_l + \mathcal{K}_l + \mathbf{G}_l) \simeq H_{l,\alpha;l',\alpha'} (|\mathcal{K}_l|)$ for each term (higher order terms needs to be kept if $H_{l,\alpha;l',\alpha'} (|\mathcal{K}_l|) = 0$, like in tBLG), and the interlayer tunneling matrix (for $l \neq l'$) is

$$[T_i(\mathcal{K}_l)]_{\alpha\alpha'} \equiv w_{\alpha\alpha'} (|\mathcal{K}_l|) e^{i \mathbf{G}_l \cdot (\boldsymbol{\tau}_{l,\alpha} - \boldsymbol{\tau}_{l',\alpha'})} e^{-i \mathbf{G}_l \cdot \mathbf{d}}. \tag{2.9}$$

Note: Here all terms taking value around the small region \mathcal{K}_l , like $h_{\alpha\alpha'}^l (\mathcal{K}_l)$, $V_{\alpha\alpha'}^l (\mathcal{K}_l)$ and $[T_i(\mathcal{K}_l)]$ can be safely treated as constants.

To be more specific, let us consider the C_3 -rotation invariant case when $\mathcal{K}_l = \mathbf{K}_l$. Still if we denote $\mathbf{q}_1 \equiv \mathbf{K}_l - \mathbf{K}_{l'}$, the set of ALL symmetry-allowed momentum differences will contain only three elements $\{\mathbf{q}_1, \mathbf{q}_2, \mathbf{q}_3\}$ from three equivalent \mathbf{K}_l -point, where $\mathbf{q}_2 \equiv (\mathbf{K}_l + \mathbf{b}_{2,l}) - (\mathbf{K}_{l'} - \mathbf{b}_{2,l'}) = C_3 \mathbf{q}_1$ and $\mathbf{q}_3 \equiv (\mathbf{K}_l - \mathbf{b}_{1,l}) - (\mathbf{K}_{l'} - \mathbf{b}_{1,l'}) = C_3^2 \mathbf{q}_1$, corresponding to $\mathbf{G}_{l,i} \in \{\mathbf{0}, \mathbf{b}_{2,l}, \mathbf{b}_{1,l}\}$. So for AA-stacking region where $\mathbf{d} = 0$, the tunneling matrix reads

$$[T_1] = \begin{pmatrix} w_{AA} & w_{AB} \\ w_{BA} & w_{BB} \end{pmatrix}, \quad [T_2] = \begin{pmatrix} w_{AA} & w_{AB} e^{i \frac{2\pi}{3}} \\ w_{BA} e^{-i \frac{2\pi}{3}} & w_{BB} \end{pmatrix}, \quad [T_3] = \begin{pmatrix} w_{AA} & w_{AB} e^{-i \frac{2\pi}{3}} \\ w_{BA} e^{i \frac{2\pi}{3}} & w_{BB} \end{pmatrix}.$$

In particularly, it turns out to be helpful to introduce a lattice formed by iterative addition of $\{\mathbf{q}_1, \mathbf{q}_2, \mathbf{q}_3\}$, as is shown in Fig.2.4. The sites can be into two groups: from the top layer and from the bottom layer (they can only differ by some \mathbf{q}_i). Each group possesses a triangular lattice structure with common reciprocal vectors $\mathbf{b}_{M1} \equiv \mathbf{q}_1 - \mathbf{q}_3$ and $\mathbf{b}_{M2} \equiv \mathbf{q}_2 - \mathbf{q}_1$, which coincide exactly with the moiré reciprocal vectors. Inspired by Ref. [66], we can introduce two layer-dependent grids spanned by such small reciprocal vectors $\mathbf{Q}_l = m_{1,l} \mathbf{b}_{M1} + m_{2,l} \mathbf{b}_{M2}$, and one *common* moiré-scale crystal momentum \mathbf{k}_M satisfying $\mathbf{k}_l \equiv \mathbf{k}_M + \mathbf{K}_l + \mathbf{Q}_l \equiv \delta \mathbf{k}_l + \mathbf{K}_l$, then the momentum conservation condition reduces to $\sum_i \delta_{\delta \mathbf{k}_l - \delta \mathbf{k}'_{l'}, \mathbf{q}_i} \Rightarrow \sum_i \delta_{\mathbf{Q}_l - \mathbf{Q}_{l'}, \mathbf{q}_i}$. The Hamiltonian matrix Eq.(2.8) then can be expressed in such \mathbf{Q}_l -grids, which clearly exhibits a sparse matrix form.

2. If the target region \mathcal{K}_l is NOT at these high symmetry points around the zone boundary, like the case for twisted cuprates where nodal region dominates the tunnelings, and twisted monolayer NbSe₂ or TaS₂ where Γ -pockes dominates the tunnelings, then the collection $\{\mathcal{K}_l + \mathbf{G}_l\}$ will not introduce any other new crystal momentum within the BZ. Consequently, $\mathbf{q}_1 \equiv \mathcal{K}_l - \mathcal{K}_{l'}$ is the only rotation-symmetry allowed crystal momentum difference, and the general form of the momentum-space Hamiltonian re-

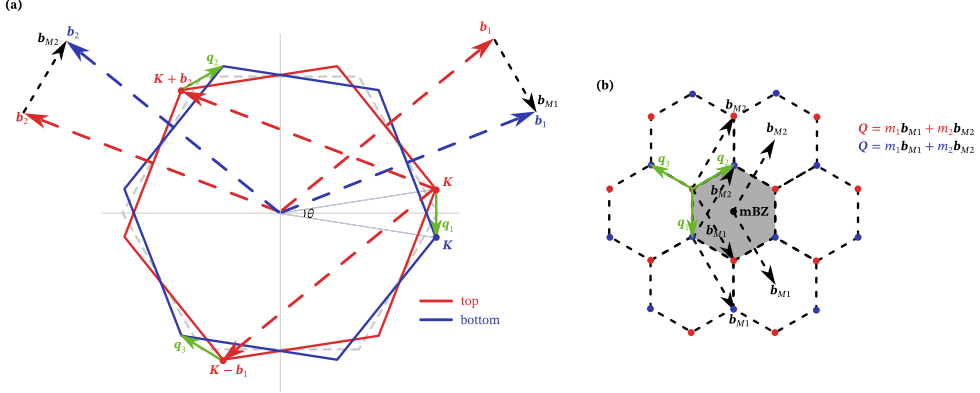


Figure 2.4: **Twisted BZ with K -valley Target Regions, mBZ , and Q_l Grids.** (a). Green arrows are three target-region crystal momentum differences $\{q_1, q_2, q_3\}$. (b). Iterative addition of the momentum differences forms two pair of triangular lattice $Q_l = m_{1,l}b_{M1} + m_{2,l}b_{M2}$ spanned by the moiré reciprocal vectors (red dots and blue dots).

duces to

$$\begin{aligned} \langle \mathbf{k}_l, \alpha | H | \mathbf{k}'_{l'}, \alpha' \rangle &= \delta_{l,l'} \delta_{\mathbf{k}_l, \mathbf{k}'_{l'}} \left[h_{\alpha\alpha'}^l(|\mathcal{K}_l|) + V_{\alpha\alpha'}^l \sum_{\mathbf{G}_l \neq 0} e^{-i\mathbf{G}_l \cdot \mathbf{d}} \right] \\ &\quad + (1 - \delta_{l,l'}) \delta_{\delta \mathbf{k}_l - \delta \mathbf{k}'_{l'}, \mathbf{q}_1} w_{\alpha,\alpha'}(|\mathcal{K}_l|). \end{aligned} \quad (2.10)$$

2.2 Fractional Quantum Hall Effect

2.2.1 Jain's Composite Fermion

Fractional quantum Hall effects (FQHE) are first discovered in GaAs/AlGaAs heterostructures with low carrier density and extremely strong magnetic fields [18, 1], where the Hall conductance is quantized to be $\sigma_{xy} = \nu \frac{e^2}{h}$ with plateaus $\nu = \frac{1}{3}, \frac{2}{5}, \frac{3}{7}, \dots$. Laughlin's celebrated wavefunction [67]

$$\psi_{1/m} = \prod_{i < j} (z_j - z_i)^m e^{-\sum_n \frac{|z_n|^2}{4}}$$

works well for main odd-denominator states $\nu = 1/m$, but fails to explain more general plateaus like $\nu = \frac{2}{5}, \frac{3}{7}, \dots$.

Jain's composite fermion theory [68, 69, 70] provides a more general framework to understand the fractional quantum Hall effect, for the plateaus of Jain's sequence $\nu = \frac{p}{2ps+1}$. The basic idea is to bound each electron with even number of fluxes, and taking the composite particle, i.e., the *composite fermions* (CF) as a good mean-field description of the FQHE, so that the strong-interacting electronic problem reduces to weakly-interacting CF problem, as is shown in Fig. 2.5. Now that composite fermions, as *fermionic* particles, fully fill p -CF Landau levels, the CF wavefunction must be Slater determinant $\chi_p(z, \bar{z})$. Plus the $2s$ flux-attachment

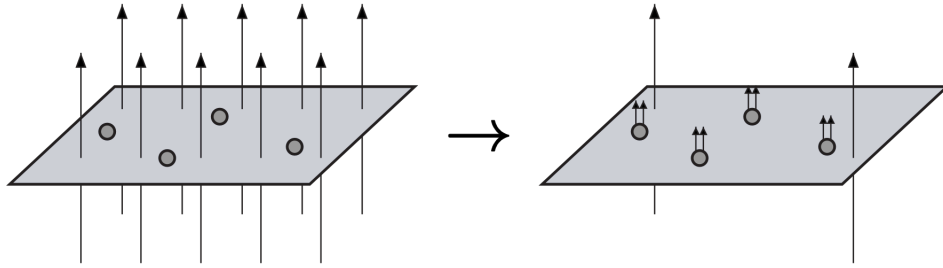


Figure 2.5: **Jain's Composite Fermion Theory** adapted from Ref. [13].

implemented with the Jastraw factor $(z_i - z_j)^{2s}$, the total electronic wavefunction then takes the form

$$\psi_{p/(2ps+1)} = \mathcal{P}_{\text{LLL}} \prod_{i < j} (z_i - z_j)^{2s} \chi_p(z, \bar{z}),$$

where \mathcal{P}_{LLL} is the necessary projection operator to the lowest Landau level (LLL) because the CF wavefunction may not live within LLL.

2.2.2 Murthy-Shankar's Algebraic Description of Composite Fermion

Jain's wavefunction successfully explain almost all plateaus in FQHE, and has been extensively examined by numerical simulations like overlap calculation with exact diagonalizations. However, the LLL projection \mathcal{P}_{LLL} is actually hard to implement in numerics. That motivates Murthy and Shankar to propose an algebraic description of composite fermion [71] that keeps electronic part of wavefunction live within the LLL.

The fundamental differences of Jain's theory and Murthy-Shankar's theory is that, Jain's CFs are composite particles of electrons and their attached fluxes, where magnetic fluxes pierces through ALL LLs so the LLL projection \mathcal{P}_{LLL} must be performed. While in Murthy-Shankar's theory every flux quanta is replaced with its dual vortex description, similar to the Abrikosov vortices in type-II superconductors where magnetic fluxes are pinned [72], and CFs are the composite particles of electrons and the vortices.

In such vortex-binding picture, both electrons and vortices clearly live within the LLL governed by the guiding-center coordinates \mathcal{R} , and the CF degrees of freedom of Jain's sequence $\nu = \frac{p}{2ps+1}$ can be constructed as [71, 73, 74]

$$\mathcal{R} = \frac{\mathcal{R}_e - c^2 \mathcal{R}_v}{1 - c^2}, \quad \eta = \frac{c}{1 - c^2} (\mathcal{R}_v - \mathcal{R}_e), \quad (2.11)$$

or inversely

$$\mathcal{R}_e = \mathcal{R} + c\eta, \quad \mathcal{R}_v = \mathcal{R} + \frac{1}{c}\eta. \quad (2.12)$$

Note: CFs can live in multiples of CF LLs, so both guiding-center coordinates \mathcal{R} and cyclotron motion coordinates η get involved in CF degrees of freedom. Another thing one needs to keep in mind is that, Murthy-Shankar's CF substitution Eq.(2.11) and Eq.(2.12) is well-defined only for continuum limit. If one tries to write down a composite fermion on a *finite-size sample*, further changes must be made to ensure the com-

pabilities, either in the gauge fixing related to symmetry operations, or in the dimensionality of each kind of Hilbert space. We will discuss this in the next section.

In practice, the strongly-interacting electronic Hamiltonian reads

$$H_e \equiv H_0 + U = \sum_i \frac{\eta_{e,i}^2}{2m\ell_e^2} + \frac{1}{2} \sum_{ij} \sum_{\mathbf{q}} v(q) e^{i\mathbf{q} \cdot (\mathbf{r}_i - \mathbf{r}_j)}.$$

which in the LLL reduces to (here we just ignore the zero point energy)

$$H_{e,\text{LLL}} = H_e[\mathcal{R}_e] = \frac{1}{2} \sum_{ij} \sum_{\mathbf{q}} v(q) e^{-q^2 \ell_e^2 / 4} e^{i\mathbf{q} \cdot (\mathcal{R}_i - \mathcal{R}_j)}. \quad (2.13)$$

To solve the problem, we can **enlarge the electronic Hilbert space by introducing the vortex Hilbert space** $\text{span}\{\mathcal{R}_e\}$, so that the CF description can be simply obtained by replacing both electron and **vortex degrees of freedom with the CF's ones using Eq.(2.12)**, on which mean-field calculation can be reliably performed. Note: here clearly the procedure enlarging to vortex Hilert space is a *gauge degree of freedom* because it commutes with the projected Hamiltonian.

One may ask that why do we need to switch to the CF description to perform the mean-field calculation (like Hartree-Fock approximation)? This is because the electronic Hamiltonian Eq.(2.13) lives in a highly degenerate LLL, which frustrate both perturbative analysis and any mean-field calculations. In contrast, in the CF description, the Hartree-Fock ground state is naturally non-degenerate, corresponding to p -filled CF LLs. Therefore, there is no problem to perform the mean-field calculation in the CF description.

2.2.3 Remarks of FCI

FQHE is a typical phenomena governed by Coulomb interactions in 2D electronic systems where kinetic part of the Hamiltonian is quenched. The extremely high magnetic fields plays a crucial role to split out the relevant LLs (in most case the LLL) with the other LLs, so that the energy hierarchy is established:

$$|\varepsilon_{\mathbf{k}}| \ll U_{\text{Coulomb}} \ll \Delta,$$

where LL separation $\Delta \sim \hbar\omega_c \propto B$. In fact, the only key ingredients of FQHE is a group of *well-separated Landau levels*, forming with an extremely clean sample and an extremely high magnetic field.

If one wants to realize the FQHE on lattice, i.e., extend from FQHE to FCI, where LLs are replaced by energy bands, a natural direction is to mimicking the LLs — by examining the properties of LLs and thinking about what kinds of conditions do we need. For example, the flatness of LLs can be replaced by the flatness of energy bands, and the Chern number $|C| = 1$ of LLs can be replaced by the non-trivial topology of Chern bands. There are plenty of thoeretical works embarking along such route. For example, by assuming the Girvin-MacDonald-Platzman (GMP) algebra [75] as the key feature of the LLL, one can try to reproduce such algebra for Chern bands, with the replacement of external magnetic fields with the Berry curvature of the system, giving rise to the so-called *trace conditions* [76]. By assuming some specific form of the electronic

wavefunctions (as a natural extension to Jastraw factors), the *vortexability* constraint can be proposed [77].

However, a critical thinking to this route is, now that FQHE is a phenomena of Coulomb interactions, do we focus too much on mimicking the properties of LLs? Do we rely too much on Laughlin's/Jain's wavefunctions? For example, on the topology of the LLs, one can ask about what would it be if we partially fill a flat *trivial* band? In fact, there indeed has been theoretical proofs to stabilize FCI for a topological trivial band with zero Berry curvature everywhere [78]. In our work in the next section, we obtain a different class of many-body wavefunctions using projective construction, which turns out to be more suitable for FCI, but takes different from Jain's wavefunctions (as a general structure of hyperdeterminant).

Chapter 3

Projective Construction of Composite Fermion States in Fractional Chern Insulators

3.1 Introduction

Fractional Chern insulators (FCI) were theoretically proposed about a decade ago [55, 56, 57, 79, 58, 80] as fractional quantum Hall states in the absence of the external magnetic field. Different from the traditional fractional quantum Hall (FQH) states realized in Landau Levels (LL), in FCI the electrons partially fill a nearly flat Chern band, and the Berry's curvature from the Chern band plays the role of the magnetic field. When Coulomb interactions are strong enough compared with the bandwidth of the Chern band, fractional quantum Hall states may be realized, which may host Abelian or non-Abelian anyon excitations. Although the theoretical possibility of such fascinating correlated states of matter in realistic materials has been known for quite some time, and intensive experimental efforts have been made in various candidate materials [7], only recently the experimental signatures of FCI have been reported in twisted MoTe₂ bilayer systems [8, 41, 9, 42] and rhombohedral pentalayer graphene/hBN moiré superlattice [40].

In traditional FQH states, the energy scale of the excitations is determined by the Coulomb energy scale $\frac{e^2}{\epsilon l_B}$, where l_B is the magnetic length and ϵ is the dielectric constant. In FCI, however, l_B should be essentially replaced by the lattice constant a of the crystalline order. This suggests that FCI states, as a matter of principle, may host dynamics with much larger energy scales, and could be ideal experimental platforms to investigate quantum phenomena like anyon statistics. The ongoing theoretical development mainly focus on clarifying the criterion to realize FCI phases, from ideal flatband condition to vortexability [81, 82, 83, 84, 77], and on constructing analytic ground state wavefunctions in certain limits [85, 86, 83]. However, the microscopic theoretical tools suitable to study FCI states are limited: the main theoretical tools currently available include exact diagonalization (ED) and density matrix renormalization group (DMRG) numerics [87, 88, 89, 90, 91, 92, 93].

Several outstanding issues are directly related to the ongoing experimental efforts, yet they are challenging to answer using the available theoretical tools. Below, we remark on some of them.

Some of these issues concern the ground state properties of FCI systems. One crucial question is whether the experimental FCI states realize entirely new states of matter, that are not adiabatically connected to the traditional LL FQH states. Theoretically, from the classification viewpoint, such new states of matter could exist from two perspectives. First, the topological order, namely the anyon contents of the FCI states may not be realized in traditional FQH states. Second, even if the topological orders of the FCI states is identical to the traditional FQH states, the presence of the crystalline symmetry may enrich the topological orders, giving rise to different symmetry-enriched topological (SET) states [39, 94]. One such SET phenomenon that has been discussed in the literature is the analog of the Wen-Zee shift [95] for the discrete crystalline rotation symmetry group [96, 97, 98, 99], which is related to the spin angular momentum carried per quasiparticle. Nontrivial Wen-Zee shift would lead to, for instance, fractionally quantized charges at lattice disclinations in the bulk [98, 99].

In the traditional FQH context, the composite fermion states [68] are associated with a simple mean-field picture. After the flux attachment [70], the electron in a physical LL becomes a composite fermion (CF) that sees an effective magnetic field – a fraction of the physical magnetic field. Consequently, the CF fills an integer number of effective composite fermion LLs. The Jain's sequence at filling $\nu = \frac{p}{2ps+1}$ corresponds to attaching $2s$ -unit of flux to the electron, and the CF fills p CF LLs. Note that the CF wavefunction is a free fermion state in this mean-field picture – a Slater determinant. The physical electronic wavefunction, e.g., the Laughlin's wavefunctions, obviously, is not a Slater determinant.

In the FCI context, this mean-field picture is expected to be modified naturally: the electron LL is replaced by a Chern band, while the CF Chern bands also replace the CF LLs. Physically, the different CF LLs are characterized by the spin angular momentum carried per CF: for the n -th ($n = 0, 1, 2, \dots$) CF LL, the CF carries spin angular momentum $l = n$. Although continuous rotation symmetry is absent in the FCI context, the angular momentum mod m is still sharply defined for C_m crystalline rotation symmetry.

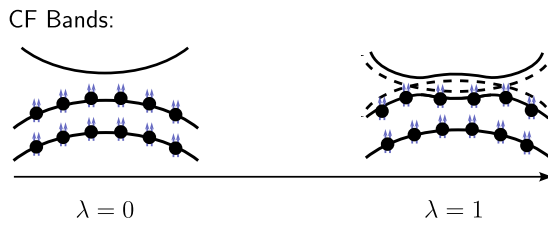


Figure 3.1: Illustration for the possible change of Wen-Zee shift due to the CF band inversion when tuning the parameter λ , so that the CF states at $\lambda = 0$ and $\lambda = 1$ belongs to different SET phases.

As a thought experiment, one may imagine smoothly deforming the electronic Hamiltonian $H(\lambda)$ with a parameter λ while preserving the physical symmetries so that a LL CF state at $\lambda = 0$ is connected with an FCI CF state at $\lambda = 1$. The question is whether or not the two states are in the same quantum phase. The physics of topological insulators teaches us that band inversion may give rise to new states of matter. Indeed, when the CF Chern bands have a full band inversion from $\lambda = 0$ to $\lambda = 1$, the system would have a corresponding change of the Wen-Zee shift, in which case the two states are in different SET phases. See

FIG.3.1 for illustration.

Some other theoretical issues are about the dynamical properties of the FCI states. For instance, the magnetorotons are the charge-neutral bulk excitations and have been experimentally probed using Raman scattering in the traditional FQH systems [100, 101, 102]. In the presence of the Galilean invariance, the magnetoroton at wavevector $q = 0$ has been recently interpreted by Haldane as the collective mode of the geometry fluctuations [103, 104], analogous to the graviton, carrying angular momentum $l = \pm 2$ [105]. In the FCI systems, there is no reason these magnetorotons necessarily carry angular momentum $l = \pm 2$. What are the crystalline quantum numbers carried by the magnetorotons in FCI systems? How to theoretically compute the magnetoroton spectra in FCI systems? These questions are also relevant to the quantum phase transitions involving FCI states. For instance, when magnetorotons become gapless at certain momenta, the system is expected to break translational symmetry and develop charge density wave order.

Due to the limitation of the small system sizes for ED and the difficulty of implementing DMRG on sizable torus samples, answering questions about the crystalline quantum numbers has been challenging for FCI systems. Developing new theoretical tools to investigate these important questions would be desirable.

On the other hand, a different class of quantum systems hosting topologically ordered phases is the quantum spin liquids. There, a nice theoretical tool is available: projective constructions such as the Schwinger-boson and Abrikosov-fermion methods [106, 107, 108, 109, 110, 111, 30, 112, 113]. These projective constructions are very helpful: they provide mean-field theories for the topologically ordered states by enlarging the physical Hilbert space. The mean-field wavefunctions can be improved by projection back to the physical space, leading to physical wavefunctions that can be directly compared with other numerical methods, e.g., ED and DMRG. The detailed microscopic information, such as the crystalline symmetry quantum numbers carried by the ground states and excited states, is accessible in these methods. However, in FCI systems, similar projective construction has been lacking.

Motivated by these issues, we establish a projective construction for the composite fermion states in fractional Chern insulators in this paper. Our main results can be summarized as a general procedure. The procedure input is the Hamiltonian \mathbf{H}_{CB} describing a partially filled Chern band with Chern number $C = \pm 1$, which we want to investigate. The procedure output is two-fold. First, on the mean-field level, the procedure outputs a Hartree-Fock (HF) mean-field Hamiltonian for the CF states in an enlarged Hilbert space, whose ground state is the CF wavefunction $|\psi_{CF}^{MF}\rangle$ and is a Slater determinant. The excitations of the system (e.g., the magnetoroton collective modes) can be calculated within the time-dependent Hartree-Fock (TDHF) framework. Second, beyond the mean-field level, the CF wavefunction can be projected into the physical electronic wavefunction $|\psi_e(\psi_{CF}^{MF})\rangle = \mathbf{P}|\psi_{CF}^{MF}\rangle$ (\mathbf{P} is a projector), which turns out to be a so-called hyperdeterminant of a tensor and can be compared with wavefunctions obtained from ED.

The paper is organized as follows. Because we will discuss both $|\psi_{CF}^{MF}\rangle$ and $|\psi_e(\psi_{CF}^{MF})\rangle$, to avoid confusion, below we will denote the former wavefunction as the mean-field (MF) CF state, while the latter wavefunction as the electronic (or projected) CF state. To present a self-contained discussion, in Sec.3.2 we briefly review several related pieces of previous works, including Jain's CF construction [70], Murthy-Shankar's Hamiltonian formalism [74], the construction of $\nu = 1$ bosonic composite Fermi liquid developed by Pasquier-

Haldane [114] and Read [115]. In Sec.3.3 we discuss the general projective construction on finite-size crystalline systems for composite fermion states (either in the Jain's sequence or the composite Fermi liquid), which is based on Murthy-Shankar's construction. This projective construction leads to the MF CF ground states and excited states on the mean-field level, as well as a projection operation \mathbf{P} to go beyond the mean-field. In Sec.3.3.5, we study the mathematical details of the projection \mathbf{P} operation and show that the general projected CF states are hyperdeterminants of tensors. We then connect our results with previous works including Jain's construction in the traditional FQH context and the parton construction in the FCI context. Interestingly, despite the current construction reproduces Jain's wavefunctions in the traditional Galilean invariant Landau level context, in the absence of the Galilean invariance (e.g. in a FCI system), the present construction and the naive generalization of Jain's prescription are *different* in general. In Sec.3.4, we apply this general procedure to two microscopic FCI models: a toy model of mixed Landau levels introduced by Murthy and Shankar [116], and the realistic model for the twisted bilayer MoTe₂ [117]. Experimentally relevant properties of the FCI states are computed, such as the magnetoroton quantum numbers and spectra. Finally, we discuss possible future developments of our construction and conclude in Sec.3.5

3.2 A brief review of related previous works

3.2.1 Jain's composite-fermion construction

Jain's wavefunctions for composite fermion states [68, 69, 70, 13, 118] are based on the seminal idea of the flux attachment. To describe the fractional quantum Hall states at filling $\nu = \frac{p}{2ps+1}$ where $p, s \in \mathbb{Z}$ are integers, Jain proposed the following wavefunctions in the symmetric gauge of the lowest Landau level with the open boundary condition [119]:

$$\psi_{\frac{p}{2ps+1}} = \mathcal{P}_{\text{LLL}} \prod_{i < j} (z_i - z_j)^{2s} \cdot \chi_p(z, \bar{z}) \quad (3.1)$$

Here $\chi_p(z, \bar{z})$ is the Jain's composite fermion wavefunction with p -filled Landau levels. The flux attachment in this scheme is achieved by the Jastrow factor $(z_i - z_j)^{2s}$: when one electron moves around another electron by a circle, this factor gives a $4\pi s$ phase shift, similar to when an electron moves around 2s-flux tube. The projection operation \mathcal{P}_{LLL} ensures the final wavefunction is within the lowest Landau level (LLL). Precisely, Jain proposes the prescription to replace \bar{z} by the derivative $\mathcal{P}_{\text{LLL}} : \bar{z} \rightarrow 2l_e^2 \frac{\partial}{\partial z}$, where l_e is the electron's magnetic length. By moving all the derivatives to the left, the obtained wavefunction is holomorphic as required by the LLL. Jain's wavefunctions, after adapted to appropriated boundary conditions, have been demonstrated to have excellent overlap with those obtained from the exact diagonalization.

Jain's composite fermion wavefunction $\chi_p(z, \bar{z})$ is a single Slater determinant. In the simplest $p = 1$ case,

it is the Vandermonde determinant together with the Gaussian factor:

$$\chi_{p=1} = \det \begin{vmatrix} z_1^0 & z_2^0 & z_3^0 & \dots \\ z_1^1 & z_2^1 & z_3^1 & \dots \\ z_1^2 & z_2^2 & z_3^2 & \dots \\ \vdots & \vdots & \vdots & \ddots \end{vmatrix} \exp \left[-\sum_i \frac{|z_i|^2}{4l_e^2} \right] \\ = \prod_{i < j} (z_i - z_j) \exp \left[-\sum_i \frac{|z_i|^2}{4l_e^2} \right]. \quad (3.2)$$

In this particular case, the projection \mathcal{P}_{LLL} is unnecessary since \bar{z} is not present, and Jain's wavefunctions becomes Laughlin's wavefunctions [67].

Despite the success of Jain's wavefunctions in the FQHE, how to generalize them to the context of FCI remains unclear. In fact, we want to mention two conceptual puzzles in Jain's original construction, which motivated us to develop the new construction. First, the physical meaning of the composite fermion Landau levels needs to be clarified. For instance, how many composite fermion Landau levels are there? In a finite-size system, the dimension of the physical electronic Hilbert space is finite. It would be unphysical to have a construction involving an infinite number of composite fermion Landau levels. So, if this number is finite for a finite-size sample, what is it?

Second, let us pay attention to the Gaussian factor $\exp \left[-\sum_i \frac{|z_i|^2}{4l_e^2} \right]$ in the composite fermion state Eq.(3.2). The puzzle is the appearance of the *electronic* magnetic length l_e . On the one hand, this is required by Jain's prescription to obtain a wavefunction $\psi_{\frac{p}{2ps+1}}$ within the LLL of the electrons. On the other hand, physically, if the composite fermion sees a weaker magnetic field with an effective magnetic length $l_{CF} > l_e$, wouldn't l_{CF} be appearing in the Gaussian?

We will come back to these two puzzles in Sec.3.3.6, where we demonstrate that the new construction solves both puzzles naturally.

3.2.2 Murthy-Shankar's Hamiltonian theory

Focusing on the composite fermion states, Murthy and Shankar developed a Hamiltonian theory for FQHE [74]. Let us first set up some basic notations. The electron's full position operator \mathbf{r}_e can be separated into the mutually commuting guiding-center \mathcal{R}_e and cyclotron η_e degrees of freedom:

$$\mathbf{r}_e = \mathcal{R}_e + \eta_e, \quad (3.3)$$

satisfying the algebra:

$$[\mathcal{R}_{e,x}, \mathcal{R}_{e,y}] = -il_e^2, \quad [\eta_{e,x}, \eta_{e,y}] = il_e^2 \quad (3.4)$$

For the dynamics within the LLL, the η_e degrees of freedom are frozen and one needs to focus on the

guiding-center part of the density operator (i labels the particle)

$$\boldsymbol{\rho}_e(\mathbf{q}_e) = \sum_i e^{i\mathbf{q}_e \cdot \mathcal{R}_{e(i)}}, \quad (3.5)$$

which satisfies the Girvin-MacDonald-Platzman (GMP) algebra [75]

$$[\boldsymbol{\rho}_e(\mathbf{q}_e), \boldsymbol{\rho}_e(\mathbf{q}'_e)] = 2i \sin \left[\frac{\mathbf{q}_e \times \mathbf{q}'_e}{2} l_e^2 \right] \boldsymbol{\rho}_e(\mathbf{q}_e + \mathbf{q}'_e) \quad (3.6)$$

The electron Hamiltonian constrained within the LLL can be represented using this density operator. For instance, for the Coulomb interaction,

$$\mathbf{H}_e = \frac{1}{2A} \sum_{\mathbf{q}_e} e^{-\frac{\mathbf{q}_e^2 l_e^2}{2}} v(\mathbf{q}_e) : \boldsymbol{\rho}_e(\mathbf{q}_e) \boldsymbol{\rho}_e(-\mathbf{q}_e) :, \quad (3.7)$$

where $v(\mathbf{q}_e) = \frac{2\pi e^2}{\epsilon |\mathbf{q}_e|}$ and A is the real-space sample size.

To achieve the flux attachment, Murthy and Shankar introduced auxiliary degrees of freedom, the vortex guiding-center \mathcal{R}_v , to enlarge the Hilbert space:

$$[\mathcal{R}_{v,x}, \mathcal{R}_{v,y}] = il_v^2. \quad (3.8)$$

Here the vortex magnetic length $l_v = \frac{l_e}{c}$ with $c = \sqrt{\frac{2ps}{2ps+1}}$. Physically, \mathcal{R}_v describes the vortex that carries an electric charge q_v that has an opposite sign of the electron's electric charge q_e : $q_v = -\frac{2ps}{2ps+1} q_e$. With these auxiliary degrees of freedom, the full composite fermion degrees of freedom can be constructed, including the mutually commuting guiding-center and the cyclotron components:

$$\mathcal{R}_{CF} = \frac{\mathcal{R}_e - c^2 \mathcal{R}_v}{1 - c^2}, \quad \eta_{CF} = \frac{c}{1 - c^2} (\mathcal{R}_v - \mathcal{R}_e), \quad (3.9)$$

satisfying the algebra:

$$[\mathcal{R}_{CF,x}, \mathcal{R}_{CF,y}] = -il_{CF}^2, \quad [\eta_{CF,x}, \eta_{CF,y}] = il_{CF}^2. \quad (3.10)$$

Here the CF magnetic length $l_{CF} = \frac{l_e}{\sqrt{1-c^2}} = \sqrt{2ps+1} l_e$, which can be interpreted as the CF electric charge $q_{CF} = \frac{q_e}{2ps+1}$. We also list the inverse transformation of Eq.(3.9):

$$\mathcal{R}_e = \mathcal{R}_{CF} + c \cdot \eta_{CF}, \quad \mathcal{R}_v = \mathcal{R}_{CF} + \frac{1}{c} \eta_{CF} \quad (3.11)$$

If we denote the electron's and the vortex's single-particle Hilbert spaces as \mathcal{H}_e and \mathcal{H}_v , the composite fermion lives in an enlarged Hilbert space $\mathcal{H}_{CF} = \mathcal{H}_e \otimes \mathcal{H}_v$, that can be decomposed into CF's guiding-center and the cyclotron components: $\mathcal{H}_{CF} = \mathcal{H}_{\mathcal{R}_{CF}} \otimes \mathcal{H}_{\eta_{CF}}$.

Any physical operator \hat{O}_e acting in the electronic Fock space, including the Hamiltonian \mathbf{H}_e , then can be mapped to the composite fermion Fock space. As a fundamental example, the electron's density operator can

be identified with:

$$\rho_e(\mathbf{q}_e) = \sum_i e^{i\mathbf{q}_e \cdot \mathcal{R}_{e(i)}} \rightarrow \sum_i e^{i\mathbf{q}_e \cdot [\mathcal{R}_{CF(i)} + c \cdot \eta_{CF(i)}]} \quad (3.12)$$

The composite fermion states with p -filled CF LLs can be viewed as the Hartree-Fock mean-field ground states of \mathbf{H}_e . In addition, the bulk excitations such as the magnetorotons spectra can be computed within the time-dependent Hartree-Fock framework [71, 73]. These mean-field results are qualitatively consistent with other calculation methods.

More recently, Murthy and Shankar generalized this Hamiltonian approach to the context of FCI [116]. This generalization is based on two important observations. First, the bloch states in a Chern band with Chern number $C = \pm 1$ can be mapped to the wavefunctions in the LLL on a torus [120]. Accordingly, an FCI Hamiltonian with $C = \pm 1$ can be exactly mapped to an electronic Hamiltonian in the LLL, with the presence of a crystalline potential. Second, the density operators as $\rho_e(\mathbf{q}_e)$ in Eq.(3.5) on a finite-size torus actually form a complete basis for any fermion bilinears (i.e., single-body operators). Therefore, any density-density interactions can also be straightforwardly mapped into the LLL problem based on Eq.(3.12).

In Murthy-Shankar's Hamiltonian construction, the physical origin of the CF LL is clear as it is a consequence of the enlarged Hilbert space. The relation with Jain's wavefunctions, however, remains a puzzle. It is also unclear how to improve beyond the mean-field treatment, a challenge related to the gauge structure of the construction that was first studied by Read [115] in the context of the bosonic $\nu = 1$ composite Fermi liquid, as we will discuss shortly.

3.2.3 Pasquier-Haldane-Read construction for the bosonic $\nu = 1$ composite fermion liquid

The Pasquier-Haldane's work [114] considered bosonic charged particles at $\nu = 1$. Here, one may argue that after attaching one unit flux, the boson becomes a composite fermion that sees no effective magnetic field, which forms a composite Fermi sea. The boson's Fock space is enlarged by introducing fermions with two indices c_{mn} satisfying the usual algebra:

$$\{c_{mn}, c_{m'n'}^\dagger\} = \delta_{mm'}\delta_{nn'}. \quad (3.13)$$

Here $m, n \in 1, 2, \dots, N$, and N is the number of bosonic particles and the number of orbitals in the LLL. The basis states of the physical Fock space of bosons are then constructed as

$$|m_1, m_2, \dots, m_N\rangle = \epsilon^{n_1, n_2, \dots, n_N} c_{n_1 m_1}^\dagger c_{n_2 m_2}^\dagger \dots c_{n_N m_N}^\dagger |0\rangle, \quad (3.14)$$

where $|0\rangle$ is the vacuum of the c_{mn} fermion's Fock space, and ϵ is the fully antisymmetric Levi-Civita symbol, and we have used the Einstein notation. Read [115] studied the mean-field theory and gauge fluctuations of this theory. As any theory involving an enlarged Hilbert space, the physical state is obtained only when the gauge redundancy is removed. In the present case, the constraint that the physical states need to satisfy is

exactly the invariance under the $SU(N)_R$ transformation generated by (apart from the trace):

$$\boldsymbol{\rho}_{nn'}^R = c_{nm}^\dagger c_{mn'} \quad (3.15)$$

On the other hand, the physical density operators are:

$$\boldsymbol{\rho}_{mm'}^L = c_{nm'}^\dagger c_{mn} \quad (3.16)$$

Note that $\boldsymbol{\rho}_R$ and $\boldsymbol{\rho}_L$ commute. The constraint can then be implemented as the identity on the operator level: $\boldsymbol{\rho}_{nn'}^R = \delta_{nn'}$, which is treated using the Hartree-Fock and time-dependent Hartree-Fock approximation (also called the conserving approximation) in Ref.[115].

The Pasquier-Haldane-Read construction, although only applicable to the bosonic $\nu = 1$ CFL, is closely related to the Murthy-Shankar Hamiltonian theory, which we will explain below.

3.3 The projective construction on a finite-size system

In this section, step by step, we present a general projective construction of CF states applicable for both traditional FQHE and FCI systems. Several steps of this construction are based on Murthy-Shankar's Hamiltonian theory but on finite-size systems.

In this paper, to avoid confusion, we will always use the regular font for operators in the single-particle Hilbert spaces and the bold font for corresponding operators in many-particle Fock spaces.

3.3.1 Mapping a Chern band to the lowest Landau level

Soon after the theoretical proposal of the FCI, it is understood that a generic Chern band with Chern number $C = \pm 1$ can be mapped to the LLL preserving the crystalline symmetries[121, 122, 123]. Recently, further investigations have been made on various ideal Chern band conditions which could allow exact mapping of ground state wavefunctions between FCI systems and FQH systems, in the presence of certain short-range interactions[81, 82, 83, 84, 85, 77, 86]. However, in the present work, we are motivated to investigate generic FCI states which potentially are far away from the FQH systems. Therefore, we will focus on the generic Chern band mapping[121, 122, 123] without invoking ideal band conditions.

In this section, we present a detailed construction for such a mapping. The main results are summarized as follows. We construct the bloch basis in the LLL in Eq.(3.30,3.36), represented using the Jabobi's ϑ -function introduced by Haldane and Rezayi[120] as illustrated in Fig.3.2. A Hamiltonian in a generic Chern band \mathbf{H}_{CB} can then be exactly mapped to a Hamiltonian in the LLL \mathbf{H}_e following the Hilbert space mapping in Eq.(3.46). The crystalline translation/rotation symmetries in \mathbf{H}_{CB} are mapped into the magnetic translation/rotation symmetries in \mathbf{H}_e in Eq.(3.45). Note that since the Hamiltonian \mathbf{H}_e in the LLL faithfully contains all the lattice-scale physics of \mathbf{H}_{CB} , \mathbf{H}_e generally does not have Galilean invariance as in the traditional FQH problems. Finally, for the purpose of performing practical calculations, it is convenient to represent \mathbf{H}_e using the electron density operators in the LLL as shown in Eq.(3.50).

Firstly, let us introduce the single-particle bloch basis in the LLL. The mutually commuting guiding-center and cyclotron degrees of freedom in the LLL are ($e > 0$):

$$\mathcal{R}_e = \mathbf{r}_e - \eta_e, \quad \eta_e = \frac{l_e^2}{\hbar} \hat{\mathbf{z}} \times (\mathbf{p}_e + e\mathbf{A}_e), \quad (3.17)$$

where the magnetic length $l_e \equiv \sqrt{\frac{\hbar}{eB_e}}$. The usual kinetic Hamiltonian only depends on the η_e :

$$H_K = \frac{(\mathbf{p}_e + e\mathbf{A}_e)^2}{2m_e} = \frac{\hbar^2}{2m_e l_e^4} \eta_e^2. \quad (3.18)$$

Without loss of generality, we choose the Landau gauge $\mathbf{A}_e = (B_e y, 0)$ in this section. The subscript e highlights the objects for physical electrons, because, in the next step, we will introduce similar objects for vortices and composite fermions.

Throughout this paper, unless explicitly stated otherwise, we focus on the case with $B_e > 0$, whose LLL has a Chern number $C = -1$. For Chern band systems whose Chern number $C = +1$, one needs to perform a time-reversal transformation to map to the LLL discussed here.

To save notation, we will interchangeably use the complex number $z \equiv x + iy$ to represent a vector $\mathbf{r} \equiv (x, y)$.

The single-particle magnetic translation operator is

$$D_e(z_0) \equiv U_{T,e}(z_0) T_e(z_0), \quad (3.19)$$

where $T_e(z_0)$ is the usual translation operator: $T_e(z_0)\psi_e(z) = \psi_e(z - z_0)$, and $U_{T,e}(z_0)$ is the associated gauge transformation that is fixed up to a $U(1)$ phase factor. One choice to fix this $U(1)$ phase ambiguity is to define $D_e(z_0)$ as the density operator:

$$D_e(z_0) \equiv \rho_e(\mathbf{q}_{e,z_0}) = e^{i\mathbf{q}_{e,z_0} \cdot \mathcal{R}_e}, \quad \text{where } \mathbf{q}_{e,z_0} \equiv i \frac{z_0}{l_e^2}. \quad (3.20)$$

We will fix this definition in the discussion below. One may straightforwardly check that the explicit form of $U_{T,e}(z_0)$ is now

$$U_{T,e}(z_0) = e^{\frac{i}{2l_e^2}(x_0 y_0 - 2y_0 x)} \quad (3.21)$$

The magnetic translations satisfy the algebra:

$$D_e(z_0) D_e(z_1) = e^{\frac{i}{2l_e^2}(x_0 y_1 - y_0 x_1)} D_e(z_0 + z_1), \quad (3.22)$$

and consequently, they satisfy the commutation relation

$$[D_e(z_0), D_e(z_1)] = 2i \sin \frac{x_0 y_1 - y_0 x_1}{2l_e^2} D_e(z_0 + z_1). \quad (3.23)$$

This is just another way to write down the GMP algebra Eq.(3.6).

Note that, although on the single-particle level we have Eq.(3.20), the many-particle versions of the density operator and the magnetic translation operator in the Fock spaces are defined differently. In the first-quantization language:

$$\begin{aligned}\boldsymbol{\rho}_e(\mathbf{q}_e) &\equiv \sum_i \rho_e(\mathbf{q}_e)_{(i)} \\ \mathbf{D}_e(z_0) &\equiv \prod_i D_e(z_0)_{(i)},\end{aligned}\tag{3.24}$$

where the subscript- i means the operator is acting on the i -th particle. They satisfy:

$$\mathbf{D}_e(z_0)\boldsymbol{\rho}_e(\mathbf{q}_e)\mathbf{D}_e(z_0)^\dagger = e^{i\mathbf{q}_e \cdot z_0} \boldsymbol{\rho}_e(\mathbf{q}_e)\tag{3.25}$$

We will come back to these many-particle operators later.

On a finite-size torus, the boundary conditions can be described by the operator identities:

$$D_e(L_1) = e^{-i\varphi_{e,1}}, \quad D_e(L_1\tau) = e^{-i\varphi_{e,2}},\tag{3.26}$$

where $L_1 > 0$, τ is a complex number with positive imaginary part capturing the shape of the sample, and L_1 and $|L_1\tau|$ specify the real-space sample size. Note that $D_e(L_1)$ and $D_e(L_1\tau)$ must commute to apply the boundary conditions, leading to the flux quantization condition: the total number of fluxes through the sample is an integer $N_{\phi,e}$.

Haldane and Rezayi [120] pointed out that the orbital wavefunctions in the LLL, in the present gauge, can be compactly written in terms of the odd Jacobi- ϑ function, parameterized by $N_{\phi,e}$ zeros z_ν ($\nu = 1, 2, \dots, N_{\phi,e}$) and a complex number k (Note that the convention for the magnetic translation in the present work differs from that in Ref.[120] by a minus sign.):

$$\begin{aligned}\psi_e(z) &\propto f(z)e^{-\frac{y^2}{2l_e^2}}, \\ \text{with } f(z) &= e^{ikz} \prod_{\nu=1}^{N_{\phi,e}} \vartheta_1(\pi(z - z_\nu)/L_1|\tau),\end{aligned}\tag{3.27}$$

where the value of k and the sum of zeros $z_{sum} \equiv \sum_\nu z_\nu$ need to be consistent with the boundary conditions:

$$\begin{aligned}e^{ikL_1} &= (-1)^{N_{\phi,e}} \cdot e^{i\varphi_{e,1}}, \\ e^{i2\pi z_{sum}/L_1} &= (-1)^{N_{\phi,e}} \cdot e^{i\varphi_{e,2}-ikL_1\tau}.\end{aligned}\tag{3.28}$$

Although it appears that the wavefunction can be smoothly tuned, there are only $N_{\phi,e}$ linearly independent wavefunctions. Let $(k_0, z_{sum,0})$ be one solution of Eq.(3.28), the other solutions have the form:

$$k = k_0 + \frac{2\pi l_1}{L_1}, \quad z_{sum} = z_{sum,0} + l_2 L_1 - l_1 L_1 \tau, \quad l_i \in \mathbb{Z}\tag{3.29}$$

In order to study a Chern-band sample with $N_{1,e} \cdot N_{2,e}$ unit cells, one can construct the corresponding bloch basis in the LLL. Namely, we consider the two real-space basis vectors $\mathbf{a}_{1,e}, \mathbf{a}_{2,e}$ with $L_1 = N_1 \mathbf{a}_{1,e}$, and $L_1 \tau = N_2 \mathbf{a}_{2,e}$. $D_e(\mathbf{a}_{1,e})$ and $D_e(\mathbf{a}_{2,e})$ need to commute as the usual lattice translations. To have a one-to-one mapping between the Chern band and the LLL, one further chooses the area spanned by $\mathbf{a}_{1,e}, \mathbf{a}_{2,e}$ contains exactly one flux unit, so that $N_{1,e} \cdot N_{2,e} = N_{\phi,e}$. With this setup, the minimal magnetic translations along $\mathbf{a}_{1,e}, \mathbf{a}_{2,e}$ directions allowed by the boundary conditions are $\frac{\mathbf{a}_{1,e}}{N_{2,e}}, \frac{\mathbf{a}_{2,e}}{N_{1,e}}$, respectively.

The bloch basis in the LLL is formed by $N_{1,e} \cdot N_{2,e}$ simultaneous eigenstates of $\mathbf{a}_{1,e}, \mathbf{a}_{2,e}$ magnetic translations:

$$\begin{aligned} D_e(\mathbf{a}_{1,e})|\mathbf{k}_e\rangle_{\text{LLL}} &= e^{-i\mathbf{k}_e \cdot \mathbf{a}_{1,e}}|\mathbf{k}_e\rangle_{\text{LLL}}, \\ D_e(\mathbf{a}_{2,e})|\mathbf{k}_e\rangle_{\text{LLL}} &= e^{-i\mathbf{k}_e \cdot \mathbf{a}_{2,e}}|\mathbf{k}_e\rangle_{\text{LLL}}, \end{aligned} \quad (3.30)$$

where

$$\begin{aligned} \mathbf{k}_{e,(m_{1,e},m_{2,e})} &\equiv \frac{m_{1,e} + \varphi_{1,e}/(2\pi)}{N_{1,e}} \mathbf{G}_{1,e} + \frac{m_{2,e} + \varphi_{2,e}/(2\pi)}{N_{2,e}} \mathbf{G}_{2,e}, \\ \mathbf{G}_{1,e} &= \frac{-i\mathbf{a}_{2,e}}{l_e^2}, \quad \mathbf{G}_{2,e} = \frac{i\mathbf{a}_{1,e}}{l_e^2}. \end{aligned} \quad (3.31)$$

Here, $\mathbf{G}_{i,e}$ are the reciprocal basis vectors of $\mathbf{a}_{i,e}$, where the complex factor i is used in the last line because the reciprocal vector is expressed in complex coordinates, and one may choose a Brillouin Zone (BZ) with $m_{i,e} \in [0, N_{i,e} - 1]$ being integers. These bloch states can be written in terms of infinite sums, as performed in Ref.[123, 116] for the case of a square lattice. Here, instead, we simply represent them using Haldane-Rezayi's Jacobi- ϑ function via parameters k and z_ν .

To satisfy the eigen-condition Eq.(3.30), obviously the zeros z_ν of $|\mathbf{k}_e\rangle_{\text{LLL}}$ need to form a $N_{1,e} \cdot N_{2,e}$ grid in the real-space:

$$z_\nu = z_1 + n_1 \mathbf{a}_{1,e} + n_2 \mathbf{a}_{2,e}, \quad (3.32)$$

where $n_i \in [0, N_{i,e} - 1]$ are integers, and z_1 can be completely determined by z_{sum} (see FIG.3.2 for an illustration). Different $|\mathbf{k}_e\rangle_{\text{LLL}}$'s correspond to different values of z_1 . According to Eq.(3.29), one finds that the possible values of z_1 are related as:

$$z_1 = z_{1,0} + l_2 \frac{\mathbf{a}_{1,e}}{N_{2,e}} - l_1 \frac{\mathbf{a}_{2,e}}{N_{1,e}}, \quad (3.33)$$

where $z_{1,0}$ is determined by $z_{sum,0}$. Since the pattern of zeros returns to itself after $l_i \rightarrow l_i + N_{i,e}$ in Eq.(3.32), the linearly independent choices of z_1 correspond to $l_i \in [0, N_{i,e} - 1]$. These allowed values of $z_{1,0}$ also form a grid (see FIG.3.2 for an illustration), related by magnetic translations $D_e(l_2 \frac{\mathbf{a}_{1,e}}{N_{2,e}} - l_1 \frac{\mathbf{a}_{2,e}}{N_{1,e}})$. There is a one-to-one mapping between the values of \mathbf{k}_e in Eq.(3.31) and the values of z_1 in Eq.(3.33).

At this point, an instructive observation is that the magnetic translations $D_e(l_2 \frac{\mathbf{a}_{1,e}}{N_{2,e}} - l_1 \frac{\mathbf{a}_{2,e}}{N_{1,e}})$ are exactly

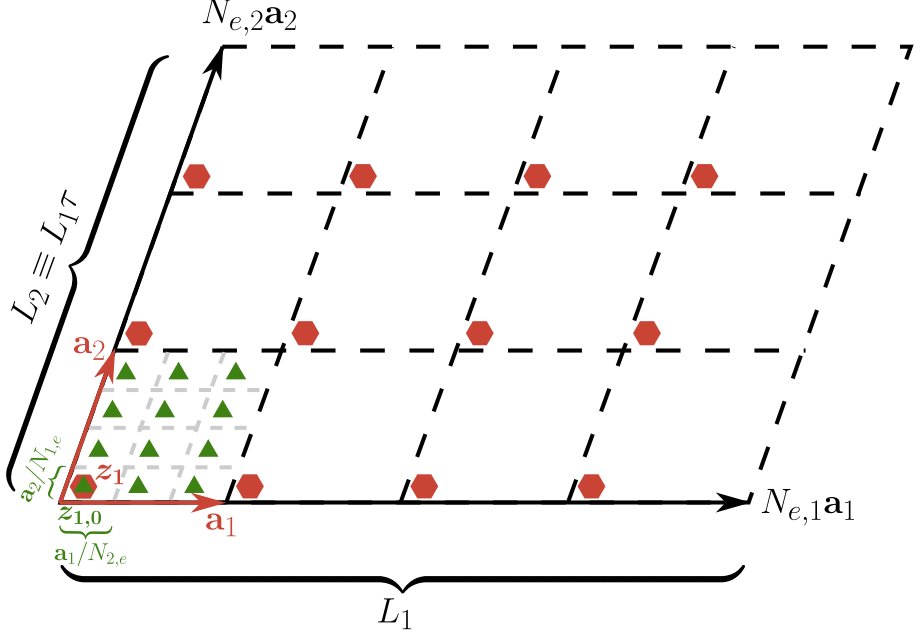


Figure 3.2: Geometry Setup of the LLL Bloch Basis: The torus sample, equivalent to a parallelogram, is parameterized by a real length L_1 and a modular parameter τ . The $N_{1,e} \cdot N_{2,e}$ zeros $\{z_\nu\}$ (red hexagons) of the Haldane-Rezayi wave function are equally distributed on the torus sample by construction, see Eq.(3.32). There are also $N_{1,e} \cdot N_{2,e}$ independent groups of $\{k, z_{sum}\}$ satisfying the boundary condition Eq.(3.28), i.e. $N_{1,e} \cdot N_{2,e}$ independent basis parameterized by different values of $z_{1,0}$, which also forms a $N_{2,e} \cdot N_{1,e}$ grids as green triangles, see Eq.(3.33).

the density operators in Eq.(3.5) for the finite-size sample. The relation Eq.(3.20) leads to the correspondence

$$D_e \left(l_2 \frac{\mathbf{a}_{1,e}}{N_{2,e}} - l_1 \frac{\mathbf{a}_{2,e}}{N_{1,e}} \right) = \rho_e \left(\mathbf{q}_e = \frac{l_1}{N_{1,e}} \mathbf{G}_{1,e} + \frac{l_2}{N_{2,e}} \mathbf{G}_{2,e} \right) \quad (3.34)$$

Due to the GMP algebra, we know that for $\mathbf{q}_e = \frac{l_1}{N_{1,e}} \mathbf{G}_{1,e} + \frac{l_2}{N_{2,e}} \mathbf{G}_{2,e}$,

$$\rho_e(\mathbf{q}_e) |\mathbf{k}_e\rangle_{LLL} \propto |\mathbf{q}_e + \mathbf{k}_e\rangle_{LLL}. \quad (3.35)$$

Therefore, if one chooses $z_{1,0}$ corresponding to $\mathbf{k}_{e,(0,0)}$ in Eq.(3.31), we have the identification $l_i = m_{i,e}$ between Eq.(3.33) and Eq.(3.31), as expected.

To have a concrete discussion, we still need to fix a gauge for these bloch states. In this paper, we choose the Landau-like gauge of $|\mathbf{k}_e\rangle_{LLL}$ so that:

$$\begin{aligned} \rho_e \left(\mathbf{q}_e = \frac{\mathbf{G}_{1,e}}{N_{1,e}} \right) |\mathbf{k}_{e,(m_{1,e}, m_{2,e})}\rangle_{LLL} \\ = e^{\frac{2\pi i}{N_{\phi,e}} (m_{2,e} + \varphi_{2,e}/(2\pi))} |\mathbf{k}_{e,(m_{1,e}+1, m_{2,e})}\rangle_{LLL}, \\ \rho_e \left(\mathbf{q}_e = \frac{\mathbf{G}_{2,e}}{N_{2,e}} \right) |\mathbf{k}_{e,(m_{1,e}, m_{2,e})}\rangle_{LLL} \\ = |\mathbf{k}_{e,(m_{1,e}, m_{2,e}+1)}\rangle_{LLL}. \end{aligned} \quad (3.36)$$

The phase factor in the first line is to satisfy the GMP algebra. Applying the GMP algebra, the matrix elements

of any density operator are analytically known in this LLL bloch basis. In particular, as noted in Ref.[116], *the $N_{\phi,e}^2$ density operators with $l_1, l_2 \in [0, N_{\phi,e} - 1]$ form a complete basis of single-body operators in the LLL.* In fact, one can show that for any single-body operator $\hat{\mathbf{A}}_e$, one can expand it by the density operators:

$$\hat{\mathbf{A}}_e = \sum_{l_1, l_2 \in [0, N_{\phi,e} - 1]} a_{l_1 l_2} \cdot \boldsymbol{\rho}_e \left(\mathbf{q}_e = l_1 \frac{\mathbf{G}_{1,e}}{N_{1,e}} + l_2 \frac{\mathbf{G}_{2,e}}{N_{2,e}} \right), \quad (3.37)$$

where

$$a_{l_1 l_2} = \frac{1}{N_{\phi,e}} \text{Tr} \left[\hat{\mathbf{A}}_e \rho_e \left(\mathbf{q}_e = -l_1 \frac{\mathbf{G}_{1,e}}{N_{1,e}} - l_2 \frac{\mathbf{G}_{2,e}}{N_{2,e}} \right) \right], \quad (3.38)$$

which follows the GMP algebra and the fact that $\rho_e(\mathbf{q}_e)$ is traceless unless \mathbf{q}_e is a linear superposition of $N_{2,e} \mathbf{G}_{1,e}$ and $N_{1,e} \mathbf{G}_{2,e}$ with integer coefficients.

One could extend the smooth gauge Eq.(3.36) of the LLL bloch states beyond the BZ specified by $m_{i,e} \in [0, N_{i,e} - 1]$, leading to the BZ boundary condition:

$$\begin{aligned} |\mathbf{k}_e + \mathbf{G}_{1,e}\rangle_{\text{LLL}} &= |\mathbf{k}_e\rangle_{\text{LLL}} \\ |\mathbf{k}_e + \mathbf{G}_{2,e}\rangle_{\text{LLL}} &= e^{-i\mathbf{k}_e \cdot \mathbf{a}_{1,e}} |\mathbf{k}_e\rangle_{\text{LLL}} \end{aligned} \quad (3.39)$$

It is known that the bloch wavefunctions in a $C = \pm 1$ Chern band (CB) can be mapped to the orbitals in the LLL, preserving the rotation and translation symmetries [123]. To this end we need to discuss the magnetic rotation operation by an angle θ in the LLL:

$$\psi_e(z) \rightarrow U_{R,e}(\theta) R_e(\theta) \psi_e(z) = U_{R,e}(\theta) \psi_e(e^{-i\theta} z), \quad (3.40)$$

where $R_e(\theta) : \psi_e(z) \rightarrow \psi_e(e^{-i\theta} z)$ is the usual rotation, $U_{R,e}(\theta)$ is the associated gauge transformation, determined up to a $U(1)$ phase factor. In this paper, we fix this phase ambiguity by choosing

$$U_{R,e}(\theta) = \exp \left[\frac{-i}{2l_e^2} \left[\frac{\sin 2\theta}{2} (x^2 - y^2) + (1 - \cos 2\theta) xy \right] \right], \quad (3.41)$$

satisfying $U_{R,e}(2\pi) R_e(2\pi) = \mathbf{1}$ and

$$\begin{aligned} [U_{R,e}(\theta_1) R_e(\theta_1)] [U_{R,e}(\theta_2) R_e(\theta_2)] \\ = U_{R,e}(\theta_1 + \theta_2) R_e(\theta_1 + \theta_2), \end{aligned} \quad (3.42)$$

As long as the modular parameter τ and the boundary conditions are consistent with the rotation angle (e.g., there exists $n_i \in \mathbb{Z}$ such that $e^{i\theta}\tau \equiv n_1 + n_2\tau$), the magnetic rotation in the LLL is legitimate. Generally speaking, the magnetic rotation sends $|\mathbf{k}_e\rangle_{\text{LLL}}$ to a linear superposition of the bloch basis.

If one further requires $\mathbf{a}_{i,e}$ to be consistent with the rotation, e.g., when $\mathbf{a}_{i,e}$ generates a square lattice and

$\theta = \frac{\pi}{2}$, the magnetic rotation does send $|\mathbf{k}_e\rangle_{\text{LLL}}$ to a single bloch state:

$$U_{R,e}(\theta)R_e(\theta)|\mathbf{k}_e\rangle_{\text{LLL}} = e^{i\xi(\theta, \mathbf{k}_e)}|R_\theta \mathbf{k}_e\rangle_{\text{LLL}}. \quad (3.43)$$

It turns out that, generally speaking, the rotation should be interpreted as about the $[\pi, \pi]$ -point, i.e., $R_\theta \mathbf{k}_e = e^{i\theta}(\mathbf{k}_e - \mathbf{K}_e) + \mathbf{K}_e$ where $\mathbf{K}_e = \frac{\mathbf{G}_{1,e}}{2} + \frac{\mathbf{G}_{2,e}}{2}$. This is the consequence of the magnetic translation algebra (see Appendix 3.A for details).

The phase factor $e^{i\xi(\theta, \mathbf{k}_e)}$ is fixed by the gauge choice in Eq.(3.36). One way to compute it is to realize the magnetic symmetry group compatibility condition:

$$[U_{R,e}(\theta)R_e(\theta)]D_e(z_0)[U_{R,e}(\theta)R_e(\theta)]^{-1} = D_e(e^{i\theta}z_0), \quad (3.44)$$

which can be established using Eq.(3.21,3.41). Choosing $z_0 = \frac{\mathbf{a}_{1,e}}{N_{2,e}}, \frac{\mathbf{a}_{2,e}}{N_{1,e}}$ and applying this identity to the bloch gauge condition Eq.(3.36), an equation determining $\xi(\theta, \mathbf{k}_e)$ can be obtained and solved (see Appendix 3.A for details and explicit forms of $e^{i\xi(\theta, \mathbf{k}_e)}$).

In a Chern-band (CB), we will have the usual rotation R_θ^{CB} and usual translations $T^{\text{CB}}(\mathbf{a}_{i,e})$. Generally, one can show that the following correspondence can be made:

$$T_e^{\text{CB}}(\mathbf{a}_{i,e}) \leftrightarrow (-1)D_e(\mathbf{a}_{i,e}), \quad R_\theta^{\text{CB}} \leftrightarrow U_{R,e}(\theta)R_e(\theta), \quad (3.45)$$

because the algebra satisfied by the corresponding operators is identical. The minus sign in the first relation is not required for C_2 and C_4 systems but is required for the C_3 and C_6 systems. To have a uniform discussion, *we choose this minus sign as a convention even for C_2 and C_4 systems*. Namely, the crystal momentum for the CB system will be shifted by (π, π) when mapping into the LLL:

$$|\mathbf{k}_e\rangle_{\text{CB}} \leftrightarrow |\mathbf{k}_e + \mathbf{K}_e\rangle_{\text{LLL}}. \quad (3.46)$$

Precisely, one needs to choose a smooth gauge in the CB satisfying the same BZ boundary condition as Eq.(3.39) [123]:

$$\begin{aligned} |\mathbf{k}_e + \mathbf{G}_{1,e}\rangle_{\text{CB}} &= |\mathbf{k}_e\rangle_{\text{CB}} \\ |\mathbf{k}_e + \mathbf{G}_{2,e}\rangle_{\text{CB}} &= e^{-i\mathbf{k}_e \cdot \mathbf{a}_{1,e}} |\mathbf{k}_e\rangle_{\text{CB}}, \end{aligned} \quad (3.47)$$

and the physical rotation $R_e^{\text{CB}}(\theta)$ needs to satisfy the same rule as Eq.(3.43):

$$R_e^{\text{CB}}(\theta)|\mathbf{k}_e\rangle_{\text{CB}} = e^{i\xi(\theta, \mathbf{k}_e + \mathbf{K}_e)}|e^{i\theta}\mathbf{k}_e\rangle_{\text{CB}} \quad (3.48)$$

Under conditions Eq.(3.47,3.48), the identification Eq.(3.46) allows one to map the original Hamiltonian \mathbf{H}_{CB}

in the CB into a Hamiltonian \mathbf{H}_e in the LLL, preserving the rotation symmetry. If \mathbf{H}_{CB} has the form:

$$\mathbf{H}_{\text{CB}} = \sum_{\mathbf{G}_e} h(\mathbf{G}_e) \boldsymbol{\rho}_{\text{CB}}(\mathbf{G}_e) + \frac{1}{2} \sum_{\mathbf{q}_e} V(\mathbf{q}_e) \boldsymbol{\rho}_{\text{CB}}(\mathbf{q}_e) \boldsymbol{\rho}_{\text{CB}}(-\mathbf{q}_e), \quad (3.49)$$

then \mathbf{H}_e is [116]:

$$\begin{aligned} \mathbf{H}_e = & \sum_{\mathbf{G}_e} h(\mathbf{G}_e) \left[\sum_{\mathbf{G}'_e} c(\mathbf{G}_e, \mathbf{G}'_e) \boldsymbol{\rho}_e(\mathbf{G}_e + \mathbf{G}'_e) \right] \\ & + \frac{1}{2} \sum_{\mathbf{q}_e} V(\mathbf{q}_e) \left[\sum_{\mathbf{G}'_e} c(\mathbf{q}_e, \mathbf{G}'_e) \boldsymbol{\rho}_e(\mathbf{q}_e + \mathbf{G}'_e) \right] \cdot [h.c.]. \end{aligned} \quad (3.50)$$

Here, $\boldsymbol{\rho}_{\text{CB}}(\mathbf{q}_e)$ is the density operator $\sum_i e^{i\mathbf{q}_e \cdot \mathbf{r}_i}$ projected into the CB. The first term in \mathbf{H}_{CB} represents the CB dispersion, and the second term is the density-density interaction. Because the LLL density operators $\boldsymbol{\rho}_e(\mathbf{q}_e)$ form a complete basis for single-body operators, one has the expansion:

$$\boldsymbol{\rho}_{\text{CB}}(\mathbf{q}_e) = \sum_{\mathbf{G}'_e} c(\mathbf{q}_e, \mathbf{G}'_e) \boldsymbol{\rho}_e(\mathbf{q}_e + \mathbf{G}'_e), \quad (3.51)$$

where the summation is over $N_{2,e} \cdot N_{1,e}$ reciprocal lattice vectors.

Finally we comment on the conditions Eq.(3.47,3.48). One may wonder whether certain obstruction is present in the CB so that these conditions cannot be satisfied in a smooth gauge. The BZ boundary condition Eq.(3.47) can always be satisfied provided the CB has $C = -1$ that is identical to the LLL. The rotation condition Eq.(3.48) requires further discussion. It is known that the Chern number of a band gives a constraint to the rotation eigenvalues at the high-symmetry points in the momentum space [124]. We list these constraints in Eq.(3.130) in Appendix 3.A.

These eigenvalues are preserved in the CB to LLL mapping. What if the CB and the LLL have different rotation eigenvalues? As computed in Appendix 3.A, the magnetic rotation eigenvalue for the LLL is $e^{-i\theta}$ at \mathbf{K}_e point, corresponding to the Γ -point in the CB, while it is trivial for all other high-symmetry points. It turns out that one can always redefine the physical rotation operator, after which exactly the same eigenvalues are realized in the CB, and the conditions Eq.(3.47,3.48) can be satisfied in a smooth gauge following the prescription in Ref.[123]. This redefinition is a source of the possible nontrivial Wen-Zee shift. We leave details in Appendix 3.A.

3.3.2 Composite fermion substitution

From the previous section, we have the Hamiltonian \mathbf{H}_e in the Fock space constructed with the single-particle Hilbert space \mathcal{H}_e in the LLL, which is exactly mapped from the CB problem. In this section, following the Murthy-Shankar construction [74], we need to enlarge the single-particle Hilbert space and construct the composite fermion single-particle Hilbert space for the finite-size systems:

$$\mathcal{H}_e \otimes \mathcal{H}_v = \mathcal{H}_{CF} = \mathcal{H}_{\mathcal{R}_{CF}} \otimes \mathcal{H}_{\eta_{CF}} \quad (3.52)$$

First, we introduce the vortex single-particle Hilbert space \mathcal{H}_v . \mathcal{H}_v describes the guiding-center degrees of freedom of a particle carrying charge $q_v = -c^2 q_e = -\frac{2ps}{2ps+1} q_e$ in *the same* sample size specified by L_1 and τ as the electron. Consequently, the number of flux quanta seen by the vortex, i.e., the dimension of \mathcal{H}_v , is $N_{\phi,v} = c^2 N_{\phi,e} = \frac{2ps}{2ps+1} N_{\phi,e}$. One cannot define guiding-center operators as in Eq.(3.8) for a finite system. However, the density operators (magnetic translation operators) are well-defined for discrete momentum points (discrete displacements). We define them as:

$$D_v(z_0) = \rho_v(\mathbf{q}_{v,z_0}) \equiv e^{-i\mathbf{q}_{v,z_0}\cdot\mathcal{R}_v}, \text{ where } \mathbf{q}_{v,z_0} \equiv i\frac{z_0}{l_v^2}. \quad (3.53)$$

Here, the additional minus sign in the exponent is due to the sign of the vortex's charge. The periodic boundary condition is specified as:

$$D_v(L_1) = e^{i\varphi_{1,v}}, \quad D_v(L_1\tau) = e^{i\varphi_{2,v}}. \quad (3.54)$$

A simple way to understand the vortex's density operator $\rho_v(\mathbf{q}_v) \equiv e^{-i\mathbf{q}_v\cdot\mathcal{R}_v}$ and \mathcal{H}_v is to consider the antilinear complex conjugate operator K . K sends the \bar{z} in a wavefunction in \mathcal{H}_v to z , and consequently sends \mathcal{H}_v to the Hilbert space $\bar{\mathcal{H}}_v$ of LLL wavefunctions of a particle carrying $-q_v$, with the same sign of the electrons' charge. At the same time:

$$K\rho_v(\mathbf{q}_v)K = e^{i\mathbf{q}_v\cdot\bar{\mathcal{R}}_v}, \quad (3.55)$$

where $\bar{\mathcal{R}}_v \equiv K\mathcal{R}_vK$ also satisfies the guiding-center algebra for the charge $-q_v$. Namely, our results for the density operator of electrons, e.g., Eq.(3.36), can be directly reused for the vortex case after the caution is made for the antilinear nature of K :

$$\langle v_1 | \rho_v(\mathbf{q}_v) | v_2 \rangle = \langle \bar{v}_1 | e^{i\mathbf{q}_v\cdot\bar{\mathcal{R}}_v} | \bar{v}_2 \rangle^*, \quad (3.56)$$

for any $|v_i\rangle \in \mathcal{H}_v$ and $|\bar{v}_i\rangle \equiv K|v_i\rangle \in \bar{\mathcal{H}}_v$.

Next, we decompose the tensor product of the enlarged Hilbert space $\mathcal{H}_e \otimes \mathcal{H}_v$ by introducing the full composite fermion with both the guiding-center and cyclotron degrees of freedom. We consider two cases separately: the Jain's sequence for $\nu = \frac{p}{2ps+1}$, and the composite Fermi liquid (CFL) case for $\nu = \frac{1}{2s}$. In the main text below, we focus on the Jain's sequence, and the CF substitution for CFL can be found in Appendix 3.B.

- *Jain's sequence.* The CF carries an electric charge $q_{CF} = \frac{1}{2ps+1}q_e$ as dictated by the algebra Eq.(3.10). To save notation, we neglect the subscripts for \mathcal{R}_{CF} and η_{CF} from now on. We similarly define the density operators (magnetic translation operators) for the CF degrees of freedom on finite-size systems:

$$\begin{aligned} D_{\mathcal{R}}(z_0) &= \rho_{\mathcal{R}}(\mathbf{q}_{\mathcal{R},z_0}) \equiv e^{i\mathbf{q}_{\mathcal{R},z_0}\cdot\mathcal{R}}, \text{ where } \mathbf{q}_{\mathcal{R},z_0} \equiv i\frac{z_0}{l_{CF}^2}, \\ D_{\eta}(z_0) &= \rho_{\eta}(\mathbf{q}_{\eta,z_0}) \equiv e^{-i\mathbf{q}_{\eta,z_0}\cdot\eta}, \text{ where } \mathbf{q}_{\eta,z_0} \equiv i\frac{z_0}{l_{CF}^2}. \end{aligned} \quad (3.57)$$

	\mathcal{R}_e	\mathcal{R}_v	\mathcal{R}	η
# of particles	N	N	N	N
sample-size	A	A	A	$2ps(2ps+1)A$
charge q/q_e	1	$-\frac{2ps}{2ps+1}$	$\frac{1}{2ps+1}$	$-\frac{1}{2ps+1}$
# of fluxes	$\frac{2ps+1}{p}N$	$2sN$	$\frac{1}{p}N$	$2s(2ps+1)N$
filling-fraction	$\frac{p}{2ps+1}$	$\frac{1}{2s}$	p	$\frac{1}{2s(2ps+1)}$

Table 3.1: Counting of the electronic guiding-center degrees of freedom \mathcal{R}_e , vortice's guiding-center degrees of freedom \mathcal{R}_v , and composite-fermion's both guiding-center \mathcal{R} and cyclotron η degrees of freedom on a finite-size sample for Jain's sequences $\nu = \frac{p}{2sp+1}$.

The CF guiding-center \mathcal{R} lives on a real-space sample with *the same* size as \mathcal{R}_e and \mathcal{R}_v , specified by the boundary condition:

$$D_{\mathcal{R}}(L_1) = e^{-i\varphi_{1,\mathcal{R}}}, \quad D_{\mathcal{R}}(L_1\tau) = e^{-i\varphi_{2,\mathcal{R}}}. \quad (3.58)$$

For reasons that will be clear shortly, the CF cyclotron coordinates η , however, should be viewed as living on a sample whose linear size is enlarged by a factor $\frac{c}{1-c^2} = \sqrt{2ps(2ps+1)}$ where $c = \sqrt{\frac{2ps}{2ps+1}}$, satisfying the boundary condition:

$$D_{\eta}\left(\frac{c}{1-c^2}L_1\right) = e^{i\varphi_{1,\eta}}, \quad D_{\eta}\left(\frac{c}{1-c^2}L_1\tau\right) = e^{i\varphi_{2,\eta}}. \quad (3.59)$$

Consequently, the total number of flux quanta seen by \mathcal{R} is $N_{\phi,\mathcal{R}} = \frac{1}{2ps+1}N_{\phi,e}$, while that seen by η is $N_{\phi,\eta} = \frac{1}{2ps+1} \cdot \left(\frac{c}{1-c^2}\right)^2 N_{\phi,e} = 2psN_{\phi,e}$. The Hilbert space dimensions must be consistent with the decomposition relation Eq.(3.52):

$$N_{\phi,e} \cdot N_{\phi,v} = N_{\phi,\mathcal{R}} \cdot N_{\phi,\eta} \quad (3.60)$$

Note that states in the space \mathcal{H}_{η} label the CF LL indices. Namely, *on a finite-size system, the number of CF LLs is finite and is equal to $N_{\phi,\eta}$* . We list these results in Table.3.1 for the convenience of readers.

After taking the exponential, the linear superposition Eq.(3.9,3.11) in an infinite system becomes the operator identities together with boundary condition relations:

$$\begin{aligned} D_e(z_0) &= D_{\mathcal{R}}\left(\frac{1}{1-c^2}z_0\right) D_{\eta}\left(-\frac{c}{1-c^2}z_0\right), \\ D_v(z_0) &= D_{\mathcal{R}}\left(-\frac{c^2}{1-c^2}z_0\right) D_{\eta}\left(\frac{c}{1-c^2}z_0\right), \\ e^{-i\varphi_{i,e}} &= e^{-i(2ps+1)\varphi_{i,\mathcal{R}} - i\varphi_{i,\eta}}, \\ e^{i\varphi_{i,v}} &= e^{i(2ps)\varphi_{i,\mathcal{R}} + i\varphi_{i,\eta}} \end{aligned} \quad (3.61)$$

and their inverse:

$$\begin{aligned} D_{\mathcal{R}}(z_0) &= D_e(z_0)D_v(z_0), & D_{\eta}(z_0) &= D_e(cz_0)D_v(z_0/c), \\ e^{-i\varphi_{i,\mathcal{R}}} &= e^{-i\varphi_{i,e} + i\varphi_{i,v}}, & e^{i\varphi_{i,\eta}} &= e^{i(2ps+1)\varphi_{i,v} - i(2ps)\varphi_{i,e}}. \end{aligned} \quad (3.62)$$

These identities can be translated as identities of the density operators.

$$\begin{aligned}\rho_e(\mathbf{q}_e) &= \rho_{\mathcal{R}}(\mathbf{q}_e)\rho_{\eta}(-c\mathbf{q}_e), \\ \rho_v(\mathbf{q}_v) &= \rho_{\mathcal{R}}(-\mathbf{q}_v)\rho_{\eta}(\mathbf{q}_v/c),\end{aligned}\tag{3.63}$$

and the inverse

$$\begin{aligned}\rho_{\mathcal{R}}(\mathbf{q}_{\mathcal{R}}) &= \rho_e\left(\frac{1}{1-c^2}\mathbf{q}_{\mathcal{R}}\right)\rho_v\left(\frac{c^2}{1-c^2}\mathbf{q}_{\mathcal{R}}\right), \\ \rho_{\eta}(\mathbf{q}_{\eta}) &= \rho_e\left(\frac{c}{1-c^2}\mathbf{q}_{\eta}\right)\rho_v\left(\frac{c}{1-c^2}\mathbf{q}_{\eta}\right)\end{aligned}\tag{3.64}$$

One can check that the dictionary above indeed provides a one-to-one mapping between the (finite number of) single-body operators in the electron/vortex spaces and those in the CF space.

Importantly, after choosing the bloch bases in \mathcal{H}_v , $\mathcal{H}_{\mathcal{R}}$ and \mathcal{H}_{η} similar to that in \mathcal{H}_e (See Eq.(3.30,3.31)), as well as the real-space magnetic translation unit cell choice in Eq.(3.75)), this dictionary also specifies the fusion coefficients $\langle \mathbf{k}_{\mathcal{R}}, \mathbf{k}_{\eta} | \mathbf{k}_e, \mathbf{k}_v \rangle$ (up to an unimportant overall phase factor):

$$|\mathbf{k}_e\rangle \otimes |\mathbf{k}_v\rangle = \sum_{\mathbf{k}_{\mathcal{R}}, \mathbf{k}_{\eta}} \langle \mathbf{k}_{\mathcal{R}}, \mathbf{k}_{\eta} | \mathbf{k}_e, \mathbf{k}_v \rangle |\mathbf{k}_{\mathcal{R}}\rangle \otimes |\mathbf{k}_{\eta}\rangle.\tag{3.65}$$

One way to compute these fusion coefficients is as follows. In the first step, due to Eq.(3.36), one knows the matrix form of the *four fundamental density operators* $\rho_e(\mathbf{q}_e = \frac{\mathbf{G}_{i,e}}{N_{i,e}})$ and $\rho_v(\mathbf{q}_v = \frac{\mathbf{G}_{i,v}}{N_{i,v}})$ (where $i = 1, 2$) in the *electron-vortex basis* $\{|\mathbf{k}_e\rangle \otimes |\mathbf{k}_v\rangle\}$. All other density operators can be generated by these four fundamental ones. Second, again due to Eq.(3.36), one similarly knows the matrix form of $\rho_{\mathcal{R}}(\mathbf{q}_{\mathcal{R}} = \frac{\mathbf{G}_{i,\mathcal{R}}}{N_{i,\mathcal{R}}})$ and $\rho_{\eta}(\mathbf{q}_{\eta} = \frac{\mathbf{G}_{i,\eta}}{N_{i,\eta}})$ (where $i = 1, 2$) in the *CF basis* $\{|\mathbf{k}_{\mathcal{R}}\rangle \otimes |\mathbf{k}_{\eta}\rangle\}$. In the third step, due to Eq.(3.63), one knows the matrix form of $\rho_e(\mathbf{q}_e = \frac{\mathbf{G}_{i,e}}{N_{i,e}})$ and $\rho_v(\mathbf{q}_v = \frac{\mathbf{G}_{i,v}}{N_{i,v}})$ (where $i = 1, 2$) in the *CF basis* $\{|\mathbf{k}_{\mathcal{R}}\rangle \otimes |\mathbf{k}_{\eta}\rangle\}$. Finally, using results from step-1 and step-3, we are left with a linear algebra problem: finding the unitary transformation U between the electron-vortex basis and the CF basis so that the matrices of the four fundamental density operators are transformed from one basis to another basis. Because $\rho_e(\mathbf{q}_e = \frac{\mathbf{G}_{1,e}}{N_{1,e}})$ and $\rho_v(\mathbf{q}_v = \frac{\mathbf{G}_{1,v}}{N_{1,v}})$ commute with each other, it is straightforward to diagonalize both operators simultaneously, in either set of basis. The unitary transformation U must transform an eigenvector of these two operators in the electron-vortex basis to the corresponding eigenvector in the CF basis, with the same eigenvalues. One, therefore, can fix U up to $N_{\phi,e} \cdot N_{\phi,v}$ phase factors, each of which is for one eigenvector. These phase factors can then be fixed by the matrix elements of $\rho_e(\mathbf{q}_e = \frac{\mathbf{G}_{2,e}}{N_{2,e}})$ and $\rho_v(\mathbf{q}_v = \frac{\mathbf{G}_{2,v}}{N_{2,v}})$, up to an unimportant overall phase factor.

The composite fermion substitution can now be performed. The number of electrons, vortices and composite fermions are all the same. Following Eq.(3.63), the Hamiltonian \mathbf{H}_e in Eq.(3.50) is then mapped to the composite fermion Hamiltonian $\mathbf{H}_e \rightarrow \mathbf{H}_{CF}$ by substituting $\rho_e(\mathbf{q}_e) = \rho_{\mathcal{R}}(\mathbf{q}_e)\rho_{\eta}(-c\mathbf{q}_e)$. One can perform the Hartree-Fock as well as time-dependent Hartree-Fock analysis for \mathbf{H}_{CF} , after caution is taken with respect to the constraint. However, before that, we need to discuss the consequence of the auxiliary vortex

space.

3.3.3 Gauge redundancy and projective symmetries

The Fock spaces for electrons \mathcal{K}_e and composite fermions \mathcal{K}_{CF} (including both the CF guiding-center and cyclotron degrees of freedom) are fermionic spaces. The vortex Fock space \mathcal{K}_v should be bosonic: fusing a fermionic electron with a bosonic vortex gives rise to a composite fermion. On the other hand, the construction above leads to a vast gauge redundancy. Given a state $|\psi_e\rangle \in \mathcal{K}_e$, one can tensor with an arbitrary state $|\psi_v\rangle \in \mathcal{K}_v$ and obtains a state $|\psi_e\rangle \otimes |\psi_v\rangle \in \mathcal{K}_{CF}$. Note that the reverse is not true: it is generally impossible to write a state in \mathcal{K}_{CF} as a linear superposition of states in $\mathcal{K}_e \otimes \mathcal{K}_v$. Namely, $\mathcal{K}_e \otimes \mathcal{K}_v \subsetneq \mathcal{K}_{CF}$.

In order to go back to the physical Fock space \mathcal{K}_e , one needs to constrain states in \mathcal{K}_{CF} by explicitly choosing some state $|\psi_v^g\rangle \in \mathcal{K}_v$, and only consider states in \mathcal{K}_{CF} with the form $|\psi_e\rangle \otimes |\psi_v^g\rangle$. This choice of $|\psi_v^g\rangle$ is a gauge choice (hence the superscript g), and in principle, it can be arbitrary. One may write the constraint as the projector

$$\mathbf{P}_g \equiv |\psi_v^g\rangle\langle\psi_v^g|, \quad (3.66)$$

and the partition function of \mathbf{H}_{CF} and the original \mathbf{H}_e are identical after the projection:

$$\mathcal{Z} = \text{Tr}[e^{-\beta\mathbf{H}_e}] = \text{Tr}[e^{-\beta\mathbf{H}_{CF}} \cdot \mathbf{P}_g] \quad (3.67)$$

A physical electronic state can be obtained from any state $|\psi_{CF}\rangle \in \mathcal{K}_{CF}$ using this projector:

$$|\psi_e^g(\psi_{CF})\rangle \otimes |\psi_v^g\rangle \equiv \mathbf{P}_g|\psi_{CF}\rangle = |\psi_v^g\rangle\langle\psi_v^g|\psi_{CF}\rangle. \quad (3.68)$$

Here $|\psi_e^g(\psi_{CF})\rangle \in \mathcal{K}_e$ is the projected wavefunction in the physical Fock space. We may view ψ_{CF} as a “label” for the physical state $|\psi_e^g(\psi_{CF})\rangle$. As in all projective constructions, this is a many-to-one labeling, and caution needs to be taken when considering the symmetry and low energy fluctuations of $|\psi_e^g(\psi_{CF})\rangle$.

In terms of the first quantization, this projection is implemented as follows. The bosonic state $|\psi_v^g\rangle$ can be expanded in the bloch basis using the wavefunction:

$$|\psi_v^g\rangle = \sum_{\{\mathbf{k}_{v_i}\}} \psi_v^g(\mathbf{k}_{v_1}, \mathbf{k}_{v_2}, \dots, \mathbf{k}_{v_N}) |\mathbf{k}_{v_1}, \mathbf{k}_{v_2}, \dots, \mathbf{k}_{v_N}\rangle. \quad (3.69)$$

We may expand the fermionic state $|\psi_{CF}\rangle$ in the bloch bases in \mathcal{H}_e and \mathcal{H}_v :

$$|\psi_{CF}\rangle = \sum_{\{\mathbf{k}_{e_i}, \mathbf{k}_{v_i}\}} \psi_{CF}^{e,v}(\mathbf{k}_{e_1}, \mathbf{k}_{v_1}, \dots, \mathbf{k}_{e_N}, \mathbf{k}_{v_N}) \cdot |\mathbf{k}_{e_1}, \mathbf{k}_{v_1}, \dots, \mathbf{k}_{e_N}, \mathbf{k}_{v_N}\rangle. \quad (3.70)$$

The electronic state is then:

$$|\psi_e^g(\psi_{CF})\rangle = \sum_{\{\mathbf{k}_{e_i}\}} \psi_e^g(\mathbf{k}_{e_1}, \mathbf{k}_{e_2}, \dots, \mathbf{k}_{e_N}) |\mathbf{k}_{e_1}, \mathbf{k}_{e_2}, \dots, \mathbf{k}_{e_N}\rangle, \quad (3.71)$$

where

$$\begin{aligned} & \psi_e^g(\mathbf{k}_{e_1}, \mathbf{k}_{e_2}, \dots, \mathbf{k}_{e_N}) \\ &= \sum_{\{\mathbf{k}_{v_i}\}} \psi_v^{g*}(\mathbf{k}_{v_1}, \mathbf{k}_{v_2}, \dots, \mathbf{k}_{v_N}) \psi_{CF}^{e,v}(\mathbf{k}_{e_1}, \mathbf{k}_{v_1}, \dots, \mathbf{k}_{e_N}, \mathbf{k}_{v_N}). \end{aligned} \quad (3.72)$$

The fully symmetric nature of ψ_v^g and the fully antisymmetric nature of $\psi_{CF}^{e,v}$ dictate that ψ_e^g is fully antisymmetric.

In the case of bosonic $\nu = 1$ CFL, this projection can be exactly implemented by the $SU(N)_R$ (N is the number of physical particles) singlet condition, giving rise to a field theory treatment by Read [115]. This is because in that case, electron is bosonic, and vortex is fermionic, both at filling fraction $\nu = 1$. This leads to a simple and technically helpful fact: the fermionic Fock space \mathcal{K}_v is only one-dimensional because one is filling N fermionic vortices in a N -dimensional single-particle Hilbert space. Eq.(3.14) is simply the second-quantization version of Eq.(3.72).

However, in the present fermionic electron case, we do not know how to implement \mathbf{P}_g in an elegant field-theory fashion. Instead, in this paper, we will focus on the wave function perspective of the projective construction, and comment on the associated effective field theories towards the end of the paper in the Discussion Section.3.5.

In the remaining part of this section, we implement physical symmetries in the enlarged single-particle Hilbert space \mathcal{H}_{CF} , including the magnetic translation $D_e(\mathbf{a}_{i,e})$ and the magnetic rotation $U_{R,e}(\theta)R_e(\theta)$. In principle, one may combine the physical symmetry operations in \mathcal{H}_e with an *arbitrary* operation in \mathcal{H}_v , as long as $|\psi_v^g\rangle$ is invariant under that operation up to a phase factor. Namely, there is a gauge choice for the symmetry operation in \mathcal{H}_v . In order to have symmetries in \mathcal{H}_{CF} consistent with physical intuitions of composite fermions (see Eq.(3.74) below), we choose the projective symmetry transformation as:

$$\begin{aligned} D_e(\mathbf{a}_{i,e}) &\rightarrow D_e(\mathbf{a}_{i,e}) \otimes D_v(\mathbf{a}_{i,e}) = D_{\mathcal{R}}(\mathbf{a}_{i,e}), \\ U_{R,e}(\theta)R_e(\theta) &\rightarrow U_{R,e}(\theta)R_e(\theta) \otimes U_{R,v}(\theta)R_v(\theta) \\ &= U_{R,\mathcal{R}}(\theta)R_{\mathcal{R}}(\theta) \otimes U_{R,\eta}(\theta)R_{\eta}(\theta). \end{aligned} \quad (3.73)$$

In addition, we will choose $|\psi_v^g\rangle$ to be symmetric under $D_v(\mathbf{a}_{i,e})$ and $U_{R,v}(\theta)R_v(\theta)$. Here, the magnetic translations in various spaces were already defined before, and the magnetic rotations $U_{R,\alpha}(\theta)R_{\alpha}(\theta)$ ($\alpha = v, \mathcal{R}, \eta$) are defined similarly to Eq.(3.41) after the magnetic length is replaced $l_e \rightarrow l_{\alpha}$ and complex conjugate is taken for $\alpha = v, \eta$, i.e., $i \rightarrow -i$ in Eq.(3.41) due to the negativity of charges. For an infinite system, consistent with

Eq.(3.9), these transformations are:

$$\begin{aligned} \begin{pmatrix} \mathcal{R}_e \\ \mathcal{R}_v \end{pmatrix} \rightarrow \begin{pmatrix} \mathcal{R}_e + \mathbf{a}_{i,e} \\ \mathcal{R}_v + \mathbf{a}_{i,e} \end{pmatrix} &\iff \begin{pmatrix} \mathcal{R} \\ \eta \end{pmatrix} \rightarrow \begin{pmatrix} \mathcal{R} + \mathbf{a}_{i,e} \\ \eta \end{pmatrix} \\ \begin{pmatrix} \mathcal{R}_e \\ \mathcal{R}_v \end{pmatrix} \rightarrow e^{i\theta} \begin{pmatrix} \mathcal{R}_e \\ \mathcal{R}_v \end{pmatrix} &\iff \begin{pmatrix} \mathcal{R} \\ \eta \end{pmatrix} \rightarrow e^{i\theta} \begin{pmatrix} \mathcal{R} \\ \eta \end{pmatrix} \end{aligned} \quad (3.74)$$

It is convenient to choose the bloch bases in $\mathcal{H}_v, \mathcal{H}_{\mathcal{R}}, \mathcal{H}_\eta$ so that these projective symmetries are (partially) explicit. For instance, one can choose the real-space basis vectors and lattice sizes as:

$$\begin{aligned} \mathbf{a}_{1,v} &= \frac{1+2ps}{2ps} \mathbf{a}_{1,e}, & N_{1,v} &= \frac{2ps}{1+2ps} N_{1,e}, \\ \mathbf{a}_{2,v} &= \mathbf{a}_{2,e}, & N_{2,v} &= N_{2,e}; \\ \mathbf{a}_{1,\mathcal{R}} &= (1+2ps)\mathbf{a}_{1,e}, & N_{1,\mathcal{R}} &= \frac{1}{1+2ps} N_{1,e}, \\ \mathbf{a}_{2,\mathcal{R}} &= \mathbf{a}_{2,e}, & N_{2,\mathcal{R}} &= N_{2,e}; \\ \mathbf{a}_{1,\eta} &= \frac{c}{1-c^2} \frac{1}{2ps} \mathbf{a}_{1,e}, & N_{1,\eta} &= (2ps)N_{1,e}, \\ \mathbf{a}_{2,\eta} &= \frac{c}{1-c^2} \mathbf{a}_{2,e}, & N_{2,\eta} &= N_{2,e}. \end{aligned} \quad (3.75)$$

Here we have assumed that the lattice size $N_{1,e}$ is a multiple of $(1+2ps)$. Note that the unit cell size needs to enclose one flux quantum in the corresponding space. For instance, the unit cell for \mathcal{R} is enlarged $(1+2ps)$ -times along the \mathbf{a}_1 direction. On the other hand, the \mathbf{a}_2 for v and \mathcal{R} are purposely chosen to be identical to $\mathbf{a}_{2,e}$, so that the $D_e(\mathbf{a}_{2,e})$ -projective symmetry is explicit. With these bloch bases, the $D_e(\mathbf{a}_{2,e})$ -projective symmetry dictates the selection rule for the fusion coefficients:

$$\begin{aligned} \langle \mathbf{k}_e, \mathbf{k}_v | \mathbf{k}_{\mathcal{R}}, \mathbf{k}_\eta \rangle &\neq 0 \\ \text{only if } m_{2,e} - m_{2,v} &= m_{2,\mathcal{R}} \mod N_{2,\mathcal{R}}. \end{aligned} \quad (3.76)$$

Notice that we choose the convention for the momentum eigenvalues as (the signs in the exponents are due to the signs of the charges):

$$\begin{aligned} D_e(\mathbf{a}_{i,e})|\mathbf{k}_e\rangle &= e^{-i\mathbf{k}_e \cdot \mathbf{a}_{i,e}} |\mathbf{k}_e\rangle \\ D_v(\mathbf{a}_{i,v})|\mathbf{k}_v\rangle &= e^{i\mathbf{k}_v \cdot \mathbf{a}_{i,v}} |\mathbf{k}_v\rangle \\ D_{\mathcal{R}}(\mathbf{a}_{i,\mathcal{R}})|\mathbf{k}_{\mathcal{R}}\rangle &= e^{-i\mathbf{k}_{\mathcal{R}} \cdot \mathbf{a}_{i,\mathcal{R}}} |\mathbf{k}_{\mathcal{R}}\rangle \\ D_\eta(\mathbf{a}_{i,\eta})|\mathbf{k}_\eta\rangle &= e^{i\mathbf{k}_\eta \cdot \mathbf{a}_{i,\eta}} |\mathbf{k}_\eta\rangle \end{aligned} \quad (3.77)$$

and $m_{i,\alpha} \in \mathbb{Z}$ are the momentum quantum numbers defined as Eq.(3.31) for the relevant spaces.

The $D_e((1 + 2ps)\mathbf{a}_{1,e})$ symmetry is also explicit, leading to the selection rule:

$$\begin{aligned} \langle \mathbf{k}_e, \mathbf{k}_v | \mathbf{k}_{\mathcal{R}}, \mathbf{k}_{\eta} \rangle &\neq 0 \\ \text{only if } (1 + 2ps)m_{1,e} - (2ps)m_{1,v} &= m_{1,\mathcal{R}} \mod N_{1,\mathcal{R}}. \end{aligned} \quad (3.78)$$

How about the $D_e(\mathbf{a}_{1,e})$ -projective symmetry? For instance, in CF space $\mathcal{H}_{\mathcal{R}}$, it is implemented as $D_{\mathcal{R}}(\mathbf{a}_{1,e}) = \frac{1}{1+2ps}\mathbf{a}_{1,\mathcal{R}}$. According to the bloch basis gauge choice Eq.(3.36) (after modified for the $\mathcal{H}_{\mathcal{R}}$ space), we know that

$$D_{\mathcal{R}}(\mathbf{a}_{1,e})|\mathbf{k}_{\mathcal{R}}\rangle = \left| \mathbf{k}_{\mathcal{R}} + \frac{\mathbf{G}_{2,\mathcal{R}}}{1+2ps} \right\rangle. \quad (3.79)$$

If the CF mean-field state satisfies this projective symmetry, it means that the CF band structure will have a $(1 + 2ps)$ -fold periodicity in the CF BZ – a well-known phenomenon for *translational symmetry fractionalization* [30, 125, 126]. Similarly,

$$D_v(\mathbf{a}_{1,e})|\mathbf{k}_v\rangle = \left| \mathbf{k}_v + \frac{(2ps)\mathbf{G}_{2,v}}{1+2ps} \right\rangle. \quad (3.80)$$

As a remark, in order to respect $D_e(\mathbf{a}_{1,e})$ -projective symmetry, the sample size $N_{2,e}$ must also be a multiple of $(1 + 2ps)$ in the current construction (we have already assumed that $N_{1,e}$ is a multiple of $(1 + 2ps)$ in Eq.(3.75).), otherwise $D_v(\mathbf{a}_{1,e})$ and $D_{\mathcal{R}}(\mathbf{a}_{1,e})$ changes the boundary conditions in \mathcal{H}_v and $\mathcal{H}_{\mathcal{R}}$. To implement $D_e(\mathbf{a}_{1,e})$ -projective symmetry in the case that $\text{mod}(N_{2,e}, (1 + 2ps)) \neq 0$, the construction needs to be generalized which we will leave as a future project.

The projective magnetic rotation symmetry, when implemented in the $\alpha = v, \mathcal{R}, \eta$ spaces, sends a bloch basis state $|\mathbf{k}_{\alpha}\rangle$ to a linear superposition of bloch basis states. These transformation rules can be computed analytically using the gauge conditions similar to Eq.(3.36) and numerically using Haldane-Rezayi wave function.

3.3.4 Hartree-Fock and time-dependent Hartree-Fock

In this section, we describe how to perform the Hartree-Fock analysis for the CF mean-field ground state, and to perform the time-dependent Hartree-Fock analysis for CF excited states.

In an exact study, one should have implemented the full constraint as in Eq.(3.67), and only states of the form $|\psi_e\rangle \otimes |\psi_v^g\rangle \in \mathcal{K}_{CF}$ are physical. In a Hartree-Fock analysis or time-dependent Hartree-Fock analysis, this constraint is implemented on a mean-field level: the variational states under consideration are free CF states $|\psi_{CF}^{MF}\rangle$ (i.e., single Slater-determinants in \mathcal{K}_{CF}) satisfying

$$\langle \psi_{CF}^{MF} | \boldsymbol{\rho}_v(\mathbf{q}_v) | \psi_{CF}^{MF} \rangle = \langle \psi_v^g | \boldsymbol{\rho}_v(\mathbf{q}_v) | \psi_v^g \rangle, \quad \forall \boldsymbol{\rho}_v(\mathbf{q}_v). \quad (3.81)$$

Note that since $\boldsymbol{\rho}_v(\mathbf{q}_v)$'s form a complete basis for single-body operators, Eq.(3.81) means that the expectation value of any single-body operator in $|\psi_{CF}^{MF}\rangle$ is the same as in $|\psi_v^g\rangle$.

We have not specified the bosonic vortex state $|\psi_v^g\rangle$ yet. But we know it should respect the magnetic symmetries in the vortex space, and at the filling fraction $\nu = \frac{1}{2s}$. We make a natural choice: $|\psi_v^g\rangle$ will be one of the $2s$ -fold degenerate bosonic $\nu = \frac{1}{2s}$ Laughlin wavefunction $|\psi_{\nu=1/2s,v}^{Laughlin}\rangle$ on the torus in our discussion below. We will comment on exactly which state we choose for practical simulations in the $2s$ -dimensional subspace in Appendix 3.F.

With this choice, we know that [35], apart from the trivial condition for $\mathbf{q}_v = 0$, $\langle\psi_v^g|\rho_v(\mathbf{q}_v)|\psi_v^g\rangle = 0$ except for a few specific values of $\mathbf{q}_v = \frac{i(n_1 \frac{L_1}{2s} + n_2 \frac{L_1 \tau}{2s})}{l_v^2}$ ($n_1, n_2 \in [0, 2s - 1]$ are integers). Even for these specific values of \mathbf{q}_v , $\langle\psi_v^g|\rho_v(\mathbf{q}_v)|\psi_v^g\rangle$ exponentially decays to zero as the system size increases (see Appendix 3.C for a detailed discussion).

For the simplicity of presentation, we choose the thermodynamic limit values for $\langle\psi_v^g|\rho_v(\mathbf{q}_v)|\psi_v^g\rangle$ for the discussion below, and require the CF mean-field state to satisfy:

$$\langle\psi_{CF}^{MF}|\boldsymbol{\rho}_v(\mathbf{q}_v)|\psi_{CF}^{MF}\rangle = 0, \quad \forall \mathbf{q}_v \neq 0. \quad (3.82)$$

Notice that $[\boldsymbol{\rho}_v(\mathbf{q}_v), \mathbf{H}_{CF}] = 0$ by construction. This mean-field level constraint is imposed via Lagrangian multipliers. In terms of second quantization, the CF mean-field Hamiltonian obtained from the Hartree-Fock treatment of the interacting Hamiltonian Eq.(3.50) (after the CF substitution), can be expressed as:

$$\begin{aligned} \mathbf{H}_{CF}^{MF} &= \sum_{\mathbf{k}_{\mathcal{R}}} \sum_{\mathbf{k}_{\eta_i}, \mathbf{k}_{\eta_j}} f_{\mathbf{k}_{\mathcal{R}}, \mathbf{k}_{\eta_i}}^\dagger h_{\mathbf{k}_{\eta_i}, \mathbf{k}_{\eta_j}}(\mathbf{k}_{\mathcal{R}}) f_{\mathbf{k}_{\mathcal{R}}, \mathbf{k}_{\eta_j}} \\ &\quad + \sum_{\mathbf{q}_v} \lambda_{\mathbf{q}_v} \boldsymbol{\rho}_v(\mathbf{q}_v), \end{aligned} \quad (3.83)$$

where we have used the bloch bases defined in Eq.(3.75), and $f_{\mathbf{k}_{\mathcal{R}}, \mathbf{k}_{\eta_i}}^\dagger$ are the corresponding CF creation operators. Here $\mathbf{k}_{\mathcal{R}}$ being conserved in \mathbf{H}_{CF}^{MF} is a consequence of the translation symmetry, implemented projectively as Eq.(3.74). $\boldsymbol{\rho}_v(\mathbf{q}_v)$ operators can be expressed using the CF operators as described in Eq.(3.63). When the sample size is consistent with $D_e(\mathbf{a}_{i,e})$ -projective symmetry (i.e., a multiple of $(1 + 2ps)$ along both directions), these projective symmetry can be exactly implemented in \mathbf{H}_{CF}^{MF} , and consequently expectation values $\langle\psi_{CF}^{MF}|\boldsymbol{\rho}_v(\mathbf{q}_v)|\psi_{CF}^{MF}\rangle$ may be nonzero only when $\mathbf{q}_v = \mathbf{G}_e$ is a reciprocal lattice vector of electrons. In this situation only lagrangian multipliers $\lambda_{\mathbf{G}_e}$ are needed.

\mathbf{H}_{CF}^{MF} and its ground state $|\psi_{CF}^{MF}\rangle$ are determined self-consistently as in a standard Hartree-Fock calculation, during which the projective symmetries can be implemented exactly (as long as the sample size is consistent with them.). The mean-field energy does have a variational meaning despite the fact that the Hilbert space is enlarged.

After $|\psi_{CF}^{MF}\rangle$ is determined, one may proceed to perform the time-dependent Hartree-Fock (TDHF) calculation for the excitations. TDHF is an approximation scheme to compute excited states (e.g., particle-hole excitations or collective modes) in quantum systems. We are not aware of a systematic TDHF treatment in the presence of constraints and lagrangian multipliers in the literature. We briefly present the main procedure and leave the details in Appendix 3.D.

TDHF is known to be a conserving approximation. Similar to static Hartree-Fock, in TDHF one considers

the Slater determinant states, which are completely determined by their single-body density matrix \mathcal{P} . Let the static Hartree-Fock self-consistent solution be \mathcal{P}_0 , the perturbed state can be parameterized by $\mathcal{P} = \mathbf{U}\mathcal{P}_0\mathbf{U}^\dagger$, where $\mathbf{U} = e^{i\phi}$ is a unitary rotation generated by a small composite fermion bilinear operator ϕ . The time-evolution of ϕ can be computed self-consistently: $\mathcal{L} \cdot \phi = i\hbar\dot{\phi}$, where \mathcal{L} is a linear operator acting in a space \mathcal{W} , spanned by fermion bilinears having nontrivial commutator with \mathcal{P}_0 . The eigenvalues of \mathcal{L} are the energies of the excitation modes.

In the present situation, constraints Eq.(3.82) need to be imposed on both \mathcal{P}_0 and \mathcal{P} . This reduces the dimension of \mathcal{W} by N_c , the number of nontrivial constraints. $N_c = N_{\phi,v}^2 - 1$, since the $\mathbf{q}_v = 0$ constraint is trivial. In addition, each symmetry generator $\rho_v(\mathbf{q}_v)$ (except for $\mathbf{q}_v = 0$) leads to an exact zero mode (the Goldstone mode) in TDHF. There are also totally N_c exact zero modes. The nonzero eigenmodes can be found in the remaining subspace $\mathcal{V} \subset \mathcal{W}$, whose dimension is $2N_c$ smaller than the dimension of \mathcal{W} . In the subspace \mathcal{V} , the eigenproblem of \mathcal{L} can be mapped to the diagonalization problem of a free boson Hamiltonian using the symplectic Bogoliubov transformation: The eigenvalues are real and form $\pm\hbar\omega$ pairs.

A single composite fermion transforms projectively under the symmetry group, as mentioned before. The fermion bilinear ϕ , however, transform as a regular representation of the symmetry group. Namely, ϕ carries well-defined crystalline momentum under $D_e(\mathbf{a}_{i,e})$: $\phi_{\mathbf{q}_e}$, where \mathbf{q}_e is inside the Brillouin Zone (BZ) of the electronic Chern band. The magnetoroton collective modes in the FCI phase form a gapped band structure $\hbar\omega_a(\mathbf{q}_e)$, where a labels the bands. At the high symmetry points in the BZ, the crystalline rotation eigenvalues of the magnetorotons can be computed explicitly using the TDHF eigenstate $\phi_{\mathbf{q}_e}$.

Special consideration needs to be made for $\mathbf{q}_e = 0$. Here, there is a $\pm\hbar\omega_0$ pair of approximate zero modes in the TDHF calculation, and ω_0 goes to zero in the thermodynamic limit. This is again related to the gauge redundancy in the projective construction. In the infinite system, the guiding center \mathcal{R}_v is a well-defined operator at $\mathbf{q} = 0$, corresponding to $\mathcal{R}_v = \mathcal{R} + \frac{1}{c}\eta$ on the CF side. Just like $\rho_v(\mathbf{q}_v)$, this operator does not act in physical Hilbert space and commutes with \mathbf{H}_{CF} , giving a pair of exact zero modes.

To appreciate the physical picture of \mathcal{R}_v , let us consider the CF state in the traditional LL case. It is convenient to write \mathcal{R}_v in terms of the ladder operators as in Eq.(3.90): $a_v^\dagger \propto a_{\mathcal{R}} + \frac{1}{c}a_\eta^\dagger$. For instance, Laughlin's $\nu = 1/3$ state is represented as a single filled CF LLL: $|\psi_{CF}\rangle = |\psi_{\mathcal{R}}\rangle \otimes \prod_i |0_\eta\rangle_i$, where $|\psi_{\mathcal{R}}\rangle$ is the fully filled state in the \mathcal{R} -space, and all composite fermions have the same wavefunction in the η -space: the coherent state $|0_\eta\rangle$ that can be annihilated by a_η . It is then easy to see that of $\sum_i a_{v,i}^\dagger |\psi_{CF}\rangle \propto \sum_i a_{\eta,i}^\dagger |\psi_{CF}\rangle$ since $|\psi_{\mathcal{R}}\rangle$ is annihilated by $\sum_i a_{\mathcal{R},i}$. Because $a_\eta^\dagger |0_\eta\rangle = |1_\eta\rangle$, \mathcal{R}_v is creating the $\mathbf{q}_e = 0$ particle-hole excitations between the CF LLL and the first LL. This excitation was known to be a zero mode in an infinite-system TDHF calculation previously [73]. Here we have shown the physical origin of this zero mode.

The exact zero modes $\rho_v(\mathbf{q}_v)$ as well as the zero mode due to \mathcal{R}_v are gauge modes and do not correspond to physical excitations. One way to see this is via the projective construction: the electronic ground state is given by $|\psi_e^{GS}\rangle \otimes |\psi_v\rangle = \mathbf{P}_g |\psi_{CF}\rangle$, and the would-be excited state corresponding to $\rho_v(\mathbf{q}_v)$ is $|\psi_e^{EX}\rangle \otimes |\psi_v^g\rangle = \mathbf{P}_g \rho_v(\mathbf{q}_v) |\psi_{CF}\rangle$. The latter one can be equivalently obtained via $\tilde{\mathbf{P}}_g \equiv |\tilde{\psi}_v^g\rangle \langle \tilde{\psi}_v^g|$: $|\psi_e^{EX}\rangle \otimes |\tilde{\psi}_v^g\rangle = \tilde{\mathbf{P}}_g |\psi_{CF}\rangle$, where $|\tilde{\psi}_v^g\rangle \equiv \rho_v(\mathbf{q}_v)^\dagger |\psi_v^g\rangle$. But the difference between \mathbf{P}_g and $\tilde{\mathbf{P}}_g$ is really a gauge choice: In an exact study, $|\psi_{CF}\rangle = |\psi_v\rangle \otimes |\psi_e^{GS}\rangle$ where $|\psi_v\rangle$ can be an arbitrary state in \mathcal{K}_v . Therefore $|\psi_e^{EX}\rangle \propto |\psi_e^{GS}\rangle$ is the same

wavefunction in the exact study (unless $|\psi_v\rangle$ being orthogonal to $|\tilde{\psi}_v^g\rangle$, in which case $|\psi_e^{\text{EX}}\rangle = 0$ is annihilated by the projection).

3.3.5 Projection to physical states: Hyperdeterminant

We have demonstrated the procedure to perform static Hartree-Fock calculations to obtain the mean-field CF ground state $|\psi_{CF}^{MF}\rangle$ and to perform TDHF calculations for excited states. The physical electronic state is obtained via the projection \mathbf{P}_g as in Eq.(3.68,3.72). In this section, we study the mathematical structure of $|\psi_e^g(\psi_{CF})\rangle$.

We will focus on a single slater determinant $|\psi_{CF}\rangle$ before the projection ($|\psi_{CF}\rangle$ could be either the mean-field ground state $|\psi_{CF}^{MF}\rangle$ or the unitary rotated states $e^{i\phi}|\psi_{CF}^{MF}\rangle$ related to excitations). It turns out that $|\psi_e^g(\psi_{CF})\rangle$ is mathematically represented as the combinatorial hyperdeterminant of a tensor.

Given a rank m tensor T_{i_1, i_2, \dots, i_m} , with each index $i_s = 1, 2, \dots, N$ (N is the dimension of the tensor), the combinatorial hyperdeterminant [127] is a direct generalization of the determinant of a matrix:

$$\begin{aligned} \text{Hyperdet}(T) \equiv & \sum_{P_1, P_2, \dots, P_{m-1} \in S_N} (-1)^{P_1} (-1)^{P_2} \dots (-1)^{P_{m-1}} \\ & \cdot T_{1, P_1(1), P_2(1), \dots, P_{m-1}(1)} T_{2, P_1(2), P_2(2), \dots, P_{m-1}(2)} \cdot \dots \\ & \cdot T_{N, P_1(N), P_2(N), \dots, P_{m-1}(N)}, \end{aligned} \quad (3.84)$$

where S_N is the permutation group and $(-1)^P$ is the signature of the permutation.

We will demonstrate the FCI states in Jain's sequence at $\nu = \frac{p}{2ps+1}$ with $s = 1$ as an example. To perform the projection, we need an expression for the bosonic Laughlin's state at $\nu = 1/2$ since $|\psi_v^g\rangle = |\psi_{\nu=1/2,v}^{\text{Laughlin}}\rangle$. It turns out that, the state $|\psi_{\nu=1/2,v}^{\text{Laughlin}}\rangle$ can be constructed via the same projective construction mentioned before, but for $s = 1/2$. We will prove this later in Sec.3.3.6. Precisely, one views the bosonic v -particle as the “electron”, and then attaches a single unit of flux ($2s = 1$) to form a composite fermion. The corresponding vortices and composite fermions for v -particles will be denoted as $v - v$ and $v - CF$ respectively, both are fermionic. Following the projective construction:

$$|\psi_{\nu=1/2,v}^{\text{Laughlin}}\rangle |\psi_{v-v}^g\rangle \equiv |\psi_{v-v}^g\rangle \langle \psi_{v-v}^g | \psi_{v-CF}^{MF} \rangle \quad (3.85)$$

But here, both $|\psi_{v-v}^g\rangle$ and $|\psi_{v-CF}^{MF}\rangle$ are single slater determinants: $|\psi_{v-v}^g\rangle$ is the full filled state in the Fock space \mathcal{K}_{v-v} , which is only one-dimensional. $|\psi_{v-CF}^{MF}\rangle$ is the filled $v - CF$ LLL state. In terms of the first quantization, We may represent them using the filled orbitals as:

$$\begin{aligned} |\psi_{v-v}^g\rangle &= \sum_{P \in S_N} (-1)^P |\phi_{P(1)}^{v-v} \phi_{P(2)}^{v-v} \dots \phi_{P(N)}^{v-v}\rangle \\ |\psi_{v-CF}^{MF}\rangle &= \sum_{P \in S_N} (-1)^P |\phi_{P(1)}^{v-CF} \phi_{P(2)}^{v-CF} \dots \phi_{P(N)}^{v-CF}\rangle \end{aligned} \quad (3.86)$$

It is easy to see that, if one chooses a basis $\{\phi_\alpha^v\}$ in \mathcal{H}_v , the wavefunction of $|\psi_{\nu=1/2,v}^{Laughlin}\rangle$ will be the hyperdeterminant of a rank-3 tensor C formed by the fusion coefficients similar to Eq.(3.65):

$$\langle \phi_{\alpha_1}^v \phi_{\alpha_2}^v \dots \phi_{\alpha_N}^v | \psi_{\nu=1/2,v}^{Laughlin} \rangle = \text{Hyperdet}(C), \text{ where} \\ C_{ijk} = \langle \phi_{\alpha_i}^v | \langle \phi_j^{v-v} | \phi_k^{v-CF} \rangle. \quad (3.87)$$

Next, we will perform the projection $|\psi_{\nu=1/2,v}^{Laughlin}\rangle \langle \psi_{\nu=1/2,v}^{Laughlin} | \psi_{CF}^{MF}\rangle$, where the CF mean-field state $|\psi_{CF}^{MF}\rangle$ is a single slater determinant filling p -CF bands:

$$|\psi_{CF}^{MF}\rangle = \sum_{P \in S_N} (-1)^P |\phi_{P(1)}^{CF} \phi_{P(2)}^{CF} \dots \phi_{P(N)}^{CF}\rangle \quad (3.88)$$

Similarly, after choosing a basis $\{\phi_\alpha^e\}$ in \mathcal{H}_e , the wavefunction of $|\psi_e^g(\psi_{CF})\rangle$ will be the hyperdeterminant of a rank-4 tensor T formed by the fusion coefficients in the projective construction:

$$\langle \phi_{\alpha_1}^e \phi_{\alpha_2}^e \dots \phi_{\alpha_N}^e | \psi_e^g(\psi_{CF}) \rangle = \text{Hyperdet}(T), \text{ where} \\ T_{ijkl} = \langle \phi_{\alpha_i}^e | \langle \phi_j^{v-CF} | \phi_k^{v-v} \rangle | \phi_l^{CF} \rangle. \quad (3.89)$$

A very special situation is when the tensor T can be represented as a product of matrices: $T_{i_1,i_2,\dots,i_m} = A_{i_1,i_2}^{(1)} \cdot A_{i_1,i_3}^{(2)} \cdot \dots \cdot A_{i_1,i_m}^{(m-1)}$, in which case the hyperdeterminant is the product of the conventional determinants of the matrices: $\text{Hyperdet}(T) = \prod_{j=1}^{m-1} \det(A^{(j)})$. This is exactly the situation for the Laughlin's $\nu = 1/(m-1)$ states with the open boundary condition, when the electron basis $\{\phi_\alpha^e\}$ is chosen to be the over-complete basis of coherent states (see Sec.3.3.6).

Generally speaking, the tensor T *cannot* be decomposed as a product of matrices, and computing a generic hyperdeterminant is known to be a NP-hard problem [128]. Nevertheless, the crystalline momentum conservation leads to the selection rules in the bloch bases (see Eq.(3.76,3.78)), slightly reducing the computation complexity. Following the algorithm in Ref.[129], utilizing the selection rules, we have tested that on a laptop computer, computing one hyperdeterminant of a rank-4 tensor for $N = 8$ electrons takes about two seconds. This allows us to perform variational Monte Carlo calculations for the projected FCI wavefunctions and compare them with the wavefunctions obtained from exact diagonalization (see Sec.3.4).

3.3.6 Connections with Jain's wavefunctions

We have shown that the projected wavefunction $|\psi_e^g(\psi_{CF})\rangle$ is represented as the hyperdeterminant of a tensor. In this section, we first analytically show that under the open boundary condition and in the traditional LL context, these projected wavefunctions are identical to the ones obtained from Jain's construction.

We will use the coherent state basis extensively in this section. For this purpose, we define the ladder operators satisfying $[a, a^\dagger] = 1$ in the relevant single-particle Hilbert spaces:

$$a_e \equiv \frac{\mathcal{R}_{e,x} - i\mathcal{R}_{e,y}}{\sqrt{2}l_e}, \quad a_v \equiv \frac{\mathcal{R}_{v,x} + i\mathcal{R}_{v,y}}{\sqrt{2}l_v},$$

$$a_{\mathcal{R}} \equiv \frac{\mathcal{R}_x - i\mathcal{R}_y}{\sqrt{2}l_{CF}}, \quad a_{\eta} \equiv \frac{\eta_x + i\eta_y}{\sqrt{2}l_{CF}}. \quad (3.90)$$

The relation Eq.(3.9) between e, v and CF \mathcal{R}, η spaces becomes the bosonic Bogoliubov transformation between these ladder operators:

$$\begin{aligned} a_{\mathcal{R}} &= \frac{1}{\sqrt{1-c^2}}(a_e - ca_v^\dagger), & a_{\eta} &= \frac{1}{\sqrt{1-c^2}}(-ca_e^\dagger + a_v) \\ a_e &= \frac{1}{\sqrt{1-c^2}}(a_{\mathcal{R}} + ca_\eta^\dagger), & a_v &= \frac{1}{\sqrt{1-c^2}}(ca_{\mathcal{R}}^\dagger + a_\eta) \end{aligned} \quad (3.91)$$

These operators and the magnetic translation operators defined in Eq.(3.20,3.53,3.57) satisfy the algebra:

$$\begin{aligned} D_e^\dagger(z_0)a_eD_e(z_0) &= a_e + \frac{\bar{z}_0}{\sqrt{2}l_e} \\ D_v^\dagger(z_0)a_vD_v(z_0) &= a_v + \frac{z_0}{\sqrt{2}l_v} \\ D_{\mathcal{R}}^\dagger(z_0)a_{\mathcal{R}}D_{\mathcal{R}}(z_0) &= a_{\mathcal{R}} + \frac{\bar{z}_0}{\sqrt{2}l_{CF}} \\ D_\eta^\dagger(z_0)a_\eta D_\eta(z_0) &= a_\eta + \frac{z_0}{\sqrt{2}l_{CF}} \end{aligned} \quad (3.92)$$

Let $|0_\alpha\rangle$ ($\alpha = e, v, \mathcal{R}, \eta$) be the coherent state annihilated by the a_α operator, the coherent state basis can be obtained via magnetic translation: $|z_\alpha\rangle \equiv D_\alpha(z)|0_\alpha\rangle$. In addition, the occupation number basis can also be defined: $|n_\alpha\rangle \equiv \frac{a_\alpha^{\dagger n}}{\sqrt{n!}}|0_\alpha\rangle$. For instance, the n -th CF LL corresponds to $|n_\eta\rangle$.

We will work *in the symmetric gauge in this section*. The many-particle wavefunctions can be obtained using the coherent state basis. We focus on the CF space as a demonstration. Defining the position basis for CF $|\zeta_{CF}\rangle$ corresponding to a δ -function located at ζ , one may project it into the n -th CF LL. After choosing the appropriate normalization factor, it turns out that:

$$|n_\eta\rangle\langle n_\eta|\zeta_{CF}\rangle = (-1)^n|n_\eta\rangle \cdot D_{\mathcal{R}}(\zeta)|n_{\mathcal{R}}\rangle. \quad (3.93)$$

We leave its derivation in Appendix 3.E. Therefore, for a single CF in the n -th LL: $|\phi_{CF}\rangle = |\phi_{\mathcal{R}}\rangle|n_\eta\rangle$, its wavefunction is:

$$\langle\zeta_{CF}|\phi_{CF}\rangle = (-1)^n\langle n_{\mathcal{R}}|D_{\mathcal{R}}(\zeta)^\dagger|\phi_{\mathcal{R}}\rangle \quad (3.94)$$

If $n = 0$, the wavefunction is identical to the overlap with the coherent state basis $\langle\zeta_{CF}|\phi_{CF}\rangle = \langle\zeta_{\mathcal{R}}|\phi_{\mathcal{R}}\rangle$.

Since the e and v particles only contain the guiding-center d.o.f., they may be viewed as if they are in the LLL:

$$\begin{aligned} \psi_e(z_1, z_2, \dots, z_N) &= \langle z_{1,e}, z_{2,e} \dots z_{N,e} | \psi_e \rangle, \\ \psi_v(\omega_1, \omega_2, \dots, \omega_N) &= \langle \omega_{1,v}, \omega_{2,v} \dots \omega_{N,v} | \psi_v \rangle \end{aligned} \quad (3.95)$$

For instance, the Laughlin state $|\psi_{\nu=1/2s,v}^{\text{Laughlin}}\rangle$ in the vortex space is:

$$\begin{aligned}\psi_{\nu=1/2s,v}^{\text{Laughlin}}(\omega_1, \omega_2, \dots, \omega_N) &= \prod_{i < j} (\bar{\omega}_i - \bar{\omega}_j)^{2s} e^{-\frac{\sum_j |\omega_j|^2}{4l_v^2}} \\ &\equiv g_v^*(\{\omega_j\}) e^{-\frac{\sum_j |\omega_j|^2}{4l_v^2}},\end{aligned}\quad (3.96)$$

where we introduced the polynomial $g_v(\{\omega_j\}) = \prod_{i < j} (\omega_i - \omega_j)^{2s}$.

Next, we study the many-body CF wavefunction with p -filled CF LLs, which is a Slater determinant:

$$\begin{aligned}\psi_{CF}^{p-LL}(\zeta_1, \zeta_2, \dots, \zeta_N) &= \langle \zeta_{1,CF}, \zeta_{2,CF}, \dots, \zeta_{N,CF} | \psi_{CF}^{p-LL} \rangle \\ &= \left| \begin{array}{cccc} \bar{\zeta}_1^{p-1} & \bar{\zeta}_2^{p-1} & \dots & \bar{\zeta}_N^{p-1} \\ \bar{\zeta}_1^{p-1} \zeta_1 & \bar{\zeta}_2^{p-1} \zeta_1 & \dots & \bar{\zeta}_N^{p-1} \zeta_N \\ \dots & \dots & \dots & \dots \\ \bar{\zeta}_1^{p-1} \zeta_1^{M-1} & \bar{\zeta}_2^{p-1} \zeta_2^{M-1} & \dots & \bar{\zeta}_N^{p-1} \zeta_N^{M-1} \\ \bar{\zeta}_1^{p-2} & \bar{\zeta}_2^{p-2} & \dots & \bar{\zeta}_N^{p-2} \\ \dots & \dots & \dots & \dots \\ \dots & \dots & \dots & \dots \\ \bar{\zeta}_1^2 \zeta_1^{M-1} & \bar{\zeta}_2^2 \zeta_2^{M-1} & \dots & \bar{\zeta}_N^2 \zeta_N^{M-1} \\ \bar{\zeta}_1 & \bar{\zeta}_2 & \dots & \bar{\zeta}_N \\ \bar{\zeta}_1 \zeta_1 & \bar{\zeta}_2 \zeta_2 & \dots & \bar{\zeta}_N \zeta_N \\ \dots & \dots & \dots & \dots \\ \bar{\zeta}_1 \zeta_1^{M-1} & \bar{\zeta}_2 \zeta_2^{M-1} & \dots & \bar{\zeta}_N \zeta_N^{M-1} \\ 1 & 1 & \dots & 1 \\ \zeta_1 & \zeta_2 & \dots & \zeta_N \\ \dots & \dots & \dots & \dots \\ \zeta_1^{M-1} & \zeta_2^{M-1} & \dots & \zeta_N^{M-1} \end{array} \right| e^{-\frac{\sum_k |\zeta_k|^2}{4l_{CF}^2}} \\ &\equiv g_{CF}^{p-LL}(\{\bar{\zeta}_k, \zeta_k\}) e^{-\frac{\sum_k |\zeta_k|^2}{4l_{CF}^2}},\end{aligned}\quad (3.97)$$

where $M \equiv N/p$, and $g_{CF}^{p-LL}(\{\bar{\zeta}_k, \zeta_k\})$ is the polynomial part of the Slater determinant.

In order to perform the projection, it is crucial to compute the fusion coefficient in the e, v -coherent state bases $\langle z_e | \langle \omega_v | \zeta_{CF} \rangle$. Using properties of the transformation in Eq.(3.91), it can be computed:

$$\begin{aligned}\langle z_e | \langle \omega_v | \zeta_{CF} \rangle &= \sqrt{\frac{1+c}{1-c}} e^{-\frac{1}{4l_v^2} |\omega|^2 + \frac{1}{2l_v^2} \bar{\omega} \left(-\frac{z}{c} + \frac{(1+c)\zeta}{c} \right)} \\ &\cdot e^{\frac{-1}{4l_{CF}^2} \frac{1+c}{1-c} |\zeta|^2 + \frac{1}{2l_{CF}^2} \frac{\bar{\zeta} z}{1-c}} \cdot e^{-\frac{|z|^2}{4l_e^2}}\end{aligned}\quad (3.98)$$

We leave its derivation in Appendix 3.E.

Using the resolution of identity in coherent state basis, e.g., $\frac{1}{2\pi l_v^2} \int d\omega |\omega_v\rangle \langle \omega_v| = 1$, following Eq.(3.68),

we know that for an *arbitrary* CF wavefunction:

$$\psi_{CF}(\{\zeta_k\}) \equiv \langle \{\zeta_{k,CF}\} | \psi_{CF} \rangle = g_{CF}(\{\bar{\zeta}_k, \zeta_k\}) e^{-\frac{\sum_k |\zeta_k|^2}{4l_{CF}^2}}, \quad (3.99)$$

the electronic projected wavefunction is given by:

$$\begin{aligned} \psi_e(\{z_i\}) &= \int \prod_j \frac{d\omega_j}{2\pi l_v^2} \prod_k \frac{d\zeta_k}{2\pi l_{CF}^2} \psi_{\nu=1/2s,v}^{Laughlin *}(\{\omega_j\}) \\ &\cdot \psi_{CF}(\{\zeta_k\}) \cdot \langle z_{i,e} | \langle \omega_{i,v} | \zeta_{CF,i} \rangle, \end{aligned} \quad (3.100)$$

One only needs to integrate out the complex variables $\{\omega_j\}, \{\zeta_k\}$. Noticing the identity:

$$\int \frac{d\omega}{2\pi l^2} \bar{\omega}^m \omega^n e^{-\frac{|\omega|^2}{2l^2} + \frac{z\bar{\omega}}{2l^2}} = \left(2l^2 \frac{d}{dz} \right)^m z^n, \quad (3.101)$$

one finds that:

$$\begin{aligned} \psi_e(\{z_i\}) &= e^{-\frac{1}{4l_e^2} \sum_i |z_i|^2} \\ &\cdot \left[g_v \left(\left\{ \frac{1+c}{c} \zeta_i - \frac{z_i}{c} \right\} \right) g_{CF} \left(\left\{ \frac{2l_e^2}{1+c} \frac{\partial}{\partial \zeta_i}, \zeta_i \right\} \right) \right] \Big|_{\zeta_i=z_i}. \end{aligned} \quad (3.102)$$

Here, the derivatives $\frac{\partial}{\partial \zeta_i}$ should be moved to the leftmost of the polynomial expression in the second line. The identification $\omega_i = \frac{1+c}{c} \zeta_i - \frac{z_i}{c}$ is anticipated: from Eq.(3.9), we know the operator $\zeta_{CF} = \frac{1}{1+c} \mathcal{R}_e + \frac{c}{1+c} \mathcal{R}_v$. \mathcal{R}_e and \mathcal{R}_v can be viewed as the position operators z_e and ω_v projected into the LLL, leading to $\zeta_{CF} = \frac{1}{1+c} z_e + \frac{c}{1+c} \omega_v$.

However, in Jain's prescription, the electronic wavefunction is obtained as:

$$\begin{aligned} \psi_e^{\text{Jain}}(\{z_i\}) &= e^{-\frac{1}{4l_e^2} \sum_i |z_i|^2} \\ &\cdot \left[g_v(\{\zeta_i\}) g_{CF} \left(\left\{ 2l_e^2 \frac{\partial}{\partial \zeta_i}, \zeta_i \right\} \right) \right] \Big|_{\zeta_i=z_i}. \end{aligned} \quad (3.103)$$

which is apparently different from Eq.(3.102).

In fact, for a generic CF wavefunction ψ_{CF} in the FCI systems, *Jain's prescription and our prescription Eq.(3.102) indeed give different electronic wavefunctions!* However, for the Galilean invariant CF wavefunction $g_{CF} = g_{CF}^{p-LL}$ in Eq.(3.97), the two prescriptions give identical electronic wavefunctions, which we show below.

One may rewrite Eq.(3.102) and Eq.(3.103) in an equivalent fashion:

$$\begin{aligned} \psi_e(\{z_i\}) &= e^{-\frac{1}{4l_e^2} \sum_i |z_i|^2} \left[g_v(\{\omega_i\}) g_{CF} \left(\left\{ \frac{2l_e^2}{c} \left(\frac{\partial}{\partial \omega_i} + \frac{c}{1+c} \frac{\partial}{\partial \zeta_i} \right), \zeta_i \right\} \right) \right] \Big|_{\zeta_i=\omega_i=z_i}, \\ \psi_e^{\text{Jain}}(\{z_i\}) &= e^{-\frac{1}{4l_e^2} \sum_i |z_i|^2} \left[g_v(\{\omega_i\}) g_{CF} \left(\left\{ 2l_e^2 \left(\frac{\partial}{\partial \omega_i} + \frac{\partial}{\partial \zeta_i} \right), \zeta_i \right\} \right) \right] \Big|_{\zeta_i=\omega_i=z_i}. \end{aligned} \quad (3.104)$$

Due to the particular form of g_{CF}^{p-LL} in Eq.(3.97), it is easy to see that the derivatives $\frac{\partial}{\partial \zeta_i}$ can be neglected in

both expressions. Consequently, up to the unimportant overall normalization factor, they give identical electronic wavefunctions. Essentially, any term involving $\frac{\partial}{\partial \zeta_i}$ would appear in the determinant as $(\frac{\partial}{\partial \omega_i})^m (\frac{\partial}{\partial \zeta_i})^n \zeta_i^l$. Varying i , these terms form a row in the determinant, which will be canceled by another row formed by $(\frac{\partial}{\partial \omega_i})^m (\frac{\partial}{\partial \zeta_i})^{n-1} \zeta_i^{l-1}$, unless $n = 0$.

Basically, in the traditional Galilean invariant FQH context, we find that the single projection $\mathbf{P}_g = |\psi_v^g\rangle\langle\psi_v^g|$ in Eq.(3.68) in the present construction, after choosing $|\psi_v^g\rangle = |\psi_{\nu=\frac{1}{2s}}^{\text{Laughlin}}\rangle$, plays the role of both the Jastrow factor $\prod_{i < j} (z_i - z_j)^2$ and the LLL projection \mathcal{P}_{LLL} in the original Jain's construction Eq.(3.1). For the present construction, \mathcal{P}_{LLL} is unnecessary because we have always been working within the electronic LLL.

A nice feature of the current projective construction is the clarification of the Gaussian factor: in Jain's construction, the Gaussian factor $e^{-\frac{|z|^2}{4l_e^2}}$ is attached to the CF mean-field state, which is physically alarming since the CF should have the magnetic length l_{CF} , not l_e . *In the current construction, the Gaussian factor is indeed $e^{-\frac{|\zeta|^2}{4l_{CF}^2}}$ for the CF mean-field state. Only after the projection the Gaussian factor $e^{-\frac{|z|^2}{4l_e^2}}$ emerges.*

Finally, we comment on the torus boundary condition. In this case, Jain's construction becomes more sophisticated [130], and we do not pursue the analytical relationship with the present construction. However, Laughlin's wavefunctions are still well-known and represented using the Jacobi's ϑ -function [120]. We have numerically tested that, for small system sizes with $N = 3, 4$ electrons, the projected $|\psi_e^g(\psi_{CF})\rangle$ is indeed identical to one of m -fold degenerate Laughlin's wavefunction. Here, a technical detail needs to be clarified: in order to define the CF LLL, one needs to define the coherent state $|0_\eta\rangle$ on a finite-size torus corresponding to \mathcal{H}_η . It is known that there exist different definitions of coherent states on a finite torus. We find that one needs to use the so-called *continuous coherent state* [131] for $|0_\eta\rangle$ in order to reproduce Laughlin's wavefunctions on the torus after projection. We leave the discussion for the continuous coherent state on torus in Appendix 3.F.

3.3.7 Connections with parton states for FCI systems

Previously, there have been efforts to write down FCI wavefunctions using the parton construction [132]. For example, in order to construct a $\nu = 1/3$ FCI state with the same topological order as the Laughlin's state, one splits the electron c into three fermionic partons $f^{(\alpha)}$ ($\alpha = 1, 2, 3$) in the real-space [69]:

$$c_{\mathbf{r}} = f_{\mathbf{r}}^{(1)} f_{\mathbf{r}}^{(2)} f_{\mathbf{r}}^{(3)}. \quad (3.105)$$

Each parton carries $1/3$ of the electron's charge and transform projectively under the crystalline symmetry group. It is then possible to have each $f^{(i)}$ to fill a Chern band with Chern number $C = -1$. The electron wavefunction after the identification Eq.(3.105) is obviously a product of three Slater determinants $\psi_{f^{(i)}}$:

$$\psi_e(\mathbf{r}_1, \mathbf{r}_2, \dots, \mathbf{r}_N) = \prod_{\alpha=1}^3 \psi_{f^{(\alpha)}}(\mathbf{r}_1, \mathbf{r}_2, \dots, \mathbf{r}_N), \quad (3.106)$$

where $\psi_{f^{(\alpha)}} = \det[\phi_i^{(\alpha)}(\mathbf{r}_j)]$ is formed by the wavefunction of the filled parton orbitals $|\phi_i^{(\alpha)}\rangle$.

Although this parton construction is conceptually useful in classifying symmetry fractionalization, as fo-

cused in Ref.[132], it has difficulty dealing with practical microscopics. One problem is that the electronic wavefunction ψ_e in Eq.(3.106) does not need to be within the electronic CB. In the regime where electronic band mixing can be neglected, such as the system in Eq.(3.49), one would need another projection \mathbf{P}_{CB} to project ψ_e into the electronic Chern band. A related problem is that the construction Eq.(3.105) involves the real-space wannier orbitals, which necessarily go beyond a single electronic CB. From the practical variational wavefunction viewpoint, this construction involves an unnecessarily large number of fictitious degrees of freedom.

First, we would like to point out that, after projection to CB, $\mathbf{P}_{CB}|\psi_e\rangle$ is nothing but a hyperdeterminant. Introducing the fusion tensor:

$$\langle \phi_i^e | \phi_j^{(1)}, \phi_k^{(2)}, \phi_l^{(3)} \rangle \equiv \int d\mathbf{r} \langle \phi_i^e | \mathbf{r} \rangle \langle \mathbf{r} | \phi_j^{(1)} \rangle \langle \mathbf{r} | \phi_k^{(2)} \rangle \langle \mathbf{r} | \phi_l^{(3)} \rangle, \quad (3.107)$$

where ϕ_i^e 's are a collection of electronic orbitals in the CB, one can easily show that the following overlap is the hyperdeterminant of this tensor:

$$\langle \phi_1^e, \phi_2^e, \dots, \phi_N^e | \mathbf{P}_{CB} | \psi_e \rangle = \text{Hyperdet}[\langle \phi_i^e | \phi_j^{(1)}, \phi_k^{(2)}, \phi_l^{(3)} \rangle] \quad (3.108)$$

Second, we want to mention that the current projective construction is *not* equivalent to the usual parton construction for Jain's series in the absence of Galilean invariance. This is mostly easily seen in the disc geometry using the symmetric gauge, as discussed in Sec.3.3.6. In the usual construction, one would consider the $(2s+1)$ fermionic partons: $f_{\mathbf{r}}^{(1)}$ ($i = 1, 2, \dots, 2s+1$). The first $(2s)$ partons each carry $p/(2ps+1)$ of the electron's charge at $\nu = 1$, while the last parton carries $1/(2ps+1)$ of the electron's charge at $\nu = p$ [69]:

- *usual parton construction:*

$$c_{\mathbf{r}} = f_{\mathbf{r}}^{(1)} f_{\mathbf{r}}^{(2)} \dots f_{\mathbf{r}}^{(2s)} f_{\mathbf{r}}^{(2s+1)}. \quad (3.109)$$

Putting the first $(2s)$ partons each in the lowest LL, and putting the last parton in p CF Chern bands (note that here we are considering generic FCI systems in the absence of Galilean invariance, but with the disk geometry), we have the wavefunction for each parton as:

$$\begin{aligned} \psi_{f(\alpha)}(\{\omega_j\}) &= e^{-\frac{p \sum_j |\omega_j|^2}{4(2ps+1)t_e^2}} \prod_{i < j} (\omega_i - \omega_j), \quad \alpha = 1, 2, \dots, 2s. \\ \psi_{f^{(2s+1)}}(\{\zeta_k\}) &= e^{-\frac{\sum_k |\zeta_k|^2}{4(2ps+1)t_e^2}} g_{CF}(\{\bar{\zeta}_k, \zeta_k\}) \end{aligned} \quad (3.110)$$

The usual parton construction Eq.(3.109) identifies $\omega_i = \zeta_i = z_i$, where z_i 's are the coordinates of electrons. After projecting into the LLL of the electrons, one reproduces the Jain's prescription in Eq.(3.103):

$$\psi_e^{\text{usual-parton}}(\{z_i\}) = \psi_e^{\text{Jain}}(\{z_i\}). \quad (3.111)$$

As discussed earlier, this is not the same wavefunction obtained by the current projective construction in

Eq.(3.102). This brings up an interesting question: Is there a real-space prescription similar to Eq.(3.109) to obtain the projected wavefunction in the current construction?

It turns out that the projected wavefunction in Eq.(3.102) can be obtained using the following real-space prescription:

- *current construction:*

$$c_z = \int d\zeta e^{\frac{-(1+c)}{4t_e^2}(\bar{\zeta}z - \bar{z}\zeta)} f_{\frac{1+c}{c}\zeta - \frac{z}{c}}^{(1)} f_{\frac{1+c}{c}\zeta - \frac{z}{c}}^{(2)} \dots f_{\frac{1+c}{c}\zeta - \frac{z}{c}}^{(2s)} f_{\zeta}^{(2s+1)}, \quad (3.112)$$

where we used complex numbers to label the positions of particles. Again the identification $\omega_v = \frac{1+c}{c}\zeta_{CF} - \frac{1}{c}z_e$ is involved, where ω_v is the position of the first ($2s$) partons that corresponds to the vortex. Different from the usual parton construction Eq.(3.109), the electron operator is *not* the on-site combination of parton operators.

3.4 Benchmark results

3.4.1 Models

We will study two models in this section: a toy model describing Landau levels mixed due to a periodic potential with C_4 rotation symmetry and a realistic model for twisted bilayer MoTe₂ with C_3 rotation symmetry.

3.4.1.1 Mixed Landau level (MLL) model

Landau levels inherently possess a uniform distribution of Berry curvature with Chern number $C = -1$. One way to introduce the FCI physics into the system is to turn on a periodic potential $V_{pp}(\mathbf{r}_e) \equiv \sum_{\mathbf{G}_e} V_{pp}(\mathbf{G}_e) e^{i\mathbf{G}_e \cdot \mathbf{r}_e}$ between LLs; e.g. between $n = 0$ and $n = 1$ LLs. Such an LL-based model, named *Mixed Landau level model*, or MLL, is previously introduced in Ref.[116]. The periodic potential has three effects: it mixes the LLs and thus modifies the Coulomb interaction projected into the lowest Chern band, which has a nonzero bandwidth, and leading to a non-constant distribution of Berry curvature.

For illustrative purposes, we consider the square lattice potential and keep only the lowest harmonics of it, corresponding to $\pm G_{1,e}, \pm G_{2,e}$ with the constant coefficient $V_{pp}(\mathbf{G}_e) = V_{10}/2$. The matrix element of periodic potential in the bloch basis between $n_1, n_2 = 0, 1$ LLs then reads

$$\begin{aligned} & \frac{V_{10}}{2} \langle n_1 | e^{i\mathbf{G}_e \cdot \eta_e} | n_2 \rangle \langle \mathbf{k}_e | e^{i\mathbf{G}_e \cdot \mathbf{R}_e} | \mathbf{k}_e \rangle \\ &= \frac{V_{10}}{2} \rho_{n_2, n_1}(\mathbf{G}_e) e^{-\frac{i\ell_e^2}{2} G_{e,x} G_{e,y}} e^{i\ell_e^2 (G_{e,x} k_{e,y} - G_{e,y} k_{e,x})}, \end{aligned} \quad (3.113)$$

where the cyclotron part of the matrix element takes the form of (see, for example, the Appendix of Ref.[74])

$$\langle n_1 | e^{i\mathbf{G}_e \cdot \eta_e} | n_2 \rangle \equiv \rho_{n_2, n_1}(\mathbf{q}_e)$$

$$= e^{-\frac{q_e^2 \ell_e^2}{4}} \sqrt{\frac{n_<!}{n_>!}} L_{n<}^{|n_1 - n_2|} \left[\frac{q_e^2 \ell_e^2}{2} \right] \begin{cases} \left(\frac{i \ell_e \tilde{z}_{q_e}}{\sqrt{2}} \right)^{|n_1 - n_2|}, & n_1 > n_2 \\ \left(\frac{i \ell_e z_{q_e}}{\sqrt{2}} \right)^{|n_1 - n_2|}, & n_1 \leq n_2 \end{cases}$$

and the guiding-center matrix element follows from the guiding-center algebra Eq.(3.4). As a result, the MLL model is represented in the LL bloch basis [116] as

$$H = \begin{bmatrix} \frac{\tilde{V}}{\sqrt{\pi}} (\cos k_{e,x} + \cos k_{e,y}) & \tilde{V} (-i \sin k_{e,x} - \sin k_{e,y}) \\ \tilde{V} (i \sin k_{e,x} - \sin k_{e,y}) & \omega + \frac{\pi-1}{\sqrt{\pi}} \tilde{V} (\cos k_{e,x} + \cos k_{e,y}) \end{bmatrix}, \quad (3.114)$$

where we define $\tilde{V} \equiv e^{-\pi/2} \sqrt{\pi} V_{10}$, and the LL separation $\text{diag}\{0, \omega\}$ is inserted. The MLL model Eq.(3.114) stays in a topological regime with Chern number $C = -1$, as long as the periodic potential satisfies $V_{10} \leq V_{10}^c \equiv \frac{e^{\pi/2}}{2\pi} \omega \approx 0.766\omega$.

We consider the bare Coulomb interaction $V(\mathbf{q}_e) = \frac{2\pi e^2}{\epsilon |\mathbf{q}_e|}$. This interaction is projected to the lowest Chern band, and we fix the LL separation to be $\omega = 2$ in unit of $\frac{e^2}{\epsilon l_e}$, leaving periodic potential V_{10} as the only remaining tunable parameter. When $V_{10} = 0$ the system returns to the traditional LL problem, whose many-body gap (magnetoroton gap) has been estimated ~ 0.066 in units of $\frac{e^2}{\epsilon l_e}$ [133], in the thermodynamic limit. When V_{10} is large enough, a gap-closing quantum phase transition is expected.

3.4.1.2 TMD moiré (**tMoTe₂**) model

A very recent experimental progress on searching for the zero-field FCI phase is the reported realization in R-stacked twisted MoTe₂ [8, 41, 9]. A realistic continuum model is to consider the **K** valley moiré Hamiltonian [14, 117]

$$H_{\mathbf{K}} = \begin{bmatrix} h_b(\mathbf{r}) & T(\mathbf{r}) \\ T^\dagger(\mathbf{r}) & h_t(\mathbf{r}) \end{bmatrix}, \quad (3.115)$$

where $h_{b/t}(\mathbf{r}) \equiv -\hbar^2(\mathbf{k}_e - \mathbf{K}_{b/t})^2/2m^* + \Delta_{b/t}(\mathbf{r})$ is the top/bottom layer Hamiltonian subject to the moiré potential $\Delta_{b/t}(\mathbf{r}) = 2v \sum_{i=1,3,5} \cos(\mathbf{g}_i \cdot \mathbf{r} \pm \psi)$, and $T(\mathbf{r}) \equiv w(1 + e^{-i\mathbf{g}_2 \cdot \mathbf{r}} + e^{-i\mathbf{g}_3 \cdot \mathbf{r}})$ is the interlayer tunnelings. Here $m^* \approx 0.6m_e$ is the effective mass, $\mathbf{g}_i = \frac{4\pi}{\sqrt{3}a_M} (\cos \frac{\pi(i-1)}{3}, \sin \frac{\pi(i-1)}{3})$ are moiré reciprocal vectors with $a_M \simeq a/\theta = 3.52\text{\AA}/3.89^\circ$, and $v = 20.8\text{meV}$, $\psi = +107.7^\circ$, $w = -23.8\text{meV}$ are parameters extracted from the large-scale DFT study of tMoTe₂ [117], different from that obtained by fitting different stacking regions in Ref.[14]. The moiré Hamiltonian for **K'** valley can be obtained via time-reversal transformation: $H_{\mathbf{K}'} = [H_{\mathbf{K}}(\mathbf{k}_e \rightarrow -\mathbf{k}_e)]^*$. Due to the spin-orbit coupling, the spin and valley degrees of freedom are locked: spin up for $H_{\mathbf{K}}$ and spin down for $H_{\mathbf{K}'}$.

The observed FCI states appear at filling $\nu = -2/3, -3/5$ in the presence of ferromagnetic order. In the mean-field picture, this means that the topmost band for the minority spin is at filling $\nu = 1/3, 2/5$, while the majority spin bands are fully filled. This topmost Chern band has a bandwidth $\sim 9\text{meV}$ using the above parameters in Eq.(3.115) in the absence of the Coulomb interaction introduced below.

We consider the Coulomb interaction tMoTe₂ model:

$$H_U \equiv \frac{1}{2A} \sum_{\mathbf{q}_e} V(\mathbf{q}_e) : \rho(\mathbf{q}_e) \rho(-\mathbf{q}_e) : \quad (3.116)$$

where the electron density ρ is the summation from both valleys and both layers. $V(\mathbf{q}_e)$ is the dual-gate screening Coulomb interaction

$$V(\mathbf{q}_e) = \frac{e^2 \tanh(|\mathbf{q}_e|d)}{2\varepsilon_0 \varepsilon_r |\mathbf{q}_e|} \quad (3.117)$$

with a typical gate distance $d = 300\text{\AA}$ and the relative dielectric constant $\varepsilon_r = 15$, as is used in Ref.[117].

In our calculation, we assume the existence of ferromagnetism and project the Coulomb interaction Eq.(3.116) into the spin minority topmost Chern band. Note that the Chern number $C = +1$ ($C = -1$) for this topmost band of $H_{\mathbf{K}}$ ($H_{\mathbf{K}'}$). To map to the $C = -1$ LLL, we simulate the case $H_{\mathbf{K}'}$ being partially filled (i.e., *the minority spin is down spin*).

It is known that upon hole doping, the bandwidth of this Chern band is significantly renormalized from $\sim 9\text{meV}$ to a smaller value due to the Coulomb interactions between this band and other filled bands, as shown in Ref.[90]. Another way to see this effect is to perform a particle-hole transformation, as done in Ref.[117].

Here, as a benchmarking exercise, we are motivated to investigate the effect of bandwidth in the FCI system. Therefore, we choose the bandwidth via a tuning parameter λ instead of fixing a specific value. Precisely speaking, we simulate the model:

$$H = \lambda P H_{\mathbf{K}'} P + P H_U P \quad (3.118)$$

with the projection operation P eliminates any fermion operator c_k or c_k^\dagger outside the partially filled Chern band. When $\lambda = 0$ the CB is completely flat.

3.4.2 Exact diagonalization, Hartree-Fock and time-dependent Hartree-Fock

3.4.2.1 CF mean-field ground states

We construct both the MLL model and the tMoTe₂ model on 6×4 , 6×6 , and 9×9 samples at the same filling fraction $\nu = 1/3$. The original models have trivial periodic boundary conditions. However, to map to the LLL, for the 9×9 sample of the tMoTe₂ model, twisted boundary conditions in the LLL $\varphi_{1,e} = \varphi_{2,e} = \pi$ are introduced, due to the identification of the operator algebra in Eq.(3.45). Other samples have trivial periodic boundary conditions after mapping to the LLL $\varphi_{1,e} = \varphi_{2,e} = 0$. In the projected wavefunction simulations, we always choose the vortex space \mathcal{H}_v to have trivial periodic boundary conditions: $\varphi_{1,v} = \varphi_{2,v} = 0$.

For both samples of 6×6 and 9×9 unit cells, the system sizes are consistent with the $D_{\mathcal{R}}(\mathbf{a}_{i,e})$ projective translational symmetry in both directions as well as the projective C_n rotation symmetry for the CF ($n = 4$ for the MLL model and $n = 3$ for the tMoTe₂ model). Particularly, Eq.(3.79) tells that CF dispersion will display a 3-fold periodicity in the CF Brillouin Zone (BZ), a well-known feature due to the translation-symmetry fractionalization. We perform Hartree-Fock self-consistent study for the 9×9 sample to obtain the composite-

fermion band dispersion (see FIG.3.3 for the filled CF Chern band).

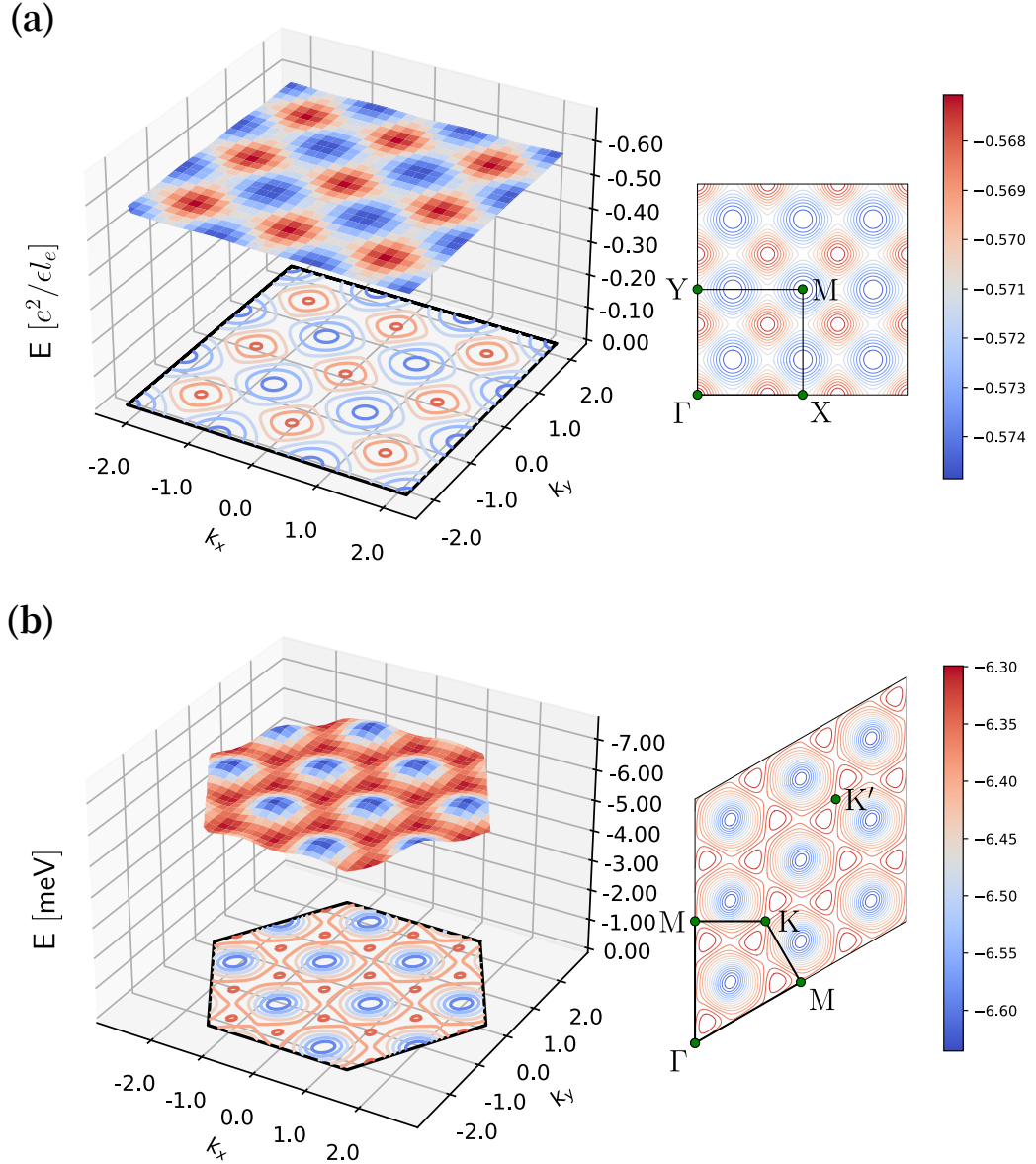


Figure 3.3: Filled CF band dispersion obtained using the Hartree-Forck approximation. The calculation is done for MLL model (a) with parameter $V_{10} = 0.12$ units of $\frac{e^2}{\epsilon l_e}$ and MoTe₂ model (b) with parameter $\lambda = 0.6$ on a 9×9 lattice. These Hartree-Fock CF bands turn out to be *nearly flat*. As is shown in Eq.(3.79), a three-fold periodicity of CF band dispersion emerges as a manifestation of the translation-symmetry fractionalization, as is seen in both subfigures on the right. Note that we have used the *electron's Brillouin Zone* (BZ) to plot the CF dispersion for better visualization of the symmetry fractionalization (in the tMoTe₂ model the electron's BZ is the moiré BZ.). The CF's BZ should be 1/3 of the electron's BZ due to the enlarged real-space unit cell along the a_1 direction.

3.4.2.2 Overlap between projected wavefunctions and ED ground states

We perform exact diagonalization (ED) on the sample of 6×4 unit cells with the tuning parameter: the periodic potential V_{10} for MLL model, and the band scaling factor λ for tMoTe₂ model. The many-body spectra for selected parameter values are shown in FIG.3.4. As the parameter is large enough, we observe a gap-closing

phase transition ($V_{10} \sim 0.18 \frac{e^2}{\epsilon l_e}$ for the MLL model and $\lambda \sim 1.0$ for the tMoTe₂ model).

Both the Laughlin state and our proposed projected wavefunction (in the form of *combinatorial hyperdeterminants*) can be obtained by projecting the CF states back to the electronic many-body Fock space. The only difference is that for Laughlin's state *non-optimized* mean-field states are used (corresponding to fully filled CF LLL), while for our projective construction, the Hartree-Fock self-consistent mean-field states $|\Psi_{CF}^{MF}\rangle$ are used (corresponding to fully filled lowest-energy CF Chern band).

Due to the 6×4 system size, the projected wavefunction $\mathbf{P}_g |\Psi_{CF}^{MF}\rangle$ is not translational symmetric along the $\mathbf{a}_{1,e}$ direction with 6 unit cells. Namely, $\mathbf{P}_g |\Psi_{CF}^{MF}\rangle$ is a superposition of sectors with the center of mass (COM) crystalline momentum at Γ , $\frac{1}{3}\mathbf{G}_{1,e}$ and $\frac{2}{3}\mathbf{G}_{1,e}$. When we perform the overlap calculation with the three-fold ground states obtained from ED at these three COM momenta, we use the corresponding COM sector of the same projected wavefunction $\mathbf{P}_g |\Psi_{CF}^{MF}\rangle$.

It turns out that, *this projective construction outperforms Laughlin's states across the entire parameter space for all the three COM sectors*, as is shown in Fig.3.5. Notice that our optimization is performed only for the CF mean-field ground states, *not* on the level of the projected electronic wavefunctions. These benchmark results indicate the present projective construction can indeed capture the microscopics of the FCI states.

3.4.2.3 Magnetoroton spectra and quantum numbers

For the samples of 6×6 and 9×9 unit cells, we obtain the magnetoroton spectra using the time-dependent Hartree-Fock (TDHF) approximation, where eigenmodes come into pairs $\pm \hbar\omega_a(\mathbf{q}_e)$, with a labels the magnetoroton band. The positive bands correspond to excitations above the ground state. In our TDHF calculation a nearly dispersionless CF particle-hole (PH) continuum in both models is observed, consistent with the nearly flat mean-field CF bands. This PH continuum occurs at energy $\sim 0.23 \frac{e^2}{\epsilon l_e}$ for the MLL model at $V_{10} = 0.04 \frac{e^2}{\epsilon l_e}$, and at energy ~ 11.2 meV for the tMoTe₂ model at $\lambda = 0.2$.

Below the PH continuum, we observe four (three) branches of magnetoroton bands for the MLL (tMoTe₂) model. We plot the magnetoroton bands $\omega_a(\mathbf{q}_e)$ from the TDHF calculation in FIG.3.6. In both models, *the lowest energy magnetorotons are found near the BZ boundary*. The high energy magnetoroton bands (i.e., band-3 and band-4 for the MLL model and band-3 for the tMoTe₂ model) are visible below the PH continuum only in a small region of the BZ. Even the lowest magnetoroton band (band-1) merges into the PH continuum near the Γ -point. The rotation eigenvalues for the high-symmetry points of the magnetoroton bands are computed in Table.3.2.

We find that the energy scale of the magnetoroton excitations obtained using the TDHF approximation is larger than the excitation energy scale obtained from ED (by a factor ~ 3 in both models for the parameters chosen in Fig.3.6). Performing the projection \mathbf{P}_g is expected to improve the energetics significantly. Due to the complexity of the calculation, we leave computing the projected magnetoroton energies as a future project.

Finally, for the models studied here, no CF LL band inversion is observed. Namely, the FCI quantum phase remains adiabatically connected to the traditional Laughlin's wavefunctions. It would be very interesting to identify and simulate a model where CF band inversion actually occurs. We again leave this as a future direction.

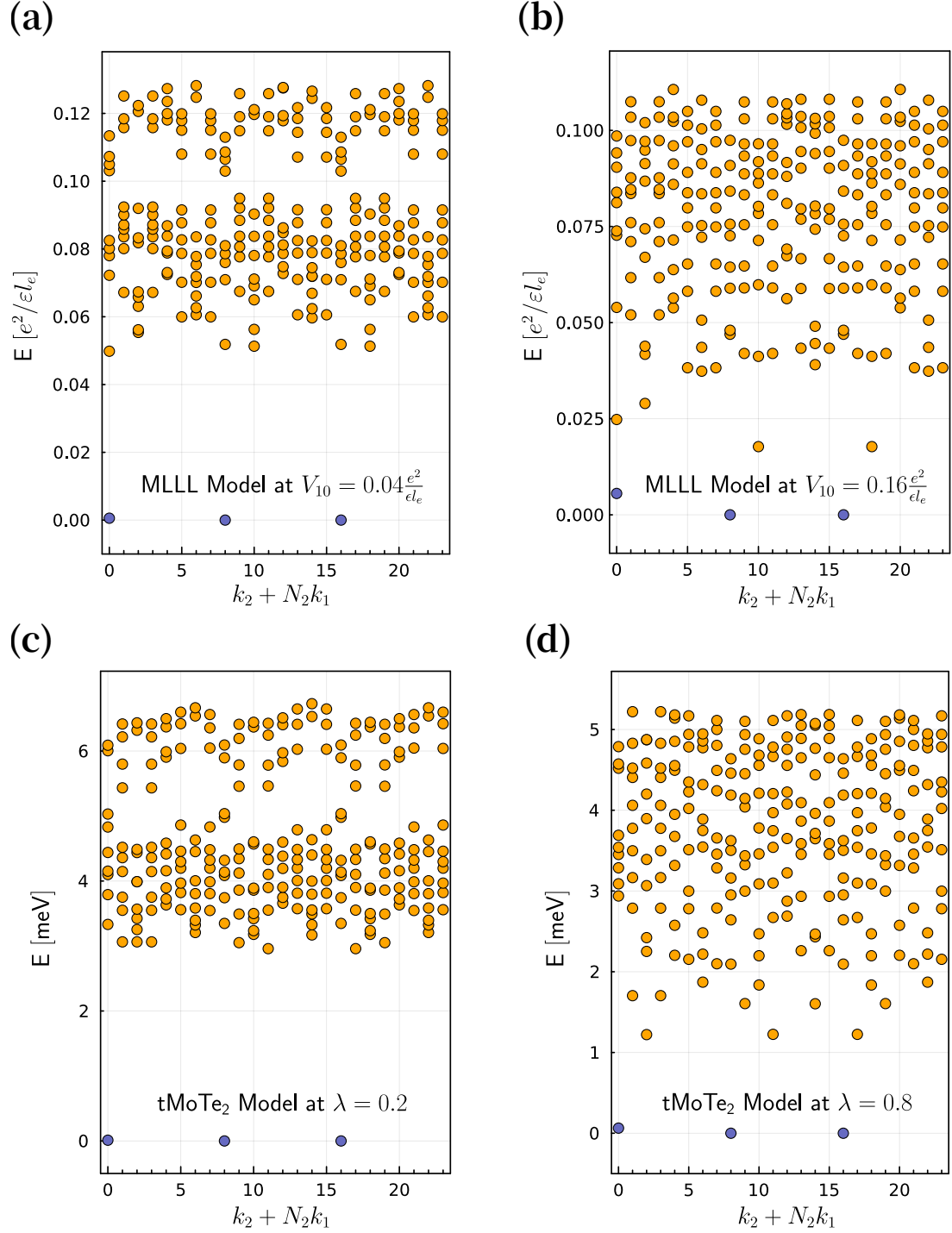


Figure 3.4: Selected many-body spectrum obtained from exact diagonalization on 6×4 unit cells. (a),(b) for MLL model and (c),(d) for tMoTe₂ model. (a) and (c) are close to the flat band limit, while (b) and (d) have much smaller many-body gaps. The three nearly degenerate topological ground states are highlighted in dark purple.

MLL Model :

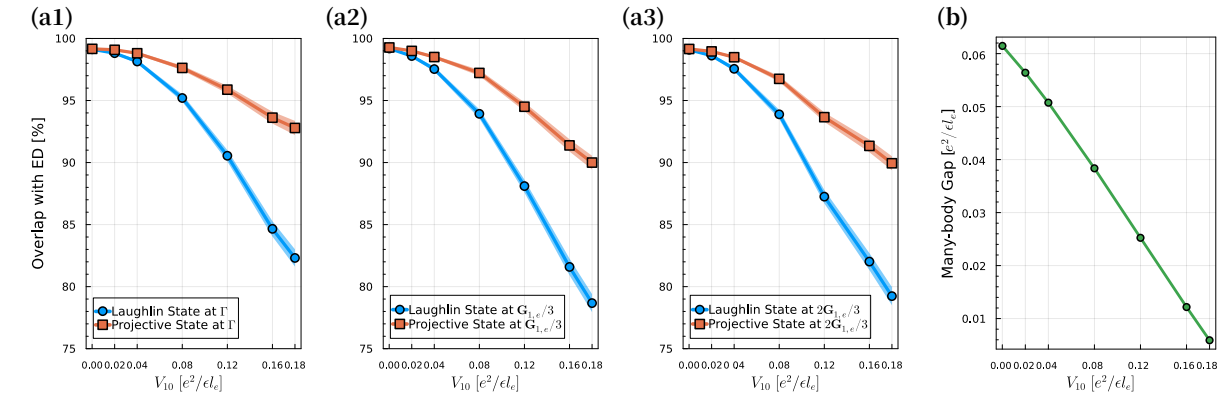
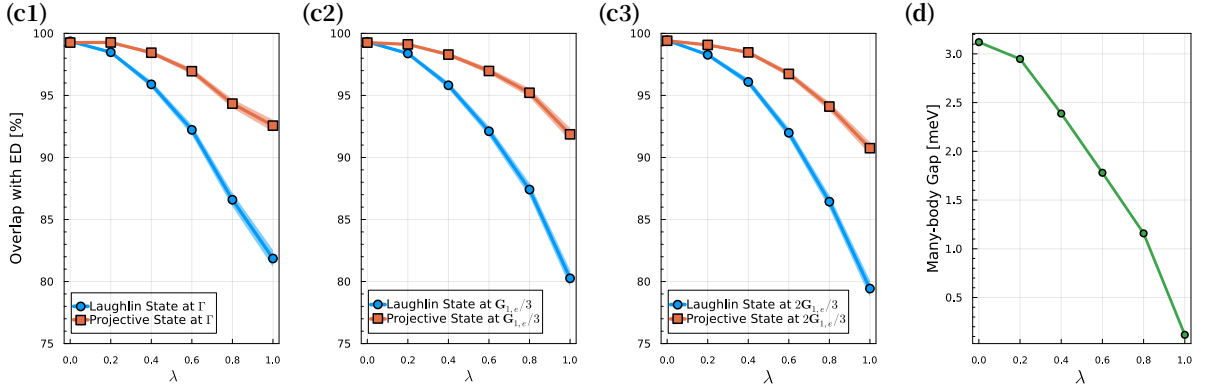
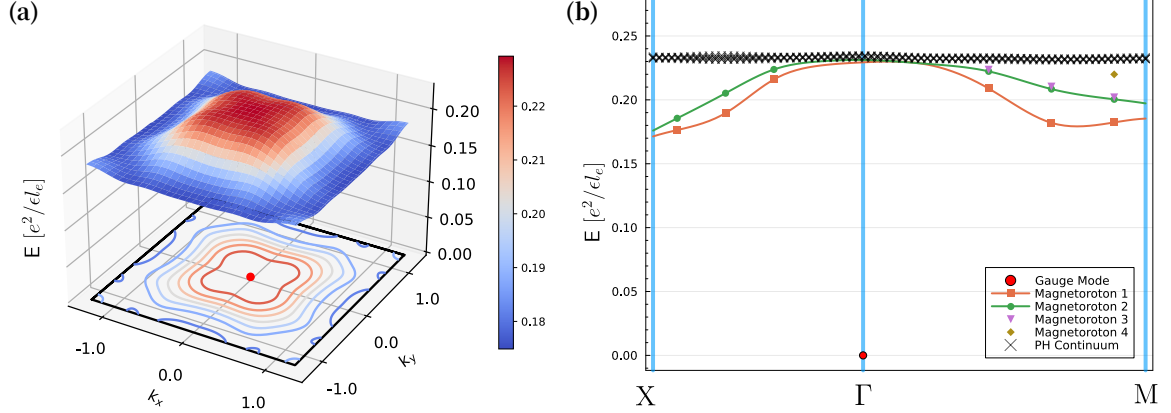
tMoTe₂ Model :

Figure 3.5: (a1)-(a3) and (c1)-(c3) exhibit the overlaps between our electronic hyperdeterminant states and the ED ground states (red line), and the overlaps between Laughlin's states and the ED ground states (blue line) for both MLL model and tMoTe₂ model. Here, the overlap is defined as $|\langle \psi_{\text{ED}} | \psi_{\text{Proj}} \rangle|$ where the two wavefunctions are obtained from ED and the projective construction respectively. There exists three sectors of ground states carrying center-of-mass momentum Γ , $\frac{1}{3}\mathbf{G}_{1,e}$, and $\frac{2}{3}\mathbf{G}_{1,e}$ (the dark purple points in FIG.3.4). The ribbon around each overlap curve represents the error bar due to variational Monte Carlo samplings. The many-body gap (i.e., the energy difference between the ground state manifold and the first excited state.) as a function of the tuning parameter is plotted in (b) and (d).

	band #	Γ	X or Y	M
MLL model	1		-1	$-i$
	2		1	1
	3		-1	-1
	4		i	i
	band #	Γ	K	K'
tMoTe ₂ model	1		1	1
	2		$e^{-i2\pi/3}$	$e^{-i2\pi/3}$
	3		$e^{i2\pi/3}$	$e^{i2\pi/3}$

Table 3.2: Rotation eigenvalues for high-symmetry points of TDHF bands. For MLL model, unlike Γ or M points, the rotation eigenvalue for X and Y points are defined for C_2 rotation instead of C_4 . For tMoTe₂ model, all high symmetry points are defined for C_3 rotation, and the magnetorotons at K and K' points are related by the $C_{2y}\mathcal{T}$ symmetry [14] and thus have identical eigenvalues. Note: when the magnetoroton band merges into the particle-hole(PH) continuum, the corresponding rotation eigenvalue is not presented since one cannot separate the magnetoroton state from the PH continuum. See Fig.3.6 for details.

MLL Model :



tMoTe₂ Model :

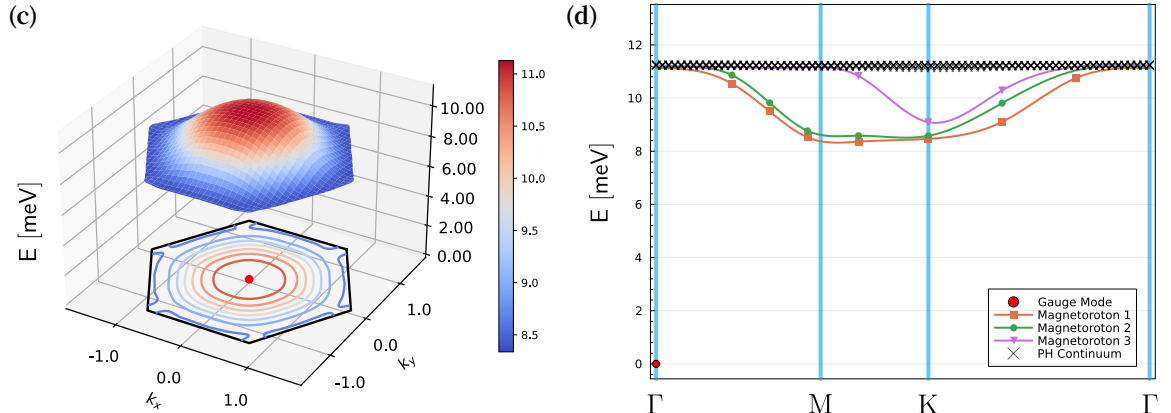


Figure 3.6: Magnetoroton bands for samples of 9×9 unit cells obtained using the TDHF approximation. (a), (b) are for the MLL model with the parameter $V_{10} = 0.04$ units of e^2/ϵ_{l_e} , and (c), (d) are for the tMoTe₂ model with the parameter $\lambda = 0.2$. (a) and (c) are the fitted 2D surface contour of the lowest magnetoroton band (band-1), while (b) and (d) exhibit the full magnetoroton spectra, where scattering points represent the raw data along the path, and the higher horizontal crosses are from the particle-hole (PH) continuum. See Fig. 3.3 for the definitions of the high-symmetry points. Note: there is no raw data point along the X-M line in the MLL model due to the choice of 9×9 sample size. We provide the raw data for a smaller 6×6 MLL sample in the Appendix. 3.G for comparison. We do not perform band fitting for the magnetoroton band-3 and band-4 for the MLL model due to the limited number of points outside the PH continuum. The appearance of the nearly zero-energy modes (red dots in all four figures) at the Γ -point is due to the \mathcal{R}_v gauge degrees of freedom discussed in the main text near the end of Sec. 3.3.4.

3.5 Discussion and Conclusions

In this paper, we present a general projective construction for the composite fermion states in a partially filled Chern band with Chern number ± 1 . In the context of the traditional fractional Quantum Hall liquids, the current construction clarifies a few physical puzzles and unifies several previous studies. In the context of FCI, the current construction paves a route to extract important and experimental relevant microscopic information for the FCI states, including magnetoroton spectrum, magnetoroton quantum numbers, and anyon quasiparticle band structures and crystalline symmetry fractionalization pattern, the Fermi surface shape of the composite Fermi liquid, etc. Some of these seem difficult to access using other methods. We demonstrate how to apply our construction and extract microscopic information in some model systems, including the model for the twisted bilayer MoTe₂.

This work also leaves many open questions. A practical question is about the computation of a hyperdeterminant, which is known to be NP-hard. In the present work, we have used translational symmetry to slightly reduce the computational complexity. This allows us to compute hyperdeterminant exactly up to a system size comparable to those used in exact diagonalization. Is it possible to compute hyperdeterminants for larger systems? There may be two directions to proceed. First, instead of computing hyperdeterminant exactly, there may be algorithms to perform the projection approximately. Second, instead of considering the general hyperdeterminant wavefunctions, one may focus on a subclass of wavefunctions whose hyperdeterminants are easier to compute.

On the conceptual side, one open question is about the non-abelian fractional quantum Hall states. The simplest state in this regard may be the Pfaffian state obtained via pairing on the composite Fermi surface [134, 135, 136, 137, 138]. We expect the present construction, after moderate revision, can be applied to such states in the FCI context. The mathematically relevant object is the so-called hyperpfaffian [139], which is the natural generalization of pfaffian, but defined for tensors.

Another crucial conceptual question that we did not answer in this work is the effective theories associated with the projected wavefunctions. We have demonstrated that in the context of the Galilean invariant traditional Fractional quantum Hall liquids, the projected wavefunctions in our construction are identical to those obtained by Jain's prescription, whose low energy Chern-Simons effective theories have been studied previously using various methods [140, 141, 94, 142, 143, 144, 145, 146, 147]. Even in this Galilean invariant case, finding the correct long-wavelength effective theories can be nontrivial. A remarkable example was established by Dong and Senthil recently [148], where they investigated the composite Fermi liquid for the $\nu = 1$ bosonic system. This system has two apparently different theories: the Halperin-Lee-Read theory (HLR) theory [149] and the Pasquier-Haldane-Read (PHR) theory [114, 115]. The former theory is not within the LLL, leading to an effective theory with a Chern-Simons term. The latter theory is within the LLL, but apparently leads to an effective theory with no Chern-Simons term. Dong and Senthil showed that the effective theory of PHR is defined in a noncommutative space. After approximately mapping to a commutative field theory, the same Chern-Simons term as HLR emerges.

The present construction includes the effects of the crystalline potential and generally applies to Jain's sequence and the composite Fermi liquid in FCI systems. Similar to the PHR theory, our construction is

explicitly within the partially filled Chern band. The HLR theory, however, is parallel to the usual parton construction *without* projecting into the Chern band (see Eq.(3.109)). We leave the investigation of the long-wavelength effective theories for the proposed projected wavefunctions in future works.

Acknowledgement.— We thank Senthil Todadri, Ashvin Vishwanath, Yong Baek Kim and Yuan-Ming Lu for helpful discussions. We acknowledge the HPC resources from Andromeda cluster at Boston College. D.X. acknowledges support from the Center on Programmable Quantum Materials, an Energy Frontier Research Center funded by DOE BES under award DE-SC0019443.

Note added.— After the completion of the manuscript, we became aware that Junren Shi [150] generalizes the Pasquier-Haldane-Read's construction for the $\nu = 1$ bosonic composite Fermi liquid to the case of Galilean invariant $\nu = 1/2$ fermionic composite Fermi liquid in the disc geometry, where a projection to the $\nu = 1/2$ bosonic Laughlin state in the vortex space is used, and coincides with our construction in this case.

3.A The rotation transformations of LLL bloch states and the CB-LLL mapping

Let us consider a 2D rotation symmetric sample with $e^{i\theta}\mathbf{a}_{i,e} = \sum_j r_{ij}\mathbf{a}_{j,e}$ and $N_{1,e} = N_{2,e} \equiv N$, where $r_{ij} \in \mathbb{Z}$ and $i, j \in \{1, 2\}$. Choosing $z_0 = \mathbf{a}_{i,e}$ in Eq.(3.44), then

$$\begin{aligned} D_e(\mathbf{a}_{i,e}) &= [U_{R,e}(\theta)R_e(\theta)]^{-1}D_e(e^{i\theta}\mathbf{a}_{i,e})[U_{R,e}(\theta)R_e(\theta)] \\ &= [U_{R,e}(\theta)R_e(\theta)]^{-1}D_e\left(\sum_{ij}\mathbf{a}_{j,e}\right)[U_{R,e}(\theta)R_e(\theta)]. \end{aligned} \quad (3.119)$$

Applying to the bloch basis $|\mathbf{k}_e\rangle_{\text{LLL}}$, and expanding $D_e(\sum_{ij}\mathbf{a}_j)$ using the GMP algebra

$$D_e\left(\sum_j r_{ij}\mathbf{a}_{j,e}\right) = e^{i\pi r_{i1}r_{i2}}D_e(r_{i1}\mathbf{a}_{1,e})D_e(r_{i2}\mathbf{a}_{2,e}), \quad (3.120)$$

we have

$$e^{-i\mathbf{k}_e \cdot \mathbf{a}_{i,e}} = e^{i\pi r_{i1}r_{i2}}e^{-i(R_\theta\mathbf{k}_e) \cdot (e^{i\theta}\mathbf{a}_{i,e})}. \quad (3.121)$$

Using the identity $(-1)^{r_{i1}+r_{i2}+1} = (-1)^{r_{i1}r_{i2}}$ (because r_{i1}, r_{i2} cannot be both even, since $\det(r_{ij}) = 1$), and noting that $e^{-i\mathbf{k}_e \cdot \mathbf{a}_{i,e}} \equiv e^{-i(e^{i\theta}\mathbf{k}_e) \cdot (e^{i\theta}\mathbf{a}_{i,e})}$, one can obtain the expression:

$$\begin{aligned} e^{-i(R_\theta\mathbf{k}_e) \cdot (e^{i\theta}\mathbf{a}_{i,e})} &= e^{-i(e^{i\theta}(\mathbf{k}_e - \mathbf{K}_e) + \mathbf{K}_e) \cdot (e^{i\theta}\mathbf{a}_{i,e})}, \\ \text{where } \mathbf{K}_e &\equiv \frac{\mathbf{G}_{1,e}}{2} + \frac{\mathbf{G}_{2,e}}{2}. \end{aligned} \quad (3.122)$$

Therefore, generally speaking, the rotation should be viewed as about the $[\pi, \pi]$ -point \mathbf{K}_e of the BZ. For the C_2 and C_4 systems, the phase factor $e^{i\pi r_{i1}r_{i2}}$ is trivial and the rotation can also be viewed as about the

$[0, 0]$ -point. However, for the C_3 and C_6 systems, this phase factor is nontrivial, and one does need to view the rotation as about the $[\pi, \pi]$ -point (or momentum points differ by a reciprocal lattice vector). *To have a uniform discussion, in this paper we always view the rotation as about the $[\pi, \pi]$ -point in the LLL.*

Choosing $z_0 = \frac{\mathbf{a}_{i,e}}{N}$ in Eq.(3.44), we have:

$$\begin{aligned} & [U_{R,e}(\theta)R_e(\theta)]\rho_e\left(\frac{\mathbf{G}_{1,e}}{N}\right)[U_{R,e}(\theta)R_e(\theta)]^{-1} \\ &= \rho_e(e^{i\theta}\frac{\mathbf{G}_{1,e}}{N}) = e^{i\pi\frac{r_{21}r_{22}}{N^2}}\rho_e(r_{22}\frac{\mathbf{G}_{1,e}}{N})\rho_e(-r_{21}\frac{\mathbf{G}_{2,e}}{N}) \\ & [U_{R,e}(\theta)R_e(\theta)]\rho_e\left(\frac{\mathbf{G}_{2,e}}{N}\right)[U_{R,e}(\theta)R_e(\theta)]^{-1} \\ &= \rho_e(e^{i\theta}\frac{\mathbf{G}_{2,e}}{N}) = e^{i\pi\frac{r_{11}r_{12}}{N^2}}\rho_e(-r_{12}\frac{\mathbf{G}_{1,e}}{N})\rho_e(r_{11}\frac{\mathbf{G}_{2,e}}{N}) \end{aligned} \quad (3.123)$$

Applying to Eq.(3.36), one obtains:

$$\begin{aligned} & e^{i\xi(\theta, \mathbf{k}_e + \frac{\mathbf{G}_{1,e}}{N})} e^{i\frac{\mathbf{k}_e \cdot \mathbf{a}_{2,e}}{N}} \\ &= e^{i\pi\frac{r_{21}r_{22}}{N^2}} e^{ir_{22}\frac{(R_\theta \mathbf{k}_e - r_{21}\frac{\mathbf{G}_{2,e}}{N}) \cdot \mathbf{a}_{2,e}}{N}} e^{i\xi(\theta, \mathbf{k}_e)} \\ & e^{i\xi(\theta, \mathbf{k}_e + \frac{\mathbf{G}_{2,e}}{N})} \\ &= e^{i\pi\frac{r_{11}r_{12}}{N^2}} e^{-ir_{12}\frac{(R_\theta \mathbf{k}_e + r_{11}\frac{\mathbf{G}_{2,e}}{N}) \cdot \mathbf{a}_{2,e}}{N}} e^{i\xi(\theta, \mathbf{k}_e)}. \end{aligned} \quad (3.124)$$

Namely:

$$\begin{aligned} e^{i\xi(\theta, \mathbf{k}_e + \frac{\mathbf{G}_{1,e}}{N})} &= e^{-i\pi\frac{r_{21}r_{22}}{N^2}} e^{-i\frac{\mathbf{k}_e \cdot \mathbf{a}_{2,e}}{N}} e^{ir_{22}\frac{R_\theta \mathbf{k}_e \cdot \mathbf{a}_{2,e}}{N}} e^{i\xi(\theta, \mathbf{k}_e)} \\ e^{i\xi(\theta, \mathbf{k}_e + \frac{\mathbf{G}_{2,e}}{N})} &= e^{-i\pi\frac{r_{11}r_{12}}{N^2}} e^{-ir_{12}\frac{R_\theta \mathbf{k}_e \cdot \mathbf{a}_{2,e}}{N}} e^{i\xi(\theta, \mathbf{k}_e)}. \end{aligned} \quad (3.125)$$

These equations fully determine $e^{i\xi(\theta, \mathbf{k}_e)}$ up to an overall shift, which can be fixed by computing $e^{i\xi(\theta, \mathbf{0})}$.

For instance, for a C_4 symmetric lattice, the matrix $(r_{ij}) = i\sigma_y$, $R_\theta \mathbf{k}_e \equiv R_\theta(k_1\frac{\mathbf{G}_{1,e}}{2\pi} + k_2\frac{\mathbf{G}_{2,e}}{2\pi}) = ((-k_2 + 2\pi)\frac{\mathbf{G}_{1,e}}{2\pi} + k_1\frac{\mathbf{G}_{2,e}}{2\pi})$, one finds:

$$C_4 : e^{i\xi(\frac{\pi}{2}, \mathbf{k}_e)} = e^{-i\frac{k_1 k_2}{2\pi}}. \quad (3.126)$$

Using the BZ boundary condition Eq.(3.39), the rotation eigenvalues are:

C_4 systems:

$$\begin{aligned} C_4([(0, 0) \text{ shifted by } (\pi, \pi)]) &= (-i), \\ C_4([(0, 0) \text{ shifted by } (\pi, \pi)]) &= 1, \\ C_2([(0, 0) \text{ shifted by } (\pi, \pi)]) &= 1. \end{aligned} \quad (3.127)$$

For a C_6 symmetric lattice, we choose $\mathbf{a}_{2,e} = e^{i\frac{2\pi}{3}}\mathbf{a}_{1,e}$ and the (r_{ij}) matrix becomes $\begin{pmatrix} 1 & 1 \\ -1 & 0 \end{pmatrix}$. Consequently $\mathbf{G}_{2,e} = e^{i\frac{\pi}{3}}\mathbf{G}_{1,e}$. As is mentioned before, the rotation center is shifted to $[\pi, \pi]$, so $R_\theta \mathbf{k}_e \equiv$

$$R_\theta(k_1 \frac{\mathbf{G}_{1,e}}{2\pi} + k_2 \frac{\mathbf{G}_{2,e}}{2\pi}) = (-(k_2 - \pi) + \pi) \frac{\mathbf{G}_{1,e}}{2\pi} + ((k_1 - \pi) + (k_2 - \pi) + \pi) \frac{\mathbf{G}_{2,e}}{2\pi} = (-k_2 + 2\pi) \frac{\mathbf{G}_{1,e}}{2\pi} + (k_1 + k_2 - \pi) \frac{\mathbf{G}_{2,e}}{2\pi},$$

and one finds:

$$C_6 : e^{i\xi(\frac{\pi}{3}, \mathbf{k}_e)} = e^{-i\frac{\pi}{12}} e^{-i\frac{k_1 k_2 + \frac{1}{2} k_2 (k_2 - 2\pi)}{2\pi}}. \quad (3.128)$$

The rotation eigenvalues are:

C_6 systems:

$$\begin{aligned} C_6([(0, 0) \text{ shifted by } (\pi, \pi)]) &= e^{-i\frac{\pi}{3}}, \\ C_3([(\frac{2\pi}{3}, \frac{2\pi}{3}) \text{ shifted by } (\pi, \pi)]) &= 1, \\ C_2([(\frac{\pi}{2}, 0) \text{ shifted by } (\pi, \pi)]) &= 1. \end{aligned} \quad (3.129)$$

The rotation transformation for C_2 and C_3 can be obtained by the square of the C_4 and C_6 . These results show that in the LLL, the magnetic rotation eigenvalues are $e^{-i\theta}$ at the $\mathbf{K}_e = (\pi, \pi)$ -point, and are trivial everywhere else.

In a general Chern band, The Chern number put a constraint on the rotation eigenvalues at these high-symmetry points [124]:

C_2 systems :

$$(-1)^C = C_2[(0, 0)] \cdot C_2[(\pi, \pi)] \cdot C_2[(\pi, 0)] \cdot C_2[(0, \pi)]$$

C_4 systems :

$$e^{i\frac{\pi}{2}C} = (-1)^F C_4[(0, 0)] \cdot C_4[(\pi, \pi)] \cdot C_2[(\pi, 0)]$$

C_3 systems :

$$e^{i\frac{2\pi}{3}C} = (-1)^F C_3[(0, 0)] \cdot C_3[(\frac{2\pi}{3}, \frac{2\pi}{3})] \cdot C_3[-(\frac{2\pi}{3}, \frac{2\pi}{3})]$$

C_6 systems :

$$e^{i\frac{\pi}{3}C} = (-1)^F C_6[(0, 0)] \cdot C_3[(\frac{2\pi}{3}, \frac{2\pi}{3})] \cdot C_2[(\frac{\pi}{2}, 0)], \quad (3.130)$$

where $(C_n)^n = (-1)^F$. Here, we have $C = -1$ and choose the convention that $(-1)^F = 1$. It is straightforward to redefine the rotation operation to describe the case of $(-1)^F = -1$.

Due to the mapping Eq.(3.46), we know that if the CB has a rotation eigenvalue $e^{-i\theta}$ at the Γ -point and trivial everywhere else (coined “*the fundamental case*” below), a smooth gauge satisfying Eq.(3.47,3.48) can be found following the prescription of Ref.[123]. If the rotation eigenvalues do not match the fundamental case, one needs to redefine the rotation operation $R_{\text{CB}}(\theta)$ following two steps as below, without changing the algebra satisfied by $R_{\text{CB}}(\theta)$ and $T_{\text{CB}}(\mathbf{a}_{i,e})$.

In the first step, one redefines $R_{\text{CB}}(\theta)$ by multiplying a factor $e^{-im\theta}$ ($m \in \mathbb{Z}$): $R_{\text{CB}}(\theta) \rightarrow e^{-im\theta} R_{\text{CB}}(\theta)$, so that the eigenvalue $C_n[(0, 0)] = e^{-i\theta}$, matching the fundamental case. This step induces a possible nontrivial Wen-Zee shift. After this step, the eigenvalues at the other high-symmetry points still may not match the

fundamental case, in which case we need the second step.

In the second step, we redefine $R_{\text{CB}}(\theta)$ by combining a translation. For example, for C_4 systems, after the first step, it is possible that $C_4[(\pi, \pi)] = C_2[(\pi, 0)] = -1$. In this case, one redefine $R_{\text{CB}}(\theta) \rightarrow T_{\text{CB}}(\mathbf{a}_{1,e})R_{\text{CB}}(\theta)$, and the redefined rotation eigenvalues match the fundamental case. Physically, if $R_{\text{CB}}(\theta)$ is the C_4 rotation about a square lattice site, then $T_{\text{CB}}(\mathbf{a}_{1,e})R_{\text{CB}}(\theta)$ is the C_4 rotation about a plaquette center. Similar redefinitions can be made for C_2 (using either the link center or the plaquette center rotations) and C_3 systems (using the plaquette center rotation). For C_6 systems, the second step is not needed since one must have $C_3[(\frac{2\pi}{3}, \frac{2\pi}{3})] = C_2[(\frac{\pi}{2}, 0)] = 1$ after the first step. After these two steps of redefinition, a complete match with the fundamental case can always be made.

3.B Composite fermion substitution for the case of $\nu = \frac{1}{2s}$ composite Fermi liquid

In the case of $\nu = \frac{1}{2s}$, the bosonic vortex carries $q_v = -q_e$, and forms a $\nu = \frac{1}{2s}$ fractional quantum hall liquid. This corresponds to the $p \rightarrow \infty$ case of the Jain's sequence. In the disc geometry with the open boundary condition, \mathcal{R}_e and \mathcal{R}_v satisfies the algebra:

$$[\mathcal{R}_{e,x}, \mathcal{R}_{e,y}] = -il_e^2, \quad [\mathcal{R}_{v,x}, \mathcal{R}_{v,y}] = il_e^2. \quad (3.131)$$

They can be used to construct the charge-neutral composite fermion variables:

$$\begin{aligned} r_x &= \frac{1}{2}(\mathcal{R}_{e,x} + \mathcal{R}_{v,x}) \\ r_y &= \frac{1}{2}(\mathcal{R}_{e,y} + \mathcal{R}_{v,y}) \\ k_x &= \frac{-1}{l_e^2}(\mathcal{R}_{e,y} - \mathcal{R}_{v,y}) \\ k_y &= \frac{1}{l_e^2}(\mathcal{R}_{e,x} - \mathcal{R}_{v,x}) \end{aligned} \quad (3.132)$$

It is straightforward to check that these CF variables satisfy $[r_x, k_x] = [r_y, k_y] = i$, while all other commutators vanish. Note that \mathbf{k} can be represented as:

$$\mathbf{k} = \frac{1}{l_e^2}\hat{z} \times (\mathcal{R}_e - \mathcal{R}_v), \quad (3.133)$$

indicating that the CF's momentum is related to its electric dipole moment.

On a finite size system with $N_{1,e} \cdot N_{2,e}$ unit cells, one may choose either the real-space or momentum-space basis for the CF. For example, the momentum-space basis is given by the eigenstates of the translation operator:

$$T_{CF}(z) = e^{-i\mathbf{k} \cdot z} = D_e(z) \cdot D_v(z) \quad (3.134)$$

The boundary-condition-allowed z is given by $z = l_2 \frac{\mathbf{a}_{1,e}}{N_{2,e}} - l_1 \frac{\mathbf{a}_{2,e}}{N_{1,e}}$, $l_i \in \mathbb{Z}$. And the physically distinct \mathbf{k} eigenvalues are:

$$\mathbf{k} = (m_1 + \frac{\varphi_{1,e} - \varphi_{1,v}}{2\pi}) \frac{\mathbf{G}_{1,e}}{N_{1,e}} + (m_2 + \frac{\varphi_{2,e} - \varphi_{2,v}}{2\pi}) \frac{\mathbf{G}_2}{N_{2,e}}, \quad (3.135)$$

where $m_i \in [0, N_{1,e} \cdot N_{2,e} - 1]$ are integers. Since the number of fluxes $N_{\phi,e} = N_{\phi,v} = N_{1,e} \cdot N_{2,e}$, one finds that these $N_{\phi,e}^2$ number of momentum eigenstates exactly reproduce the dimension of the Hilbert space $\mathcal{H}_e \otimes \mathcal{H}_v$.

In the presence of crystalline potential, these momentum eigenstates will hybridize and form the CF band structure with the Brillouin Zone characterized by $\mathbf{G}_{i,e}$, and each band has $N_{\phi,e}$ momentum points. On the mean-field level, the composite Fermi liquid is formed by filling the lowest (mean-field) energy band by the filling fraction $\frac{1}{2s}$. This CFL mean-field state can then be fed into the projector \mathbf{P}_g to obtain the projected electronic wavefunction, which is still a hyperdeterminant.

3.C Density operator expectation values in Laughlin states on the torus

The discussion here largely follows Ref.[35], apart from the numerical results. It is known that Laughlin's states at $\nu = 1/m$ form a m -fold irreducible representation of the many-body magnetic translation algebra on a torus:

$$\begin{aligned} \mathbf{D}_e(z_1)\mathbf{D}_e(z_2) &= e^{\frac{i}{2} \frac{z_1 \times z_2}{l_e^2} N_e} \mathbf{D}_e(z_1 + z_2) \\ &= e^{i \frac{z_1 \times z_2}{l_e^2} N_e} \mathbf{D}_e(z_2)\mathbf{D}_e(z_1) \end{aligned} \quad (3.136)$$

For convenience of discussion below, we introduce the minimal translation displacement δ_1 (δ_2) along the L_1 ($L_1\tau$) direction of the sample that is consistent with the torus boundary condition.

$$\delta_1 \equiv \frac{L_1}{N_{\phi,e}}, \quad \delta_2 \equiv \frac{L_1\tau}{N_{\phi,e}}, \quad (3.137)$$

leading to

$$\mathbf{D}_e(\delta_1)\mathbf{D}_e(\delta_2) = e^{i \frac{2\pi}{m}} \mathbf{D}_e(\delta_2)\mathbf{D}_e(\delta_1). \quad (3.138)$$

One can choose a gauge for the m -fold Laughlin's states $|\psi_i\rangle$ ($i \in [0, m-1]$) as the eigenstates of $\mathbf{D}_e(\delta_1)$, satisfying:

$$\mathbf{D}_e(\delta_1)|\psi_i\rangle = e^{i\phi_1} e^{i \frac{2\pi i}{m}} |\psi_i\rangle, \quad \mathbf{D}_e(\delta_2)|\psi_i\rangle = |\psi_{i+1}\rangle, \quad (3.139)$$

where $|\psi_{i+m}\rangle \equiv e^{i\phi_2} |\psi_i\rangle$ and the phase factors $e^{i\phi_i}$ depend on the boundary condition.

N_ϕ	$\tau = i$	$\tau = e^{i\frac{2\pi}{3}}$
2	1	1
4	$-\sqrt{2}$	-1.156(1)
6	1.267(1)	1.000(1)
8	-0.8652(4)	-0.5591(7)
10	0.5658(7)	0.3273(7)
12	-0.3423(8)	-0.1831(9)
14	0.1993(8)	0.0932(5)
16	-0.1139(3)	-0.0461(3)
18	0.0641(4)	0.0228(2)

Table 3.3: $\mathbf{A}(n_1 = 1, n_2 = 0)$ (see Eq.(3.142)) for Laughlin's $\nu = 1/2$ state, with the sample shape parameter $\tau = i$ and $\tau = e^{i\frac{2\pi}{3}}$, and boundary condition $\varphi_{1,e} = \varphi_{2,e} = 0$ (see Eq.(3.26)).

The many-particle density operator satisfies a relation with the magnetic translation operator:

$$\mathbf{D}_e(z_0)\boldsymbol{\rho}_e(\mathbf{q}_e = \frac{iz_1}{l_e^2})\mathbf{D}_e(z_0)^\dagger = e^{i\frac{z_0 \times z_1}{l_e^2}} \boldsymbol{\rho}_e(\mathbf{q}_e = \frac{iz_1}{l_e^2}). \quad (3.140)$$

Plugging in $z_0 = m\delta_1$ or $z_0 = m\delta_2$, using Eq.(3.139), the above identity leads to:

$$\langle \psi_i | \boldsymbol{\rho}_e(\mathbf{q}_e) | \psi_j \rangle \neq 0 \\ \text{only if } \mathbf{q}_e = \mathbf{q}_e(n_1, n_2) \equiv \frac{i(n_1 \frac{L_1}{m} + n_2 \frac{L_1 \tau}{m})}{l_e^2}, \quad (3.141)$$

where $n_i \in [0, m - 1]$ are integers.

Let's define the operators:

$$\mathbf{A}(n_1, n_2) \equiv \mathbf{D}_e(n_1 \delta_1 + n_2 \delta_2)^{-1} \boldsymbol{\rho}_e(\mathbf{q}_e(n_1, n_2)). \quad (3.142)$$

One can show that $\mathbf{A}(n_1, n_2)$ commutes with both $\mathbf{D}_e(\delta_1)$ and $\mathbf{D}_e(\delta_2)$, and consequently must be a constant in the ground state manifold.

We have checked numerically that $A(n_1, n_2) \sim e^{-c \cdot N_{\varphi,e}}$ in the ground state manifold exponentially decay in the thermodynamic limit (c is a constant for a given τ and boundary condition.). For instance, in Table.3.3 we list the values of $\mathbf{A}(n_1 = 1, n_2 = 0)$ in the ground state manifold for Laughlin's $\nu = 1/2$ states (electron is bosonic), computed via variational Monte Carlo.

3.D Time-dependent Hartree-Fock approximation in the presence of constraints

Here we describe the general prescription to compute the excitation spectrum in the framework of TDHF in the presence of constraints and Lagrange multipliers. The original many-body Hamiltonian $\mathbf{H} = \mathbf{H}_0 + \mathbf{V}$,

where \mathbf{H}_0 is the two-body term. For simplicity, we consider \mathbf{V} as the density-density interaction:

$$\mathbf{V} = \frac{1}{2} \sum_{\mathbf{q}} V_{\mathbf{q}} \boldsymbol{\rho}(\mathbf{q}) \boldsymbol{\rho}(-\mathbf{q}), \quad (3.143)$$

where $\boldsymbol{\rho}(\mathbf{q})$ is a fermion bilinear. We assume a collection of linearly independent Hermitian symmetry generators $\{\mathbf{S}_i\}$ that are fermion bilinears. They commute with \mathbf{H} , and form a closed algebra:

$$\begin{aligned} [\mathbf{S}_i, \mathbf{H}] &= 0, \quad \forall i, \\ [\mathbf{S}_i, \mathbf{S}_j] &= i \sum_k c_{ijk} \mathbf{S}_k \end{aligned} \quad (3.144)$$

In the main text, the symmetry generators $\{\mathbf{S}_i\}$ are vortices density operators $\{\boldsymbol{\rho}_v(\mathbf{q}_v)\}$.

The mean-field *free-fermion states* $|\psi\rangle$'s under consideration are those that satisfy the constraints:

$$\langle \psi | \mathbf{S}_i | \psi \rangle = 0. \quad \forall i \quad (3.145)$$

$|\psi\rangle$ is completely captured by its single-body density matrix:

$$\mathcal{P} \equiv \sum_{\alpha, \beta} \langle \psi | f_{\beta}^{\dagger} f_{\alpha} | \psi \rangle f_{\alpha}^{\dagger} f_{\beta}, \quad (3.146)$$

where α, β labels a basis in the single-particle Hilbert space.

For any single-body density matrix \mathcal{P} , we define the Hartree-Fock approximated Hamiltonian:

$$\mathbf{H}_{HF}(\mathcal{P}) \equiv \mathbf{H}_0 + \mathbf{V}_{HF}(\mathcal{P}), \quad (3.147)$$

where

$$\begin{aligned} \mathbf{V}_{HF}(\mathcal{P}) \equiv \frac{1}{2} \sum_{\mathbf{q}} V_{\mathbf{q}} &\left[\text{Tr}[\boldsymbol{\rho}(\mathbf{q}) \mathcal{P}] \boldsymbol{\rho}(-\mathbf{q}) + \boldsymbol{\rho}(\mathbf{q}) \text{Tr}[\boldsymbol{\rho}(-\mathbf{q}) \mathcal{P}] \right. \\ &\left. - \boldsymbol{\rho}(\mathbf{q}) \mathcal{P} \boldsymbol{\rho}(-\mathbf{q}) - \boldsymbol{\rho}(-\mathbf{q}) \mathcal{P} \boldsymbol{\rho}(\mathbf{q}) \right]. \end{aligned} \quad (3.148)$$

The standard static Hartree-Fock calculation boils down to finding \mathcal{P}_0 that minimizes the variational energy $\langle \psi | \mathbf{H} | \psi \rangle$, subject to the constraints Eq.(3.145). One can show that under a small perturbation $\mathcal{P}_0 \rightarrow \mathcal{P}_0 + \delta \mathcal{P}$, the linear order change of variational energy is:

$$0 = \delta \langle \psi | \mathbf{H} | \psi \rangle = \text{Tr}[\mathbf{H}_{HF}(\mathcal{P}_0) \delta \mathcal{P}]. \quad (3.149)$$

Quite generally, such a small perturbation can be parameterized by a small unitary rotation $\mathcal{P}_0 \rightarrow \mathbf{U} \mathcal{P}_0 \mathbf{U}^{\dagger}$ where $\mathbf{U} = e^{i\phi}$, ϕ is a small fermion bilinear operator. To the leading order, $\delta \mathcal{P} = i[\phi, \mathcal{P}_0]$, so

$$0 = i \text{Tr}[\mathbf{H}_{HF}(\mathcal{P}_0) [\phi, \mathcal{P}_0]] = -i \text{Tr}[\phi [\mathbf{H}_{HF}(\mathcal{P}_0), \mathcal{P}_0]], \quad (3.150)$$

where we have used the trace identity $\text{Tr}[\mathbf{A}[\mathbf{B}, \mathbf{C}]] = \text{Tr}[\mathbf{B}[\mathbf{C}, \mathbf{A}]]$.

At this point, it is helpful to introduce the symplectic structure of the space of the fermion bilinear operators. We can separate any fermion bilinear operator \mathbf{A} into two parts:

$$\begin{aligned}\mathbf{A} &= \{\mathbf{A}\}_{phys} + \{\mathbf{A}\}_{unphys}, \quad \text{where} \\ \{\mathbf{A}\}_{phys} &\equiv [[\mathbf{A}, \mathcal{P}_0], \mathcal{P}_0] \\ &= (\mathbf{1} - \mathcal{P}_0)\mathbf{A}\mathcal{P}_0 + \mathcal{P}_0\mathbf{A}(\mathbf{1} - \mathcal{P}_0).\end{aligned}\tag{3.151}$$

Using the fact that \mathcal{P}_0 is a projector, one can easily show that $[\mathbf{A}, \mathcal{P}_0] = [\{\mathbf{A}\}_{phys}, \mathcal{P}_0]$. Namely, to consider the small unitary rotation above, it is sufficient to consider the linear space spanned by $\{\mathbf{A}\}_{phys}$, which we denote as \mathcal{W} . Note that for one has $[\mathbf{A}, \mathcal{P}_0] \in \mathcal{W}$, \forall fermion bilinear \mathbf{A} , and there is a useful identity:

$$\text{Tr}[\mathcal{P}_0[\mathbf{A}, \mathbf{B}]] = \text{Tr}[\mathcal{P}_0[\{\mathbf{A}\}_{phys}, \{\mathbf{B}\}_{phys}]]\tag{3.152}$$

In \mathcal{W} , we can define two different inner products. The first (single angle bracket) is a conventional one while the second (double angle bracket) is a symplectic one.

$$\begin{aligned}\langle \{\mathbf{A}\}_{phys}, \{\mathbf{B}\}_{phys} \rangle &\equiv \text{Tr}[\{\mathbf{A}^\dagger\}_{phys} \cdot \{\mathbf{B}\}_{phys}] \\ \langle\langle \{\mathbf{A}\}_{phys}, \{\mathbf{B}\}_{phys} \rangle\rangle &\equiv \text{Tr}[\{\mathbf{A}^\dagger\}_{phys} \cdot [\{\mathbf{B}\}_{phys}, \mathcal{P}_0]] \\ &= \text{Tr}[\mathcal{P}_0[\{\mathbf{A}^\dagger\}_{phys}, \{\mathbf{B}\}_{phys}]].\end{aligned}\tag{3.153}$$

The condition that $\delta\mathcal{P}$ does not change the constraint relations Eq.(3.145) can also be written as $-i \text{Tr}[\mathcal{P}_0[\mathbf{S}_i, \phi]] = 0$, or in terms of the symplectic inner product introduced above:

$$\langle\langle \{\mathbf{S}_i\}_{phys}, \{\phi\}_{phys} \rangle\rangle = 0.\tag{3.154}$$

We may denote the subspace in \mathcal{W} spanned by $\{\mathbf{S}_i\}_{phys}$ as \mathcal{W}_S . The above condition means that $\{\phi\}_{phys} \in \overline{\mathcal{W}_S}$, where $\overline{\mathcal{W}_S}$ is the symplectic complement of \mathcal{W}_S . Drastically different from the conventional complement subspace, here we have:

$$\mathcal{W}_S \subset \overline{\mathcal{W}_S},\tag{3.155}$$

which is a consequence of Eq.(3.144). The variational minimization problem now becomes finding \mathcal{P}_0 so that Eq.(3.150) is satisfied for all $\phi \in \overline{\mathcal{W}_S}$.

If the objective was to find \mathcal{P}_0 so that Eq.(3.150) is satisfied for all ϕ in the *entire space* \mathcal{W} , then it would lead to the well-known self-consistent condition $[\mathbf{H}_{HF}(\mathcal{P}_0), \mathcal{P}_0] = 0$. However, since $\overline{\mathcal{W}_S}$ is smaller than \mathcal{W} , as long as $[\mathbf{H}_{HF}(\mathcal{P}_0), \mathcal{P}_0] \in \overline{\mathcal{W}_S}^\perp$, \mathcal{P}_0 is a legitimate optimal solution to satisfy Eq.(3.150) satisfied. Here $\overline{\mathcal{W}_S}^\perp$ is the conventional complement subspace of $\overline{\mathcal{W}_S}$ (Here and below we always use \cdot^\perp to denote the conventional complement and \cdot^- to denote the symplectic complement).

One can show that $\overline{\mathcal{W}_S}^\perp$ is actually the symplectic dual of the subspace \mathcal{W}_S . Namely, they are orthogonal to each other w.r.t. the conventional inner product, have the same dimension, and the linear map $\mathbf{x} \mapsto [\mathbf{x}, \mathcal{P}_0]$ is a one-to-one mapping between the two subspaces. One way to see this is to decompose $\overline{\mathcal{W}_S}$ into the direct sum of two mutually orthogonal subspaces (w.r.t. the conventional inner product): $\overline{\mathcal{W}_S} = \mathcal{W}_S \oplus \mathcal{V}$. It follows that, by definition, \mathcal{W} is the direct sum of three mutually orthogonal (w.r.t. the conventional inner product) subspaces:

$$\mathcal{W} = \mathcal{W}_S \oplus \overline{\mathcal{W}_S}^\perp \oplus \mathcal{V} \quad (3.156)$$

Now by choosing an arbitrary $\mathbf{x} \in \mathcal{W}_S$, from above decomposition we know $\langle\langle \mathcal{W}_S, \mathbf{x} \rangle\rangle = \langle\langle \mathcal{V}, \mathbf{x} \rangle\rangle = 0$, i.e., $\langle \mathcal{W}_S, [\mathbf{x}, \mathcal{P}_0] \rangle = \langle \mathcal{V}, [\mathbf{x}, \mathcal{P}_0] \rangle = 0$. Thus we must have $[\mathbf{x}, \mathcal{P}_0] \in \overline{\mathcal{W}_S}^\perp$. Noting that $[[\mathbf{x}, \mathcal{P}_0], \mathcal{P}_0] = \mathbf{x}$, we showed that $\mathbf{x} \mapsto [\mathbf{x}, \mathcal{P}_0]$ is a one-to-one mapping between \mathcal{W}_S and $\overline{\mathcal{W}_S}^\perp$. This mapping also sends \mathcal{V} back to \mathcal{V} .

Therefore, there exist a collection of Lagrange multipliers λ_i , so that $[\mathbf{H}_{HF}(\mathcal{P}_0), \mathcal{P}_0] = -[\sum_i \lambda_i \mathbf{S}_i, \mathcal{P}_0]$. This is equivalent to the condition:

$$[\tilde{\mathbf{H}}_{HF}(\mathcal{P}_0), \mathcal{P}_0] \equiv \left[\mathbf{H}_{HF}(\mathcal{P}_0) + \sum_i \lambda_i \mathbf{S}_i, \mathcal{P}_0 \right] = 0. \quad (3.157)$$

This is the well-known prescription: one can introduce Lagrange multipliers so that the ground state of $\tilde{\mathbf{H}}_{HF}(\mathcal{P}_0)$ satisfies the constraints Eq.(3.145), and perform the self-consistent calculation as usual.

Now we are ready to study the time-evolution of the single-body density matrix near \mathcal{P}_0 :

$$[\tilde{\mathbf{H}}_{HF}(\mathcal{P}), \mathcal{P}] = i\hbar \dot{\mathcal{P}} \quad (3.158)$$

To the linear order of ϕ , this leads to:

$$\begin{aligned} & [\tilde{\mathbf{H}}_{HF}(\mathcal{P}_0), [\phi, \mathcal{P}_0]] + [\mathbf{V}_{HF}([\phi, \mathcal{P}_0]), \mathcal{P}_0] \\ & + (-i) \left[\sum_i \delta \lambda_i(\phi) \mathbf{S}_i, \mathcal{P}_0 \right] = i\hbar [\dot{\phi}, \mathcal{P}_0]. \end{aligned} \quad (3.159)$$

$\delta \lambda_i(\phi) \propto \phi$ is the adjustment of the Lagrange multipliers due to ϕ , so that the ground state of $\tilde{\mathbf{H}}_{HF}(\mathcal{P})$ satisfies the constraints Eq.(3.145). Equivalently, we can define the operator \mathcal{H} :

$$\begin{aligned} \mathcal{H} \cdot \{\phi\}_{phys} & \equiv [[\tilde{\mathbf{H}}_{HF}(\mathcal{P}_0), \{\phi\}_{phys}], \mathcal{P}_0] \\ & + [\mathbf{V}_{HF}([\{\phi\}_{phys}, \mathcal{P}_0]), \mathcal{P}_0], \end{aligned} \quad (3.160)$$

and introduce the linear operator \mathcal{L} to represent the eigen equation (using Jacobi identity and static condition)

$$\mathcal{L} \cdot \{\phi\}_{phys} \equiv [\mathcal{H} \cdot \{\phi\}_{phys}, \mathcal{P}_0] + (-i) \sum_i \delta \lambda_i(\phi) \{\mathbf{S}_i\}_{phys}$$

$$= i\hbar \{\dot{\phi}\}_{phys} = \hbar\omega \{\phi\}_{phys}. \quad (3.161)$$

One can show that if $\{\phi\}_{phys} \in \overline{\mathcal{W}_S}$, then $\mathcal{L} \cdot \{\phi\}_{phys} \in \overline{\mathcal{W}_S}$ as well. To see this, it is sufficient to show $[\mathcal{H} \cdot \{\phi\}_{phys}, \mathcal{P}_0] \in \overline{\mathcal{W}_S}$, or equivalently $\mathcal{H} \cdot \{\phi\}_{phys} \in \overline{\mathcal{W}_S}^\perp$.

In fact, one can show that the operator \mathcal{H} is Hermitian (w.r.t the conventional inner product) in the full space \mathcal{W} . It follows that $\forall i$ and $\{\phi\}_{phys} \in \overline{\mathcal{W}_S}$,

$$\langle \{\mathbf{S}_i\}_{phys}, \mathcal{H} \cdot \{\phi\}_{phys} \rangle = \langle \{\phi\}_{phys}, \mathcal{H} \cdot \{\mathbf{S}_i\}_{phys} \rangle^* = 0 \quad (3.162)$$

This is because

$$\mathcal{H} \cdot \{\mathbf{S}_i\}_{phys} \in \overline{\mathcal{W}_S}^\perp, \quad (3.163)$$

as a consequence of the symmetry, which we will explain next.

TDHF is known to be a conserving approximation. For instance, the Goldstone mode computed in TDHF is gapless. This can be demonstrated explicitly. A symmetry generator \mathbf{S}_i should satisfy both $[\mathbf{S}_i, \mathbf{H}_0] = 0$ and $[\mathbf{S}_i, \mathbf{V}] = 0$. The latter condition leads to an important identity:

$$[\mathbf{S}_i, \mathbf{V}_{HF}(\mathcal{P})] = \mathbf{V}_{HF}([\mathbf{S}_i, \mathcal{P}]) \quad (3.164)$$

Therefore, if \mathcal{P}_0 is a static Hartree-Fock solution with Lagrange multipliers λ_j , then $e^{i\epsilon\mathbf{S}_i} \mathcal{P}_0 e^{-i\epsilon\mathbf{S}_i}$ is automatically another static Hartree-Fock solution with Lagrange multipliers unitary rotated by $e^{i\epsilon\mathbf{S}_i}$. One finds that

$$\mathcal{L} \cdot \{\mathbf{S}_i\}_{phys} = 0, \text{ with } \delta\lambda_j(\mathbf{S}_i) = \sum_k c_{kij} \lambda_k \quad (3.165)$$

Namely, each \mathbf{S}_i corresponds to an exact zero mode – the Goldstone mode. This result in turn tells that $[\mathcal{H} \cdot \{\mathbf{S}_i\}_{phys}, \mathcal{P}_0] \in \mathcal{W}_S$, which, under the one-to-one correspondence $\mathbf{x} \mapsto [\mathbf{x}, \mathcal{P}_0]$, $\mathcal{W}_S \rightarrow \overline{\mathcal{W}_S}^\perp$, also establishes the validity of Eq.(3.163).

We are now ready to find all the eigen modes in TDHF. Note the decomposition of \mathcal{W} in Eq.(3.156). We should solve the eigenproblem of \mathcal{L} in $\overline{\mathcal{W}_S} = \mathcal{W}_S \oplus \mathcal{V}$, and the subspace \mathcal{W}_S is the null space of \mathcal{L} . One then only needs to consider the operator \mathcal{L} in the subspace \mathcal{V} , where the eigenvalues are generically nonzero. Introducing the projector \mathbf{P}_V into the subspace \mathcal{V} , we need to solve the eigenproblem for the operator \mathcal{L}_V :

$$\begin{aligned} \mathcal{L}_V \cdot \phi &= [\mathcal{H}_V \cdot \phi, \mathcal{P}_0], \\ \text{where } \mathcal{L}_V &\equiv \mathbf{P}_V \cdot \mathcal{L} \cdot \mathbf{P}_V \text{ and } \mathcal{H}_V \equiv \mathbf{P}_V \cdot \mathcal{H} \cdot \mathbf{P}_V. \end{aligned} \quad (3.166)$$

If $\mathcal{L}_V \cdot \phi = \hbar\omega\phi$ with $\omega \neq 0$ for $\phi \in \mathcal{V}$, one can always extend ϕ to $\overline{\mathcal{W}_S}$ by adding a unique component in \mathcal{W}_S so that Eq.(3.161) holds.

The eigenproblem of \mathcal{L}_V can be shown to be equivalent to diagonalizing a free boson Hamiltonian via the

bosonic Bogoliubov transformation (i.e., symplectic transformation): the eigenvalues are real and appear as $\pm \hbar\omega$ pairs. This is because \mathcal{H}_V satisfies the following conditions:

$$\mathcal{H}_V \cdot \phi^\dagger = (\mathcal{H}_V \cdot \phi)^\dagger, \quad (3.167)$$

which can be easily seen from Eq.(3.160) using $[\mathbf{A}^\dagger, \mathbf{B}^\dagger] \equiv -[\mathbf{A}, \mathbf{B}]^\dagger$. Consequently, if $\mathcal{L}_V \phi = \hbar\omega \phi$, then $\mathcal{L}_V \phi^\dagger = -\hbar\omega \phi^\dagger$.

Let's summary some main results here. Let the dimension of the linear space \mathcal{W} be $D_{\mathcal{W}}$. In the energy eigenbasis of $\tilde{\mathbf{H}}_{HF}(\mathcal{P}_0)$, \mathcal{W} is spanned by the fermion bilinears $c_\alpha^\dagger d_i$ and $d_i^\dagger c_\alpha$, where i labels the filled single-particle orbitals and α labels the empty single-particle orbitals. Only these bilinears have nontrivial commutator with \mathcal{P}_0 . Therefore $D_{\mathcal{W}} = 2 \cdot N_{filled} \cdot N_{empty}$, where N_{filled} (N_{empty}) is the number of filled (empty) single-particle orbitals.

In the presence of N_c constraints, the perturbations corresponding to violation of the constraints span a subspace $\overline{\mathcal{W}_S}^\perp$, which is N_c dimensional. The exact zero energy Goldstone modes, span a subspace \mathcal{W}_S , which is also N_c dimensional. The nonzero energy modes can be found by studying the subspace \mathcal{V} , which is $D_{\mathcal{W}} - 2 \cdot N_c$ dimensional. \mathcal{W} has the important decomposition Eq.(3.156).

3.E Derivation of Eq.(3.93) and Eq.(3.98)

We always work within the symmetric gauge in this appendix. First of all, let us prove Eq.(3.93). The basic idea is to realize that the Dirac delta function at the origin carries zero angular momentum $L_z = a_\eta^\dagger a_\eta - a_R^\dagger a_R = 0$, so that the non-vanishing expansion of it comes from states with equal n_R and n_η :

$$|0_{CF}\rangle = \sum_n (-1)^n |n_R, n_\eta\rangle, \quad (3.168)$$

which can be seen from the known Laguerre polynomial wavefunctions of $|n_R\rangle |n_\eta\rangle$:

$$\langle \zeta_{CF} | n_R \rangle |n_\eta\rangle = (-1)^n L_n \left(\frac{|\zeta|^2}{2l_{CF}^2} \right) e^{-\frac{|\zeta|^2}{4l_{CF}^2}}. \quad (3.169)$$

So the projection to n -th LL reads

$$\begin{aligned} |n_\eta\rangle \langle n_\eta | \zeta_{CF} \rangle &= |n_\eta\rangle \langle n_\eta | \hat{T}(\zeta) |0_{CF}\rangle \\ &= |n_\eta\rangle \langle n_\eta | D_R(\zeta/2) D_\eta(\zeta/2) |0_{CF}\rangle \\ &= |n_\eta\rangle \langle n_\eta | D_R(\zeta/2) D_\eta(\zeta/2) e^{\frac{i}{2l_{CF}^2} (\zeta_x \hat{y} - \zeta_y \hat{x})} |0_{CF}\rangle \\ &= |n_\eta\rangle \langle n_\eta | D_R(\zeta/2) D_\eta(\zeta/2) D_R(\zeta/2) D_\eta(-\zeta/2) |0_{CF}\rangle \\ &= D_R(\zeta) |n_\eta\rangle \langle n_\eta | 0_{CF}\rangle \\ &= (-1)^n |n_\eta\rangle D_R(\zeta) |n_R\rangle. \end{aligned} \quad (3.170)$$

Here, in the second line, we use an identity of the *usual* translation operator $\hat{T}(\zeta)$ introduced in Eq.(3.188), and in the third line we insert an identity using the exponential operator (since the position operator is vanishing when acting on $|0_{CF}\rangle$), and in the fourth line we use the operator identity Eq.(3.187). Thus Eq.(3.93) is established.

Following the notation in Eq.(3.98) in the main text, we will first compute a simpler fusion coefficient:

$$A(\zeta) \equiv \langle \zeta_{CF}|0_e\rangle|0_v\rangle. \quad (3.171)$$

Notice that the bosonic Bogoliubov transformation Eq.(3.91) is generated by the unitary:

$$U(c) \equiv e^{\text{arctanh}(c)(a_e^\dagger a_v^\dagger - a_e a_v)} = e^{\text{arctanh}(c)(a_\mathcal{R}^\dagger a_\eta^\dagger - a_\mathcal{R} a_\eta)}. \quad (3.172)$$

$U(c)$ satisfies $U(c)^\dagger = U(-c)$ and:

$$U(c)a_e U(c)^\dagger = a_\mathcal{R}, \quad U(c)a_v U(c)^\dagger = a_\eta, \quad (3.173)$$

We thus have the relation between the coherent states and the occupation number basis:

$$|0_e\rangle|0_v\rangle = U(-c)|0_\mathcal{R}\rangle|0_\eta\rangle = \sqrt{1-c^2} \sum_{n=0}^{\infty} (-c)^n |n_\mathcal{R}\rangle|n_\eta\rangle, \quad (3.174)$$

leading to:

$$A(\zeta) = \sqrt{1-c^2} \sum_n (-c)^n \langle \zeta_{CF}|n_\mathcal{R}\rangle|n_\eta\rangle \quad (3.175)$$

where zero angular momentum wavefunctions $\langle \zeta_{CF}|n_R, n_\eta\rangle$ are the Laguerre polynomials (3.169). In addition, the Laguerre polynomials have the generating function:

$$\sum_n t^n L_n(x) = \frac{1}{1-t} e^{-\frac{tx}{1-t}}. \quad (3.176)$$

In the current situation, $t = c$, and one has:

$$\begin{aligned} A(\zeta) &= \sqrt{1-c^2} \frac{1}{1-c} \exp \left[-\frac{c}{1-c} \frac{|\zeta|^2}{2l_{CF}^2} - \frac{|\zeta|^2}{4l_{CF}^2} \right] \\ &= \sqrt{\frac{1+c}{1-c}} \exp \left[-\left(\frac{1+c}{1-c} \right) \frac{|\zeta|^2}{4l_{CF}^2} \right] \end{aligned} \quad (3.177)$$

Next, we compute the complex conjugate of Eq.(3.98):

$$B(z, \omega, \zeta) \equiv \langle \zeta_{CF}|z_e\rangle|\omega_v\rangle = \langle \zeta_{CF}|D_e(z)D_v(\omega)|0_e\rangle|0_v\rangle. \quad (3.178)$$

Using Eq.(3.61), one can show:

$$D_e(z)D_v(\omega) = D_{\mathcal{R}}(X)D_{\eta}(Y). \quad (3.179)$$

where

$$X \equiv \frac{z - c^2\omega}{1 - c^2}, \quad Y \equiv \frac{c(\omega - z)}{1 - c^2}. \quad (3.180)$$

Introducing:

$$s \equiv \frac{X + Y}{2}, \quad d \equiv \frac{X - Y}{2}, \quad (3.181)$$

one has:

$$\begin{aligned} & D_e(z)D_v(\omega) \\ &= \Theta\left(\frac{d}{\sqrt{2}l_{CF}}, \frac{2s}{\sqrt{2}l_{CF}}\right) D_{\mathcal{R}}(d)D_{\eta}(-d)D_{\mathcal{R}}(s)D_{\eta}(s), \end{aligned} \quad (3.182)$$

where we have defined the phase factor involved in the magnetic translation algebra:

$$\Theta(\alpha, \beta) \equiv e^{\frac{\alpha\bar{\beta} - \bar{\alpha}\beta}{2}}, \quad (3.183)$$

whose exponent is bilinear in α, β and satisfies:

$$\begin{aligned} \Theta(\alpha, \beta) &= \bar{\Theta}(\beta, \alpha) \\ \Theta(\bar{\alpha}, \bar{\beta}) &= \bar{\Theta}(\alpha, \beta). \end{aligned} \quad (3.184)$$

For instance:

$$\begin{aligned} D_e(z_0)D_e(z_1) &= \Theta\left(\frac{\bar{z}_0}{\sqrt{2}l_e}, \frac{\bar{z}_1}{\sqrt{2}l_e}\right) D_e(z_0 + z_1) \\ D_v(\omega_0)D_v(\omega_1) &= \Theta\left(\frac{\omega_0}{\sqrt{2}l_v}, \frac{\omega_1}{\sqrt{2}l_v}\right) D_v(\omega_0 + \omega_1). \end{aligned} \quad (3.185)$$

Finally, in the symmetric gauge:

$$\begin{aligned} \eta_x &= \frac{\hat{x}}{2} - l_{CF}^2 \hat{k}_y, & \eta_y &= \frac{\hat{y}}{2} + l_{CF}^2 \hat{k}_x, \\ \mathcal{R}_x &= \frac{\hat{x}}{2} + l_{CF}^2 \hat{k}_y, & \mathcal{R}_y &= \frac{\hat{y}}{2} - l_{CF}^2 \hat{k}_x. \end{aligned} \quad (3.186)$$

leading to the operator identities:

$$D_{\mathcal{R}}(z)D_{\eta}(-z) = e^{\frac{i}{l_{CF}^2}(x\hat{y}-y\hat{x})} \quad (3.187)$$

$$D_{\mathcal{R}}(z)D_{\eta}(z) = \hat{T}(2z), \quad (3.188)$$

where $z = x + iy$ and $\hat{T}(z) = e^{-i(x\hat{k}_x+y\hat{k}_y)}$ is the usual translation operator in the CF space. Therefore,

$$\begin{aligned} D_{\mathcal{R}}(-d)D_{\eta}(d)|\zeta_{CF}\rangle &= \Theta\left(\frac{d}{\sqrt{2}l_{CF}}, \frac{2\zeta}{\sqrt{2}l_{CF}}\right)|\zeta_{CF}\rangle \\ D_{\mathcal{R}}(-s)D_{\eta}(-s)|\zeta_{CF}\rangle &= |(\zeta - 2s)_{CF}\rangle \end{aligned} \quad (3.189)$$

Plugging these results into Eq.(3.182,3.178), one finds:

$$B(z, \omega, \zeta) = \Theta\left(\frac{d}{\sqrt{2}l_{CF}}, \frac{2s - 2\zeta}{\sqrt{2}l_{CF}}\right)A(\zeta - 2s). \quad (3.190)$$

After some basic manipulations and taking the complex conjugate, Eq.(3.98) is established.

3.F Continuous coherent state and the projective construction for Laughlin's states on the torus

The mean-field CF picture for the Laughlin's state corresponds to fully fill the CF LLL. On a finite torus, one needs to define the coherent state $|0_{\eta}\rangle$ in the cyclotron space of the CF. One natural definition for such a coherent state is to project the δ -function at the origin $|\zeta_{CF} = 0\rangle$ to the CF LLL, which has been termed as the continuous coherent state in Ref.[131]. We have numerically tested for a small number of electrons $N = 3, 4$, the projected CF wavefunction is identical to one of the m -fold degenerate Laughlin's states on the torus.

This choice of $|0_{\eta}\rangle$ naturally preserves the magnetic rotation symmetry. Namely, when the sample size and the boundary conditions are consistent with the magnetic rotation symmetry, the projected wavefunction obtained with this prescription is a rotational eigenstate.

3.G Extended Data

In Fig.3.7, we provide the magnetoroton bands raw data of the 6×6 sample for the MLL model, as a supplement to Fig.3.6 in the main text. Still, the points mixed with the particle-hole continuum are removed.

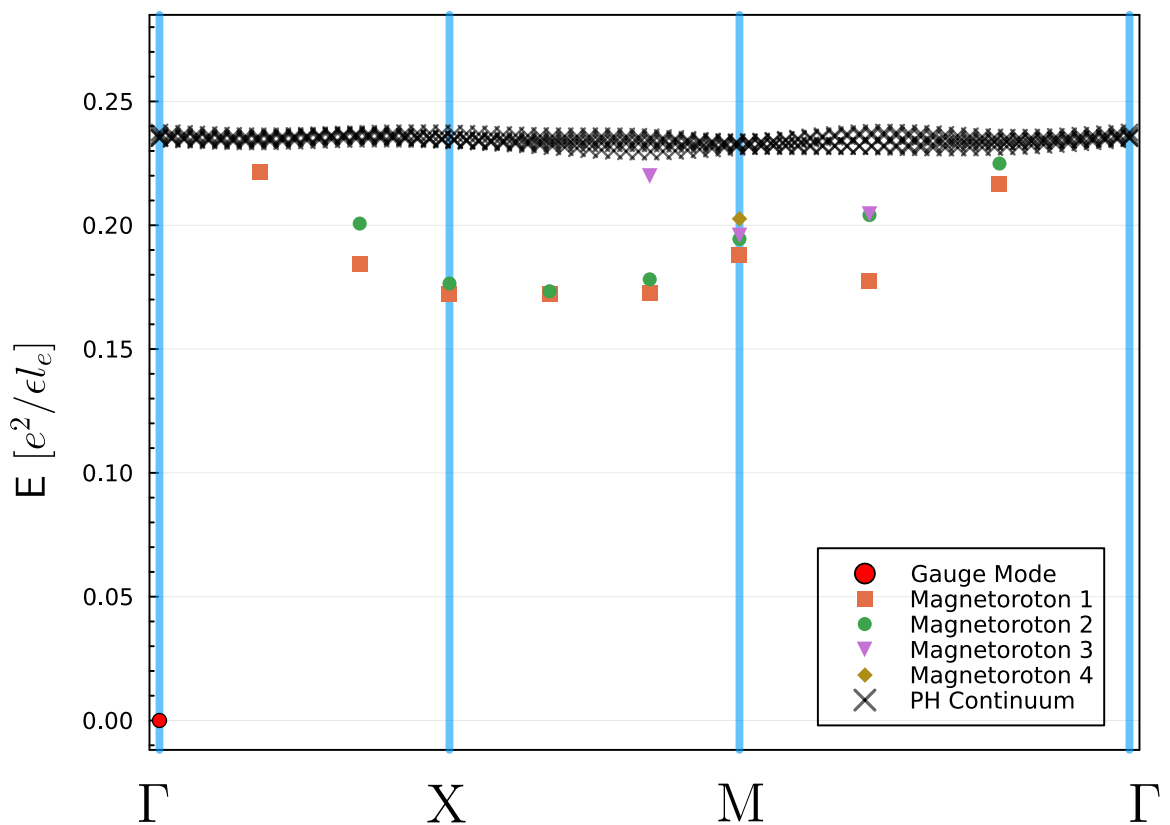


Figure 3.7: Magnetoroton bands for the 6×6 MLL model.

Chapter 4

Supercurrent-induced Anomalous Thermal Hall Effect as a New Probe to Superconducting Gap Anisotropy

4.1 Introduction

The discovery of the correlated insulating phases and superconductivity in twisted bilayer graphene (TBG) [6, 45] has spurred intense interest in twisted two-dimensional (2D) heterostructures, leading to the notion of *twistronics* as a new form of electronic device. To understand the (possibly unconventional) superconductivity realized in these systems, intense experimental investigations have been on-going [151, 152, 153]. While the majority of transport studies on twisted bilayers focuses on electrical transport at the moment, thermal transport has long been established as a powerful and complementary tool for investigating the nature of elementary excitations, particularly in superconductors where ordinary electric transport measurement is ineffective [154, 155, 156, 157, 158, 159]. More recently, quantized thermal Hall conductivity at low temperature became a signature of the topologically ordered ground states in correlated materials [160, 161]. In this work, we show that the thermal Hall response can be a sensitive probe of the *gap anisotropy* in twisted bilayer superconductors, or TBS for short.

The gap function Δ_k of a superconductor has immense implications for the underlying pairing mechanism and the quasiparticle transport. It may be deduced in the angle-resolved photoemission spectroscopy (ARPES) [162, 163, 164], or through the quasiparticle interference (QPI) imaging in scanning tunneling spectroscopy [165, 166]. Resolving the gap anisotropy in ARPES becomes challenging though for low temperature superconductors where Δ_k is smaller than the experimental resolution. For twisted heterostructures, resolving the momentum space structure within a small moiré Brillouin zone (BZ) necessitates the QPI imaging over a formidably large area in the real space. As the demand to resolve the gap structure in TBS grows, limitations of existing experimental probes seem to loom larger. A natural question to ask, at this stage, is whether

it is possible to invent a new probe of the gap anisotropy for very small Δ_k . Here we propose a supercurrent-induced anomalous thermal Hall effect (SATHE) as one possible way to directly probe the gap anisotropy in TBS.

Fig 4.1.(a) shows the schematic setup for SATHE. The TBS may be a vertical Josephson junction (JJ) formed by stacking two atomically thin superconducting films with a certain twist angle, or an intrinsic twisted bilayer superconductor as in TBG. SATHE is a nonlinear response of heat, created by simultaneously applying a *vertical* supercurrent J_S and an *in-plane* temperature gradient, with the resulting *transverse in-plane* flow of heat. In contrast to the conventional thermal Hall effect (THE) which occurs when the ground state breaks the time-reversal symmetry (TRS), SATHE can occur for ground states that preserve the TRS. No external magnetic field is required to observe SATHE.

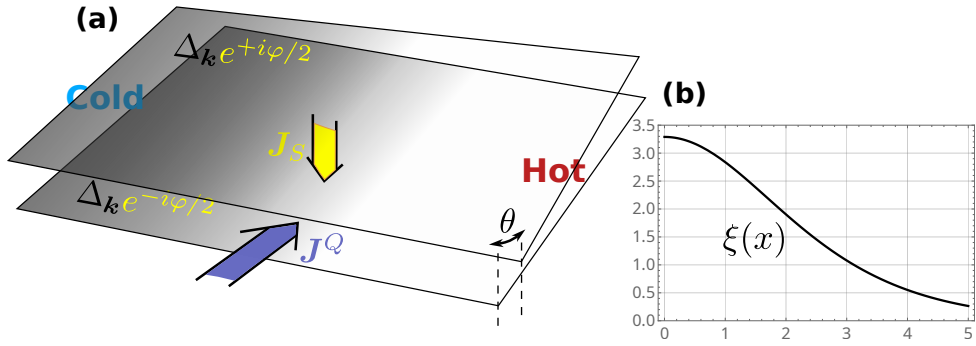


Figure 4.1: (a) SATHE for bilayer-SC. The vertical supercurrent J_S , or equivalently, a pairing phase twist φ between the two layers of, either a vertical JJ or an intrinsic bilayer superconductor, would induce an in-plane thermal Hall effect in a bilayer superconductor. In the former case, an insulating buffer layer may be present (not shown). (b) an illustration for the dimensionless function $\xi(x)$ in Eq.(4.2).

Our proposal thus differs for most proposals of THE including, for instance, Ref. [3] where the JJ spontaneously breaks TRS in the absence of applied supercurrent. It bears resemblance to the Sodemann-Fu proposal for nonlinear electrical Hall effect [167, 168], in that in both proposals the *unperturbed* ground state preserves TRS. One can think of the nonlinear electrical Hall effect as arising from the first electric field driving an imbalance of the fermion distribution, and the second electric field is used to probe the Hall response. In our proposal, the supercurrent is employed to drive Berry curvature out of its equilibrium form, then a temperature gradient is applied to induce the thermal Hall response. In this sense, SATHE can be taken as a thermal analogue of the nonlinear Hall effect.

When the supercurrent is not too large, one can linearize the current-phase relation $J_S \propto \varphi$ and SATHE becomes the perturbative change of the thermal Hall conductivity $\delta\kappa_{xy}$ proportional to the phase twist, $\delta\kappa_{xy} \simeq \varphi \cdot \chi_{\varphi xy}$, with $\chi_{\varphi xy}$ capturing the nonlinear response of the system. Similar to nonlinear Hall effect, the breaking of inversion symmetry is necessary to elicit the desired responses. The observation of SATHE additionally requires the breaking of in-plane and out-of-plane mirror symmetries, which are not conditions normally present in the family of nonlinear Hall effects, but are naturally satisfied in the TBS. The conditions for observing SATHE are therefore not any more stringent than those of other proposed nonlinear Hall effect, at least from the perspective of symmetry requirement.

4.2 Main Results

For TBS with a multiband electronic structure, the pairing Hamiltonian is generally $\sum_{a,b} \Delta_{\mathbf{k}}^{a,b} c_{a,\mathbf{k}}^\dagger c_{b,-\mathbf{k}}^\dagger$, with a, b ranging over the bands. We firstly study the simple situation where only the *intraband pairing* is present: $\Delta_{\mathbf{k}}^{a,b} = 0$ for $a \neq b$. Assuming that $|\Delta_{\mathbf{k}}|$ is much smaller than the energy difference between bands in the normal state, we find that a small pairing phase difference φ between the layers in the TBS induces a change of the Berry curvature and leads to the SATHE formula

$$\begin{aligned} \frac{\delta\kappa_{xy}^{\text{intra.}}}{T} &= \varphi \cdot \frac{\chi_{\varphi xy}^{\text{intra.}}}{T} = \varphi \cdot \frac{k_B^2}{16\pi^2\hbar} \sum_{\text{FS}} \text{sign}(v_F) \\ &\quad \times \oint_{\text{FS}} dk_{\parallel} \xi\left(\frac{\Delta_{\mathbf{k}}(T)}{k_B T}\right) \cdot \partial_{k_{\parallel}} [\langle u_{\mathbf{k}} | \hat{L} | u_{\mathbf{k}} \rangle]. \end{aligned} \quad (4.1)$$

Here $\chi_{\varphi xy}^{\text{intra.}}$ is the intraband transport coefficient for SATHE, $\xi(x)$ is the dimensionless function (see Fig. 4.1 (b))

$$\xi(x) \equiv \int_{|x|}^{\infty} dx' \sqrt{x'^2 - x^2} \frac{x'}{1 + \cosh(x')}, \quad (4.2)$$

and $|u_{\mathbf{k}}\rangle$ is the Bloch state at the Fermi level in the *normal* state. The dimensionless Hermitian operator \hat{L} is the generator of Doppler shift due to φ , and equals $\hat{L} = \text{diag}\{\mathbf{1}, -\mathbf{1}\}$ in the layer space for a vertical JJ but gets more complicated for an intrinsic bilayer superconductor (see below and Supplemental Material (SM) [169]). The loop integral is performed over each Fermi surface (FS) and k_{\parallel} is the counterclockwise tangential momentum at the Fermi surface. The $\text{sign}(v_F) = \pm 1$ characterizes whether the FS is electron-like or hole-like (a single band may host multiple FS's). Clearly if $\Delta_{\mathbf{k}}$ is \mathbf{k} -independent, the loop integral over the FS reduces to a total derivative and vanishes identically.

4.3 The \hat{L} operator and Doppler shift

The normal state tight-binding Hamiltonian for the bilayer can be written in a block form:

$$H_0(\mathbf{k}) = \begin{pmatrix} H_0^t(\mathbf{k}) & T_{\perp}(\mathbf{k}) \\ T_{\perp}^\dagger(\mathbf{k}) & H_0^b(\mathbf{k}) \end{pmatrix}, \quad (4.3)$$

where t/b labels the top/bottom layer, and T_{\perp} represents the interlayer hopping. In the superconducting state, pairing terms are introduced. Introducing the pairing phase difference φ due to the applied supercurrent is equivalent to performing a gauge transformation $H_0 \rightarrow U(\varphi)H_0U^\dagger(\varphi)$ (Doppler shift) while keeping the pairing terms unchanged, and \hat{L} is its generator: $U(\varphi) \equiv e^{-i\frac{\varphi}{4}\hat{L}}$. For a vertical JJ, $\hat{L} = \text{diag}\{\mathbf{1}, -\mathbf{1}\}$. For an intrinsic superconductor, \hat{L} depends on the atomic orbital positions normal to the bilayer plane (see SM [169] and also Ref. [170] therein).

For a JJ, since $|u_{\mathbf{k}}\rangle$ is the eigenstate of $H_0(\mathbf{k})$, $\langle u_{\mathbf{k}} | \hat{L} | u_{\mathbf{k}} \rangle \in [1, -1]$ serve as the indicator of the layer-component of the state. If T_{\perp} is absent, top/bottom layers decouple and $\langle u_{\mathbf{k}} | \hat{L} | u_{\mathbf{k}} \rangle = \pm 1$, leading to vanishing

SATHE according to Eq.(4.1), consistent with physical intuitions.

4.4 Derivation of Eq. (4.1)

Here we show how to derive the SATHE formula of Eq. (4.1) while leaving the more technical parts to [169]. The thermal Hall conductance in a 2D superconductor is related to the superconducting Berry curvature [171, 172] as

$$\frac{\kappa_{xy}}{T} = -\frac{k_B^2}{2\hbar} \int_{-\infty}^{\infty} dE \frac{E^2}{(k_B T)^2} \boldsymbol{\sigma}(E) f'(E), \quad (4.4)$$

where $f(E)$ is the Fermi-Dirac function, and

$$\boldsymbol{\sigma}(E) \equiv - \sum_{\mathbf{a}} \int_{E_{\mathbf{k}} < E} \frac{d^2 k}{(2\pi)^2} \boldsymbol{\Omega}_{\mathbf{k}}^{\mathbf{a}}. \quad (4.5)$$

(Bold fonts are used for quantities related to the superconducting BdG state, to be distinguished from the normal state ones.) Here $\boldsymbol{\Omega}_{\mathbf{k}}^{\mathbf{a}} = -2 \text{Im} \langle \partial_{k_x} \mathbf{u}_{\mathbf{k}}^{\mathbf{a}} | \partial_{k_y} \mathbf{u}_{\mathbf{k}}^{\mathbf{a}} \rangle$ is the superconducting Berry curvature while \mathbf{a} labels bands of the Bogoliubov-de Gennes (BdG) Hamiltonian

$$\mathbf{H}(\mathbf{k}) = \begin{pmatrix} H_0(\mathbf{k}) & \boldsymbol{\Delta}_{\mathbf{k}} \\ \boldsymbol{\Delta}_{\mathbf{k}} & -H_0(\mathbf{k}) \end{pmatrix}. \quad (4.6)$$

The BdG Hamiltonian (4.6) is written in the Nambu basis $\{\psi_{\mathbf{k}}, \Lambda^\dagger \psi_{-\mathbf{k}}^\dagger\}$ where $\psi_{\mathbf{k}}$ is a collection of fermion operators in the band basis, and $\boldsymbol{\Delta}_k^\dagger = \boldsymbol{\Delta}_k$. The time reversal transformation works on $\psi_{\mathbf{k}}$ as $\psi_{\mathbf{k}} \rightarrow \Lambda K \psi_{\mathbf{k}}$, where K is complex conjugation and Λ is some unitary operation.

The energy eigenvalues of the BdG Hamiltonian are ordered into pairs $\pm \mathbf{E}_{1,\mathbf{k}}, \pm \mathbf{E}_{2,\mathbf{k}}, \dots$ with $\mathbf{E}_{1,\mathbf{k}} < \mathbf{E}_{2,\mathbf{k}} < \dots$ and $\mathbf{a} = \pm 1, \pm 2, \dots$ are used to label the bands such that $\mathbf{E}_{-\mathbf{a},\mathbf{k}} = -\mathbf{E}_{\mathbf{a},\mathbf{k}}$. Assuming only the intraband pairing is present, we have $\mathbf{E}_{|\mathbf{a}|,\mathbf{k}} = (\epsilon_{|\mathbf{a}|,\mathbf{k}}^2 + \Delta_{|\mathbf{a}|,\mathbf{k}}^2)^{1/2}$, where $\epsilon_{a,\mathbf{k}}$ is the normal state band energy ($a = 1, 2, \dots$). We assume that only the $a = 1$ band crosses the Fermi level, and all other bands lie strictly above or below it. This allows us to define the interband energy scale as $t \equiv \min |\epsilon_{b,\mathbf{k}}|$ ($b \neq 1$). The gap function of the first band is defined as $\Delta_{\mathbf{k}} \equiv \Delta_{1,\mathbf{k}}$. We will consider the weak-pairing limit $|\Delta_{\mathbf{k}}| \ll t$, so only the lowest-energy states with $\mathbf{a} = \pm 1$ need to be included to the leading-order $\Delta_{\mathbf{k}}/t$ expansion of the Berry curvature

$$\boldsymbol{\Omega}_{\mathbf{k}}^{\mathbf{a}} \doteq -\text{Im} \left\{ \frac{\text{Tr}[\mathbf{P}_{\mathbf{a}} \partial_{k_x} \mathbf{H} \mathbf{P}_{-\mathbf{a}} \partial_{k_y} \mathbf{H} \mathbf{P}_{\mathbf{a}}]}{(\mathbf{E}_{\mathbf{a}} - \mathbf{E}_{-\mathbf{a}})^2} - (x \leftrightarrow y) \right\}, \quad (4.7)$$

where $\mathbf{P}_{\mathbf{a}} \equiv |\mathbf{u}_{\mathbf{k}}^{\mathbf{a}}\rangle \langle \mathbf{u}_{\mathbf{k}}^{\mathbf{a}}|$ is the projector in the Nambu space.

After a small phase twist φ is turned on, $\mathbf{H}, \mathbf{E}_{\pm\mathbf{a}}, \mathbf{P}_{\pm\mathbf{a}}$ appearing in Eq. (4.7) all receive some corrections, which propagate through the THE formulas in Eqs. (4.4) and (4.5). However, as shown in [169], only the change in $\mathbf{P}_{\pm\mathbf{a}}$ is important when the unperturbed ground state obeys TRS. In the end, the intraband pairing

contribution gives

$$\begin{aligned} \delta\Omega_{\mathbf{k}}^{\mathbf{a},\text{intra.}} &\doteq \varphi \sum_{\mathbf{b}\neq\pm\mathbf{a}} 4\text{Im Tr}[(\partial_{k_x}\mathbf{P}_{\mathbf{a}})(\partial_{k_y}\mathbf{P}_{-\mathbf{a}})\mathbf{P}_{\mathbf{b}}(\partial_{\varphi}\mathbf{P}_{\mathbf{a}})\mathbf{P}_{\mathbf{a}}] \\ &\quad - (x \leftrightarrow y), \end{aligned} \quad (4.8)$$

To the leading order of $\Delta_{\mathbf{k}}/t$ expansion and focusing on the $\mathbf{a} = \mathbf{1}$ band, we find

$$\delta\Omega_{\mathbf{k}}^{\mathbf{1},\text{intra.}} = -\varphi \cdot \frac{\Delta_{\mathbf{k}}^2}{4\mathbf{E}_1^3} (v_x\partial_{k_y} - v_y\partial_{k_x}) \langle u_{\mathbf{k}}^1 | \hat{L} | u_{\mathbf{k}}^1 \rangle, \quad (4.9)$$

with $v_{x,y} \equiv \partial_{k_{x,y}}\epsilon_{1,\mathbf{k}}$ the normal state Fermi velocity.

The change in Berry curvature is now fully described with normal state wave functions, and exhibits high concentration near the Fermi surface due to \mathbf{E}_1^3 in the denominator. Identifying $\hat{L}|u_{\mathbf{k}}^1\rangle = 4i\partial_{\varphi}|u_{\mathbf{k}}^1\rangle$, the derivative $\partial_{k_y}\langle u_{\mathbf{k}}^1 | \hat{L} | u_{\mathbf{k}}^1 \rangle = 4\Omega_{y,\varphi}$ becomes the φ -twist Berry curvature, with one component along the momentum direction and the other along the phase twist φ .

Equation (4.9) thus demonstrates how the change of Berry curvature in the superconducting state is intricately composed of the gap function, and a mixed Berry curvature in the momentum-phase space. Plugging Eq. (4.9) into Eq. (4.4) and after some efforts, the main result of our paper Eq. (4.1) is established.

4.5 Interband pairing and nodal superconductivity

When interband pairing is present, the calculation becomes more sophisticated but the final result turns out to be simple. Introducing the normal state projector $P_c \equiv |u_{\mathbf{k}}^c\rangle\langle u_{\mathbf{k}}^c|$, the interband pairing gives $\Delta_{\mathbf{k}}^{\text{inter.}} = \sum_{b\neq c} P_b \Delta_{\mathbf{k}} P_c$, which can be eliminated from the BdG Hamiltonian in Eq. (4.6) by a small unitary rotation

$$e^{i\mathcal{S}\otimes\tau_2} \mathbf{H}(\mathbf{k}) e^{-i\mathcal{S}\otimes\tau_2} \doteq H_0(\mathbf{k}) \otimes \tau_3 + \Delta_{\mathbf{k}}^{\text{intra.}} \otimes \tau_1. \quad (4.10)$$

Here τ are Pauli matrices in the Nambu space, and $\mathcal{S} \equiv \sum_{a\neq b} P_a \Delta_{\mathbf{k}} P_b / (\epsilon_{a,\mathbf{k}} - \epsilon_{b,\mathbf{k}})$ can be viewed small simply because $\Delta_{\mathbf{k}}/(\epsilon_{a,\mathbf{k}} - \epsilon_{b,\mathbf{k}}) \sim \Delta_{\mathbf{k}}/t$ is small in the weak-pairing limit. Based on this useful property, all previous perturbative analysis for the intraband pairing can be extended to interband pairing as well, with only one modification replacing the projector $\mathbf{P}_{\mathbf{a}}$ by $\tilde{\mathbf{P}}_{\mathbf{a}} = e^{-i\mathcal{S}\otimes\tau_2} \mathbf{P}_{\mathbf{a}} e^{i\mathcal{S}\otimes\tau_2}$. Collecting all φ -linear terms contributing to the change of the Berry curvature in Eq. (4.7) seems to be more complicated, but to the leading order of $\Delta_{\mathbf{k}}/t$ the interband contribution can be neatly arranged as [169]

$$\begin{aligned} \delta\Omega_{\mathbf{k}}^{\mathbf{1},\text{inter.}} &= \varphi \cdot \frac{-\mathbf{d}_{\mathbf{k}} \cdot (\partial_{k_x}\mathbf{d}_{\mathbf{k}} \times \partial_{k_y}\mathbf{d}_{\mathbf{k}})}{2\mathbf{E}_1^3}, \\ \mathbf{d}_{\mathbf{k}} &\equiv (\Delta_{\mathbf{k}}, G_{\mathbf{k}}, \epsilon_{1,\mathbf{k}}), \quad G_{\mathbf{k}} \equiv \frac{-1}{2} \text{Re}[\langle u_{\mathbf{k}}^1 | \Delta_{\mathbf{k}}^{\text{inter.}} \hat{L} | u_{\mathbf{k}}^1 \rangle]. \end{aligned} \quad (4.11)$$

Equation (4.11) is clearly reminiscent of the Berry curvature of the effective two-band model

$$\mathbf{H}_{\text{eff}} = \varphi \cdot \partial_{\varphi}\epsilon_{1,\mathbf{k}}\tau_0 + \epsilon_{1,\mathbf{k}}\tau_3 + \Delta_{\mathbf{k}}\tau_1 + \varphi \cdot G_{\mathbf{k}}\tau_2. \quad (4.12)$$

within the perturbative regime. Indeed, we show that \mathbf{H}_{eff} is exactly the low-energy effective Hamiltonian of the TBS itself with insertion of phase twist [169] $\mathbf{H}_{\text{eff}}^{\mathbf{a}} = \tilde{\mathbf{P}}_{\mathbf{a}} \mathbf{H}[\varphi] \tilde{\mathbf{P}}_{\mathbf{a}} \doteq \tilde{\mathbf{P}}_{\mathbf{a}} \mathbf{H} \tilde{\mathbf{P}}_{\mathbf{a}} + \varphi \cdot \tilde{\mathbf{P}}_{\mathbf{a}} (\partial_{\varphi} \mathbf{H}) \tilde{\mathbf{P}}_{\mathbf{a}}$, so could serve as a faithful model to compute $\delta\Omega_k^{1,\text{inter}}$.

In calculating $\delta\kappa_{xy}$ in Eq. (4.4) one should add the two Berry curvature contributions $\delta\Omega_k^1 = \delta\Omega_k^{1,\text{intra.}} + \delta\Omega_k^{1,\text{inter.}}$ in Eq. (4.5). Among the two, the intraband Berry curvature part can be converted to the Fermi surface integral form in Eq. (4.1) but not the interband part. For calculating the latter contribution we can directly use Eqs. (4.4)-(4.5) with $\delta\Omega_k^{1,\text{inter.}}$ given in Eq. (4.11).

Although in principle the interband contribution for SATHE cannot be neglected, there are many physical situations in which the interband pairing and thus the interband contribution to THE does become small. For instance, if each monolayer of TBS itself is superconducting as in a vertical JJ, Δ_k in Eq. (4.6) is diagonal in the monolayer band basis. For small twist angle $\theta \ll 1$, a unitary transformation to the band basis also induces interband pairing components in Δ_k , which are proportional to θ and can be ignored.

If the system is an intrinsic TBS like TBG, the intra- and inter-band pairings should be determined self-consistently. For example, for boson-mediated superconductivity, the multiband Eliashberg formulation may be applied, which is characterized by the electron-boson coupling matrix $[\alpha^2(\omega)F(\omega)]_{ab}$, where a, b label bands. Either in the regime that intraband coupling is dominant $[\alpha^2(\omega)F(\omega)]_{a=b} \gg [\alpha^2(\omega)F(\omega)]_{a \neq b}$, or in the regime that the intraband coupling is dominant $[\alpha^2(\omega)F(\omega)]_{a=b} \ll [\alpha^2(\omega)F(\omega)]_{a \neq b}$, it is easy to show that only the intraband pairing is significant [173].

However, there is one particular scenario in which the interband contributions may be dominant, and that is when the superconductivity in the TBS is nodal. In this case, the node would develop a mass gap $m_k = \varphi \cdot G_k$ right at the nodal point upon the application of a phase twist φ , and a Chern number transfer $\Delta C = \pm \frac{1}{2}$ between the low-energy BdG bands occurs per node. When the net transferred Chern numbers n from all the nodes is nonzero, the system becomes a chiral topological superconductor with quantized THE $\delta\kappa_{xy}^{\text{inter.}} \equiv \varphi \cdot \chi_{\varphi xy}^{\text{inter.}} = ng_0$ in the low-temperature limit $k_B T \ll |m|$, where $\chi_{\varphi xy}^{\text{inter.}}$ is the interband transport coefficient for SATHE, and $g_0 \equiv \pi k_B^2 T / (6\hbar)$ is the quantum of thermal conductance. In our perturbative treatment, $\chi_{\varphi xy}^{\text{inter.}}$ diverges in the low- T regime. This supercurrent-driven topological superconductivity has been discussed in the context of twisted cuprate bilayers [46, 4, 3, 174] and twisted NbSe₂ heterostructures [175].

4.6 Applications to FeSe and cuprates

To demonstrate the possibility of observing SATHE in real materials we consider two examples: vertical JJ's formed by twisted nodeless FeSe, and the nodal cuprate superconducting films. The Δ_k in both of these 2D superconductors has been well characterized by ARPES due to the large energy scale of Δ_k and high transition temperatures. Note that due to the dimensionless nature of the SATHE response, the supercurrent-induced κ_{xy} only depends on the ratio $\Delta_k/k_B T$ as in Eq. (4.1) and the SATHE response of low- T_c superconductors after appropriate rescaling must be similar to the examples we consider now.

Monolayer FeSe is reported to host a significant nodeless gap anisotropy of the form $\Delta_k = \Delta_0 + \Delta_2 \cos 2\theta_k +$

$\Delta_4 \cos 4\theta_{\mathbf{k}}$, where $\Delta_0 = 9.9\text{meV}$, $\Delta_2 = -1.4\text{meV}$, and $\Delta_4 = 1.2\text{meV}$ [164]. The C_4 -rotation-related elliptic M -pockets positioned at $(\pm\frac{\pi}{2}, \pm\frac{\pi}{2})$ within the two-iron BZ [176, 177, 178] can be described by the $\mathbf{k} \cdot \mathbf{p}$ expansion within Fe's $\{3d_{xz}, 3d_{yz}\}$ orbitals [179, 180] as $H_M = (\frac{1}{2m}(k_x^2 + k_y^2) - \mu) + ak_x k_y \tau_z$, where τ_z is a Pauli matrix in the orbital space, $\mu = 0.08\text{eV}$, $1/2m = 1.4\text{eV}\cdot\text{\AA}^2$ and $a = 0.6\text{eV}\cdot\text{\AA}^2$. Since all Fermi pockets are near the zone boundary, moiré zone folding effect comes into play, and Bistritzer-MacDonald model [44] is used to construct the normal state Hamiltonian. For example, to the lowest truncation of the moiré BZ, two hopping processes corresponding to $\delta\mathbf{q}^{t,b} = \pm 2K_M \sin \frac{\theta}{2} \hat{k}_y$ are included for all four of the M -pockets (see Fig. 2 in SM [169]). We set $T_{\perp}^{d_{xz}^t-d_{xz}^b}(\delta\mathbf{q}^{t,b}) = T_{\perp}^{d_{yz}^t-d_{yz}^b}(\delta\mathbf{q}^{t,b}) \simeq T_{\perp} = 15\text{meV}$ and ignore all interorbital hoppings. After turning on such simple T_{\perp} with a twist angle $\theta = 11.5^\circ$, the Fermi surfaces reconstruct within the moiré BZ (see Fig. 4.2 (a1)).

We secondly consider a twisted bilayer of cuprates ¹ with a d -wave gap anisotropy $\Delta_{\mathbf{k}} = \Delta_N \cos 2\theta_{\mathbf{k}}$ [181, 182] and the reported relation $8.5k_B T_c = 2\Delta_N$ [183, 184]. The normal state bilayer Hamiltonian is constructed by first taking the tight-binding model in Ref. [185] as the monolayer Hamiltonian, and then obtaining the interlayer tunneling $T_{\perp}(\mathbf{k}) = t_z(\frac{1}{4}(\cos k_x^t - \cos k_y^t)(\cos k_y^b - \cos k_y^b) + a_0)$ from the detailed orbital analysis in Refs. [174, 186]. The constant $a_0 = 0.4$ is determined from DFT simulations [186]. We set (i) $t_z = 0.025t_0$ (t_0 =leading hopping strength within the CuO₂ plane) with $\theta = 0.6^\circ$ (chiral topological superconductor) and (ii) $t_z = 0.01t_0$ with $\theta = 17.2^\circ$ (topologically trivial superconductor) and plot the corresponding Fermi surfaces in Fig. 4.2 (b1) and (c1), respectively [46, 4]. Here we neglect the moiré zone folding effect for several reasons. First, based on the two-center approximation [44], far away from the zone boundary the moiré zone folding effect may be neglected. Second, the moiré zone folding effect for the Fermi surfaces near the zone boundary does not modify the Fermi surface topology, leaving the results qualitatively unchanged.

The interband and intraband contributions to SATHE for twisted bilayers of FeSe and cuprates are plotted in Fig. 4.2(a2)-(c2). In our linearized scheme, κ_{xy} and $\chi_{\varphi xy}$ are related simply by $\kappa_{xy} = \varphi \cdot \chi_{\varphi xy}$. We plot κ_{xy} rather than $\chi_{\varphi xy}$ because the latter apparently diverges as $\varphi \rightarrow 0$ while $\kappa_{xy}^{\text{inter}}$ remains finite in a supercurrent-driven topological superconductor as shown in Fig. 4.2 (b2). For illustrative purposes, phase twist $\varphi = 1 \text{ rad}$ is chosen for computation ². The interband contribution is evaluated by using the integral formula of Eq. (4.1). For the interband contribution we rely on Eqs. (4.4)-(4.5) with the Berry curvature obtained in Eq. (4.11).

As shown in Fig. 4.2, the intraband contribution plays a dominant role for SATHE in both twisted FeSe (a2) and the topological trivial case of twisted cuprates (c2), while interband contribution dominates in topological nontrivial case of twisted cuprates (b2), especially in the low-temperature regime. Note that the κ_{xy} in the proposed SATHE can reach $\sim 10^{-1}$ of the thermal conductance quantum when the gap anisotropy is significant, e.g., in the FeSe example. We conclude that SATHE can be a sizable effect, detectable in the

¹Note that the currently available cuprate van der Waals materials is Bi2212, which is a bilayer of Cu-O planes. Consequently, twisted double bilayer is more experimental relevant at present. Our twisted bilayer model can viewed as a minimal illustration on SATHE for twisted nodal superconductors.

²Josephson phase twist $\varphi = 1 \text{ rad}$ is taken, primarily to exhibit the strength of the transport coefficient $\chi_{\varphi xy}^{\text{intra}}$ from the intraband contribution along with the quantized behavior of κ_{xy} arising from the interband one. The former component contributes to the thermal Hall conductivity simply as $\kappa_{xy}^{\text{intra.}} = \varphi \cdot \chi_{\varphi xy}^{\text{intra.}}$, as long as we remain within the *linear regime* of the sine current-phase relation, which is satisfied simply because $\sin 1.0 \doteq 0.84 \approx 1.0$. Therefore, the choice $\varphi = 1 \text{ rad}$ can still be considered small in our perturbative treatment, and with such choice the plot of κ_{xy} also directly reflects the strength of the SATHE transport coefficient $\chi_{\varphi xy}$ that we are concerned with.

foreseeable future.

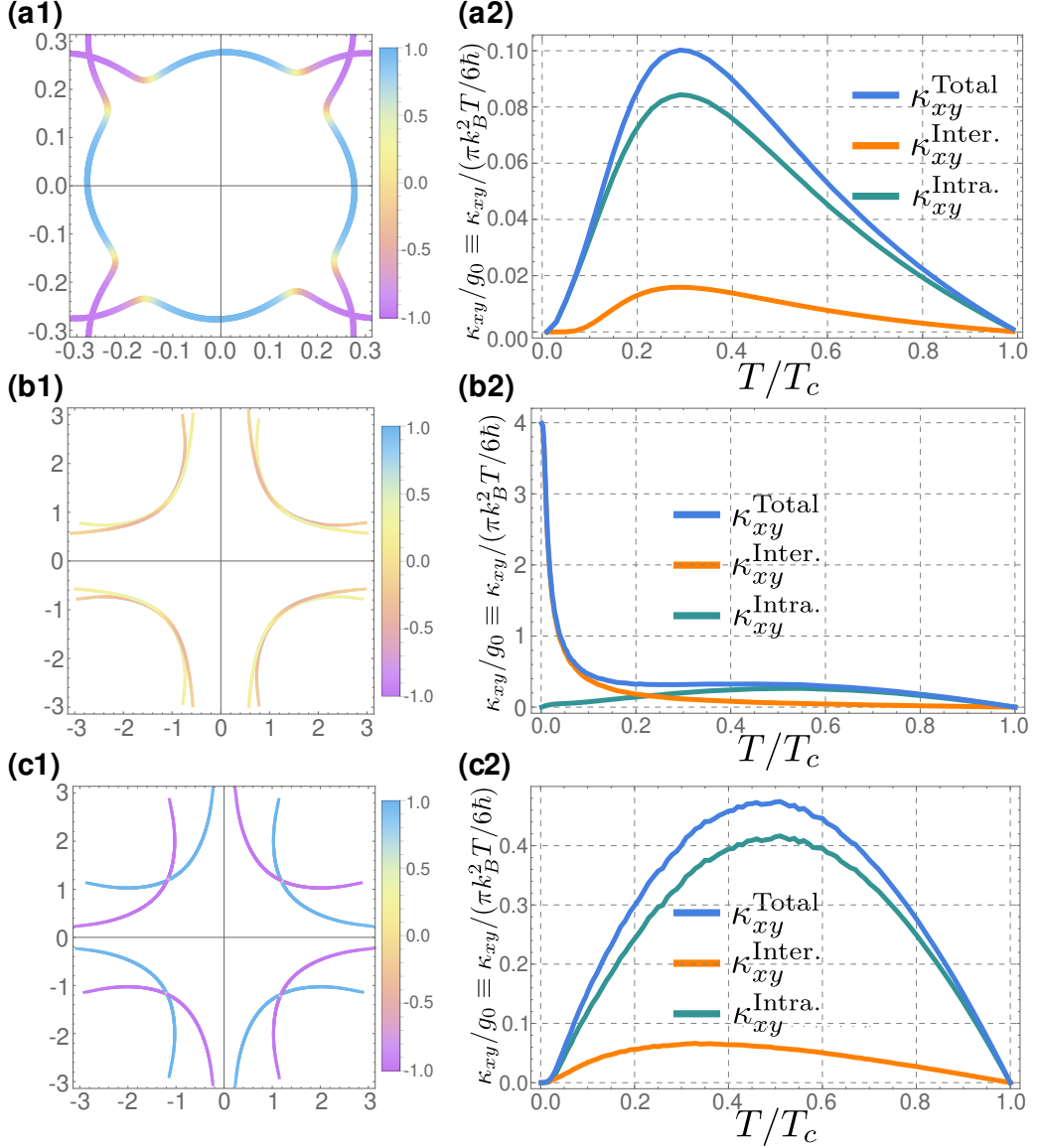


Figure 4.2: (a): JJ formed by twisted bilayer FeSe. (b) and (c): the topological non-trivial and trivial phases induced by the supercurrent in JJ formed by twisted bilayer cuprates. The twisted Fermi surfaces are shown on the left panels. For FeSe the moiré zone folding effect plays an important role on the topology of reconstructed Fermi surfaces. The color scheme on each Fermi surface represents the strength of $\langle u_k | \hat{L} | u_k \rangle \in [-1, 1]$, serving as the indicator of the layer-component of states. For all three cases, κ_{xy} is computed in unit of the thermal conductance quantum g_0 as a function of temperature, and a simple mean-field temperature-dependence of $\Delta_k(T) = \Delta_k(T=0)\sqrt{1-T/T_c}$ is implemented. For the topologically nontrivial case (b), gaps $\sim 0.2\text{meV}$ are generated around superconducting nodes, leading to a Chern number $C = 8$ topological superconductivity, while for the topological trivial case (c) the net Chern number is zero.

4.7 Conclusion and Discussion

We propose the supercurrent-induced anomalous thermal Hall effect, SATHE, as a new probe to the in-plane gap anisotropy of bilayer superconductors. Different from the conventional thermal Hall effect, the ground

state preserve the time reversal symmetry. A pair of probes — a vertically applied supercurrent and a horizontal temperature gradient — is applied to induce the in-plane nonlinear thermal Hall response. Being a thermal response, it works on 2D superconductors where usual electrical probes fail. Since no external magnetic field needs to be applied, SATHE avoids the complications of vortices in the mixed state and probes purely the quasiparticle dynamics in superconductors.

Within the BdG framework we showed that SATHE is sensitive to the in-plane gap anisotropy in the twisted bilayer superconductor, and could be large enough to serve as a new experimental probe of gap structure for atomically thin superconducting 2D crystals including twisted bilayer graphene systems, for which experimental probes have been limited due to the low dimensionality. We believe SATHE can eventually find its place as an effective probe of 2D twisted materials, in particular for low T_c superconductors where SATHE can serve as a sensitive measure of the gap anisotropy.

4.A The Doppler shift and the gauge transformation due to the supercurrent

The Doppler shift effect due to supercurrent has been discussed in textbooks and carefully in a recent paper by Crowley and Fu [170]. Below we follow the notation in the Appendix B of Ref. [170].

To model a superconducting state in the presence of a finite supercurrent with supercurrent velocity \mathbf{u} , it is convenient to consider a moving reference frame S' which is moving at a velocity \mathbf{u} relative to the lab frame S . In the moving frame S' , there is no supercurrent and the superconducting order parameter is spatially uniform.

Microscopically, the Galilean transformation between the frame- S and frame- S' is implemented by the unitary:

$$U_{\mathbf{u}} = e^{\frac{i}{\hbar} \mathbf{u} \cdot \mathbf{g}}, \quad \mathbf{g} = M\mathbf{R} - \mathbf{K}t, \quad (4.13)$$

where \mathbf{K} is the total momentum and \mathbf{R} is the center of mass:

$$\mathbf{K} = \int d\mathbf{r} c_{\mathbf{r},\sigma}^\dagger (-i\hbar\nabla) c_{\mathbf{r},\sigma}, \quad \mathbf{R} = \frac{1}{M} \int d\mathbf{r} c_{\mathbf{r},\sigma}^\dagger c_{\mathbf{r},\sigma} m\mathbf{r}. \quad (4.14)$$

Here M is the total mass, and σ labels electron's spin. Under Galilean transformation, in the real-space basis:

$$U_{\mathbf{u}}^\dagger c_{\mathbf{r},\sigma}^\dagger U_{\mathbf{u}} = c_{\mathbf{r}-\mathbf{u}t,\sigma}^\dagger e^{-\frac{i}{\hbar} m\mathbf{r} \cdot \mathbf{u} + \frac{i}{\hbar} mu^2 t/2}. \quad (4.15)$$

Namely, the electron state $c_{\mathbf{r},\sigma}^\dagger$ in frame- S is transformed into the electron state $c_{\mathbf{r}-\mathbf{u}t,\sigma}^\dagger$ in frame- S' . The *spatially uniform* pairing field in frame- S' then can be represented in the real-space basis:

$$\hat{\Delta}_{S'} = \int d\mathbf{r}_1 d\mathbf{r}_2 \Delta(\mathbf{r}_1 - \mathbf{r}_2) c_{\mathbf{r}_1-\mathbf{u}t,\sigma_1}^\dagger \epsilon_{\sigma_1,\sigma_2} c_{\mathbf{r}_2-\mathbf{u}t,\sigma_2}^\dagger, \quad (4.16)$$

where we assumed spin-singlet pairing for simplicity, and $\epsilon_{\sigma_1, \sigma_2}$ is the Levi-Civita symbol. Performing the inverse Galilean transformation, one finds the pairing field in frame- S is:

$$\hat{\Delta}_S = U_{\mathbf{u}} \hat{\Delta}_{S'} U_{\mathbf{u}}^\dagger = \int d\mathbf{r}_1 d\mathbf{r}_2 e^{\frac{i}{\hbar} m(\mathbf{r}_1 + \mathbf{r}_2) \cdot \mathbf{u}} \Delta(\mathbf{r}_1 - \mathbf{r}_2) c_{\mathbf{r}_1, \sigma_1}^\dagger \epsilon_{\sigma_1, \sigma_2} c_{\mathbf{r}_2, \sigma_2}^\dagger, \quad (4.17)$$

One concludes that in the lab frame- S , the Cooper pair carries a nonzero center-of-mass momentum $2m\mathbf{u}$ due to the supercurrent. The mean-field Hamiltonian in the frame- S is given by:

$$H_S^{MF} = H_0 + \hat{\Delta}_S, \quad (4.18)$$

where H_0 is the normal state Hamiltonian. One may now perform a space-dependent and time-independent gauge transformation \mathbf{U} (which is different from the Galilean transformation) to eliminate the spatial dependence in the pairing field $\hat{\Delta}_S$:

$$\mathbf{U} = e^{\frac{-i}{\hbar} \int d\mathbf{r} c_{\mathbf{r}, \sigma}^\dagger c_{\mathbf{r}, \sigma} m \mathbf{r} \cdot \mathbf{u}}, \quad \mathbf{U} c_{\mathbf{r}, \sigma}^\dagger \mathbf{U}^\dagger = e^{\frac{-i}{\hbar} m \mathbf{r} \cdot \mathbf{u}} c_{\mathbf{r}, \sigma}^\dagger \quad (4.19)$$

H_S^{MF} after this unitary becomes:

$$\tilde{H}_S^{MF} \equiv \mathbf{U} H_S^{MF} \mathbf{U}^\dagger = \mathbf{U} H_0 \mathbf{U}^\dagger + \int d\mathbf{r}_1 d\mathbf{r}_2 \Delta(\mathbf{r}_1 - \mathbf{r}_2) c_{\mathbf{r}_1, \sigma_1}^\dagger \epsilon_{\sigma_1, \sigma_2} c_{\mathbf{r}_2, \sigma_2}^\dagger, \quad (4.20)$$

In \tilde{H}_S^{MF} , the pairing field restores the form as if supercurrent is absent, and the normal state Hamiltonian becomes Doppler-shifted due to the gauge transformation. If we denote the phase factor $e^{\frac{-i}{\hbar} m \mathbf{r} \cdot \mathbf{u}} \equiv e^{-i\varphi(\mathbf{r})/2}$, the supercurrent density is:

$$\mathbf{J}_s = -en_s \mathbf{u} = -e \frac{\hbar n_s}{2m} \nabla \varphi(\mathbf{r}), \quad (4.21)$$

where we introduced the electron's superfluid density n_s , and $\varphi(\mathbf{r})$ can be identified as the phase of the pairing order parameter, which recovers a well-known result. Generally speaking, the superfluid density may be spatially dependent $n_s(\mathbf{r})$. For a uniform supercurrent density, due to current conservation, this implies that the superfluid velocity $\mathbf{u}(\mathbf{r})$ would be spatially dependent. Namely, $\mathbf{u}(\mathbf{r})$, or $\nabla \varphi$, would be larger when $n_s(\mathbf{r})$ is smaller. In this situation, the unitary \mathbf{U} should be modified as:

$$\mathbf{U} = e^{\frac{-i}{\hbar} \int d\mathbf{r} c_{\mathbf{r}, \sigma}^\dagger c_{\mathbf{r}, \sigma} m \int_0^{\mathbf{r}} d\mathbf{r}' \cdot \mathbf{u}(\mathbf{r}')}, \quad \mathbf{U} c_{\mathbf{r}, \sigma}^\dagger \mathbf{U}^\dagger = e^{\frac{-i}{\hbar} m \int_0^{\mathbf{r}} d\mathbf{r}' \cdot \mathbf{u}(\mathbf{r}')} c_{\mathbf{r}, \sigma}^\dagger \equiv e^{-i\varphi(\mathbf{r})/2} c_{\mathbf{r}, \sigma}^\dagger, \quad (4.22)$$

and one still has $\mathbf{u}(\mathbf{r}) = \frac{\hbar}{2m} \nabla \varphi(\mathbf{r})$.

The bottom line is that no matter the system is a bilayer Josephson junction or an intrinsic bilayer superconductor, a finite vertical supercurrent state is always modeled by the gauge transformation $c_{\mathbf{r}, \sigma}^\dagger \rightarrow e^{-i\varphi(\mathbf{r})/2} c_{\mathbf{r}, \sigma}^\dagger$ that transforms the normal state electronic structure $H_0 \rightarrow \mathbf{U} H_0 \mathbf{U}^\dagger$ while leaving the pairing field spatially uniform (as if the supercurrent is absent), as we have done in Eq.(4) in the main text. Here $\varphi(\mathbf{r})$ satisfies Eq.(4.21), and is only depending on the vertical coordinate z : $\varphi(\mathbf{r}) = \varphi(z)$.

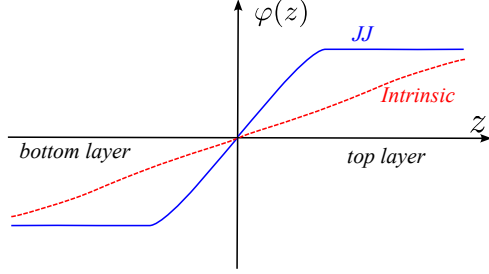


Figure 4.3: The schematic plot of the phase φ involved in the gauge transformation to describe a finite supercurrent state. The two curves represent the case of a Josephson junction (JJ) and an intrinsic bilayer superconductor (Intrinsic) respectively.

The difference between the two cases lies in the details of the profile of $\varphi(z)$. In the case of a bilayer Josephson junction, the superfluid density is concentrated in each monolayers, while between the two layers n_s is small. Consequently, the gradient of the phase $\varphi(z)$ is essentially located between the two layers. In the case of an intrinsic bilayer superconductor, $\varphi(z)$ would be a more smooth function of z . We schematically plot the phase $\varphi(z)$ of the gauge transformation for the two cases in Fig.4.A.

We now consider the situation that $\varphi(z)$ interpolates the top layer $\delta\varphi/2$ to the bottom layer $-\delta\varphi/2$. The Doppler shift unitary is generated via \hat{L} : $\mathbf{U} = e^{-i\frac{\delta\varphi}{4}\hat{L}}$.

- In the case of a vertical JJ, \hat{L} can be written in the tight-binding basis, where the $\pm\mathbf{1}$ blocks correspond to the top/bottom layers:

$$\hat{L}_{\text{JJ}} = \hat{c}^\dagger \begin{pmatrix} \mathbf{1} & 0 \\ 0 & -\mathbf{1} \end{pmatrix} c. \quad (4.23)$$

- In the case of an intrinsic bilayer superconductor, assuming the superfluid density is uniform, \hat{L} is a diagonal matrix whose diagonal matrix elements are given by $\frac{z_\alpha}{z_0}$, where z_α is the atomic coordinate of the orbital- α and $\pm z_0$ is the position of the top/bottom layers.

$$\hat{L}_{\text{Intrinsic}} = \sum_{\alpha} c_{\alpha}^\dagger \frac{z_{\alpha}}{z_0} c_{\alpha} \quad (4.24)$$

4.B Details on the Derivation of the Main Result

4.B.1 Supercurrent-induced Berry Curvature for Intraband Pairing

Here we provide details of the derivation of the main result Eq.(1) in the main text. Because only $a = \pm 1$ bands contribute to the low-energy Berry curvature, we will start with Eq.(8) in the main text.

Denoting the c -th eigenstate of $H_0(\mathbf{k})$ as $|u_{\mathbf{k}}^c\rangle$: $H_0(\mathbf{k})|u_{\mathbf{k}}^c\rangle = \epsilon_{c,\mathbf{k}}|u_{\mathbf{k}}^c\rangle$, and introducing the normal state projector $P_c \equiv |u_{\mathbf{k}}^c\rangle\langle u_{\mathbf{k}}^c|$, we can define the BdG projector into the low energy Hilbert space:

$$\mathbf{P} \equiv P_1 \otimes \tau_0, \quad (4.25)$$

where τ_0 is the identity Pauli matrix in the particle-hole space. The low-energy BdG Hamiltonian is simply the two-by-two matrix, which perfectly decouples from the high energy Hilbert space if only intraband pairing is present (which we call *intraband pairing assumption* below):

$$\mathbf{P}\mathbf{H}\mathbf{P} = P_1 \otimes (\epsilon_{1,\mathbf{k}}\tau_3 + \Delta_{\mathbf{k}}\tau_1). \quad (4.26)$$

Here $\Delta_{\mathbf{k}}$ is chosen to be real due to the time-reversal symmetry. In addition, Projector \mathbf{P} satisfies an important identity with any operator of the following form:

$$\mathbf{A}^{\vee} \equiv A \otimes \tau_0 \Rightarrow \mathbf{P}\mathbf{A}\mathbf{P} = \langle u_{\mathbf{k}}^1 | A | u_{\mathbf{k}}^1 \rangle \mathbf{P}, \quad (4.27)$$

which in turn indicates $\mathbf{P}_{-\mathbf{a}}\mathbf{A}^{\vee}\mathbf{P}_{\mathbf{a}} = 0$.

After the pairing phase twist $\delta\varphi$ are turned on, \mathbf{H} , $\mathbf{E}_{\pm\mathbf{a}}$, $\mathbf{P}_{\pm\mathbf{a}}$ all receive perturbations in Eq.(8) in the main text. $\delta\mathbf{H}$ and $\delta\mathbf{E}_{\pm\mathbf{a}}$ do not contribute because $\partial_{\varphi}\mathbf{H}$ and $\partial_{k_x}\partial_{\varphi}\mathbf{H}$ both have the form of \mathbf{A}^{\vee} *under the intraband assumption*. For instance:

$$\partial_{\varphi}\mathbf{H} = \partial_{\varphi}H_0(\mathbf{k}) \otimes \tau_0. \quad (4.28)$$

Thus we are left with the $\delta\mathbf{P}_{\pm\mathbf{a}}$ contribution only:

$$\frac{\delta\Omega^{\mathbf{a}}}{\delta\varphi} \doteq \frac{-\text{Im Tr}[\mathbf{P}_{\mathbf{a}}\partial_{k_x}\mathbf{H}\mathbf{P}_{-\mathbf{a}}\partial_{k_y}\mathbf{H}\partial_{\varphi}\mathbf{P}_{\mathbf{a}}]}{\mathbf{E}_{\mathbf{a}}^2} - (x \leftrightarrow y). \quad (4.29)$$

Here we used the time-reversal symmetry combined with the particle-hole symmetry, which dictates that the $\delta\mathbf{P}_{-\mathbf{a}}$ contribution and $\delta\mathbf{P}_{\mathbf{a}}$ contribution are identical. After inserting $\mathbf{1} = \sum_{\mathbf{c}} \mathbf{P}_{\mathbf{c}}$ in front of $\partial_{\varphi}\mathbf{P}_{\mathbf{a}}$, and noting that only terms with $\mathbf{c} \neq \pm\mathbf{a}$ contributes *under the intraband pairing assumption*, the above expression can be rewritten as:

$$\begin{aligned} \frac{\delta\Omega^{\mathbf{a}}}{\delta\varphi} &\doteq \sum_{\mathbf{b} \neq \pm\mathbf{a}} \frac{\text{Im Tr}[\mathbf{P}_{\mathbf{a}}\partial_{k_x}\mathbf{H}\mathbf{P}_{-\mathbf{a}}\partial_{k_y}\mathbf{H}\mathbf{P}_{\mathbf{b}}\partial_{\varphi}\mathbf{H}\mathbf{P}_{\mathbf{a}}]}{\mathbf{E}_{\mathbf{a}}^2(\mathbf{E}_{\mathbf{b}} - \mathbf{E}_{\mathbf{a}})} - (x \leftrightarrow y) \\ &= \sum_{\mathbf{b} \neq \pm\mathbf{a}} \frac{\text{Im Tr}[\mathbf{P}_{\mathbf{a}}\partial_{k_x}\mathbf{H}\mathbf{P}_{-\mathbf{a}}\partial_{k_y}\mathbf{P}_{\mathbf{b}}\partial_{\varphi}\mathbf{H}\mathbf{P}_{\mathbf{a}}]}{\mathbf{E}_{\mathbf{a}}^2(\mathbf{E}_{\mathbf{b}} - \mathbf{E}_{\mathbf{a}})} (\mathbf{E}_{\mathbf{b}} + \mathbf{E}_{\mathbf{a}}) - (x \leftrightarrow y) \\ &= \sum_{\mathbf{b} \neq \pm\mathbf{a}} \frac{2\text{Im Tr}[\mathbf{P}_{\mathbf{a}}\partial_{k_x}\mathbf{H}\mathbf{P}_{-\mathbf{a}}\partial_{k_y}\mathbf{P}_{\mathbf{b}}\partial_{\varphi}\mathbf{H}\mathbf{P}_{\mathbf{a}}]}{\mathbf{E}_{\mathbf{a}}(\mathbf{E}_{\mathbf{b}} - \mathbf{E}_{\mathbf{a}})} - (x \leftrightarrow y) \\ &\quad + \sum_{\mathbf{b} \neq \pm\mathbf{a}} \frac{\text{Im Tr}[\mathbf{P}_{\mathbf{a}}\partial_{k_x}\mathbf{H}\mathbf{P}_{-\mathbf{a}}\partial_{k_y}\mathbf{P}_{\mathbf{b}}\partial_{\varphi}\mathbf{H}\mathbf{P}_{\mathbf{a}}]}{\mathbf{E}_{\mathbf{a}}^2} - (x \leftrightarrow y). \end{aligned} \quad (4.30)$$

The term in the last line vanishes *under the intraband pairing assumption*: $\mathbf{P} = \mathbf{P}_1 + \mathbf{P}_{-1}$, $\sum_{\mathbf{b} \neq \pm\mathbf{a}} \partial_{k_y}\mathbf{P}_{\mathbf{b}} = -\partial_{k_y}\mathbf{P}$, and the fact that $\partial_{k_y}\mathbf{P}\partial_{\varphi}\mathbf{H}$ takes the form of \mathbf{A}^{\vee} . We therefore arrive at:

$$\frac{\delta\Omega^{\mathbf{a},\text{intra.}}}{\delta\varphi} \doteq \sum_{\mathbf{b} \neq \pm\mathbf{a}} 4\text{Im Tr}[\partial_{k_x}\mathbf{P}_{\mathbf{a}}\partial_{k_y}\mathbf{P}_{-\mathbf{a}}\mathbf{P}_{\mathbf{b}}\partial_{\varphi}\mathbf{P}_{\mathbf{a}}\mathbf{P}_{\mathbf{a}}] - (x \leftrightarrow y)$$

$$\begin{aligned}
&= \sum_{\mathbf{b} \neq \pm \mathbf{a}} \frac{2\text{Im} \text{Tr}[\mathbf{P}_{\mathbf{a}} \partial_{k_x} \mathbf{H} \mathbf{P}_{-\mathbf{a}} \partial_{k_y} \mathbf{H} \mathbf{P}_{\mathbf{b}} \partial_{\varphi} \mathbf{H} \mathbf{P}_{\mathbf{a}}]}{\mathbf{E}_{\mathbf{a}}(\mathbf{E}_{\mathbf{b}} - \mathbf{E}_{\mathbf{a}})(\mathbf{E}_{\mathbf{b}} - \mathbf{E}_{-\mathbf{a}})} - (x \leftrightarrow y) \\
&\doteq \sum_{b \neq 1} \frac{2\text{Im} \text{Tr}[\mathbf{P}_{\mathbf{a}} \partial_{k_x} \mathbf{H} \mathbf{P}_{-\mathbf{a}} \partial_{k_y} \mathbf{H} (\mathbf{P}_b + \mathbf{P}_{-b}) \partial_{\varphi} \mathbf{H} \mathbf{P}_{\mathbf{a}}]}{\mathbf{E}_{\mathbf{a}}(\epsilon_b - \epsilon_1)^2} - (x \leftrightarrow y) \\
&= \sum_{b \neq 1} \frac{2\text{Im} \text{Tr}[\mathbf{P}_{\mathbf{a}} \partial_{k_x} \mathbf{H} \mathbf{P}_{-\mathbf{a}} \partial_{k_y} \mathbf{H} P_b \otimes \tau_0 \partial_{\varphi} \mathbf{H} \mathbf{P}_{\mathbf{a}}]}{\mathbf{E}_{\mathbf{a}}(\epsilon_b - \epsilon_1)^2} - (x \leftrightarrow y)
\end{aligned} \tag{4.31}$$

Now we are ready to connect with the properties of the normal state. Introducing two-dimensional eigen-vectors $|\alpha_c\rangle$ in the particle-hole subspace:

$$|\mathbf{u}_{\mathbf{k}}^c\rangle = |u_{\mathbf{k}}^{|\mathbf{c}|}\rangle \otimes |\alpha_c\rangle, \tag{4.32}$$

and noting that

$$\partial_k \mathbf{H} = \partial_k H_0(\mathbf{k}) \otimes \boldsymbol{\tau}_3 + O(\partial_k \Delta_{\mathbf{k}}), \tag{4.33}$$

together with Eq.(4.28), one has:

$$\begin{aligned}
\frac{\delta \Omega^{\mathbf{a}, \text{intra.}}}{\delta \varphi} &\doteq \sum_{b \neq 1} \frac{2|\langle \alpha_{\mathbf{a}} | \tau_3 | \alpha_{-\mathbf{a}} \rangle|^2 \text{Im} \text{Tr}[P_1 \partial_{k_x} H_0 P_1 \partial_{k_y} H_0 P_b \partial_{\varphi} H_0 P_1]}{\mathbf{E}_{\mathbf{a}}(\epsilon_b - \epsilon_1)^2} - (x \leftrightarrow y) \\
&= \sum_{b \neq 1} \frac{2|\langle \alpha_{\mathbf{a}} | \tau_3 | \alpha_{-\mathbf{a}} \rangle|^2 v_x \text{Im} \text{Tr}[P_1 \partial_{k_y} H_0 P_b \partial_{\varphi} H_0 P_1]}{\mathbf{E}_{\mathbf{a}}(\epsilon_b - \epsilon_1)^2} - (x \leftrightarrow y) \\
&= -\frac{v_x |\langle \alpha_{\mathbf{a}} | \tau_3 | \alpha_{-\mathbf{a}} \rangle|^2}{\mathbf{E}_{\mathbf{a}}} \Omega_{k_y, \varphi} - (x \leftrightarrow y) = -\frac{\Delta_{\mathbf{k}}^2}{\mathbf{E}_{\mathbf{a}}^3} v_x \Omega_{k_y, \varphi} - (x \leftrightarrow y),
\end{aligned} \tag{4.34}$$

where $v_x \equiv \partial_{k_x} \epsilon_{1, \mathbf{k}}$, and $\Omega_{k_y, \varphi} \equiv -2\text{Im}[\langle \partial_{k_y} u_{\mathbf{k}}^1 | \partial_{\varphi} u_{\mathbf{k}}^1 \rangle]$ is the *normal-state* Berry curvature w.r.t. k_y and φ . Using the fact that $|\partial_{\varphi} u_{\mathbf{k}}^1\rangle = \frac{-i}{4} \hat{L} |u_{\mathbf{k}}^1\rangle$, the normal-state Berry curvature $\Omega_{k_y, \varphi}$ can also be expressed as

$$\Omega_{k, \varphi} = \frac{1}{4} \partial_{\mathbf{k}} \langle u_{\mathbf{k}}^1 | \hat{L} | u_{\mathbf{k}}^1 \rangle, \tag{4.35}$$

so that Eq.(10) in the main text is obtained.

4.B.2 Fermi Surface Integral

The SATHE can be computed using Eq.(5) and Eq.(6) in the main text. Define

$$\Omega(E) \equiv \sum_{\mathbf{a}} \int \frac{d^2 k}{(2\pi)^2} \Omega_{\mathbf{k}}^{\mathbf{a}} \delta(E - \mathbf{E}_{\mathbf{a}, \mathbf{k}}), \tag{4.36}$$

we have $\sigma(E) = \sigma(0) - \int_0^E dE' \Omega(E')$. Here $\sigma(0) = 0$ due to the time-reversal symmetry and the nodeless assumption.

Because the change of the Berry curvature is concentrated near the Fermi surface due to the $\mathbf{E}_{\mathbf{a}}$ denominator, and proportional to $1/\Delta_{\mathbf{k}}$ right at the Fermi surface, it is convenient to represent $\Omega(E)$ as a Fermi

surface integral as following:

$$\begin{aligned}
\frac{\delta \Omega(E)}{\delta \varphi} &\doteq \sum_{\text{FS}} \frac{1}{(2\pi)^2} \oint_{\text{FS}, \epsilon_{\mathbf{k}} = \pm \sqrt{E^2 - \Delta_{\mathbf{k}}^2}} dk_{\parallel} \frac{|E|}{|\epsilon_{\mathbf{k}}|} \frac{1}{\hbar |v_F|} \Omega_{\mathbf{k}}^{\text{sign}(E)} \\
&\doteq \sum_{\text{FS}} \frac{-2}{(2\pi)^2} \oint_{\text{FS}} dk_{\parallel} \frac{|E|}{\sqrt{E^2 - \Delta_{\mathbf{k}}^2}} \frac{1}{\hbar |v_F|} \frac{\Delta_{\mathbf{k}}^2}{E^3} (v_x \Omega_{k_y, \varphi} - v_y \Omega_{k_x, \varphi}) \\
&= \text{sign}(E) \sum_{\text{FS}} \frac{-1}{2\pi^2} \oint_{\text{FS}} dk_{\parallel} \frac{\Delta_{\mathbf{k}}^2}{E^2 \sqrt{E^2 - \Delta_{\mathbf{k}}^2}} \frac{1}{\hbar |v_F|} (v_x \Omega_{k_y, \varphi} - v_y \Omega_{k_x, \varphi}) \\
&= \text{sign}(E) \sum_{\text{FS}} \frac{-\text{sign}(v_F)}{2\pi^2 \hbar} \oint_{\text{FS}} d\vec{k}_{\parallel} \cdot (\Omega_{k_x, \varphi}, \Omega_{k_y, \varphi}) \frac{\Delta_{\mathbf{k}}^2}{E^2 \sqrt{E^2 - \Delta_{\mathbf{k}}^2}} \\
&= \text{sign}(E) \sum_{\text{FS}} \frac{-\text{sign}(v_F)}{8\pi^2 \hbar} \oint_{\text{FS}} dk_{\parallel} \partial_{k_{\parallel}} \langle u_{\mathbf{k}} | \hat{L} | u_{\mathbf{k}} \rangle \frac{\Delta_{\mathbf{k}}^2}{E^2 \sqrt{E^2 - \Delta_{\mathbf{k}}^2}}. \tag{4.37}
\end{aligned}$$

Integrating out E in advance, we get

$$\sigma(E) = \sum_{\text{FS}} \frac{\text{sign}(v_F)}{8\pi^2 \hbar} \oint_{\text{FS}} dk_{\parallel} \partial_{k_{\parallel}} \langle u_{\mathbf{k}} | \hat{L} | u_{\mathbf{k}} \rangle \frac{\sqrt{E^2 - \Delta_{\mathbf{k}}^2}}{|E|} \Theta(|E| - |\Delta_{\mathbf{k}}|). \tag{4.38}$$

We finally arrive at the result using Eq.(5) in the main text:

$$\frac{\delta \kappa_{xy}}{\delta \varphi T} = \sum_{\text{FS}} \frac{\text{sign}(v_F) k_B^2}{16\pi^2 \hbar} \oint_{\text{FS}} dk_{\parallel} \partial_{k_{\parallel}} \langle u_{\mathbf{k}} | \hat{L} | u_{\mathbf{k}} \rangle \xi\left(\frac{\Delta_{\mathbf{k}}}{T}\right). \tag{4.39}$$

4.C Supercurrent-indcued Berry Curvature for Interband Pairing

When interband pairing is present, additional terms need to be considered. However, one can always perform a small unitary rotation $e^{iS \otimes \tau_2}$ to eliminate the interband pairing:

$$S \equiv \sum_{a \neq b} \frac{P_a \Delta_{\mathbf{k}}^{\text{inter.}} P_b}{\epsilon_{a, \mathbf{k}} + \epsilon_{b, \mathbf{k}}}, \quad S^\dagger = S. \tag{4.40}$$

Since $\mathbf{H} = H_0 \otimes \tau_3 + (\Delta^{\text{intra.}} + \Delta^{\text{inter.}}) \otimes \tau_1$, we have:

$$\begin{aligned}
e^{iS \otimes \tau_2} \mathbf{H} e^{-iS \otimes \tau_2} &\doteq H_0 \otimes \tau_3 + (\Delta^{\text{intra.}} + \Delta^{\text{inter.}}) \otimes \tau_1 + (i)[S \otimes \tau_2, H_0 \otimes \tau_3] \\
&= H_0 \otimes \tau_3 + (\Delta^{\text{intra.}} + \Delta^{\text{inter.}}) \otimes \tau_1 + (i)(SH_0 + H_0S) \otimes (i)\tau_1 \\
&= H_0 \otimes \tau_3 + (\Delta^{\text{intra.}} + \Delta^{\text{inter.}}) \otimes \tau_1 + (-1)\Delta_{\mathbf{k}}^{\text{inter.}} \otimes \tau_1 \\
&= H_0 \otimes \tau_3 + \Delta^{\text{intra.}} \otimes \tau_1 \tag{4.41}
\end{aligned}$$

Denoting the projectors in the presence of interband pairing as $\tilde{\mathbf{P}}_c$, we have $\tilde{\mathbf{P}}_c \doteq e^{-iS \otimes \tau_2} \mathbf{P}_c e^{iS \otimes \tau_2}$. Basically, in all the previous derivations for the intraband case, we only need to replace \mathbf{P}_c by $\tilde{\mathbf{P}}_c$, which corresponds to performing the small unitary transformation for the operators like $\partial_{\varphi} \mathbf{H} \rightarrow e^{iS \otimes \tau_2} \partial_{\varphi} \mathbf{H} e^{-iS \otimes \tau_2}$. In this way $\partial_{\varphi} \mathbf{H}$ has a correction $[iS, \partial_{\varphi} H_0] \otimes \tau_2$ and is no longer $\propto \tau_0$. We can leave all the energies \mathbf{E}_c unchanged since they receive second order contributions from $\Delta^{\text{inter.}}$.

After inspection, to the leading order of Δ/t , one can identify three sources of interband contributions. First, we do need to consider $\delta_\varphi \partial_k \mathbf{H}$ in Eq.(8) in the main text. Second, in the first line of Eq.(4.30), $\mathbf{b} = -\mathbf{a}$ needs to be included. Third, the term in the last line of Eq.(4.30) is no longer vanishing. We term them as *Part-A,B,C* and compute them one by one below.

Part-A: For the $\delta_\varphi \partial_k \mathbf{H}$ contributions,

$$\begin{aligned}
\frac{\delta \Omega_{\mathbf{k}}^a}{\delta \varphi} \Big|_A &= \frac{-\text{Im} \text{Tr} [\mathbf{P}_a \partial_{k_x} \mathbf{H} \mathbf{P}_{-a} [iS \otimes \tau_2, \partial_{k_y} \partial_\varphi \mathbf{H}] \mathbf{P}_a]}{2E_a^2} - (x \leftrightarrow y) \\
&= \frac{-\text{Im} \text{Tr} [\mathbf{P}_a (\partial_{k_x} H_0 \otimes \tau_3 + \partial_{k_x} \Delta \otimes \tau_1) \mathbf{P}_{-a} [iS \otimes \tau_2, \partial_{k_y} \partial_\varphi H_0 \otimes \tau_0] \mathbf{P}_a]}{2E_a^2} \\
&\quad - (x \leftrightarrow y) \\
&= -\langle u_{\mathbf{k}}^1 | [iS, \partial_{k_y} \partial_\varphi H_0] | u_{\mathbf{k}}^1 \rangle \\
&\quad \times \frac{v_x \text{Im} [\langle \alpha_a | \tau_3 | \alpha_{-a} \rangle \langle \alpha_{-a} | \tau_2 | \alpha_a \rangle] + \langle u_{\mathbf{k}}^1 | \partial_{k_x} \Delta | u_{\mathbf{k}}^1 \rangle \text{Im} [\langle \alpha_a | \tau_1 | \alpha_{-a} \rangle \langle \alpha_{-a} | \tau_2 | \alpha_a \rangle]}{2E_a^2} \\
&\quad - (x \leftrightarrow y). \tag{4.42}
\end{aligned}$$

Noting a few identities:

$$\begin{aligned}
\tau_2 |\alpha_{-a}\rangle \langle \alpha_{-a}| \tau_2 &= |\alpha_a\rangle \langle \alpha_a| \\
\partial_{k_x} \mathbf{E}_a &= \text{Tr} [\mathbf{P}_a (\partial_{k_x} H_0 \otimes \tau_3 + \partial_{k_x} \Delta \otimes \tau_1) \mathbf{P}_a] = v_x \frac{\epsilon_{1,k}}{E_a} + \langle u_{\mathbf{k}}^1 | \partial_{k_x} \Delta | u_{\mathbf{k}}^1 \rangle \frac{\Delta_k}{E_a} \\
\partial_{k_x} \mathbf{E}_a &= \frac{\Delta_k \partial_{k_x} \Delta_k + \epsilon_{1,k} v_x}{E_a} \\
\Rightarrow \langle u_{\mathbf{k}}^1 | \partial_{k_x} \Delta | u_{\mathbf{k}}^1 \rangle &= \partial_{k_x} \Delta_k \\
\langle \alpha_a | \tau_1 | \alpha_a \rangle &= \frac{\Delta_k}{E_a}, \quad \langle \alpha_a | \tau_3 | \alpha_a \rangle = \frac{\epsilon_{1,k}}{E_a} \tag{4.43}
\end{aligned}$$

we have:

$$\frac{\delta \Omega_{\mathbf{k}}^a}{\delta \varphi} \Big|_A = -\frac{\langle u_{\mathbf{k}}^1 | [iS, \partial_{k_y} \partial_\varphi H_0] | u_{\mathbf{k}}^1 \rangle}{2E_a^3} (-\Delta_k v_x + \epsilon_{1,k} \partial_{k_x} \Delta_k) - (x \leftrightarrow y) \tag{4.44}$$

Part-B: This term is:

$$\frac{\text{Im} \text{Tr} [\mathbf{P}_a \partial_{k_x} \mathbf{H} \mathbf{P}_{-a} \partial_{k_y} \mathbf{H} \mathbf{P}_{-a} \partial_\varphi \mathbf{H} \mathbf{P}_a]}{E_a^2 (E_{-a} - E_a)} - (x \leftrightarrow y) \tag{4.45}$$

Note that $\mathbf{P}_{-a} \partial_{k_y} \mathbf{H} \mathbf{P}_{-a} = \partial_{k_y} \mathbf{E}_{-a} \mathbf{P}_{-a}$,

$$\begin{aligned}
\frac{\delta \Omega_{\mathbf{k}}^a}{\delta \varphi} \Big|_B &= \frac{\partial_{k_y} \mathbf{E}_a}{2E_a^3} \text{Im} \text{Tr} [\mathbf{P}_a (\partial_{k_x} H_0 \otimes \tau_3 + \partial_{k_x} \Delta \otimes \tau_1) \mathbf{P}_{-a} [iS, \partial_\varphi H_0] \otimes \tau_2 \mathbf{P}_a] - (x \leftrightarrow y) \\
&= \frac{\partial_{k_y} \mathbf{E}_a}{2E_a^3} \langle u_{\mathbf{k}}^1 | [iS, \partial_\varphi H_0] | u_{\mathbf{k}}^1 \rangle \text{Im} \text{Tr} [\mathbf{P}_a (\partial_{k_x} H_0 \otimes \tau_3 + \partial_{k_x} \Delta \otimes \tau_1) \mathbf{P}_{-a} \tau_2 \mathbf{P}_a] - (x \leftrightarrow y) \\
&= \frac{\partial_{k_y} \mathbf{E}_a}{2E_a^3} \langle u_{\mathbf{k}}^1 | [iS, \partial_\varphi H_0] | u_{\mathbf{k}}^1 \rangle \text{Im} \text{Tr} [\mathbf{P}_a (\partial_{k_x} H_0 \otimes \tau_3 + \partial_{k_x} \Delta \otimes \tau_1) \tau_2 \mathbf{P}_a] - (x \leftrightarrow y)
\end{aligned}$$

$$\begin{aligned}
&= \frac{\partial_{k_y} \mathbf{E}_\mathbf{a}}{2\mathbf{E}_\mathbf{a}^3} \langle u_\mathbf{k}^1 | [iS, \partial_\varphi H_0] | u_\mathbf{k}^1 \rangle (-v_x \langle \boldsymbol{\alpha}_\mathbf{a} | \boldsymbol{\tau}_1 | \boldsymbol{\alpha}_\mathbf{a} \rangle + \langle u_\mathbf{k}^1 | \partial_{k_x} \Delta | u_\mathbf{k}^1 \rangle \langle \boldsymbol{\alpha}_\mathbf{a} | \boldsymbol{\tau}_3 | \boldsymbol{\alpha}_\mathbf{a} \rangle) - (x \leftrightarrow y) \\
&= \frac{\partial_{k_y} \mathbf{E}_\mathbf{a}}{2\mathbf{E}_\mathbf{a}^4} \langle u_\mathbf{k}^1 | [iS, \partial_\varphi H_0] | u_\mathbf{k}^1 \rangle (-\Delta_\mathbf{k} v_x + \epsilon_{1,\mathbf{k}} \partial_{k_x} \Delta_\mathbf{k}) - (x \leftrightarrow y) \\
&= \frac{(v_y \epsilon_{1,\mathbf{k}} + \Delta_\mathbf{k} \partial_{k_y} \Delta_\mathbf{k})}{2\mathbf{E}_\mathbf{a}^5} \langle u_\mathbf{k}^1 | [iS, \partial_\varphi H_0] | u_\mathbf{k}^1 \rangle (-\Delta_\mathbf{k} v_x + \epsilon_{1,\mathbf{k}} \partial_{k_x} \Delta_\mathbf{k}) - (x \leftrightarrow y)
\end{aligned} \tag{4.46}$$

After $(x \leftrightarrow y)$ antisymmetrization, we get

$$\left. \frac{\delta \Omega_\mathbf{k}^\mathbf{a}}{\delta \varphi} \right|_B = \frac{-1}{2\mathbf{E}_\mathbf{a}^3} \langle u_\mathbf{k}^1 | [iS, \partial_\varphi H_0] | u_\mathbf{k}^1 \rangle v_x \partial_{k_y} \Delta_\mathbf{k} - (x \leftrightarrow y) \tag{4.47}$$

Part-C: Note that

$$\partial_{k_y} \tilde{\mathbf{P}}_\mathbf{b} \doteq \partial_{k_y} [\mathbf{P}_\mathbf{b} + [-iS \otimes \boldsymbol{\tau}_2, \mathbf{P}_\mathbf{b}]] \doteq e^{-iS \otimes \boldsymbol{\tau}_2} \partial_{k_y} \mathbf{P}_\mathbf{b} e^{iS \otimes \boldsymbol{\tau}_2} + [-i\partial_{k_y} S \otimes \boldsymbol{\tau}_2, \mathbf{P}_\mathbf{b}] \tag{4.48}$$

The contribution from the last line of Eq.(4.30) becomes:

$$\begin{aligned}
\left. \frac{\delta \Omega_\mathbf{k}^\mathbf{a}}{\delta \varphi} \right|_C &\doteq \frac{-\text{Im Tr}[\mathbf{P}_\mathbf{a} \partial_{k_x} \mathbf{H} \mathbf{P}_{-\mathbf{a}} \partial_{k_y} \mathbf{P} [iS \otimes \boldsymbol{\tau}_2, \partial_\varphi \mathbf{H}] \mathbf{P}_\mathbf{a} + \mathbf{P}_\mathbf{a} \partial_{k_x} \mathbf{H} \mathbf{P}_{-\mathbf{a}} [-i\partial_{k_y} S \otimes \boldsymbol{\tau}_2, \mathbf{P}] \partial_\varphi \mathbf{H} \mathbf{P}_\mathbf{a}]}{\mathbf{E}_\mathbf{a}^2} \\
&\quad - (x \leftrightarrow y) \\
&= \frac{-1}{\mathbf{E}_\mathbf{a}^3} (-\Delta_\mathbf{k} v_x + \epsilon_{1,\mathbf{k}} \partial_{k_x} \Delta_\mathbf{k}) \text{Re Tr}[\partial_{k_y} P_1 [iS, \partial_\varphi H_0] P_1 + P_1 i \partial_{k_y} S \partial_\varphi H_0 P_1] \\
&\quad - (x \leftrightarrow y) \\
&= \frac{-1}{2\mathbf{E}_\mathbf{a}^3} (-\Delta_\mathbf{k} v_x + \epsilon_{1,\mathbf{k}} \partial_{k_x} \Delta_\mathbf{k}) \text{Re Tr}[2\partial_{k_y} P_1 [iS, \partial_\varphi H_0] P_1 + P_1 [i\partial_{k_y} S, \partial_\varphi H_0] P_1] \\
&\quad - (x \leftrightarrow y)
\end{aligned} \tag{4.49}$$

Let's add part-A and part-C together.

$$\begin{aligned}
\left. \frac{\delta \Omega_\mathbf{k}^\mathbf{a}}{\delta \varphi} \right|_{A+C} &= \frac{-1}{2\mathbf{E}_\mathbf{a}^3} (-\Delta_\mathbf{k} v_x + \epsilon_{1,\mathbf{k}} \partial_{k_x} \Delta_\mathbf{k}) \partial_{k_y} [\text{Re Tr}[P_1 [iS, \partial_\varphi H_0] P_1]] - (x \leftrightarrow y) \\
&= \frac{-1}{2\mathbf{E}_\mathbf{a}^3} (-\Delta_\mathbf{k} v_x + \epsilon_{1,\mathbf{k}} \partial_{k_x} \Delta_\mathbf{k}) \partial_{k_y} \langle u_\mathbf{k}^1 | [iS, \partial_\varphi H_0] | u_\mathbf{k}^1 \rangle - (x \leftrightarrow y)
\end{aligned} \tag{4.50}$$

The quantity $\langle u_\mathbf{k}^1 | [iS, \partial_\varphi H_0] | u_\mathbf{k}^1 \rangle$ here and in part-B can be easily computed, which we denote as $G_\mathbf{k}$:

$$\begin{aligned}
G_\mathbf{k} \equiv \langle u_\mathbf{k}^1 | [iS, \partial_\varphi H_0] | u_\mathbf{k}^1 \rangle &= -2\text{Im}[\langle u_\mathbf{k}^1 | S \partial_\varphi H_0 | u_\mathbf{k}^1 \rangle] = -2 \sum_{b \neq 1} \text{Im}[\langle u_\mathbf{k}^1 | S | u_\mathbf{k}^b \rangle \langle u_\mathbf{k}^b | \partial_\varphi H_0 | u_\mathbf{k}^1 \rangle] \\
&= -2 \sum_{b \neq 1} \text{Im}\left[\frac{\langle u_\mathbf{k}^1 | \Delta^{\text{inter.}} | u_\mathbf{k}^b \rangle \langle u_\mathbf{k}^b | \partial_\varphi H_0 | u_\mathbf{k}^1 \rangle}{\epsilon_{1,\mathbf{k}} + \epsilon_{b,\mathbf{k}}} \right] \doteq -2 \sum_{b \neq 1} \text{Im}\left[\frac{\langle u_\mathbf{k}^1 | \Delta^{\text{inter.}} | u_\mathbf{k}^b \rangle \langle u_\mathbf{k}^b | \partial_\varphi H_0 | u_\mathbf{k}^1 \rangle}{-\epsilon_{1,\mathbf{k}} + \epsilon_{b,\mathbf{k}}} \right] \\
&= 2 \sum_{b \neq 1} \text{Im}[\langle u_\mathbf{k}^1 | \Delta^{\text{inter.}} | u_\mathbf{k}^b \rangle \langle u_\mathbf{k}^b | \partial_\varphi u_\mathbf{k}^1 \rangle] = 2\text{Im}[\langle u_\mathbf{k}^1 | \Delta^{\text{inter.}} | \partial_\varphi u_\mathbf{k}^1 \rangle] \\
&= \frac{-1}{2} \text{Re}[\langle u_\mathbf{k}^1 | \Delta^{\text{inter.}} \hat{L} | u_\mathbf{k}^1 \rangle]
\end{aligned} \tag{4.51}$$

Putting together, we finally get

$$\begin{aligned} \frac{\delta\Omega_k^{\text{a,inter}}}{\delta\varphi} &= \left. \frac{\delta\Omega_k^{\text{a}}}{\delta\varphi} \right|_{A+B+C} = \\ &= \frac{-1}{2\mathbf{E}_{\text{a}}^3} (-\Delta_{\mathbf{k}} v_x + \epsilon_{1,\mathbf{k}} \partial_{k_x} \Delta_{\mathbf{k}}) \partial_{k_y} G_{\mathbf{k}} + \frac{-1}{2\mathbf{E}_{\text{a}}^3} G_{\mathbf{k}} v_x \partial_{k_y} \Delta_{\mathbf{k}} - (x \leftrightarrow y) \end{aligned} \quad (4.52)$$

It is also instructive to study the behavior of $\partial_{\varphi}\mathbf{H}$ in the low energy subspace:

$$\begin{aligned} \tilde{\mathbf{P}} \partial_{\varphi} \mathbf{H} \tilde{\mathbf{P}} &= \mathbf{P} \partial_{\varphi} \mathbf{H} \mathbf{P} + \mathbf{P} [iS \otimes \tau_2, \partial_{\varphi} \mathbf{H}] \mathbf{P} \\ &= \langle u_{\mathbf{k}}^1 | \partial_{\varphi} H_0 | u_{\mathbf{k}}^1 \rangle \mathbf{P} + \langle u_{\mathbf{k}}^1 | [iS, \partial_{\varphi} H_0] | u_{\mathbf{k}}^1 \rangle \mathbf{P} \tau_2 \mathbf{P} \end{aligned} \quad (4.53)$$

The low energy effective Hamiltonian in the presence of $\delta\varphi$ becomes:

$$\mathbf{H}_{\text{eff}} = \delta\varphi \partial_{\varphi} \epsilon_{1,\mathbf{k}} \boldsymbol{\tau}_0 + \epsilon_{1,\mathbf{k}} \boldsymbol{\tau}_3 + \Delta_{\mathbf{k}} \boldsymbol{\tau}_1 + \delta\varphi G_{\mathbf{k}} \boldsymbol{\tau}_2 = \delta\varphi \partial_{\varphi} \epsilon_{1,\mathbf{k}} \boldsymbol{\tau}_0 + \mathbf{d}_{\mathbf{k}} \cdot \vec{\tau}, \quad (4.54)$$

where we introduced vector $\mathbf{d}_{\mathbf{k}} \equiv (\Delta_{\mathbf{k}}, \delta\varphi G_{\mathbf{k}}, \epsilon_{1,\mathbf{k}})$. We merely showed that the interband contribution can be faithfully computed using this effective 2-by-2 Hamiltonian:

$$\begin{aligned} \delta\Omega_k^{\text{a,inter}} &= -2\text{Im} \text{Tr}[p_{\text{a}} \partial_{k_x} p_{\text{a}} \partial_{k_y} p_{\text{a}}] \\ &= \frac{-d_{\mathbf{k}} \cdot (\partial_{k_x} \mathbf{d}_{\mathbf{k}} \times \partial_{k_y} \mathbf{d}_{\mathbf{k}})}{2\mathbf{a}|\mathbf{d}_{\mathbf{k}}|^3} \doteq \frac{-\mathbf{d}_{\mathbf{k}} \cdot (\partial_{k_x} \mathbf{d}_{\mathbf{k}} \times \partial_{k_y} \mathbf{d}_{\mathbf{k}})}{2\mathbf{E}_{\text{a}}^3} \propto \delta\varphi \end{aligned} \quad (4.55)$$

$p_{\text{a}} = \frac{1}{2}(1 + \mathbf{a} \frac{\mathbf{d}_{\mathbf{k}} \cdot \vec{\tau}}{|\mathbf{d}_{\mathbf{k}}|})$ is the projector in this effective model.

When the superconductivity is nodal, near a node, the effective theory becomes a Dirac equation:

$$\mathbf{H}_{\text{eff}}^{\text{node}} = \delta\varphi \partial_{\varphi} \epsilon_{1,\mathbf{k}} \boldsymbol{\tau}_0 + \hbar v_F k_{\perp} \boldsymbol{\tau}_3 + \hbar v_{\Delta} k_{\parallel} \boldsymbol{\tau}_1 + m \boldsymbol{\tau}_2, \quad (4.56)$$

where $\hbar v_{\Delta} = \frac{\partial \Delta_{\mathbf{k}}}{\partial k_{\parallel}}$, and $m = \delta\varphi G_{\mathbf{k}_{\text{node}}}$ is the mass gap generated by the supercurrent. It is easy to show that the nodal contribution to $\sigma(E)$ is

$$\sigma^{\text{node}}(E) = \begin{cases} \frac{C}{2\pi}, & \text{if } -|m| < E < |m|, \\ \frac{C|m|}{2\pi|E|}, & \text{otherwise.} \end{cases} \quad (4.57)$$

Here $C = \pm \frac{1}{2}$ is the Chern number transferred due to m . Performing the energy integral in Eq.(5) in the main text, in the low temperature limit $k_B T \ll |m|$ one recovers the quantized $\kappa_{xy}^{\text{node}}/T = \frac{k_B^2}{\hbar} \frac{C\pi}{12}$. However, in the high-temperature limit $m \ll k_B T$, we have:

$$\frac{\kappa_{xy}^{\text{node}}}{T} \doteq -\frac{k_B^2}{\hbar} \frac{C|m|}{2\pi k_B T} \int_0^\infty x f'(x) dx = \frac{k_B^2}{\hbar} \frac{C \ln 2}{2\pi} \frac{|m|}{k_B T}. \quad (4.58)$$

Namely there is a $1/T$ tail in $\frac{\kappa_{xy}}{T}$.

As a final remark, in the absence of $\delta\varphi$, it is easy to show that the Berry curvature is nonsingular near

the Fermi surface. Consequently, one does not need to consider the contribution to SATHE from $\partial_\varphi \mathbf{E}_a$ in the leading order of Δ/t expansion.

4.D Fermi Surface Reconstruction for Twisted Bilayer FeSe

The effective $\mathbf{k} \cdot \mathbf{p}$ model in the main text is written in the orbital space of $\{3d_{xz}, 3d_{yz}\}$. Because the dominant hopping processes occur within *the same* orbitals, we can treat each orbital separately, or equivalently go back to the single-iron Brillouin zone to work with one ellipse on each direction. The right horizontal elliptic M -pocket of monolayer FeSe is simply described with

$$h = -\tilde{\mu} + a(k_x - k_M)^2 + b k_y^2 \quad (4.59)$$

with $\mu = -0.08\text{eV}$, $a = 1.08\text{eV} \cdot \text{\AA}^2$ and $b = 1.6\text{eV} \cdot \text{\AA}^2$. Denoting the rotated monolayer Hamiltonian as $h_{\pm\theta/2}(\mathbf{k})$, the rotated bilayer Hamiltonian *without* interlayer tunnelings is then simply a two-by-two diagonal matrix $H_{w/o T_\perp} = \text{diag}\{h_{\theta/2}(\mathbf{k}), h_{-\theta/2}(\mathbf{k})\}$.

Under small twisting angles, two-center approximation applies [44] and the general tunneling strength between the top/bottom Bloch states $|\psi_{\alpha,\mathbf{k}^t}^t\rangle$ and $|\psi_{\beta,\mathbf{k}^b}^b\rangle$ takes the form of

$$t_{\mathbf{k}^t, \mathbf{k}^b}^{\alpha\beta} \equiv \langle \psi_\alpha^t | H | \psi_\beta \rangle = \frac{1}{V} \sum_{\mathbf{G}^t, \mathbf{G}^b} \delta_{\mathbf{k}^t + \mathbf{G}^t, \mathbf{k}^b + \mathbf{G}^b} \cdot e^{-i\mathbf{G}^b \cdot \tau_\alpha^b} \cdot t_{\alpha\beta}(\mathbf{k}^t + \mathbf{G}^t) \cdot e^{i\mathbf{G}^t \cdot \tau_\beta^t}, \quad (4.60)$$

where $\mathbf{G}^{t,b}$ are the reciprocal vector of the top/bottom layer and τ_α^t and τ_β^b are the sublattice position of the wannier centers of top/bottom states. Now that only one state is left in the single-iron Brillouin zone, we can simply take $t_{\alpha\beta}(\mathbf{k}^t + \mathbf{G}^t) = \delta_{\alpha\beta} t(\mathbf{k}^t + \mathbf{G}^t)$.

The low-energy form of the interlayer tunnelings can be obtained with the expansion $\mathbf{k}^{t,b} \equiv \mathbf{q}^{t,b} + \mathbf{K}_M^{t,b}$, $|\mathbf{q}^{t,b}| \ll 1$. Assuming that the tunneling function $t(\mathbf{k}^t + \mathbf{G}^t)$ only depends on the norm of its arguments, we can take the approximation that

$$t(\mathbf{k}^t + \mathbf{G}^t) \equiv t(\mathbf{q}^t + \mathbf{K}_M^t + \mathbf{G}^t) \doteq t(|\mathbf{K}_M|).$$

Since $|\mathbf{K}_M| \gg |\mathbf{q}^{t,b}|$, only terms with momentum differences $\mathbf{k}^t + \mathbf{G}^t - \mathbf{k}^b - \mathbf{G}^b \propto \theta$ will be left due to the delta function in Eq.(4.60). Taking the right M -pocket as an example, up to the lowest-order truncation on the grids of the scattering vectors, only two terms of $\delta\mathbf{q}^t$ and $\delta\mathbf{q}^b$ need to be included, as is seen in Fig.4.4. Denoting $t(|\mathbf{K}_M|)/V \equiv w$, such truncation gives rise to the minimal moiré Hamiltonian

$$H^{\text{moir\'e}}(\mathbf{k}) = \begin{pmatrix} h_{\theta/2}(\mathbf{k}) & w & w \\ w & h_{-\theta/2}(\mathbf{k} + \delta\mathbf{q}^t) & 0 \\ w & 0 & h_{-\theta/2}(\mathbf{k} + \delta\mathbf{q}^b) \end{pmatrix}. \quad (4.61)$$

The moiré pattern-induced Fermi surface reconstruction is then obtained by diagonalization Eq.(4.61), which

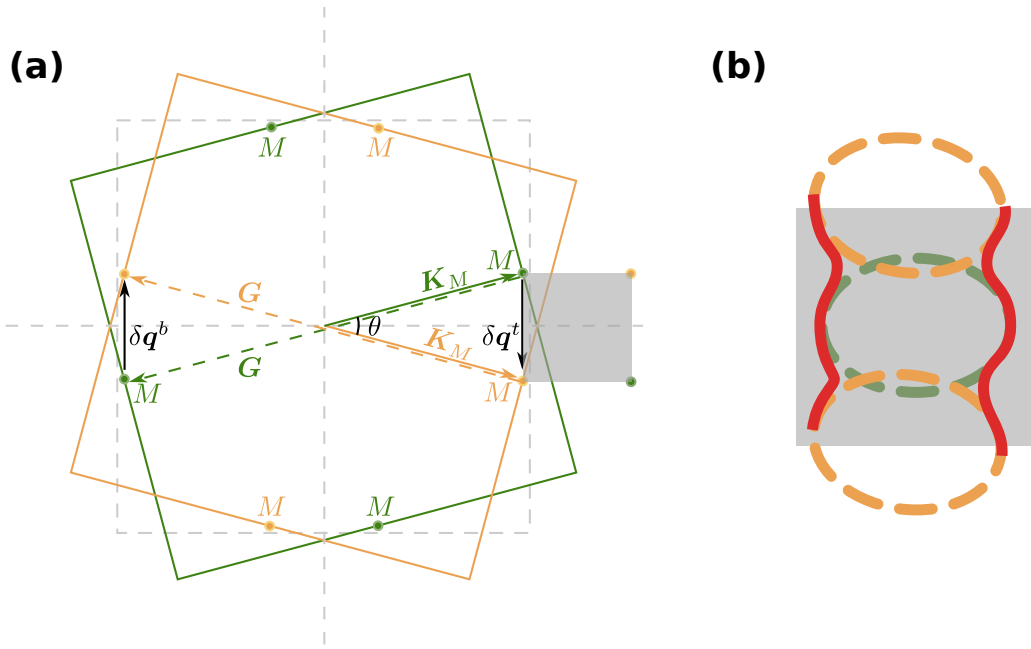


Figure 4.4: (a) Rotated top layer (green) and bottom layer (orange). The interference of all different hopping processes capture the spatial variation of interlayer tunnelings, which determines the moiré Brillouin zone (gray square). Up to the lowest truncation on such moiré k-shell, there are just two vertical hopping vectors δq^t and δq^b involved in the reconstruction of the left/right M -pockets (ditto for the top/bottom ones under a C_4 -rotation). (b) Illustration for the moiré-pattern-involved Fermi surface reconstruction. Taking the top layer elliptic Fermi surface (green dashed lines) as the reference, both the rotated bottom layer (down orange dashed lines) and the copied M -pockets due to G_x (up orange dashed lines) involve in the reconstruction of the Fermi surfaces (red solid lines).

recovers the two vertical *open* curves in (a1) of Fig.2 in the main text. The other two horizontal curves comes from the interference of the hopping processes between the up/down M -pockets.

Chapter 5

Engineering Chiral Topological Superconductivity in Twisted Ising Superconductors

5.1 Introduction

Transition metal dichalcogenides (TMD) are van der Waals (vdW) materials and can be prepared as 2D atomic crystals. They have attracted considerable interest and have demonstrated rich electronic phenomena ranging from charge-density wave order, superconductivity, exciton formation to the optical control of the valley degrees of freedom [187, 188, 189, 190, 191]. Strikingly, when prepared in few-layer forms, the so-called Ising superconductors gated-2H-MoS₂, 2H-NbSe₂, 2H-TaS₂, 2H-NbS₂ and 2H-TaSe₂ have anomalously large in-plane upper critical field, several times beyond the Pauli limit [192, 193, 194, 195, 196, 197]. The physical reason for this behavior can be attributed to strong Ising spin-orbit coupling in these materials, which pins the electrons' spin along the z -direction and is much less susceptible to an in-plane magnetic field.

Due to their 2D nature, TMD allow the fabrication of various vdW heterostructures with flexible tunability and interplay between electronic structures, superconductivity and magnetism. For instance, the ferromagnetic proximity effect in monolayer TMD has been well characterized in heterostructures such as WSe₂/CrI₃ [198, 199, 200] via optical probes. More recently, ferromagnetic Josephson junction NbSe₂/Cr₂Ge₂Te₆/NbSe₂ have been fabricated and investigated, and unconventional Josephson phase is reported [201, 202].

On the other hand, a new paradigm in the engineering of quantum phases of matter has been recently developed based on moiré patterns [45, 6, 44] introduced by stacking 2D crystals with twisting angles. Motivated by the discovery of correlated insulators and superconductivity in twisted bilayer graphene, the idea of moiré engineering has been extended into other materials including TMD [203, 53, 204, 14].

Interestingly, recent theories pointed out that twisted bilayer cuprate (Bi2212) may realize chiral topological superconductivity with nonzero Chern numbers [3, 205, 206] — a novel state of matter that yet to be

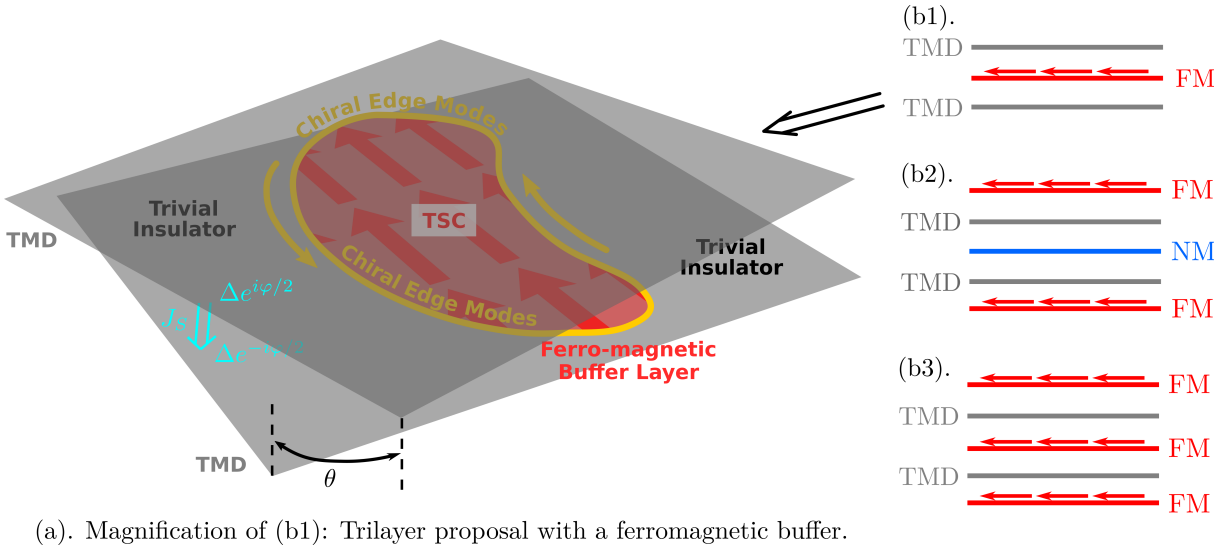
experimentally confirmed, which has triggered further experimental and theoretical investigations [207, 208]. The crucial mechanism of realizing nontrivial topology here is based on the nodal superconductivity, due to sign changes of the pairing order parameter around the Fermi surface. Intuitively, nodal superconductors are naturally located on the boundary between trivial and nontrivial band topology, and engineering topological phases via perturbations becomes possible.

In order to fabricate moiré structures, vdW 2D crystals are highly desirable. Practically, however, Bi2212 may be the only known nodal superconductor among vdW 2D crystals. This puts forward a serious constraint on the moiré-engineering of topological superconductivity. For example, the TMD superconductors are known to be nodeless and s-wave superconductors, despite theoretical discussions on the role played by magnetic fluctuations in the pairing mechanism [209]. It would be unfortunate if they cannot be included in the moiré-engineering of topological superconductivity, especially considering their fabricational flexibility and tunability.

Motivated by these experimental and theoretical efforts, we ask the following question: is it possible to moiré-engineer topological superconductivity in TMD superconductors? The answer is positive. We find that twisted Ising superconductors like 2H-NbSe₂ and 2H-TaS₂ in the presence of an proximity-induced in-plane Zeeman field (beyond the Pauli limit) and out-of-plane supercurrent can host chiral topological superconductivity with Chern number 12 or 6. The topological phases are found to be robust and occupies physically realizable parameter regimes. Under proper experimental conditions the topological pairing gap is $> 0.1\text{meV}$.

Not surprisingly, the mechanism underlying our proposal still involves pairing-gap-closing nodes, required by a trivial-to-topological phase transition. Here the pairing nodes are induced by the in-plane Zeeman field (beyond the Pauli limit) for Ising superconductors with Fermi pockets around the Γ -point in the momentum space. These Zeeman-field induced nodes were firstly pointed out theoretically by He et.al. [210], and experimental evidences for such nodal states in the presence of an external magnetic field have been reported [211, 212, 195, 213].

Unlike the proposal based on cuprates [3, 205], here the topological superconductivity in TMD twisted bilayers is limited to low temperatures $\lesssim 1\text{K}$. Nevertheless, it is worth mentioning a few advantages of the present proposal. First, different from strongly-correlated cuprates, the TMD Ising superconductivity has been fairly well-understood as conventional s-wave pairing without strong correlations. Namely the low energy physics of TMD are well under control in terms of theoretical modelling. Second, detecting the chiral majorana edge modes is the smoking-gun experiment to identify chiral topological superconductivity. In the present proposal, these edge modes are sharply located at the edge of the ferromagnetic buffer layer, and can be detected using either thermal transport or scanning tunnelling microscope (STM) (see FIG.5.1 for an illustration). In the proposal based on cuprates, these edge modes will hybridize with the nodal superconductivity due to the irregular shape of the atomically thin flakes, and could be challenging to locate in real space.



(a). Magnification of (b1): Trilayer proposal with a ferromagnetic buffer.

Figure 5.1: Setups: Proposals of twisted β -bilayer TMD heterostructures with an insulating middle buffer layer. (a,b1): The vertical cyan arrow represents the super-current J_S tuning the Josephson phase between top and bottom layers of TMD, and θ is a small twisting angle. The middle buffer layer with an *in-plane* ferromagnetic moment (red arrows) introduces an exchange Zeeman field H_{exch} for TMD layers through magnetic proximity effect, realizing the chiral topological superconducting phase. Outside the trilayer overlapping region, trivial superconductivity is realized. The gapless chiral edge modes are localized (yellow curves and arrows) at the boundary of the overlapping region. (b2,b3): Two additional proposals in the same spirits allowing more tunabilities for the parameters t_\perp , $t_{s,\perp}$ and H_{exch} : FM (NM) means a ferromagnetic (nonmagnetic) buffer layer.

5.2 Main results

Unlike twisted bilayer graphene, twisted heterostructures of TMDs have two distinct configurations differ by a 180° relative rotation, which were referred to as α and β [214]. The α -bilayer can be viewed as the building block for the bulk 2H-TMD structure, which restores the inversion symmetry. In this paper we instead focus on β -bilayer structure of Ising superconductors with Fermi pockets around the Γ -point (e.g. 2H-NbSe₂, 2H-TaS₂ but not gated 2H-MoS₂). In addition, a ferromagnetic insulating buffer layer with an *in-plane* magnetic moment is placed in the middle of the β -bilayer. At small twisting angles between the top and bottom TMD monolayers, we show that the system hosts chiral topological superconductivity when an out-of-plane supercurrent is present (see FIG.5.1 for an illustration).

Experimentally, most ferromagnetic vdW materials have an out-of-plane magnetic anisotropy. Only recently the monolayer CrCl₃ has been successfully isolated and confirmed to have an *in-plane* ferromagnetic order [198, 215]. On the other hand, theoretical first-principle calculations predicted that monolayer Cr₂I₃Cl₃ [216], 2H-VS₂ [217] and 2H-VSe₂ [218, 219] should be insulators with *in-plane* ferromagnetic order. In addition, because of a weak magnetic anisotropy, the ferromagnetic moment in CrBr₃ can be re-oriented to an *in-plane* direction by a fairly small external magnetic field ($\sim 0.5\text{T}$) [220]. These vdW materials may serve as the ferromagnetic buffer layer in the present proposal.

Apart from the intrinsic electronic structures of the monolayer TMD, the proposed heterostructures are characterized by three parameters: the Zeeman exchange field H_{exch} induced by the magnetic proximity ef-

fect, the spin-independent interlayer hopping t_{\perp} , and the spin-dependent interlayer hopping $t_{s,\perp}$. These parameters depend on the choice of the buffer layer in the setup proposed in FIG.5.1(a). Moreover, one may consider more sophisticated multilayer setups as shown in FIG.5.1(b). By choosing different setups, in principle all the three parameters can be tuned individually.

In the simplest setup in FIG.5.1(a), $H_{\text{exch.}}$ and $t_{s,\perp}$ both are originated from the ferromagnetic buffer layer. In general there is no direct relation between them. However, in a mean-field treatment, the second-order perturbation theory gives $t_{s,\perp} = \mu_B H_{\text{exch.}}$ (see Appendix 5.B). Although there is no available experimental data to quantify $H_{\text{exch.}}$ for the proposed heterostructures, similar heterostructures like WSe₂/CrI₃, MoSe₂/CrBr₃ with out-of-plane ferromagnetic layer have been well characterized experimentally and theoretically [221, 222, 223, 224, 225, 220], where a proximity-induced Zeeman splitting around $1 \sim 2\text{meV}$ is reported for electronic bands near the K point. A similar value of splitting in the proposed heterostructures corresponds to $H_{\text{exch.}} = 3 \sim 6H_p$. Notice that monolayer NbSe₂ has been reported to sustain a in-plane upper critical field $6 \sim 8H_p$ [211, 212, 195] (and about $9 \sim 10H_p$ for TaS₂ [213, 226]).

We find that the topological phase is robust at least when a small twisting angle θ is comparable with $t_{\perp}/(\hbar v_{\text{Ising}} k_F)$, where k_F is the Fermi wavevector and the velocity v_{Ising} is characterizing the Ising spin-orbit coupling near the Γ - M direction (see Eq.(5.4)). It is convenient to introduce a dimensionless parameter to capture the ratio of the two quantities:

$$\xi \equiv \arctan \frac{2t_{\perp}}{\hbar v_{\text{Ising}} k_F \theta}. \quad (5.1)$$

We consider proposed heterostructures involving either TaS₂ or NbSe₂. Their monolayer electronic structures are obtained using relaxed crystal structure based on first-principle calculations (see Appendix 5.C for details). For each TMD material, two cases for the spin-dependent hopping $t_{s,\perp}$ are investigated, corresponding to:

$$\begin{aligned} \text{case-(i): } & t_{s,\perp} = \mu_B H_{\text{exch.}} \\ \text{case-(ii): } & t_{s,\perp} = 0 \end{aligned} \quad (5.2)$$

We show the global phase diagram by tuning the spin-independent hopping t_{\perp} and the Zeeman exchange field $H_{\text{exch.}}$ in FIG.5.2, based on numerical calculations. For presentation purpose, we have fixed $\xi^{\text{TaS}_2} = 0.9$ and $\xi^{\text{NbSe}_2} = 1.1$, and fixed the Josephson phase $\varphi = \pi/2$ corresponding the maximal supercurrent state. Topological superconducting phases are found to exist when $t_{\perp} \lesssim 9\text{meV}$ for TaS₂ (and $t_{\perp} \lesssim 2.7\text{meV}$ for NbSe₂). A Chern-number-12 phase is found to occupy a large portion of the parameter space, while a Chern-number-6 phase appears for case-(i) at small values of t_{\perp} . Under appropriate conditions, the gap in the topological phase can reach 0.1meV.

These phase diagrams are also well-understood via analytical calculations. We have plotted the phase boundary (see Eq.(5.12)) between trivial and topological phases from our perturbative calculations in FIG.5.2, which is in good agreement with the numerical calculations.

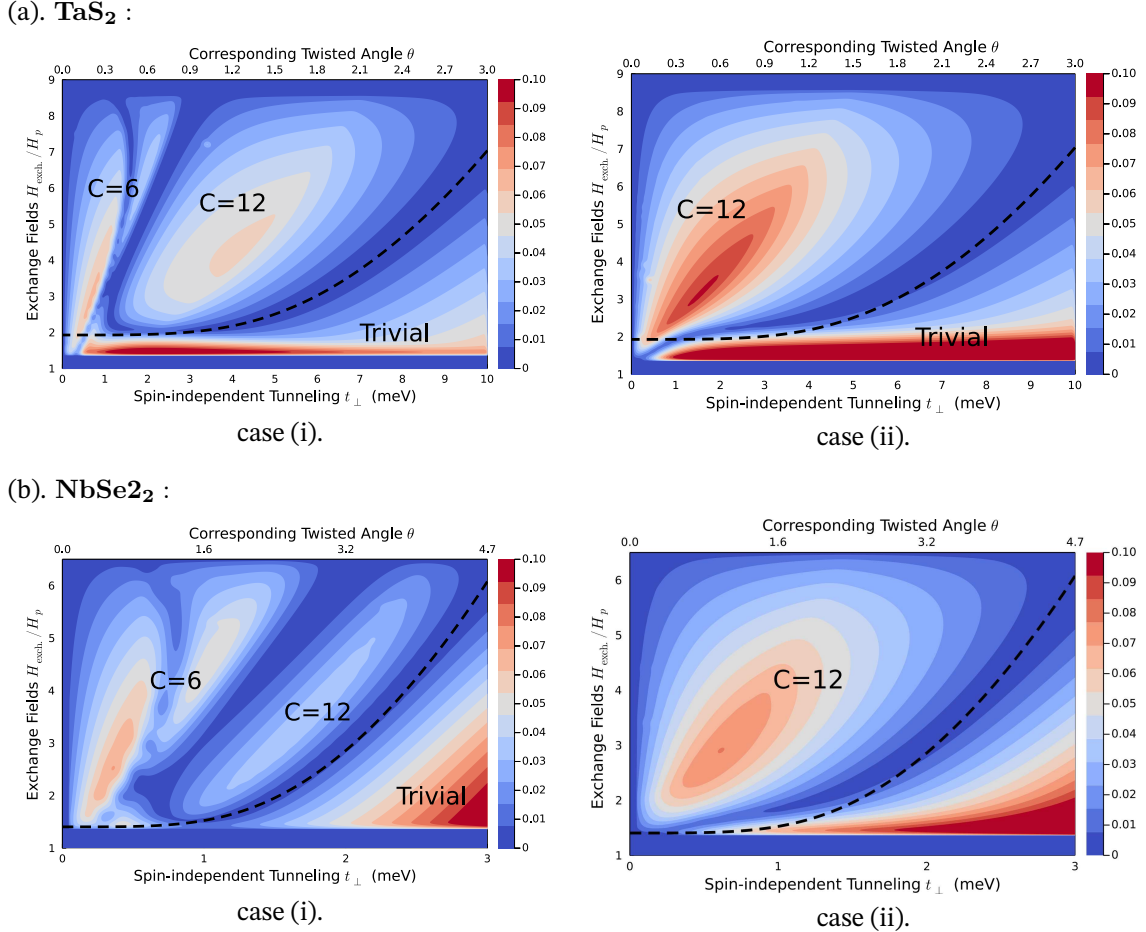


Figure 5.2: t_{\perp} - (H/H_p) Phase Diagram: The superconducting gap (gap minimum in the momentum space) and Chern numbers for proposed heterostructures involving TaS_2 (a) and NbSe_2 (b) based on numerical calculations. Here the Josephson phase is fixed to be $\varphi = \pi/2$ and the parameter ξ (see Eq.(5.1) for its definition) is fixed to be $\xi^{\text{TaS}_2} = 0.9$ and $\xi^{\text{NbSe}_2} = 1.1$. H_p in the vertical axis is the Pauli limit field strength. t_{\perp} and the corresponding twisting angle are displayed on the horizontal axis. For both materials the phase diagrams corresponding to case-(i) and case-(ii) in Eq.(5.2) are calculated. The black dashed lines exhibit the predicted topological/trivial phase boundary from analytical perturbative calculations (see Eq.(5.12)).

TMD	$\hbar v_F$ (eV·Å)	$\hbar v_{\text{Ising}}$ (eV·Å)	k_F (Å $^{-1}$)	Δ (meV)
NbSe ₂	-2.22	0.12	0.48	0.46
TaS ₂	-2.89	0.36	0.54	0.52

Table 5.1: The parameters in the $\mathbf{k} \cdot \mathbf{p}$ model.

Apart from the global phase diagrams, we also plot the phase diagrams with a few selected values of t_\perp . Fixing $H_{\text{exch.}} = 4H_p$, we tune the twisting angle θ and the Josephson phase φ , and the results are shown in FIG.5.3. Consistent with the global phase diagram, the topological phase is realized when t_\perp is not too large. Interestingly, for intermediate values of t_\perp , trivial to topological phase transitions are observed by tuning φ alone while fixing the twisting angle θ in an appropriate regime. Such a Josephson-phase-driven topological transition in a single device can lead to unique features to unambiguously identify the topological phase in experiments. For instance, the gapless chiral majorana edge modes should appear only in the topological phase, after the phase transition occurs when φ is tuned up.

5.3 Model

In an in-plane Zeeman field regime $H_{\text{exch.}} > \sqrt{2}H_p$, it was pointed out that the pairing gap around the Γ -pockets will close and nodal superconductivity is formed [210], while the pairing gap around the K -pockets remain nodeless. These nodes on Γ -pockets turn out to be the origin of the topological superconductivity in the present proposal.

The minimal model for the bands forming the Γ -pockets (which has dominant d_{z^2} orbital content of the transition metal) is as follows

$$h(\mathbf{k}) = \varepsilon_0(\mathbf{k}) + \lambda_{\text{SO}}^{\text{Ising}}(\mathbf{k})\sigma_z. \quad (5.3)$$

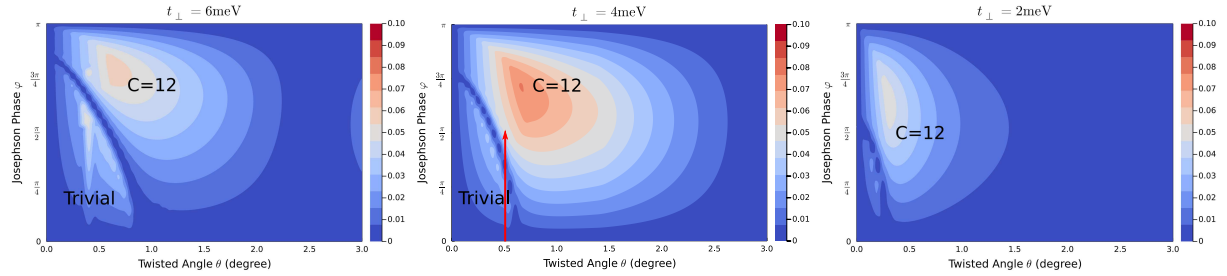
Drastically different from the usual Rashba spin-orbit coupling, here the Ising spin-orbit coupling $\lambda_{\text{SO}}^{\text{Ising}}(\mathbf{k})$ splits bands with fixed S_z -spin. In fact, due to the $z \rightarrow -z$ mirror symmetry of monolayer 2H-TMD, the Rashba spin-orbit coupling is forbidden. Time-reversal symmetry dictates that $\lambda_{\text{SO}}^{\text{Ising}}(\mathbf{k}) = -\lambda_{\text{SO}}^{\text{Ising}}(-\mathbf{k})$, so $\lambda_{\text{SO}}^{\text{Ising}}(\mathbf{k})$ necessarily has sign changes. Due to the mirror plane containing the Γ - M axis, the six Γ - M directions are exact where $\lambda_{\text{SO}}^{\text{Ising}}(\mathbf{k})$ changes sign.

We therefore begin with a first-order $\mathbf{k} \cdot \mathbf{p}$ model near the intersection point P between the Fermi surface and one Γ - M direction (k_x -direction, see Fig.5.4 for an illustration):

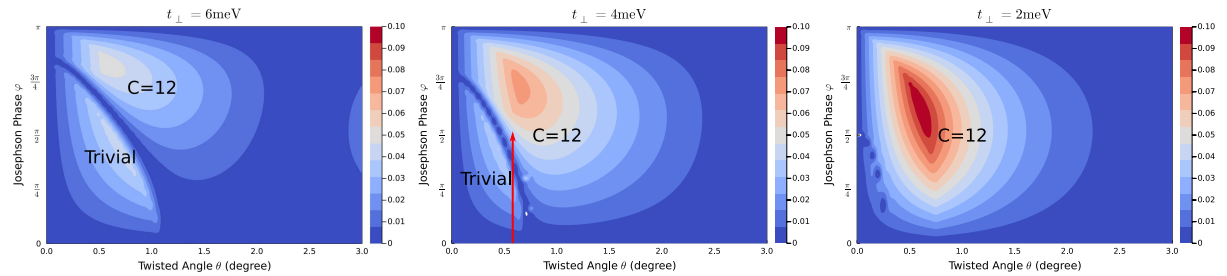
$$h^{\text{mono.}} = \hbar v_F k_x + \hbar v_{\text{Ising}} k_y \sigma_z, \quad (5.4)$$

where $\lambda_{\text{SO}}^{\text{Ising}}(\mathbf{k})$ vanishes along the k_x -direction, and $v_{\text{Ising}} \equiv \frac{\partial \lambda_{\text{SO}}^{\text{Ising}}(\mathbf{k})}{\hbar \partial k_y}$. We list these parameters for NbSe₂ and TaS₂ in Table.5.1 based on first principle calculations (Fig. 5.5 plot the band structures, full list of quartic $\mathbf{k} \cdot \mathbf{p}$ expansion parameters is given in Appendix 5.C).

(a). TaS_2 :

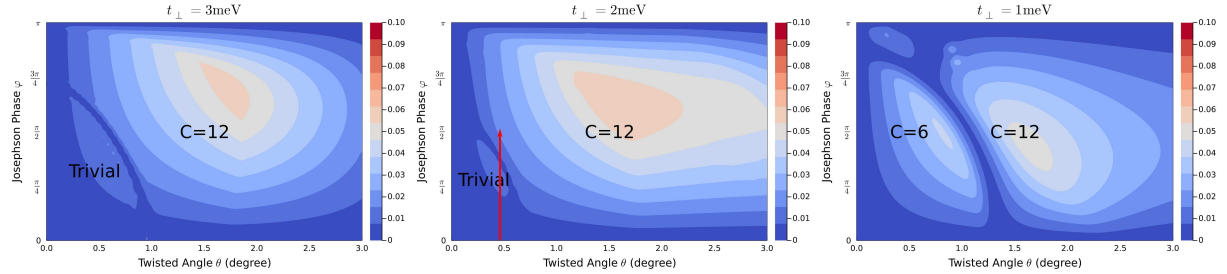


case (i)

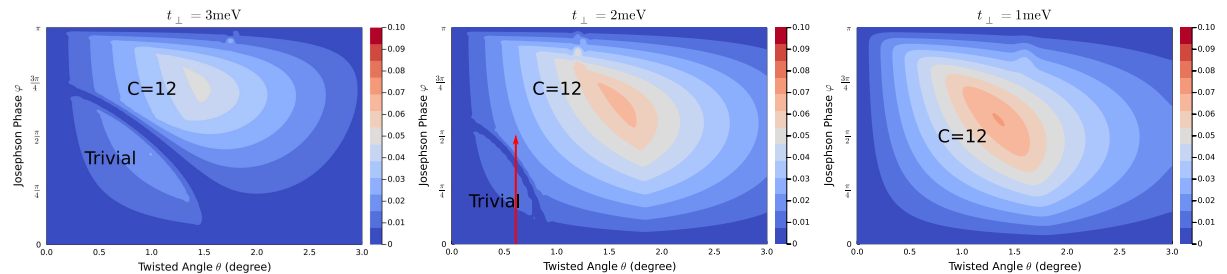


case (ii)

(b). NbSe_2 :



case (i)



case (ii)

Figure 5.3: θ - φ **Phase Diagram**: The superconducting gap (gap minimum in the momentum space) and Chern numbers by varying the twisting angle θ and the Josephson phase φ for proposed heterostructures involving TaS_2 and NbSe_2 . Here in each figure we fix the Zeeman field to be four times the Pauli limit $H_{\text{exch.}} = 4H_p$ and fix the spin-independent tunneling t_{\perp} . Red arrows are to indicate the trivial-topological phase transitions by tuning φ in a single device. Note that the regime $\varphi \leq \pi/2$ corresponds to the stable branch of the Josephson junction.

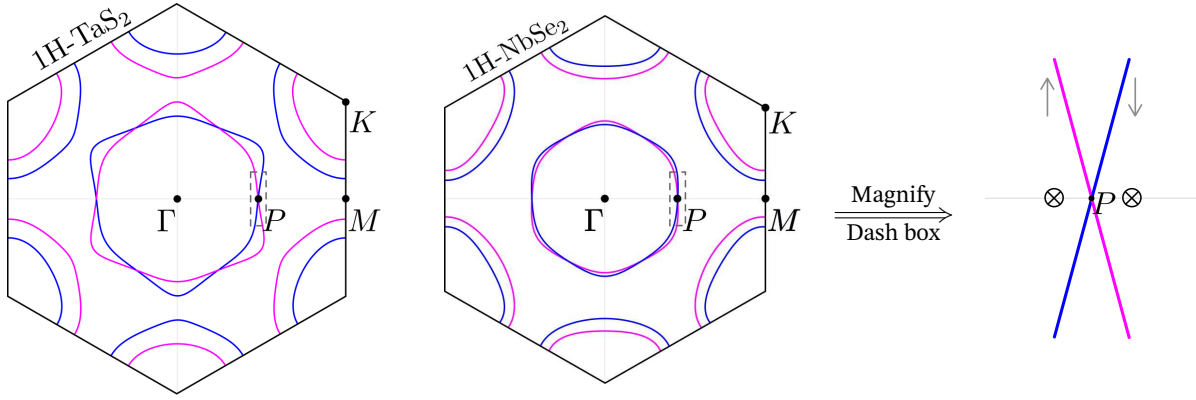


Figure 5.4: Monolayer Fermi Surfaces and Band Structures: Γ -pocket and K -pocket of monolayer NbSe₂ and TaS₂ are shown. Point P is the intersection of Γ - M line and the the Γ -pocket, where Ising SOC vanishes and two nodes (cross symbols) emerge when an in-plane Zeeman field H_{exch} exceeds the superconducting gap. Magenta and blue colors indicate the different S_z -spin components.

Monolayer: After introducing an spin-singlet pairing Δ ¹, in the Nambu basis we obtain the BCS mean-field Hamiltonian:

$$h_{\text{BCS}}^{\text{mono.}} = \hbar v_F k_x \tau_z + \hbar v_{\text{Ising}} k_y \sigma_z + \mu_B H_y \sigma_y + \Delta \sigma_y \tau_y, \quad (5.5)$$

where Pauli τ -matrices label the particle-hole space, and an Zeeman field H_y along the y -direction is introduced (the g-factor is assumed to be 2). Because the system has a spin-rotation symmetry around S_z -direction, the choice of the direction of the in-plane magnetic field is not important. Since there are three independent Γ - M -directions, related by C_3 rotations, the full electronic structure of NbSe₂ (TaS₂) has three copies of the effective theory in Eq.(5.5). Eq.(5.5) can be solved straightforwardly. A pair of Dirac nodes are found to emerge when $\mu_B H_y > \Delta$, located at $\mathbf{k}^\pm = (\pm \frac{1}{\hbar v_F} \sqrt{(\mu_B H_y)^2 - \Delta^2}, 0)$ (see Fig.5.4) for a schematic illustration, consistent with earlier works [210, 209], whose low energy effective theories are:

$$h_{\text{node}}^\pm = \pm \hbar v_F \cos \eta \delta k_x \Sigma_z + \hbar v_{\text{Ising}} \sin \eta \delta k_y \Sigma_x, \quad (5.6)$$

where $\eta = \arcsin \frac{\Delta}{\mu_B H_y}$, $\delta \mathbf{k}$ is measured from the nodal points \mathbf{k}^\pm , and Σ are Pauli matrices in the low energy space. These nodes are protected by a chiral symmetry $\sigma_x \tau_y$ in model Eq.(5.5) (corresponding to the combination of the physical time-reversal transformation $i\sigma_y K$, the particle-hole transformation $\tau_x K$ and a $S_z \sim \pi$ rotation $i\sigma_z \tau_z$) sending $h(\mathbf{k}) \rightarrow -h(\mathbf{k})$.

Twisted bilayer: Next we consider a β -bilayer (separated by an insulator buffer layer) with a twisting angle θ , which can be viewed as top/bottom monolayer twisted by angle $\pm\theta/2$ respectively. Introducing k_F being the crystal momentum of point P , we obtain the following effective theory near P :

$$\begin{aligned} h_{\text{BCS}}^{\text{bilayer}} = & \hbar v_F k_x \tau_z + \hbar v_{\text{Ising}} k_y \sigma_z + \Delta \cos \frac{\varphi}{2} \sigma_y \tau_y \\ & + \Delta \sin \frac{\varphi}{2} \sigma_y \tau_x \nu_z - \hbar v_{\text{Ising}} k_F \frac{\theta}{2} \sigma_z \nu_z + \mu_B H_y \sigma_y \end{aligned}$$

¹ Γ - M mirror symmetry protects that there is no singlet-triplet mixing at P -point.

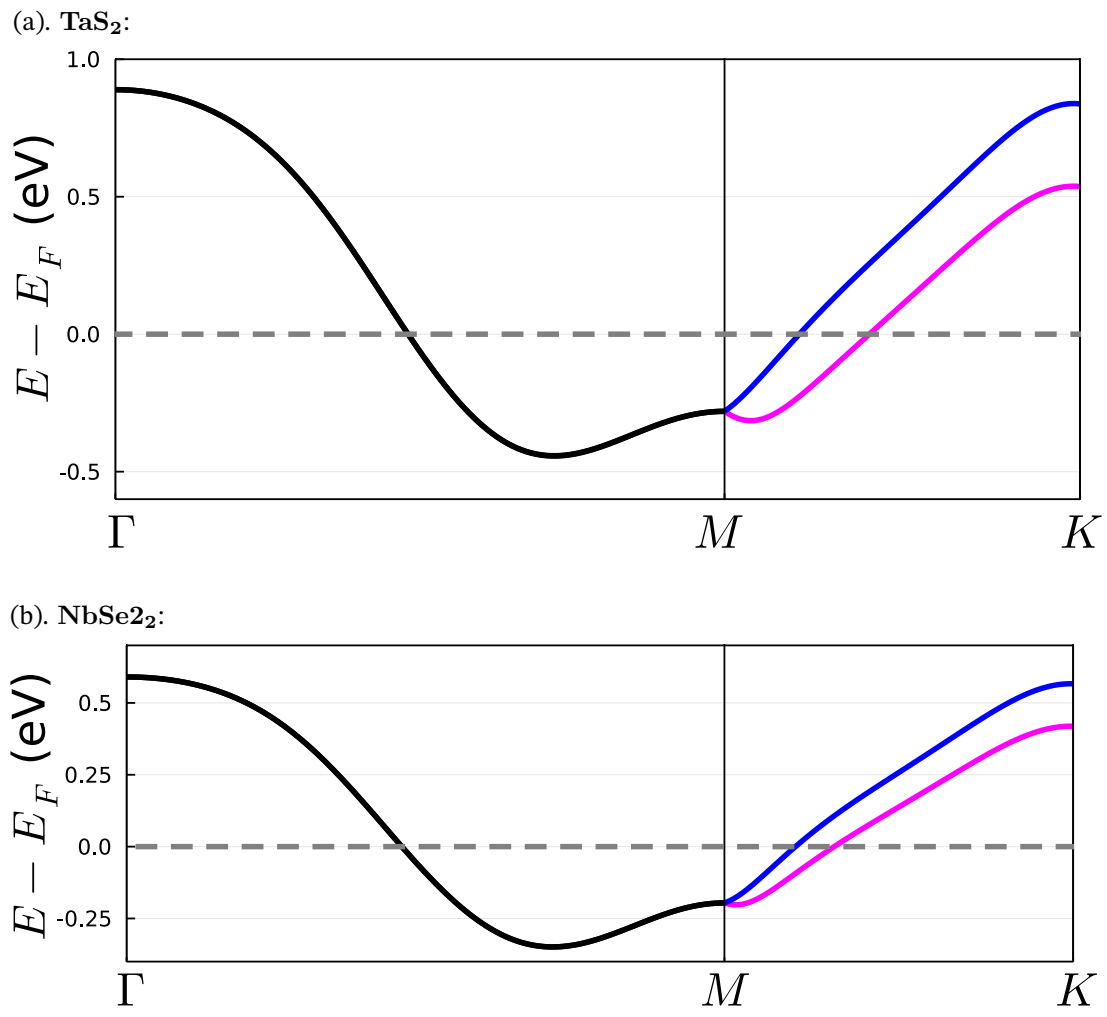


Figure 5.5: **Monolayer Band Structures.**

$$+t_{\perp}\tau_z\nu_x+t_{s_y,\perp}\sigma_y\nu_x. \quad (5.7)$$

Here the Pauli matrices ν captures the top/bottom layer space. $\Delta > 0$ and the pairing amplitude is $\Delta e^{\pm i\varphi/2}$ for the top/bottom layer respectively. The t_{\perp} and $t_{s_y,\perp}$ terms describes the spin-independent and spin-dependent interlayer hopping processes respectively. Based on the two-center approximation [44, 53], and the fact that point P is far away from the Brillouin zone boundary, the interlayer hopping processes have a weak stacking-dependence, and are considered as constants in the present work [207, 208] (see Appendix 5.E for a discussion on the two-center approximation).

The model Eq.(5.7) can be analytically solved in various perturbative regimes. To demonstrate the stability of the topological superconductivity, below we focus on one particular regime, in which $\sqrt{(\hbar v_{\text{Ising}} k_F \theta)^2 + 4t_{\perp}^2} \gg \Delta, \mu_B H_y, t_{s_y,\perp}$. The advantage of this regime is that it is always realizable in the proposed heterostructures by tuning the twisting angle θ . In this regime, we find that the topological superconductivity with Chern number 4 (corresponding to Chern number 12 for the whole heterostructure) is always realized in model Eq.(5.7) by tuning φ, θ and $\mu_B H_y \gtrsim \Delta$.

To understand this behavior, we may firstly turn off the pairing Δ and $\mu_B H_y, t_{s_y,\perp}$ in model Eq.(5.7). There are four intersection points between the spin-up and spin-down Fermi surfaces, which we label as C, D and F, G and are located at the k_y and k_x axes respectively (see FIG. 5.6). The low energy effective theory near

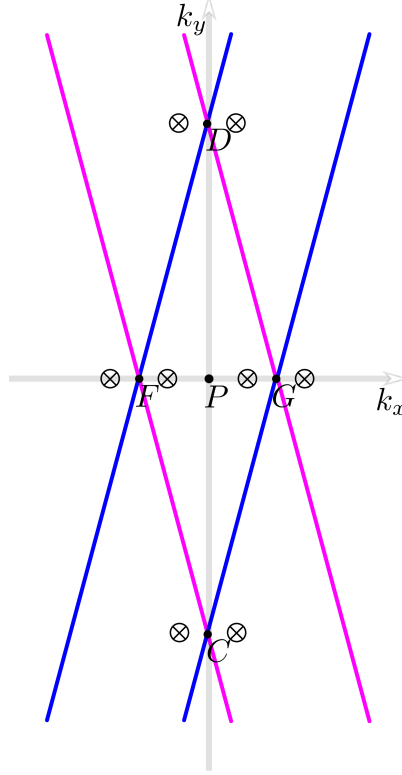


Figure 5.6: Schematic Plot of Four Fermi Surface Intersection Points in a Twisted Bilayer Near Point-P: When $\varphi = 0$, each intersection point will give rise to two pairing nodes after H_{exch} is tuned up. When $\varphi \neq 0$, these nodes open up energy gaps: The four nodes near points F and G along the Γ -M line have total Chern number zero. The four nodes near points C and D have total Chern number 4.

each point resembles Eq.(5.4) with modified v_F and v_{Ising} .

After Δ, φ are turned on but $\mu_B H_y = t_{s_y, \perp} = 0$, the pairing gap minima near C, D, F, G are found to be the same $\Delta_{C,D,F,G} = \Delta \sqrt{\cos^2 \frac{\varphi}{2} + \cos^2 \xi \sin^2 \frac{\varphi}{2}}$, where ξ is defined in Eq.(5.1). Because the connection with the $\varphi = 0$ limit, the superconducting phase so far must still be topologically trivial even though $\varphi \neq 0$ breaks the time-reversal symmetry.

When $\mu_B H_y, t_{s_y, \perp} \neq 0$ are tuned up, the behavior near the points C, D versus F, G are qualitatively different. The pairing gap minima near F, G never go to zero as long as $\varphi \neq 0$. In particular, we find:

$$\Delta_{F,G} = \begin{cases} \sqrt{(\Delta \cos \frac{\varphi}{2} - b)^2 + \Delta^2 \cos^2 \xi \sin^2 \frac{\varphi}{2}}, & b < \Delta \cos \frac{\varphi}{2} \\ \Delta \cos \xi |\sin \frac{\varphi}{2}|, & b \geq \Delta \cos \frac{\varphi}{2} \end{cases} \quad (5.8)$$

where

$$b \equiv \begin{cases} |\mu_B H_y \sin \xi - t_{s_y, \perp}| & \text{for point } F, \\ |\mu_B H_y \sin \xi + t_{s_y, \perp}| & \text{for point } G. \end{cases} \quad (5.9)$$

On the contrary, near points C, D topological phase transition occurs with four Dirac nodes (two near each point) emerging when $H_y = H_c^{\text{topo}}$, where the critical Zeeman field strength is

$$\mu_B H_c^{\text{topo}} \equiv \Delta \sqrt{\sec^2 \xi \cos^2 \frac{\varphi}{2} + \sin^2 \frac{\varphi}{2}}. \quad (5.10)$$

When $H_y > H_c^{\text{topo}}$, the four Dirac nodes acquire topological mass gap, transferring a Chern number of 4:

$$\Delta_{C,D}^{\text{topo.}} = \sin \varphi \frac{\Delta^2 \sin^2 \xi}{\hbar v_{\text{Ising}} k_F \theta} \sqrt{\left(\frac{H_y}{H_c^{\text{topo.}}} \right)^2 - 1} \quad (5.11)$$

The details of the calculations are presented in Appendix 5.D.

Note that different from $\Delta_{F,G}$, the topological gap $\Delta_{C,D}^{\text{topo.}} \propto \Delta^2$. This is because Δ -linear order gap remains zero in the present linear-order $\mathbf{k} \cdot \mathbf{p}$ effective theory, and the second order perturbation plays the dominant role: the topological phase is always realized when $H_y > H_c^{\text{topo.}}$.

When a higher order $\mathbf{k} \cdot \mathbf{p}$ expansion is considered, we do find that a non-topological Δ -linear order gap near C, D becomes nonzero (see Appendix 5.D). When this gap is large the topological superconductivity will be destroyed. Based on perturbative calculations, the topological phase requires the following criterion to be satisfied (See Appendix 5.D Eq.(5.50) for details):

$$t_{\perp}^2 < \frac{\Delta \hbar k_F v_{\text{Ising}}^2}{v_2} a(\xi, \varphi) \sqrt{\left(\frac{H_y}{H_c^{\text{topo.}}} \right)^2 - 1}, \quad (5.12)$$

$$a(\xi, \varphi) \equiv \tan \xi \sin \xi \sqrt{\sec^2 \xi \cos^2 \frac{\varphi}{2} + \sin^2 \frac{\varphi}{2}}.$$

Here v_2 is a velocity parameter (defined in Eq.(5.28)) in the quadratic-order $\mathbf{k} \cdot \mathbf{p}$ expansion, $\hbar v_2^{\text{NbSe}_2} = 0.94$ and $\hbar v_2^{\text{TaS}_2} = 3.1 \text{ eV}\cdot\text{\AA}$ based on our electronic structure calculations (See Appendix 5.C). Namely, t_{\perp} cannot be too large. This criterion serves as the phase boundary between the trivial and topological phases, and is

plotted in FIG.5.2 as the dashed black line.

The previous perturbative regime well captures the Chern-number-12 topological phase. Aiming at understanding the Chern-number-6 topological phase in the numerical phase diagrams, we have performed the analytical calculations in a different perturbative regime: $t_{\perp} \ll \Delta, \hbar v_{\text{Ising}} k_F \theta \ll \Delta$, and reproduced the Chern-number-6 topological phase (see Appendix 5.D).

5.4 Discussion and conclusions

Before concluding, we would like to remark on a few experiment-related issues.

Chiral edge modes: When topological superconductivity is realized in the proposed heterostructure in Fig.5.1(a), the edge of the ferromagnetic buffer layer is the natural boundary between the topological superconductivity and trivial superconductivity. This is because outside the buffer layer region, due to the lack of Zeeman exchange field, gapped trivial superconductivity is realized in the TMD bilayer. Majorana chiral edge modes are then sharply located at this edge, leading to well-known quantized thermal Hall conductance $\frac{\kappa_{xy}}{T} = C \frac{\pi}{12} \frac{k_B^2}{\hbar}$, where C is the Chern number. In addition, the edge modes can be detected via scanning tunnelling microscopy as mid-gap states.

Mid-gap states located at the edge of a superconducting material has non-topological explanations, such as the Yu-Shiba-Rusinov bound states. However, in an appropriate regime, as shown in Fig.5.3, we note that a single device may realize trivial to topological phase transition while the Josephson phase φ is tuned up. Such a φ -driven topological phase transition has unique experimental signatures since the majorana edge states are expected to exist only in the topological phase, which may be used to sharply identify the nature of the mid-gap states.

The effect of in-plane external magnetic field: When an in-plane magnetic field is applied to the proposed heterostructures, the Josephson phase $\varphi(x) = 2\pi x/L$ becomes spatial dependent along the in-plane transverse direction, where $L = \frac{\Phi_0}{H_{\text{ext}} d}$ and d is the effective thickness of the junction. For instance, an external magnetic field $H_{\text{ext.}} \sim 0.5\text{T}$ is needed to reorient the magnetic moment of CrBr₃ to an in-plane direction, corresponding to $L \sim 2\mu\text{m}$ if $d \sim 20\text{\AA}$ is used. Due to the fact that the Chern number flips sign when $\varphi \rightarrow -\varphi$, the topological superconductivity is expected to form spatial stripes, or domains with width $L/2$, with alternating Chern numbers, e.g., $C = \pm 12$ in which case 24 chiral majorana states are expected to form at each domain-wall. In Appendix 5.A we estimate the spatial spread l_{\perp} of the domain-wall majorana states along the transverse direction of the domain-wall. Only when l_{\perp} is much smaller than the stripe width $L/2$ are the domain-wall states well-defined. We find that for a generic magnetic field direction l_{\perp} is comparable with $L/2$ for $H_{\text{ext.}} \sim 0.5\text{T}$. However, when $H_{\text{ext.}}$ is parallel to one $\Gamma - M$ direction, 8 among the 24 domain-wall majorana states have an l_{\perp} that can be 5 ~ 10 times smaller than $L/2$. These domain wall chiral states may be observable in probes such as STM or thermal transport.

Charge-density-wave Order: It is known that Ising superconductivity in 2H-NbSe₂ or 2H-TaS₂ coexists with the charge-density-wave (CDW) order [227, 228, 229]. For the Fermi pockets around Γ , the Fermi surface

folding due to CDW occurs near the Γ - K direction, which would not qualitatively affect the low energy physics near the Γ - M direction, which we have been focusing on in this paper.

Rashba Spin-orbit Coupling: As emphasized before, the $z \rightarrow -z$ mirror symmetry forbids the Rashba spin-orbit coupling in the monolayer TMD. A Rashba spin-orbit coupling breaks an important invariance of Eq.(5.7) related to the combination of particle-hole and time-reversal transformation $\text{PH} \circ \text{TR} = \sigma_y \tau_x$. $\text{PH} \circ \text{TR}$ always sends $h_{\text{BCS}}^{\text{bilayer}}(\mathbf{k}, H_y, \varphi) \mapsto -h_{\text{BCS}}^{\text{bilayer}}(\mathbf{k}, -H_y, -\varphi)$. In the absence of the Rashba spin-orbit coupling one may flip the sign of H_y and φ by a complex conjugation since all other terms in the Hamiltonian are real: $-h_{\text{BCS}}^{\text{bilayer}}(\mathbf{k}, -H_y, -\varphi) = -(h_{\text{BCS}}^{\text{bilayer}})^*(\mathbf{k}, H_y, \varphi)$. Namely there is an invariance protecting the Bogoliubov quasiparticle spectrum being $\pm E$ symmetric at any \mathbf{k} . Such an invariance is lost in the presence of a Rashba spin-orbit coupling, leading to Bogoliubov Fermi pockets [209].

In the proposed heterostructures, despite the lack of the $z \rightarrow -z$ mirror symmetry, the intrinsic Rashba coupling induced by the vdW interlayer interactions can be safely neglected since it is extremely weak (see in Appendix 5.C). Although an extrinsic, substrate-induced Rashba coupling is possible, in this paper we do not consider this effect, since nevertheless this coupling could be tuned to zero via gating.

Interlayer Tunneling Strength: It is clear from the phase diagrams in FIG. 5.2 and criterion Eq.(5.12) that the interlayer tunneling t_{\perp} cannot be too large in order to realize the topological superconductivity ($< 10\text{meV}$). On the other hand, based on our DFT calculation (see Appendix 5.C), due to the d_{z^2} nature of Fermi pockets around Γ -point, a fairly large interlayer tunneling of the bilayer systems of NbSe_2 or TaS_2 *without* a buffer layer is found near the point- P ($> 50\text{meV}$)². This actually motivates us to consider the insulating buffer layer in the proposed heterostructures. In Appendix 5.C, as an estimate, we performed DFT calculations on a $\text{TaS}_2/\text{WS}_2/\text{TaS}_2$ heterostructure, and $t_{\perp} \sim 5\text{meV}$ is found – well within the regime where topological superconductivity is realized.

In summary, we theoretically propose twisted bilayer vdW Ising superconductors as a new flexible and tunable platform to realize chiral topological superconductivity with Chern numbers. In the simplest setup, an insulating buffer layer with an in-plane ferromagnetic moment is introduced between the TMD Ising superconductors such as NbSe_2 or TaS_2 , providing Zeeman exchange field in the TMD layers via the magnetic proximity effect. We show that the out-of-plane supercurrent induces topological superconductivity over a large parameter regime, and the characteristic majorana chiral edge modes are localized on the edge of the ferromagnetic buffer layer. We hope that the present study may motivate further experimental and theoretical investigations on such vdW heterostructures.

5.A Domain-wall chiral modes

Assuming inter-node scattering being weak, here we may use the Dirac equation for a single node to estimate the spatial size of the chiral domain-wall modes. Denoting the magnetic field direction as \hat{B} , we have the

²In literature <https://www.nature.com/articles/s41467-018-03888-4>, a smaller value of tunneling about 15meV for bilayer NbSe_2 is reported. We ascribe such discrepancy to the choice of van der Waals pseudopotentials.

spatial-dependent Josephson phase $\varphi(\mathbf{r}) = \frac{2\pi}{L} \hat{B} \times \hat{z} \cdot \mathbf{r} \equiv \frac{2\pi}{L} \hat{n} \cdot \mathbf{r}$, where we defined unit vector $\hat{n} \equiv \hat{B} \times \hat{z}$. Based on Eq.(5.11), the spatial-dependent Dirac equation becomes:

$$H = v_x p_x \Sigma_x + v_y p_y \Sigma_z + m_0 \sin \varphi(\mathbf{r}) \Sigma_y, \quad (5.13)$$

where

$$m_0 \equiv \frac{\Delta^2 \sin^2 \xi}{\hbar v_{\text{Ising}} k_F \theta} \sqrt{\left(\frac{H_y}{H_c^{\text{topo}}} \right)^2 - 1}. \quad (5.14)$$

$v_x = v_F \cos \theta^+$ and $v_y = v_{\text{Ising}} \sin \theta^+$ according to Eq.(5.44), and $v_x \gg v_y$ since θ^+ is an angle parameter of order unity. The mass-sign-changing domain walls are located at $\hat{n} \cdot \mathbf{r} = \frac{kL}{2}$, and $k \in \mathbb{Z}$. Near each domain wall, we may linearize the mass as $m_0 \sin \varphi(\mathbf{r}) \sim (-1)^k m_0 \tilde{\varphi}(\delta \mathbf{r})$, where $\tilde{\varphi}(\delta \mathbf{r}) = \varphi(\mathbf{r}) - k\pi = \frac{2\pi \hat{n} \cdot \delta \mathbf{r}}{L}$, and $\delta \mathbf{r}$ is the position measured from the domain wall.

It is now convenient to rotate into the coordinate system with axes $(x_{||}, x_{\perp})$ along and perpendicular to the domain-wall. The corresponding momentum are denoted as $(p_{||}, p_{\perp})$. Writing the cosine c and sine s of the rotation angle between the two coordinate systems, then $p_x \equiv cp_{||} - sp_{\perp}$ and $p_y \equiv sp_{||} + cp_{\perp}$, and we have

$$\begin{aligned} H = & v_x (cp_{||} - sp_{\perp}) \Sigma_x + v_y (sp_{||} + cp_{\perp}) \Sigma_z \\ & + (-1)^k m_0 \frac{2\pi x_{\perp}}{L} \Sigma_y, \end{aligned} \quad (5.15)$$

H^2 has a simple form:

$$\begin{aligned} H^2 = & v_x^2 (cp_{||} - sp_{\perp})^2 + v_y^2 (sp_{||} + cp_{\perp})^2 + m_0^2 \left(\frac{2\pi x_{\perp}}{L} \right)^2 \\ & - (-1)^k \hbar m_0 \frac{2\pi}{L} (sv_x \Sigma_z + cv_y \Sigma_x) \end{aligned} \quad (5.16)$$

Since $p_{||}$ is a good quantum number we are left with a one-dimensional harmonic oscillator involving p_{\perp}, x_{\perp} :

$$\begin{aligned} H^2 = & ((cv_x)^2 + (sv_y)^2) p_{\perp}^2 + ((sv_x)^2 + (cv_y)^2) (p_{\perp} - p_0(p_{||}))^2 \\ & + m_0^2 \left(\frac{2\pi x_{\perp}}{L} \right)^2 - (-1)^k \hbar m_0 \frac{2\pi}{L} (sv_x \Sigma_z + cv_y \Sigma_x), \end{aligned} \quad (5.17)$$

where p_0 is a linear function of $p_{||}$. The corresponding mass and frequency for this harmonic oscillator are:

$$\begin{aligned} M &= \frac{1}{2} [(sv_x)^2 + (cv_y)^2]^{-1} \\ \omega &= \sqrt{2M^{-1}} \frac{m_0 2\pi}{L}. \end{aligned} \quad (5.18)$$

The energy levels are:

$$E_n = 2\hbar\sqrt{(sv_x)^2 + (cv_y)^2} \frac{m_0 2\pi}{L} \left(n + \frac{1}{2}\right). \quad (5.19)$$

The zero energy state of H and H^2 for $p_{\parallel} = 0$, corresponding to the chiral majorana modes, is the $n = 0$ ground state of the harmonic oscillator. The last term in H^2 chooses a specific eigenstate of $(sv_x\Sigma_z + cv_y\Sigma_x)$, so that the zero-point energy in the harmonic oscillator is exactly canceled. Since we are working with complex fermion, this zero energy state corresponds to two chiral majorana modes.

The spatial spread l of the chiral model along the x_{\perp} direction can be readily read out from the harmonic oscillator ground state $\psi(x_{\perp}) \propto e^{-x_{\perp}^2/(2l_{\perp}^2)}$:

$$l_{\perp} = \sqrt{\frac{\hbar}{M\omega}} = \sqrt{\frac{\hbar[(sv_x)^2 + (cv_y)^2]^{1/2}}{2\pi m_0}} \quad (5.20)$$

l_{\perp} is proportional to the square root of the velocity $[(sv_x)^2 + (cv_y)^2]^{1/2}$. Note that $v_x \gg v_y$, for a generic magnetic field direction, $l_{\perp} \sim \sqrt{\frac{\hbar v_x L}{2\pi m_0}}$. Assuming $\hbar v_x \sim 1\text{eV}\cdot\text{\AA}$, $m_0 \sim 0.1\text{meV}$, and $L \sim 2\mu\text{m}$, one finds $l_{\perp} \sim 0.4 \cdot L/2$.

To minimize l_{\perp} , one may choose the magnetic field direction (i.e., the domain-wall direction) being along x (i.e., one Γ - M direction), leading to $l_{\perp} = \sqrt{\frac{\hbar v_y L}{2\pi m_0}}$ for 4 nodes near this Γ - M direction among the total of 12 nodes. In this case, among the 24 majorana domain wall states, 8 of them have $l_{\perp} \sim 0.2 \cdot L/2$ (for TaS_2) and $l_{\perp} \sim 0.1 \cdot L/2$ (for NbSe_2) using the parameters above.

5.B A mean-field treatment for the ferromagnetic buffer layer

We will show in this section that, for the proposed setup in Fig.5.1(a) with a ferromagnetic buffer layer, the direct couplings between the top/bottom layer and the middle layer will induce an in-plane exchange Zeeman-field $H_{\text{exch.}}$, and a spin-dependent tunneling $t_{s,\perp}$. In a simple perturbative mean-field treatment, $\mu_B H_{\text{exch.}} = t_{s,\perp}$.

Without loss of generality, we can work in the basis where the buffer layer Hamiltonian is diagonalized $\mathbf{h}^{\text{m}} = \text{diag}\{h_{\uparrow}^{\text{m}}, h_{\downarrow}^{\text{m}}\}$, where \uparrow and \downarrow indicate the spin components parallel and antiparallel to the *in-plane ferromagnetic moment direction*. For simplicity we assume $h_{\uparrow}^{\text{m}}, h_{\downarrow}^{\text{m}}$ each contains a single band, which can be easily generalized to multi-band cases.

In the absence of the middle layer, we consider the spinful TMD bilayer Hamiltonian $\mathbf{h}^{\text{bilayer}} = \text{diag}\{\mathbf{h}^{\text{t}}(\mathbf{k}), \mathbf{h}^{\text{b}}(\mathbf{k})\}$. The full Hamiltonian for the trilayer system is then:

$$H^{\text{trilayer}}(\mathbf{k}) = \begin{pmatrix} \mathbf{h}^{\text{t}}(\mathbf{k}) & & \\ & \mathbf{h}^{\text{b}}(\mathbf{k}) & \\ & & \mathbf{V} \end{pmatrix} \begin{pmatrix} & & \\ & & \\ & & \mathbf{V}^T \end{pmatrix} \begin{pmatrix} & & \\ & h_{\uparrow}^{\text{m}} & \\ & & h_{\downarrow}^{\text{m}} \end{pmatrix}, \quad (5.21)$$

where $\mathbf{V} = (\mathbf{V}_1, \mathbf{V}_2)$, $\mathbf{V}_1 = (t_{\uparrow}^{\text{t}}, 0, t_{\uparrow}^{\text{b}}, 0)^T$, and $\mathbf{V}_2 = (0, t_{\downarrow}^{\text{t}}, 0, t_{\downarrow}^{\text{b}})^T$.

Due to the $z \rightarrow -z$ mirror symmetry for the TMD bilayer at the zero twisting angle, one may assume these direct hoppings to be layer-independent $t_{\uparrow,\downarrow}^{\text{t,b}} = t_{\uparrow,\downarrow}$ at small twisting angles. Since the middle buffer layer is an insulator, $h_{\uparrow}^{\text{m}}, h_{\downarrow}^{\text{m}}$ are high energy states. Standard perturbation theory gives

$$\begin{aligned} H_{\text{induced}}^{\text{bilayer}}(\mathbf{k}) &\simeq \mathbf{h}^{\text{bilayer}} - \sum_{i=1,2} \mathbf{V}_i (\mathbf{h}^{\text{m}})^{-1} \mathbf{V}_i^T \\ &= \mathbf{h}^{\text{bilayer}} - \frac{t_{\uparrow}^2}{h_{\uparrow}^{\text{m}}} \begin{pmatrix} 1 & 0 & 1 & 0 \\ 0 & 0 & 0 & 0 \\ 1 & 0 & 1 & 0 \\ 0 & 0 & 0 & 0 \end{pmatrix} - \frac{t_{\downarrow}^2}{h_{\downarrow}^{\text{m}}} \begin{pmatrix} 0 & 0 & 0 & 0 \\ 0 & 1 & 0 & 1 \\ 0 & 0 & 0 & 0 \\ 0 & 1 & 0 & 1 \end{pmatrix} \\ &= \mathbf{h}^{\text{bilayer}} - \delta\mu\sigma_0\nu_0 + t_{\perp}\sigma_0\nu_x + \mu_B H_{\text{exch.},z}\sigma_z\nu_0 + t_{s,\perp}\sigma_z\nu_x, \end{aligned} \quad (5.22)$$

where we separate out the second-order perturbation of bilayer Hamiltonian into four parts: the chemical potential shift $\delta\mu$, the spin-independent tunneling t_{\perp} , the (proximity-induced) Zeeman field $H_{\text{exch.}}$, and the spin-dependent tunneling $t_{s,\perp}$, where.

$$-\delta\mu = t_{\perp} = -\frac{1}{2} \left(\frac{t_{\uparrow}^2}{h_{\uparrow}^{\text{m}}} + \frac{t_{\downarrow}^2}{h_{\downarrow}^{\text{m}}} \right), \quad (5.23)$$

$$\mu_B H_{\text{exch.}} = t_{s,\perp} = -\frac{1}{2} \left(\frac{t_{\uparrow}^2}{h_{\uparrow}^{\text{m}}} - \frac{t_{\downarrow}^2}{h_{\downarrow}^{\text{m}}} \right). \quad (5.24)$$

5.C Details of the phase diagram calculations and discussions on the stacking-dependence

All phase diagrams of the proposed heterostructures involving either 2H-NbSe₂ or 2H-TaS₂ are obtained by listing the gap size for all eight nodes (topological and trivial) and picking out the *minima* of them. To capture the physics among entire phase-diagrams (particularly the large- $H_{\text{exch.}}$ regions), we follow Ref.[211] to introduce the pair breaking equation throughout our numerical calculation

$$\ln(T_c/T_{c0}) + \psi \left(\frac{1}{2} + \frac{\mu_B H^2 / H_{\text{so}}}{2\pi k_B T_c} \right) - \psi(1/2) \equiv 0,$$

where ψ is the digamma function, T_{c0} is the zero-field critical temperature (3.0K for NbSe₂ [211] and 3.4K for TaS₂ [230]), and H_{so} can be taken as a fitting parameter to match the asymptotic Ginzberg-Landau behavior $H \sim H_0 \sqrt{1 - T/T_{c0}}$ for $T_c \sim T_{c0}$, where $H_0 \sim \sqrt{H_{\text{so}} H_p}$ and the Pauli limit $H_p = \frac{\Delta_0}{\sqrt{2}\mu_B} = (1.86 \text{ T/K}) \cdot T_{c0}$ assuming the g -factor equals to 2 and the BCS formula $\Delta_0 = 1.76k_B T_{c0}$ still to hold³. The best fitting of experimental data gives $H_0 = 43.6\text{T}$ for NbSe₂ and $H_0 = 65.6\text{T}$ for TaS₂ [195], so we take $H_{\text{so}}^{\text{NbSe}_2} = 340\text{T}$ and $H_{\text{so}}^{\text{TaS}_2} = 680\text{T}$ throughout our numerical calculations.

³For few-layer TaS₂, the relation is also reported to be $\Delta_0 = 2.2k_B T_{c0}$ in <https://www.nature.com/articles/s41563-018-0061-1>. Since such coefficient is material- and stacking-dependent, we will still take the value of BCS approximation $\Delta_0 = 1.76k_B T_{c0}$ as a demonstration.

All parameters we input in our numerical calculations of phase diagrams (up to fourth-order of $\mathbf{k} \cdot \mathbf{p}$ expansion) are extracted from the monolayer tight-binding models obtained from LDA calculation by QUANTUM ESPRESSO [231, 232] and Wannier90 routine [233]. Our strategies is to first build a AA-stacking β -bilayer slab system for both materials, then relax the structure with non-local van de Waals correlation functionals to get the proper layer distance and (spin-independent) tunneling strengths. For convergence reasons, we choose to use the functional vdW-DF-C6 [234, 235] for TaS₂ while vdW-DF2-C09 [236, 237] for NbSe₂. The resulting relaxed layer separation is $d_{\perp}^{\text{TaS}_2} = 6.57\text{\AA}$ and $d_{\perp}^{\text{NbSe}_2} = 6.80\text{\AA}$. Since tunneling processes only occur around the interesction points P , with their strengths to be half of the energy splitting around the Fermi energy ε_F , we can directly read them out from the the non self-consistent output at $\mathbf{k} = (k_F, 0)$, reading $t_{\perp}^{\text{TaS}_2} = 56.9\text{meV}$ and $t_{\perp}^{\text{NbSe}_2} = 116.2\text{meV}$.

Next, we take the relaxed structure as an input to build a monolayer slab system and perform a LDA calculation to obtain a monolayer electronic structure. Note that this monolayer relaxed structure weakly breaks the $z \rightarrow -z$ symmetry, but preserves the mirror planes parallel with the z -axis. The LDA result is used to fit the $\mathbf{k} \cdot \mathbf{p}$ model up to quartic order. More precisely, we fit the model consistent with the $y \rightarrow -y$ mirror symmetry:

$$H_{\text{quartic}}^{\text{mono}}(\mathbf{k}) = \left[\varepsilon_F + v_F k_x + ak_y^2 + p_5 k_x^2 + p_6 k_x k_y^2 \right. \\ \left. + p_7 k_y^4 + p_8 k_x^3 + p_9 k_x^4 + p_{10} k_x^2 k_y^2 \right] \sigma_0 \\ + p_{11} \sigma_y + \left[v_{\text{Ising}} k_y + p_{13} k_x k_y + p_{14} k_y^3 \right. \\ \left. + p_{15} k_x^2 k_y + p_{16} k_x^3 k_y + p_{17} k_x k_y^3 \right] \sigma_z. \quad (5.25)$$

The results for both TaS₂ and NbSe₂ are listed as following: (in the eV-\text{\AA} unit system and we set $\hbar = 1$, as a complement of the TABLE.5.1 given in the main text)

Materials	Coef. p_i	k_F	v_F	a	p_5	p_6	p_7	p_8	p_9
		0.54	-2.89	0.25	2.34	17.82	-8.72	11.53	-8.67
NbSe ₂	Coef. p_i	0.48	-2.22	-0.76	1.36	15.10	-2.98	9.85	-0.76
		17.20	0.00	0.36	1.41	-1.06	-0.72	-2.11	-8.45
Materials	Coef. p_i	p_{10}	p_{11}	v_{Ising}	p_{13}	p_{14}	p_{15}	p_{16}	p_{17}
		26.15	0.00	0.12	0.86	-0.20	0.25	-3.56	-4.14

The intrinsic Rashba SOC, ignored in Eq.(5.4), appears as the vanishingly small p_{11} in the above fitting. Due to the loss of the $z \rightarrow -z$ mirror symmetry in the vdW relaxed structure, in principle this coupling may be nonzero. However, we find that the raw energy splittings (corresponding to $2p_{11}$) at the point- P is less than 10^{-10}meV for both NbSe₂ and TaS₂, and conclude that weak vdW interactions cannot lead to any sizable

intrinsic Rashba SOC.

The values of aforementioned spin-independent tunnelings t_{\perp} for bilayer NbSe₂ and TaS₂ are far beyond the topological superconducting regime that we find in the numerical phase diagrams. That actually motivates us to propose the buffer layer heterostructures in FIG. 5.1. To have an estimation on the magnitude of the spin-independent tunneling t_{\perp} after the insertion of an insulating buffer layer, we build a trilayer slab system TaS₂/WS₂/TaS₂ of ABA and AAA stackings. Since 2H-TaS₂ and 2H-WS₂ have similar lattice constants, we use the lattice constants of 2H-TaS₂ for the trilayer system without enlarging the supercell ⁴ ($a = 0.331\text{nm}$ and $c = 0.121\text{nm}$ for 2H-TaS₂, and $a = 0.315\text{nm}$ and $c = 0.121\text{nm}$ for 2H-WS₂). We then again relax the positions for all atoms of the trilayer system with the non-local van der Waals functional vdW-DF-C6 [234, 235] along the out-of-plane direction. We find, after an inserting of a non-magnetic buffer layer WS₂, the separation between top and bottom TaS₂ layers for both stackings almost doubles to $d_{\perp}^{\text{TaS}_2,\text{ABA}} = 12.00\text{\AA}$ and $d_{\perp}^{\text{TaS}_2,\text{AAA}} = 13.18\text{\AA}$, and the corresponding strengths of the spin-independent tunneling reduce to $t_{\perp}^{\text{TaS}_2,\text{ABA}} = 5.0\text{meV}$ and $t_{\perp}^{\text{TaS}_2,\text{AAA}} = 4.5\text{meV}$.

5.D Details of analytical perturbative calculations

We will work with the atomic units by default throughout the derivation here. For example, $\hbar = \mu_B = 1$.

5.D.1 Perturbative theory for $\sqrt{(v_{\text{Ising}}k_F\theta)^2 + 4t_{\perp}^2} \gg \Delta$: $C = 12$ Topological Phases

In this section, we will give a perturbative analysis on the twisted bilayer Hamiltonian given in the main text. We will focus on the regime when $\sqrt{(v_{\text{Ising}}k_F\theta)^2 + 4t_{\perp}^2} \gg \Delta$ and give an explanation on the origin of $C = \pm 12$ topological phases. Mass gaps for all nodes and the phase boundary will also be also derived.

5.D.1.1 Construction of Hamiltonian

Let us start with constructing the effective Hamiltonian. We will consider a small twisting angle θ , and keep the $\mathbf{k} \cdot \mathbf{p}$ expansion up to $\mathcal{O}(\theta^2)$ (the reason will be given in the next subsection). As is discussed in the main text, in-plane mirror symmetry prohibit the existence of Rashba SOC, so the monolayer effective Hamiltonian around the intersection point P of the Fermi surface and the Γ - M line simply reads

$$h^{\text{mono}}(\mathbf{k}) = (v_F k_x + a k_y^2) + v_{\text{Ising}} k_y \sigma_z, \quad (5.26)$$

where a is the coefficient of $\mathbf{k} \cdot \mathbf{p}$ expansion. We keep a quadratic term $a k_y^2$ here because it turns out that this term contributes to the leading order deviation from the linear $\mathbf{k} \cdot \mathbf{p}$ expansion. Equation (5.26) can be easily extend to higher orders and we did use the fitting fourth-order $\mathbf{k} \cdot \mathbf{p}$ in our numerical calculations, see section V.

⁴We use the crystalline data from Springer Materials, see https://materials.springer.com/isp/crystallographic/docs/sd_0457067 and https://materials.springer.com/isp/crystallographic/docs/sd_0551013.

Without loss of generality, we can consider a bilayer system with the top layer rotated by $\theta/2$, and the bottom layer rotated by $-\theta/2$. This is achieved by simple replacement $k_x \mapsto (k_x + k_F) \cos \frac{\theta}{2} \pm k_y \sin \frac{\theta}{2} - k_F$ and $k_y \mapsto \mp(k_x + k_F) \sin \frac{\theta}{2} + k_y \cos \frac{\theta}{2}$ and expansion still up to θ^2 . The resulting bilayer Hamiltonian *without tunneling* is then

$$\begin{aligned} h^{\text{bilayer w/o tunneling}}(\mathbf{k}) &= \left(v_F k_x + a k_y^2 + \frac{a k_F^2}{4} \theta^2 - \frac{v_F k_F}{8} \theta^2 \right) + \left(-a k_F k_y \theta + \frac{\theta}{2} v_F k_y \right) \nu_z \\ &\quad + v_{\text{Ising}} k_y \sigma_z - v_{\text{Ising}} k_F \frac{\theta}{2} \sigma_z \nu_z \\ &= \left(v_F k_x + a k_y^2 - \frac{v_2 k_F}{8} \theta^2 \right) + \frac{\theta}{2} v_2 k_y \nu_z + v_{\text{Ising}} k_y \sigma_z \\ &\quad - \frac{\theta}{2} v_{\text{Ising}} k_F \sigma_z \nu_z, \end{aligned} \tag{5.27}$$

where ν_i are Pauli matrices within the layer space and we defined

$$v_2 \equiv v_F - 2a k_F. \tag{5.28}$$

In Eq.(5.27), the crucial role played by v_2 is due to the second term, which gives the leading order correction to the wavefunctions comparing with the linear $\mathbf{k} \cdot \mathbf{p}$ expansion. Next, let us try to add interlayer tunnelings to (5.27). Based on *two-center approximation* [44], it can be shown that (see in Appendix 5.B) the interlayer tunneling have a weak spatial-dependence and will be considered as a constant here $t = t_{\perp}$ (we will consider the spin-dependent tunnelings $t_{s,\perp}$ later). We thus have

$$\begin{aligned} h^{\text{bilayer}} &= \left(v_F k_x + a k_y^2 - \frac{v_2 k_F^2}{8} \theta^2 \right) \\ &\quad + \frac{\theta}{2} v_2 k_y \nu_z + v_{\text{Ising}} k_y \sigma_z - \frac{\theta}{2} v_{\text{Ising}} k_F \sigma_z \nu_z + t \nu_x. \end{aligned} \tag{5.29}$$

Hamiltonian (5.29) reduce to simple two-band model [238] (so can be readily diagonalized) for $\sigma_z = \pm 1$. Keeping up to $\mathcal{O}(\theta^2)$, we have, for $\sigma_z = +1$,

$$\varepsilon_{\pm}^{\uparrow} = \left(v_F k_x + a k_y^2 - \frac{\theta^2}{8} v_2 k_F \right) + v_{\text{Ising}} k_y \pm \frac{\Gamma}{2} \left[1 - \frac{v_2 \cdot \cos^2 \xi}{v_{\text{Ising}} k_F} k_y \right]$$

and for $\sigma_z = -1$,

$$\varepsilon_{\pm}^{\downarrow} = \left(v_F k_x + a k_y^2 - \frac{\theta^2}{8} v_2 k_F \right) - v_{\text{Ising}} k_y \pm \frac{\Gamma}{2} \left[1 + \frac{v_2 \cdot \cos^2 \xi}{v_{\text{Ising}} k_F} k_y \right],$$

where

$$\xi \equiv \arctan \frac{2t}{v_{\text{Ising}} k_F \theta}, \quad \text{and} \quad \Gamma \equiv \sqrt{(v_{\text{Ising}} k_F \theta)^2 + 4t^2}.$$

There are some crossing points between the spin-up and spin-down Fermi surfaces. Solving $\varepsilon_{\pm}^{\uparrow} = \varepsilon_{\pm}^{\downarrow} = 0$,

we find two such points F and G along the k_x direction (Γ - M line)

$$F = \left(-\frac{\Gamma}{2v_F} + \frac{v_2 k_F \theta^2}{8v_F}, 0 \right), \quad G = \left(+\frac{\Gamma}{2v_F} + \frac{v_2 k_F \theta^2}{8v_F}, 0 \right). \quad (5.30)$$

At F , the two low energy bands come from $\varepsilon_-^{\uparrow,\downarrow}$, while at G , the two low energy bands are formed by $\varepsilon_+^{\uparrow,\downarrow}$. Interestingly, there are another two such points C and D emergent along the k_y -direction that have different low-energy bands information. We also have

$$C = \left(-\frac{k_F \theta^2}{8} - \frac{at^2}{v_F v_{\text{Ising}}^2}, -\frac{\Gamma}{2v_{\text{Ising}}} \right), \quad (5.31)$$

$$D = \left(-\frac{k_F \theta^2}{8} - \frac{at^2}{v_F v_{\text{Ising}}^2}, +\frac{\Gamma}{2v_{\text{Ising}}} \right). \quad (5.32)$$

At C , the two low-energy bands are formed by $\varepsilon_-^{\uparrow}, \varepsilon_+^{\downarrow}$, while at D , the two low-energy bands are formed by $\varepsilon_+^{\uparrow}, \varepsilon_-^{\downarrow}$. They are all illustrated in the main text. In the following derivation, we will denote the k -space coordinates of the intersection points F as F_+ , G as F_- , C as C_- , and D as C_+ .

The low-energy effective Hamiltonian of each node is then the projection of (5.29) onto these bands. First of all, we need to read out the eigenstates in ν -space. Introducing the elevation angle

$$\begin{aligned} \xi_{\pm} &= \arctan \frac{t}{\frac{\theta}{2}(v_2 k_y - v_{\text{Ising}} k_F)} \\ &\simeq \arctan \left[\left(1 \pm \frac{v_2 k_y}{v_{\text{Ising}} k_F} \right) \frac{2t}{v_{\text{Ising}} k_F \theta} \right], \end{aligned}$$

we obtain:

$$\begin{aligned} \sigma_z = +1 : \quad |\nu_1\rangle &= \sin \frac{\xi_+}{2} |\nu_{\uparrow}\rangle + \cos \frac{\xi_+}{2} |\nu_{\downarrow}\rangle, \\ |\nu_2\rangle &= \cos \frac{\xi_+}{2} |\nu_{\uparrow}\rangle - \sin \frac{\xi_+}{2} |\nu_{\downarrow}\rangle, \\ \sigma_z = -1 : \quad |\nu_3\rangle &= \cos \frac{\xi_-}{2} |\nu_{\uparrow}\rangle + \sin \frac{\xi_-}{2} |\nu_{\downarrow}\rangle, \\ |\nu_4\rangle &= -\sin \frac{\xi_-}{2} |\nu_{\uparrow}\rangle + \cos \frac{\xi_-}{2} |\nu_{\downarrow}\rangle. \end{aligned}$$

We can then lift (5.29) into Nambu representation

$$H^{\text{bilayer}} = \left(v_F k_x + a k_y^2 - \frac{v_2 k_F \theta^2}{8} \right) \tau_z + \frac{\theta}{2} v_2 k_y \nu_z \tau_z + v_{\text{Ising}} k_y \sigma_z - \frac{\theta}{2} v_{\text{Ising}} k_F \sigma_z \nu_z + t \nu_x \tau_z, \quad (5.33)$$

and perform the projection. Here ν_i are Pauli matrices for the Nambu space.

Choosing the basis as following

$$\begin{aligned} \text{At } G : \quad &\{|\tau_{\uparrow}, \sigma_{\uparrow}, \nu_2\rangle, |\tau_{\uparrow}, \sigma_{\downarrow}, \nu_4\rangle, |\tau_{\downarrow}, \sigma_{\uparrow}, \nu_4\rangle, |\tau_{\downarrow}, \sigma_{\downarrow}, \nu_2\rangle, |\tau_{\uparrow}, \sigma_{\uparrow}, \nu_1\rangle, |\tau_{\uparrow}, \sigma_{\downarrow}, \nu_3\rangle, \\ &|\tau_{\downarrow}, \sigma_{\uparrow}, \nu_3\rangle, |\tau_{\downarrow}, \sigma_{\downarrow}, \nu_1\rangle\}, \end{aligned}$$

At F : $\{|\tau_\uparrow, \sigma_\uparrow, \nu_1\rangle, |\tau_\uparrow, \sigma_\downarrow, \nu_3\rangle, |\tau_\downarrow, \sigma_\uparrow, \nu_3\rangle, |\tau_\downarrow, \sigma_\downarrow, \nu_1\rangle, |\tau_\uparrow, \sigma_\uparrow, \nu_2\rangle, |\tau_\uparrow, \sigma_\downarrow, \nu_4\rangle, |\tau_\downarrow, \sigma_\uparrow, \nu_4\rangle, |\tau_\downarrow, \sigma_\downarrow, \nu_2\rangle\},$

At D : $\{|\tau_\uparrow, \sigma_\uparrow, \nu_2\rangle, |\tau_\uparrow, \sigma_\downarrow, \nu_3\rangle, |\tau_\downarrow, \sigma_\uparrow, \nu_3\rangle, |\tau_\downarrow, \sigma_\downarrow, \nu_2\rangle, |\tau_\uparrow, \sigma_\uparrow, \nu_1\rangle, |\tau_\uparrow, \sigma_\downarrow, \nu_4\rangle, |\tau_\downarrow, \sigma_\uparrow, \nu_4\rangle, |\tau_\downarrow, \sigma_\downarrow, \nu_1\rangle\},$

At C : $\{|\tau_\uparrow, \sigma_\uparrow, \nu_1\rangle, |\tau_\uparrow, \sigma_\downarrow, \nu_4\rangle, |\tau_\downarrow, \sigma_\uparrow, \nu_4\rangle, |\tau_\downarrow, \sigma_\downarrow, \nu_1\rangle, |\tau_\uparrow, \sigma_\uparrow, \nu_2\rangle, |\tau_\uparrow, \sigma_\downarrow, \nu_3\rangle, |\tau_\downarrow, \sigma_\uparrow, \nu_3\rangle, |\tau_\downarrow, \sigma_\downarrow, \nu_2\rangle\},$

then (5.33) near F and G can be shown to have the form

$$H_0(\mathbf{F}_\pm) = v_F \delta k_x \tau_z + v_{\text{Ising}} \delta k_y \sigma_z \pm \Gamma \frac{1 - \nu_z}{2} \tau_z. \quad (5.34)$$

Similarly near \mathbf{C}_\pm we have

$$H_0(\mathbf{C}_\pm) = v_F \delta k_x \tau_z + v_{\text{Ising}} \delta k_y \sigma_z \pm \Gamma \frac{1 - \nu_z}{2} \sigma_z. \quad (5.35)$$

Here we slightly abuse the notation: instead of introducing a new symbol, we use the ν -Pauli matrices to represent the low ($\nu_z = 1$) and high ($\nu_z = -1$) energy subspaces.

5.D.1.2 Low-energy Effective Theory in Nambu Space

The next step is to turn on an in-plane Zeeman exchange field and the intra-layer superconducting order parameters Δ . With out loss of generality, below we consider the in-plane Zeeman field to be along the k_y direction: $\mathbf{b} = (0, b_y)$, together with a *spin-dependent hopping* $t_{s,\perp} = t_y$ due to a ferromagnetic layer:

$$H' = b_y \sigma_y + \Delta \cos \frac{\varphi}{2} \cdot \sigma_y \tau_y + \Delta \sin \frac{\varphi}{2} \cdot \sigma_y \tau_x \nu_z + t_y \sigma_y \nu_x. \quad (5.36)$$

Here Δ is real and we add a Josephson phase difference φ between the top and bottom layer through turning on the super-current.

Still taking the basis we chose for the low-energy space for each node in the former section, we have

$$\begin{aligned} H'(\mathbf{F}_+) &= -b_y \sin \xi \cdot \sigma_y \nu_z + \Delta \cos \frac{\varphi}{2} \cdot \sigma_y \tau_y + \Delta \cos \xi \sin \frac{\varphi}{2} \cdot \sigma_x \tau_y \nu_z \\ &\quad + b_y \cos \xi \cdot \sigma_y \nu_x + \Delta \sin \xi \sin \frac{\varphi}{2} \cdot \sigma_x \tau_y \nu_x + t_y \sigma_y, \end{aligned} \quad (5.37)$$

$$\begin{aligned} H'(\mathbf{F}_+) &= b_y \sin \xi \cdot \sigma_y \nu_z + \Delta \cos \frac{\varphi}{2} \cdot \sigma_y \tau_y - \Delta \cos \xi \sin \frac{\varphi}{2} \cdot \sigma_x \tau_y \nu_z \\ &\quad + b_y \cos \xi \cdot \sigma_y \nu_x + \Delta \sin \xi \sin \frac{\varphi}{2} \cdot \sigma_x \tau_y \nu_x + t_y \sigma_y. \end{aligned} \quad (5.38)$$

And for \mathbf{C}_\pm :

$$H'(\mathbf{C}_+) = b_y \cos \xi \cdot \sigma_y + \Delta \cos \frac{\varphi}{2} \cdot \sigma_y \tau_y + \Delta \cos \xi \sin \frac{\varphi}{2} \cdot \sigma_y \tau_x \nu_z$$

$$\begin{aligned}
& - b_y \sin \xi \cdot \sigma_x \tau_z \nu_y + \Delta \sin \xi \sin \frac{\varphi}{2} \cdot \sigma_x \tau_y \nu_x \\
& - \frac{\Delta}{2v_{\text{Ising}}} \sin^2 \xi \sin \frac{\varphi}{2} \cdot v_2 \theta \cdot \sigma_x \tau_y \nu_z + \frac{\Delta}{2v_{\text{Ising}}} \cos \xi \sin \xi \sin \frac{\varphi}{2} \cdot v_2 \theta \cdot \sigma_y \tau_x \nu_x \\
& - \frac{t_y}{2v_{\text{Ising}}} \sin \xi \cdot v_2 \theta \cdot \sigma_y \nu_z + t_y \sigma_y \nu_x,
\end{aligned} \tag{5.39}$$

$$\begin{aligned}
H'(\mathbf{C}_-) = & b_y \cos \xi \cdot \sigma_y + \Delta \cos \frac{\varphi}{2} \cdot \sigma_y \tau_y - \Delta \cos \xi \sin \frac{\varphi}{2} \cdot \sigma_y \tau_x \nu_z \\
& + b_y \sin \xi \cdot \sigma_x \tau_z \nu_y + \Delta \sin \xi \sin \frac{\varphi}{2} \cdot \sigma_x \tau_y \nu_x \\
& - \frac{\Delta}{2v_{\text{Ising}}} \sin^2 \xi \sin \frac{\varphi}{2} \cdot v_2 \theta \cdot \sigma_x \tau_y \nu_z - \frac{\Delta}{2v_{\text{Ising}}} \cos \xi \sin \xi \sin \frac{\varphi}{2} \cdot v_2 \theta \cdot \sigma_y \tau_x \nu_x \\
& - \frac{t_y}{2v_{\text{Ising}}} \sin \xi \cdot v_2 \theta \cdot \sigma_y \nu_z + t_y \sigma_y \nu_x.
\end{aligned} \tag{5.40}$$

The effective Hamiltonian for the low-energy sector $|\nu_\uparrow\rangle$ then can be obtained from standard perturbation theory. We will keep the θ -linear-order and the Δ -second-order. Since both θ and Δ are small, we will drop terms proportional to $\Delta^2 \theta$. Finally:

$$\begin{aligned}
H_{\text{eff}}(\mathbf{F}_\pm) = & v_F \delta k_x \tau_z + v_{\text{Ising}} \delta k_y \sigma_z \mp (b_y \sin \xi \mp t_y) \cdot \sigma_y + \Delta \cos \frac{\varphi}{2} \cdot \sigma_y \tau_y \pm \Delta \cos \xi \sin \frac{\varphi}{2} \cdot \sigma_x \tau_y \\
& \pm \frac{1}{\Gamma} \left[\left[-b_y^2 \cos^2 \xi + \Delta^2 \sin^2 \frac{\varphi}{2} \sin^2 \xi \right] \tau_z + b_y \Delta \sin \frac{\varphi}{2} \sin 2\xi \sigma_z \tau_x \right],
\end{aligned} \tag{5.41}$$

$$\begin{aligned}
H_{\text{eff}}(\mathbf{C}_\pm) = & v_F \delta k_x \tau_z + v_{\text{Ising}} \delta k_y \sigma_z + b_y \cos \xi \cdot \sigma_y + \Delta \cos \frac{\varphi}{2} \cdot \sigma_y \tau_y \pm \Delta \cos \xi \sin \frac{\varphi}{2} \cdot \sigma_y \tau_x \\
& - \frac{\Delta v_2 \theta}{2v_{\text{Ising}}} \sin^2 \xi \sin \frac{\varphi}{2} \sigma_x \tau_y - \frac{t_y \cdot v_2 \theta}{2v_{\text{Ising}}} \sin \xi \cdot \sigma_y \\
& \pm \frac{1}{\Gamma} \left[[b_y^2 + \Delta^2 \sin^2 \xi] \sin^2 \xi \cdot \sigma_z \pm 2b_y \Delta \sin^2 \xi \sin \frac{\varphi}{2} \cdot \sigma_z \tau_x + t_y^2 \sigma_z \mp 2b_y t_y \sin \xi \cdot \tau_z \right].
\end{aligned} \tag{5.42}$$

5.D.1.3 Topological Nodes C and D

Let us first focus on the node C and D , i.e., $\mathbf{k} \sim \mathbf{C}_\pm$. It is convenient to perform a charge rotation $e^{\pm i\zeta/2\tau_z}$ to eliminate the $\pm \Delta \cos \xi \sin \frac{\varphi}{2} \cdot \sigma_y \tau_x$ term in (5.42) with $\zeta \equiv \arctan(\cos \xi \tan \frac{\varphi}{2})$. In addition, the σ_y term (and τ_z term) can be absorbed by redefining δk_y (and δk_x). Using $e^{-i\zeta/2\tau_z} \tau_y e^{i\zeta/2\tau_z} = \cos \zeta \cdot \tau_y - \sin \zeta \cdot \tau_x$, we will arrive at

$$\begin{aligned}
\tilde{H}_{\text{eff}}(\mathbf{C}_\pm) = & v_F \delta k_x \tau_z + v_{\text{Ising}} \delta k_y \sigma_z + \left[b_y^{\text{origin.}} \cos \xi - \frac{t_y \cdot v_2 \theta}{2v_{\text{Ising}}} \sin \xi \right] \cdot \sigma_y + \tilde{\Delta} \cdot \sigma_y \tau_y \\
& - \frac{\Delta v_2 \theta}{2v_{\text{Ising}}} \sin^2 \xi \sin \frac{\varphi}{2} \cdot \sigma_x \cdot (\cos \zeta \tau_y \mp \sin \zeta \tau_x) + \frac{2b_y \Delta}{\Gamma} \sin^2 \xi \sin \frac{\varphi}{2} \cdot \sigma_z (\cos \zeta \cdot \tau_x \pm \sin \zeta \cdot \tau_y), \\
= & v_F \delta k_x \tau_z + v_{\text{Ising}} \delta k_y \sigma_z + b_y \cos \xi \cdot \sigma_y + \tilde{\Delta} \cdot \sigma_y \tau_y \\
& - \frac{\Delta v_2 \theta}{2v_{\text{Ising}}} \sin^2 \xi \sin \frac{\varphi}{2} \cdot \sigma_x \cdot (\cos \zeta \tau_y \mp \sin \zeta \tau_x) + \frac{2b_y \Delta}{\Gamma} \sin^2 \xi \sin \frac{\varphi}{2} \cdot \sigma_z (\cos \zeta \cdot \tau_x \pm \sin \zeta \cdot \tau_y),
\end{aligned} \tag{5.43}$$

with $\tilde{\Delta} = \Delta \sqrt{\cos^2 \frac{\varphi}{2} + \sin^2 \frac{\varphi}{2} \cos^2 \xi} \equiv \Delta \frac{\cos \frac{\varphi}{2}}{\cos \zeta}$. In (5.43) we have denoted the original magnetic fields b_y as $b_y^{\text{origin.}}$ and rewritten the σ_y term as $b_y \cos \xi$ by introducing a new shifted field (this is why we introduce the

spin-dependent tunneling together with the the magnetic fields)

$$b_y \equiv b_y^{\text{origin.}} - \frac{t_y \cdot v_2 \theta}{2v_{\text{Ising}}} \tan \xi = b_y^{\text{origin.}} - \frac{t_y \cdot v_2 t}{v_{\text{Ising}}^2 k_F}.$$

Starting with the linear-order effective Hamiltonian (the first line of (5.43), so C_{\pm} has the same form), we find that a pair of Dirac nodes $\mathbf{k}_0^{\pm} = (\pm k_{x,0}^+, 0)$ along the δk_x direction emerges when $b_y \cos \xi > \tilde{\Delta}$. Repeating the two-band effective theory analysis (separating for $\sigma_y = \pm 1$), we find, near the \mathbf{k}_0^{\pm} Dirac nodes:

$$h_{\text{eff}\pm}^{\pm}(\mathbf{C}) = \pm(-v_F \cos \theta^+ \cdot \delta k_x \mu_z + v_{\text{Ising}} \sin \theta^+ \cdot \delta k_y \mu_x), \quad (5.44)$$

where

$$\theta^+ = \arctan \frac{\tilde{\Delta}}{v_F k_{x,0}^+}, \quad k_{x,0}^+ = \frac{1}{v_F} \sqrt{(b_y \cos \xi)^2 - \tilde{\Delta}^2}$$

These effective theories are obtained in the basis:

$$\begin{aligned} |\psi_1^+\rangle &= |\sigma_y = 1\rangle \otimes (i \sin \frac{\theta^+}{2} |\tau_z, \uparrow\rangle + \cos \frac{\theta^+}{2} |\tau_z, \downarrow\rangle), \\ |\psi_2^+\rangle &= |\sigma_y = -1\rangle \otimes (\cos \frac{\theta^+}{2} |\tau_z, \uparrow\rangle - i \sin \frac{\theta^+}{2} |\tau_z, \downarrow\rangle), \\ |\psi_1^-\rangle &= |\sigma_y = 1\rangle \otimes (\cos \frac{\theta^+}{2} |\tau_z, \uparrow\rangle - i \sin \frac{\theta^+}{2} |\tau_z, \downarrow\rangle), \\ |\psi_2^-\rangle &= |\sigma_y = -1\rangle \otimes (i \sin \frac{\theta^+}{2} |\tau_z, \uparrow\rangle + \cos \frac{\theta^+}{2} |\tau_z, \downarrow\rangle). \end{aligned}$$

To be concrete, states $|\sigma_y = \pm 1\rangle$ are defined as $|\sigma_y = 1\rangle = \frac{1}{\sqrt{2}}(|\sigma_z, \uparrow\rangle + i|\sigma_z, \downarrow\rangle)$ and $|\sigma_y = -1\rangle = \frac{1}{\sqrt{2}}(i|\sigma_z, \uparrow\rangle + |\sigma_z, \downarrow\rangle)$.

The left task to project the last line of (5.43) (as perturbation) onto these low-energy basis. We get, for C_+ ,

$$\begin{aligned} \text{At } \mathbf{k}_0^+ : & \frac{\Delta v_2 \theta}{2v_{\text{Ising}}} \sin^2 \xi \sin \frac{\varphi}{2} (\sin \zeta \cos \theta^+ \mu_x + \cos \zeta \mu_y) \\ & + \frac{2b_y \Delta}{\Gamma} \sin^2 \xi \sin \frac{\varphi}{2} \cdot (-\cos \zeta \cos \theta^+ \mu_y - \sin \zeta \mu_x), \end{aligned} \quad (5.45)$$

$$\begin{aligned} \text{At } \mathbf{k}_0^- : & \frac{\Delta v_2 \theta}{2v_{\text{Ising}}} \sin^2 \xi \sin \frac{\varphi}{2} (\sin \zeta \cos \theta^+ \mu_x - \cos \zeta \mu_y) \\ & + \frac{2b_y \Delta}{\Gamma} \sin^2 \xi \sin \frac{\varphi}{2} \cdot (-\cos \zeta \cos \theta^+ \mu_y + \sin \zeta \mu_x) \end{aligned} \quad (5.46)$$

and for C_- ,

$$\begin{aligned} \text{At } \mathbf{k}_0^+ : & \frac{\Delta v_2 \theta}{2v_{\text{Ising}}} \sin^2 \xi \sin \frac{\varphi}{2} (-\sin \zeta \cos \theta^+ \mu_x + \cos \zeta \mu_y) \\ & + \frac{2b_y \Delta}{\Gamma} \sin^2 \xi \sin \frac{\varphi}{2} \cdot (-\cos \zeta \cos \theta^+ \mu_y + \sin \zeta \mu_x), \end{aligned} \quad (5.47)$$

$$\begin{aligned} \text{At } \mathbf{k}_0^- : & \frac{\Delta v_2 \theta}{2v_{\text{Ising}}} \sin^2 \xi \sin \frac{\varphi}{2} (-\sin \zeta \cos \theta^+ \mu_x - \cos \zeta \mu_y) \\ & + \frac{2b_y \Delta}{\Gamma} \sin^2 \xi \sin \frac{\varphi}{2} \cdot (-\cos \zeta \cos \theta^+ \mu_y - \sin \zeta \mu_x). \end{aligned} \quad (5.48)$$

The new μ_x -terms brought by perturbation just shift the nodes, while the new μ_y -terms brought by perturbation open gaps. Collecting all μ_y -terms, we get the four masses m_{\pm} (each value is two-fold degenerate) for the nodes split from point intersection points C and D :

$$m_{\pm}(C_{\pm}) = \frac{2b_y\Delta}{\Gamma} \sin^2 \xi \sin \frac{\varphi}{2} \cos \zeta \cos \theta^{+} \\ \times \left(1 \pm \frac{c\theta\Gamma}{4b_y v_{\text{Ising}} \cos \theta^{+}} \right) \equiv m(1 \pm \delta). \quad (5.49)$$

Clearly it is the dimensionless number $\delta \equiv \frac{c\theta\Gamma}{4b_y v_{\text{Ising}} \cos \theta^{+}}$ that dominates the topology around C_{\pm} . If $|\delta| < 1$, we find all four Dirac nodes generate masses of *the same sign*, resulting in a total transfer of Chern Number ± 4 . In terms of the original parameters, such condition reduces to

$$v_2 t^2 < \Delta k_F v_{\text{Ising}}^2 a(\xi, \varphi) \sqrt{\left(\frac{b_y}{b_c^{\text{topo.}}} \right)^2 - 1}, \quad (5.50)$$

with

$$b_c^{\text{topo.}} \equiv \Delta \sqrt{\sec^2 \xi \cos^2 \frac{\varphi}{2} + \sin^2 \frac{\varphi}{2}}. \quad (5.51)$$

and

$$a(\xi, \varphi) = \tan \xi \sin \xi \sqrt{\sec^2 \xi \cos^2 \frac{\varphi}{2} + \sin^2 \frac{\varphi}{2}}.$$

As for the mass gap, in terms of original parameters, we have

$$m \equiv \frac{2b_y\Delta}{\Gamma} \sin^2 \xi \sin \frac{\varphi}{2} \cos \zeta \cos \theta^{+} \\ = \sin 2 \frac{\varphi}{2} \frac{\Delta^2 \sin^2 \xi}{v_{\text{Ising}} k_F \theta} \sqrt{\frac{(b_y/\Delta)^2}{\sec^2 \xi \cos^2 \frac{\varphi}{2} + \sin^2 \frac{\varphi}{2}} - 1} \\ \equiv \sin \varphi \frac{\Delta^2 \sin^2 \xi}{v_{\text{Ising}} k_F \theta} \sqrt{\left(\frac{b_y}{b_c^{\text{topo.}}} \right)^2 - 1}. \quad (5.52)$$

Recall that φ is the Josephson phase differences that we do no require to be small, so is $\xi = \arctan \frac{2t}{v_{\text{Ising}} k_F \theta}$. To have a meaningful topological gap, fraction b_y/Δ must be large enough so that the quantity inside the square root is positive definite. This requirement is satisfied for the two candidate NbSe₂ and TaS₂ we proposed in the main text — which support large in-plane magnetic fields that far beyond the Pauli limit.

5.D.1.4 Trivial Nodes F and G

Finally let us look at the intersection point F and G , i.e., $\mathbf{k} \sim \mathbf{F}_{\pm}$. Still we can absorb the last term of (5.41) by redefining δk_x . After that we get

$$\tilde{H}_{\text{eff}}(\mathbf{F}_{\pm}) = v_F \delta \tilde{k}_x \tau_z + v_{\text{Ising}} \delta k_y \sigma_z \mp (b_y^{\text{origin.}} \sin \xi \mp t_y) \cdot \sigma_y \\ + \Delta \cos \frac{\varphi}{2} \cdot \sigma_y \tau_y \pm \Delta \cos \xi \sin \frac{\varphi}{2} \cdot \sigma_x \tau_y$$

$$\pm \frac{1}{\Gamma} b_y^{\text{origin.}} \Delta \sin \frac{\varphi}{2} \sin 2\xi \sigma_z \tau_x \quad (5.53)$$

Without bothering to perform the projection one more time, as we have done for C_{\pm} , it's helpful to notice an effective ($\delta k_x \mapsto -\delta k_x$) mirror symmetry τ_y for the Δ -linear order effective Hamiltonian $\tilde{H}_{\text{eff}}(\mathbf{F}_{\pm})$. Therefore the total Chern number must vanishes for the effective theory of each intersection point (C and D). And the gap position can be easily solved from the first line of (5.53)

$$\tilde{k}_x = \pm \frac{1}{v_F} \sqrt{(b_y^{\text{origin.}} \sin \xi - t_y)^2 - \Delta^2 \cos^2 \frac{\varphi}{2}},$$

with the gap size

$$m(\mathbf{F}_{\pm}) = \Delta \cos \xi \sin \frac{\varphi}{2}. \quad (5.54)$$

As a side remark, if one includes on the second-order perturbation, it can be shown that the second-order gap is always much smaller than the linear-order gap (5.54) in the current perturbative regime.

5.D.2 A different perturbative regime: $C = 6$ Topological Phases

In this section we briefly discuss the Chern number $C = 6$ topological phases in a different perturbative regime. We start with the limit that the spin-independent hopping and the twisting angle both vanish: $t_{\perp} = 0, \theta = 0$. In addition, we let the spin-dependent hopping equal to the Zeeman exchange field: $t_y = b_y$ as in case-(i) in the main text.

Writing down the full linear order $k \cdot p$ BCS Hamiltonian near the point P :

$$\begin{aligned} H_{\text{BCS}}^{\text{bilayer}}(\mathbf{k}) = & v_F k_x \tau_z + v_{\text{Ising}} k_y \sigma_z + \cos \frac{\varphi}{2} \Delta \sigma_y \tau_y + \sin \frac{\varphi}{2} \Delta \sigma_y \tau_x \nu_z \\ & - v_{\text{Ising}} k_F \theta / 2 \sigma_z \nu_z + b_y \sigma_y + t_y \sigma_y \nu_x + t \tau_z \nu_x. \end{aligned} \quad (5.55)$$

Precisely speaking, our strategy is to firstly consider the situation of $t_y = b_y \sim \Delta$ with $t_{\perp} = 0, \theta = 0$, and finally turn on a small $t_{\perp} \ll \Delta$ and a small twisting angle $v_{\text{Ising}} k_F \theta \ll \Delta$ as perturbations. This exactly corresponds to the regime in the numerical phase diagrams where $C = 6$ is realized.

One way to see the origin of the $C = 6$ phase is to realize that when $t_y = b_y$, only the $\nu_x = 1$ subspace (a half of the bands) experiences the magnetism captured by the two terms $b_y \sigma_y + t_y \sigma_y \nu_x$. Therefore, instead of 4 topological Dirac nodes (corresponding to the $C = 12$ phase for the whole heterostructure), in the present situation Eqn.(5.55) only have 2 Dirac nodes emerging when $t_y = b_y$ is tuned up. After a small $t_{\perp} \ll \Delta$ and a small twisting angle $v_{\text{Ising}} k_F \theta \ll \Delta$ are turned on, these Dirac nodes receive topological mass gap and the $C = 6$ phase is realized.

5.E Two-center approximation

Given two Bloch states $|\psi_{\mathbf{k},\alpha}^{\text{u}}\rangle$ and $|\psi_{\mathbf{k}',\beta}^{\text{d}}\rangle$ from top and bottom layer with the crystal momentum \mathbf{k} and \mathbf{k}' and sublattice labels α and β , two-center approximation [44] tells that the tunneling strength between these

two states takes a general form of [239]

$$t_{\mathbf{k}, \mathbf{k}'}^{\alpha\beta} \equiv \langle \psi_{\mathbf{k}, \alpha}^{\text{u}} | H | \psi_{\mathbf{k}', \beta}^{\text{d}} \rangle = \frac{1}{V} \sum_{\mathbf{G}_1, \mathbf{G}_2} \delta_{\mathbf{k} + \mathbf{G}_1, \mathbf{k}' + \mathbf{G}_2} \cdot e^{-i\mathbf{G}_2 \cdot \boldsymbol{\tau}_{2\beta}} \cdot t^{\alpha\beta}(\mathbf{k} + \mathbf{G}_1) \cdot e^{i\mathbf{G}_1 \cdot \boldsymbol{\tau}_{1\alpha}} \quad (5.56)$$

if one expands the Block state with Wannier basis for each layer, i.e., $t^{\alpha\beta}(\mathbf{k} - \mathbf{G}_2) \equiv \langle \mathbf{R}_1 + \boldsymbol{\tau}_1 | H | \mathbf{R}_2 + \boldsymbol{\tau}_2 \rangle$ with $\boldsymbol{\tau}_{1,2}$ the sublattice vectors, and makes use of the Poisson resummation formula [240].

The allowed tunneling processes are constrained by the delta function in (5.56), while its concrete form mainly comes from the two exponentials. More concretely, let us consider the bilayer system with the top layer rotated by a small angle $\theta/2$, and the bottom layer rotated by $-\theta/2$, and focus on the region around the intersection point P : $\mathbf{k} = \mathbf{k}_P^{\text{t}} + \mathbf{F}^{\text{t}}$ and $\mathbf{k}' = \mathbf{k}_P^{\text{b}} + \mathbf{F}^{\text{b}}$ with $|\mathbf{F}^{\text{t,b}}| \ll 1$. Since the real-space tunneling $t(\mathbf{r}^{\text{t}} - \mathbf{r}^{\text{b}})$ is the function of the spatial separation of two Wannier states $\sqrt{(\mathbf{r}^{\text{t}} - \mathbf{r}^{\text{b}})^2 + |\mathbf{d}_{\perp}|^2}$, where inter-layer spacing $|\mathbf{d}_{\perp}| \gg \mathcal{O}(|\mathbf{r}^{\text{t}} - \mathbf{r}^{\text{b}}|)$, it should be flat enough in a large region of real space (to the same order as the Moiré pattern). Accordingly, $t^{\alpha\beta}(\mathbf{k}_P^{\text{t}} + \mathbf{F}^{\text{t}} + \mathbf{G}_1) \simeq t^{\alpha\beta}(\mathbf{k}_P^{\text{t}} + \mathbf{G}_1)$ is a good approximation and the summation over the BZ of each layer in (5.56) can be easily done:

- Since $|\mathbf{F}^{\text{t}}|, |\mathbf{F}^{\text{b}}| \gg 1$, the Kronecker delta function in (5.56) is non-vanishing only if \mathbf{G}_1 and \mathbf{G}_2 differ by a small rotation. Namely,

$$t_{\mathbf{F}^{\text{t}}, \mathbf{F}^{\text{b}}}^{\alpha\beta} = \frac{1}{V} \sum_{\mathbf{G}_1, \mathbf{G}_2} \delta_{\mathbf{G}_1, \mathbf{G}_2} \cdot e^{-i\mathbf{G}_2 \cdot \boldsymbol{\tau}_{2\beta}} \cdot t^{\alpha\beta}(\mathbf{k}_P + \mathbf{G}_1) \cdot e^{i\mathbf{G}_1 \cdot \boldsymbol{\tau}_{1\alpha}}$$

- Since the three-fold intersection point P are NOT connected with the reciprocal vectors for each layer (as a sharp contrast, in twisted bilayer graphene the three-fold K valleys are directly connected with some reciprocal vectors — this is actually how Moiré pattern enters in constraining the form of tunneling terms), the above summation only need to count the branch with $\mathbf{G}_1 = \mathbf{G}_2 = \mathbf{0}$.

As a result, we find that the tunneling strength only has a trivial momentum-dependence $t_{\mathbf{F}^{\text{t}}, \mathbf{F}^{\text{b}}}^{\alpha\beta} = t$.

Bibliography

- [1] Horst L Stormer, Daniel C Tsui, and Arthur C Gossard. The fractional quantum hall effect. *Reviews of Modern Physics*, 71(2):S298, 1999.
- [2] Bei Zeng, Xie Chen, Duan-Lu Zhou, and Xiao-Gang Wen. Quantum information meets quantum matter—from quantum entanglement to topological phase in many-body systems. *arXiv preprint arXiv:1508.02595*, 2015.
- [3] Oguzhan Can, Tarun Tummuru, Ryan P Day, Ilya Elfimov, Andrea Damascelli, and Marcel Franz. High-temperature topological superconductivity in twisted double-layer copper oxides. *Nature Physics*, 17(4):519–524, 2021.
- [4] Pavel A Volkov, Justin H Wilson, Kevin P Lucht, and JH Pixley. Magic angles and correlations in twisted nodal superconductors. *Physical Review B*, 107(17):174506, 2023.
- [5] Xingjiang Zhou, Wei-Sheng Lee, Masatoshi Imada, Nandini Trivedi, Philip Phillips, Hae-Young Kee, Päivi Törmä, and Mikhail Eremets. High-temperature superconductivity. *Nature Reviews Physics*, 3(7):462–465, 2021.
- [6] Yuan Cao, Valla Fatemi, Shiang Fang, Kenji Watanabe, Takashi Taniguchi, Efthimios Kaxiras, and Pablo Jarillo-Herrero. Unconventional superconductivity in magic-angle graphene superlattices. *Nature*, 556(7699):43–50, 2018.
- [7] Yonglong Xie, Andrew T Pierce, Jeong Min Park, Daniel E Parker, Eslam Khalaf, Patrick Ledwith, Yuan Cao, Seung Hwan Lee, Shaowen Chen, Patrick R Forrester, et al. Fractional Chern insulators in magic-angle twisted bilayer graphene. *Nature*, 600(7889):439–443, 2021.
- [8] Jiaqi Cai, Eric Anderson, Chong Wang, Xiaowei Zhang, Xiaoyu Liu, William Holtzmann, Yinong Zhang, Fengren Fan, Takashi Taniguchi, Kenji Watanabe, et al. Signatures of fractional quantum anomalous Hall states in twisted MoTe₂. *Nature*, 622(7981):63–68, 2023.
- [9] Heonjoon Park, Jiaqi Cai, Eric Anderson, Yinong Zhang, Jiayi Zhu, Xiaoyu Liu, Chong Wang, William Holtzmann, Chaowei Hu, Zhaoyu Liu, et al. Observation of fractionally quantized anomalous Hall effect. *Nature*, 622(7981):74–79, 2023.
- [10] Sajedeh Manzeli, Dmitry Ovchinnikov, Diego Pasquier, Oleg V Yazyev, and Andras Kis. 2d transition metal dichalcogenides. *Nature Reviews Materials*, 2(8):1–15, 2017.

- [11] Di Xiao, Gui-Bin Liu, Wanxiang Feng, Xiaodong Xu, and Wang Yao. Coupled spin and valley physics in monolayers of mos 2 and other group-vi dichalcogenides. *Physical Review Letters*, 108(19):196802, 2012.
- [12] Ashwin Ramasubramaniam. Large excitonic effects in monolayers of molybdenum and tungsten dichalcogenides. *Physical Review B*, 86(11):115409, 2012.
- [13] Jainendra K Jain. *Composite fermions*. Cambridge University Press, 2007.
- [14] Fengcheng Wu, Timothy Lovorn, Emanuel Tutuc, Ivar Martin, and A. H. MacDonald. Topological insulators in twisted transition metal dichalcogenide homobilayers. *Physical Review Letters*, 122(8):086402, 2019.
- [15] JJ Lee, FT Schmitt, RG Moore, S Johnston, Y-T Cui, W Li, M Yi, ZK Liu, M Hashimoto, Ya Zhang, et al. Interfacial mode coupling as the origin of the enhancement of t_c in fese films on srtio3. *Nature*, 515(7526):245–248, 2014.
- [16] B Roas, L Schultz, and G Endres. Epitaxial growth of yba₂cu₃o_{7-x} thin films by a laser evaporation process. *Applied physics letters*, 53(16):1557–1559, 1988.
- [17] Martin Grönke, Peer Schmidt, Martin Valldor, Steffen Oswald, Daniel Wolf, Axel Lubk, Bernd Büchner, and Silke Hampel. Chemical vapor growth and delamination of α -rucl 3 nanosheets down to the monolayer limit. *Nanoscale*, 10(40):19014–19022, 2018.
- [18] Daniel C Tsui, Horst L Stormer, and Arthur C Gossard. Two-dimensional magnetotransport in the extreme quantum limit. *Physical Review Letters*, 48(22):1559, 1982.
- [19] Robert Willett, James P Eisenstein, Horst L Störmer, Daniel C Tsui, Arthur C Gossard, and JH English. Observation of an even-denominator quantum number in the fractional quantum hall effect. *Physical review letters*, 59(15):1776, 1987.
- [20] Lev P Gor'kov and Vladimir Z Kresin. Colloquium: High pressure and road to room temperature superconductivity. *Reviews of Modern Physics*, 90(1):011001, 2018.
- [21] Kostya S Novoselov, Andre K Geim, Sergei V Morozov, De-eng Jiang, Yanshui Zhang, Sergey V Dubonos, Irina V Grigorieva, and Alexandr A Firsov. Electric field effect in atomically thin carbon films. *Science*, 306(5696):666–669, 2004.
- [22] AW Tsen, B Hunt, YD Kim, ZJ Yuan, S Jia, RJ Cava, J Hone, Philip Kim, CR Dean, and AN Pasupathy. Nature of the quantum metal in a two-dimensional crystalline superconductor. *Nature Physics*, 12(3):208–212, 2016.
- [23] Bevin Huang, Genevieve Clark, Efrén Navarro-Moratalla, Dahlia R Klein, Ran Cheng, Kyle L Seyler, Ding Zhong, Emma Schmidgall, Michael A McGuire, David H Cobden, et al. Layer-dependent ferromagnetism in a van der waals crystal down to the monolayer limit. *Nature*, 546(7657):270–273, 2017.

- [24] Bevin Huang, Genevieve Clark, Dahlia R Klein, David MacNeill, Efrén Navarro-Moratalla, Kyle L Seyler, Nathan Wilson, Michael A McGuire, David H Cobden, Di Xiao, et al. Electrical control of 2d magnetism in bilayer cri 3. *Nature nanotechnology*, 13(7):544–548, 2018.
- [25] K S Novoselov, Artem Mishchenko, Alexandra Carvalho, and AH Castro Neto. 2d materials and van der waals heterostructures. *Science*, 353(6298):aac9439, 2016.
- [26] F Duncan M Haldane. Nonlinear field theory of large-spin heisenberg antiferromagnets: semiclassically quantized solitons of the one-dimensional easy-axis néel state. *Physical review letters*, 50(15):1153, 1983.
- [27] F Duncan M Haldane. Continuum dynamics of the 1-d heisenberg antiferromagnet: Identification with the o (3) nonlinear sigma model. *Physics letters a*, 93(9):464–468, 1983.
- [28] Ian Affleck, Tom Kennedy, Elliott H Lieb, and Hal Tasaki. Rigorous results on valence-bond ground states in antiferromagnets. *Condensed Matter Physics and Exactly Soluble Models: Selecta of Elliott H. Lieb*, pages 249–252, 2004.
- [29] Xiao-Gang Wen. Colloquium: Zoo of quantum-topological phases of matter. *Reviews of Modern Physics*, 89(4):041004, 2017.
- [30] Xiao-Gang Wen. Quantum orders and symmetric spin liquids. *Physical Review B*, 65(16):165113, 2002.
- [31] Xie Chen, Zheng-Cheng Gu, and Xiao-Gang Wen. Classification of gapped symmetric phases in one-dimensional spin systems. *Physical review b*, 83(3):035107, 2011.
- [32] Xie Chen, Zheng-Cheng Gu, and Xiao-Gang Wen. Local unitary transformation, long-range quantum entanglement, wave function renormalization, and topological order. *Physical review b*, 82(15):155138, 2010.
- [33] Michael Levin and Xiao-Gang Wen. Detecting topological order in a ground state wave function. *Physical review letters*, 96(11):110405, 2006.
- [34] Alexei Kitaev and John Preskill. Topological entanglement entropy. *Physical review letters*, 96(11):110404, 2006.
- [35] Xiao-Gang Wen and Qian Niu. Ground-state degeneracy of the fractional quantum Hall states in the presence of a random potential and on high-genus riemann surfaces. *Physical Review B*, 41(13):9377, 1990.
- [36] Xiao-Gang Wen. Vacuum degeneracy of chiral spin states in compactified space. *Physical Review B*, 40(10):7387, 1989.
- [37] Philip W Anderson. Plasmons, gauge invariance, and mass. *Physical Review*, 130(1):439, 1963.
- [38] LD Landau. On the theory of the fermi liquid. *Sov. Phys. JETP*, 8(1):70, 1959.

- [39] Andrej Mesaros and Ying Ran. Classification of symmetry enriched topological phases with exactly solvable models. *Physical Review B*, 87(15):155115, 2013.
- [40] Zhengguang Lu, Tonghang Han, Yuxuan Yao, Aidan P Reddy, Jixiang Yang, Junseok Seo, Kenji Watanabe, Takashi Taniguchi, Liang Fu, and Long Ju. Fractional quantum anomalous hall effect in multilayer graphene. *Nature*, 626(8000):759–764, 2024.
- [41] Yihang Zeng, Zhengchao Xia, Kaifei Kang, Jiacheng Zhu, Patrick Knüppel, Chirag Vaswani, Kenji Watanabe, Takashi Taniguchi, Kin Fai Mak, and Jie Shan. Thermodynamic evidence of fractional chern insulator in moiré MoTe₂. *Nature*, 622(7981):69–73, 2023.
- [42] Fan Xu, Zheng Sun, Tongtong Jia, Chang Liu, Cheng Xu, Chushan Li, Yu Gu, Kenji Watanabe, Takashi Taniguchi, Bingbing Tong, et al. Observation of integer and fractional quantum anomalous Hall effects in twisted bilayer MoTe₂. *Physical Review X*, 13(3):031037, 2023.
- [43] Philip W Anderson. More is different: Broken symmetry and the nature of the hierarchical structure of science. *Science*, 177(4047):393–396, 1972.
- [44] Rafi Bistritzer and Allan H MacDonald. Moiré bands in twisted double-layer graphene. *Proceedings of the National Academy of Sciences*, 108(30):12233–12237, 2011.
- [45] Yuan Cao, Valla Fatemi, Ahmet Demir, Shiang Fang, Spencer L Tomarken, Jason Y Luo, Javier D Sanchez-Yamagishi, Kenji Watanabe, Takashi Taniguchi, Efthimios Kaxiras, et al. Correlated insulator behaviour at half-filling in magic-angle graphene superlattices. *Nature*, 556(7699):80–84, 2018.
- [46] Pavel A Volkov, Justin H Wilson, Kevin P Lucht, and JH Pixley. Current-and field-induced topology in twisted nodal superconductors. *Physical Review Letters*, 130(18):186001, 2023.
- [47] Yuan Cao, Daniel Rodan-Legrain, Jeong Min Park, Noah FQ Yuan, Kenji Watanabe, Takashi Taniguchi, Rafael M Fernandes, Liang Fu, and Pablo Jarillo-Herrero. Nematicity and competing orders in superconducting magic-angle graphene. *science*, 372(6539):264–271, 2021.
- [48] Yuan Cao, Debanjan Chowdhury, Daniel Rodan-Legrain, Oriol Rubies-Bigorda, Kenji Watanabe, Takashi Taniguchi, T Senthil, and Pablo Jarillo-Herrero. Strange metal in magic-angle graphene with near planckian dissipation. *Physical review letters*, 124(7):076801, 2020.
- [49] Aaron L Sharpe, Eli J Fox, Arthur W Barnard, Joe Finney, Kenji Watanabe, Takashi Taniguchi, MA Kastner, and David Goldhaber-Gordon. Emergent ferromagnetism near three-quarters filling in twisted bilayer graphene. *Science*, 365(6453):605–608, 2019.
- [50] M Serlin, CL Tschirhart, H Polshyn, Y Zhang, J Zhu, K Watanabe, T Taniguchi, L Balents, and AF Young. Intrinsic quantized anomalous hall effect in a moiré heterostructure. *Science*, 367(6480):900–903, 2020.

- [51] Zhiming Zhang, Yimeng Wang, Kenji Watanabe, Takashi Taniguchi, Keiji Ueno, Emanuel Tutuc, and Brian J LeRoy. Flat bands in twisted bilayer transition metal dichalcogenides. *Nature Physics*, 16(11):1093–1096, 2020.
- [52] Lei Wang, En-Min Shih, Augusto Ghiotto, Lede Xian, Daniel A Rhodes, Cheng Tan, Martin Claassen, Dante M Kennes, Yusong Bai, Bumho Kim, et al. Correlated electronic phases in twisted bilayer transition metal dichalcogenides. *Nature materials*, 19(8):861–866, 2020.
- [53] Trithep Devakul, Valentin Crépel, Yang Zhang, and Liang Fu. Magic in twisted transition metal dichalcogenide bilayers. *Nature Communications*, 12(1):1–9, 2021.
- [54] En Li, Jin-Xin Hu, Xuemeng Feng, Zishu Zhou, Liheng An, Kam Tuen Law, Ning Wang, and Nian Lin. Lattice reconstruction induced multiple ultra-flat bands in twisted bilayer wse2. *Nature communications*, 12(1):5601, 2021.
- [55] Titus Neupert, Luiz Santos, Claudio Chamon, and Christopher Mudry. Fractional quantum Hall states at zero magnetic field. *Physical Review Letters*, 106(23):236804, 2011.
- [56] Evelyn Tang, Jia-Wei Mei, and Xiao-Gang Wen. High-temperature fractional quantum Hall states. *Physical Review Letters*, 106(23):236802, 2011.
- [57] DN Sheng, Zheng-Cheng Gu, Kai Sun, and L Sheng. Fractional quantum Hall effect in the absence of Landau levels. *Nature Communications*, 2(1):389, 2011.
- [58] Nicolas Regnault and B Andrei Bernevig. Fractional Chern insulator. *Physical Review X*, 1(2):021014, 2011.
- [59] Kin Fai Mak, Changgu Lee, James Hone, Jie Shan, and Tony F Heinz. Atomically thin mos 2: a new direct-gap semiconductor. *Physical review letters*, 105(13):136805, 2010.
- [60] Andrea Splendiani, Liang Sun, Yuanbo Zhang, Tianshu Li, Jonghwan Kim, Chi-Yung Chim, Giulia Galli, and Feng Wang. Emerging photoluminescence in monolayer mos2. *Nano letters*, 10(4):1271–1275, 2010.
- [61] Li F Mattheiss. Band structures of transition-metal-dichalcogenide layer compounds. *Physical Review B*, 8(8):3719, 1973.
- [62] Gene Dresselhaus. Spin-orbit coupling effects in zinc blende structures. *Physical Review*, 100(2):580, 1955.
- [63] Lok C Lew Yan Voon and Morten Willatzen. *The kp method: electronic properties of semiconductors*. Springer Science & Business Media, 2009.
- [64] Andor Kormányos, Guido Burkard, Martin Gmitra, Jaroslav Fabian, Viktor Zólyomi, Neil D Drummond, and Vladimir Fal’ko. $k \cdot p$ theory for two-dimensional transition metal dichalcogenide semiconductors. *2D Materials*, 2(2):022001, 2015.

- [65] Jeil Jung, Arnaud Raoux, Zhenhua Qiao, and Allan H MacDonald. Ab initio theory of moiré superlattice bands in layered two-dimensional materials. *Physical Review B*, 89(20):205414, 2014.
- [66] Zhida Song, Zhijun Wang, Wujun Shi, Gang Li, Chen Fang, and B Andrei Bernevig. All magic angles in twisted bilayer graphene are topological. *Physical review letters*, 123(3):036401, 2019.
- [67] Robert B Laughlin. Anomalous quantum Hall effect: an incompressible quantum fluid with fractionally charged excitations. *Physical Review Letters*, 50(18):1395, 1983.
- [68] Jainendra K Jain. Composite-fermion approach for the fractional quantum Hall effect. *Physical Review Letters*, 63(2):199, 1989.
- [69] Jainendra K Jain. Incompressible quantum Hall states. *Physical Review B*, 40(11):8079, 1989.
- [70] Jainendra K Jain. Theory of the fractional quantum Hall effect. *Physical Review B*, 41(11):7653, 1990.
- [71] Ganpathy Murthy. Hamiltonian description of composite fermions: Magnetoexciton dispersions. *Physical Review B*, 60(19):13702, 1999.
- [72] Aleksey A Abrikosov. Nobel lecture: Type-ii superconductors and the vortex lattice. *Reviews of modern physics*, 76(3):975, 2004.
- [73] Ganpathy Murthy. Hamiltonian theory of the fractional quantum Hall effect: Conserving approximation for incompressible fractions. *Physical Review B*, 64(19):195310, 2001.
- [74] Ganpathy Murthy and R Shankar. Hamiltonian theories of the fractional quantum Hall effect. *Reviews of Modern Physics*, 75(4):1101, 2003.
- [75] S. M. Girvin, A. H. MacDonald, and P. M. Platzman. Magneto-roton theory of collective excitations in the fractional quantum Hall effect. *Physical Review B*, 33(4):2481, 1986.
- [76] SA Parameswaran, R Roy, and Shivaji L Sondhi. Fractional chern insulators and the $W\infty$ algebra. *Physical Review B*, 85(24):241308, 2012.
- [77] Patrick J Ledwith, Ashvin Vishwanath, and Daniel E Parker. Vortexability: A unifying criterion for ideal fractional Chern insulators. *Physical Review B*, 108(20):205144, 2023.
- [78] Steven H Simon, Fenner Harper, and N Read. Fractional chern insulators in bands with zero berry curvature. *Physical Review B*, 92(19):195104, 2015.
- [79] Kai Sun, Zhengcheng Gu, Hosho Katsura, and S. D. Sarma. Nearly flatbands with nontrivial topology. *Physical Review Letters*, 106(23):236803, 2011.
- [80] Di Xiao, Wenguang Zhu, Ying Ran, Naoto Nagaosa, and Satoshi Okamoto. Interface engineering of quantum Hall effects in digital transition metal oxide heterostructures. *Nature Communications*, 2(1):596, 2011.
- [81] Rahul Roy. Band geometry of fractional topological insulators. *Physical Review B*, 90(16):165139, 2014.

- [82] Jie Wang, Jennifer Cano, Andrew J Millis, Zhao Liu, and Bo Yang. Exact landau level description of geometry and interaction in a flatband. *Physical Review Letters*, 127(24):246403, 2021.
- [83] Jie Wang, Semyon Klevtsov, and Zhao Liu. Origin of model fractional Chern insulators in all topological ideal flatbands: Explicit color-entangled wave function and exact density algebra. *Physical Review Research*, 5(2):023167, 2023.
- [84] Benoît Estienne, Nicolas Regnault, and Valentin Crépel. Ideal chern bands as landau levels in curved space. *Physical Review Research*, 5(3):L032048, 2023.
- [85] Patrick J Ledwith, Grigory Tarnopolsky, Eslam Khalaf, and Ashvin Vishwanath. Fractional chern insulator states in twisted bilayer graphene: An analytical approach. *Physical Review Research*, 2(2):023237, 2020.
- [86] Junkai Dong, Patrick J Ledwith, Eslam Khalaf, Jong Yeon Lee, and Ashvin Vishwanath. Many-body ground states from decomposition of ideal higher Chern bands: Applications to chirally twisted graphene multilayers. *Physical Review Research*, 5(2):023166, 2023.
- [87] F. D. M. Haldane and E. H. Rezayi. Finite-size studies of the incompressible state of the fractionally quantized Hall effect and its excitations. *Physical Review Letters*, 54(3):237, 1985.
- [88] A. E. Feiguin, E. H. Rezayi, C Nayak, and S. D. Sarma. Density matrix renormalization group study of incompressible fractional quantum Hall states. *Physical Review Letters*, 100(16):166803, 2008.
- [89] Junkai Dong, Taige Wang, Tianle Wang, Tomohiro Soejima, Michael P Zaletel, Ashvin Vishwanath, and Daniel E Parker. Anomalous Hall crystals in rhombohedral multilayer graphene I: Interaction-driven Chern bands and fractional quantum Hall states at zero magnetic field. *arXiv preprint arXiv:2311.05568*, 2023.
- [90] Junkai Dong, Jie Wang, Patrick J Ledwith, Ashvin Vishwanath, and Daniel E Parker. Composite fermi liquid at zero magnetic field in twisted MoTe₂. *arXiv preprint arXiv:2306.01719*, 2023.
- [91] Jiabin Yu, Jonah Herzog-Arbeitman, Minxuan Wang, Oskar Vafeck, B Andrei Bernevig, and Nicolas Regnault. Fractional Chern insulators vs. non-magnetic states in twisted bilayer MoTe₂. *arXiv preprint arXiv:2309.14429*, 2023.
- [92] Hart Goldman, Aidan P Reddy, Nisarga Paul, and Liang Fu. Zero-field composite fermi liquid in twisted semiconductor bilayers. *arXiv preprint arXiv:2306.02513*, 2023.
- [93] Zhihuan Dong, Adarsh S Patri, and T Senthil. Theory of fractional quantum anomalous Hall phases in pentalayer rhombohedral graphene moiré structures. *arXiv preprint arXiv:2311.03445*, 2023.
- [94] Yuan-Ming Lu and Ashvin Vishwanath. Classification and properties of symmetry-enriched topological phases: Chern-Simons approach with applications to z 2 spin liquids. *Physical Review B*, 93(15):155121, 2016.

- [95] Xiao-Gang Wen and A Zee. Shift and spin vector: New topological quantum numbers for the Hall fluids. *Physical Review Letters*, 69(6):953, 1992.
- [96] Naren Manjunath, Abhinav Prem, and Yuan-Ming Lu. Rotational symmetry protected edge and corner states in abelian topological phases. *Physical Review B*, 107(19):195130, 2023.
- [97] Bo Han, Huajia Wang, and Peng Ye. Generalized wen-zee terms. *Physical Review B*, 99(20):205120, 2019.
- [98] Tianhe Li, Penghao Zhu, Wladimir A Benalcazar, and Taylor L Hughes. Fractional disclination charge in two-dimensional c_n -symmetric topological crystalline insulators. *Physical Review B*, 101(11):115115, 2020.
- [99] Yuxuan Zhang, Naren Manjunath, Gautam Nambiar, and Maissam Barkeshli. Fractional disclination charge and discrete shift in the hofstadter butterfly. *Physical Review Letters*, 129(27):275301, 2022.
- [100] A Pinczuk, B. S. Dennis, L. N. Pfeiffer, and K. W. West. Light scattering by collective excitations in the fractional quantum Hall regime. *Physica B: Condensed Matter*, 249:40–43, 1998.
- [101] Moonsoo Kang, A Pinczuk, B. S. Dennis, M. A. Eriksson, L. N. Pfeiffer, and K. W. West. Inelastic light scattering by gap excitations of fractional quantum Hall states at $1/3 \leq \nu \leq 2/3$. *Physical Review Letters*, 84(3):546, 2000.
- [102] Igor V Kukushkin, Jurgen H Smet, Vito W Scarola, Vladimir Umansky, and Klaus von Klitzing. Dispersion of the excitations of fractional quantum Hall states. *Science*, 324(5930):1044–1047, 2009.
- [103] F. D. M. Haldane. Geometrical description of the fractional quantum Hall effect. *Physical Review Letters*, 107(11):116801, 2011.
- [104] F. D. M. Haldane. Hall viscosity and intrinsic metric of incompressible fractional Hall fluids. *arXiv preprint arXiv:0906.1854*, 2009.
- [105] Bo Yang, Zi-Xiang Hu, Z Papić, and F. D. M. Haldane. Model wave functions for the collective modes and the magnetoroton theory of the fractional quantum Hall effect. *Physical Review Letters*, 108(25):256807, 2012.
- [106] Daniel P Arovas and Assa Auerbach. Functional integral theories of low-dimensional quantum heisenberg models. *Physical Review B*, 38(1):316, 1988.
- [107] Nicholas Read and Subir Sachdev. Large-n expansion for frustrated quantum antiferromagnets. *Physical Review Letters*, 66(13):1773, 1991.
- [108] Subir Sachdev and Nicholas Read. Large n expansion for frustrated and doped quantum antiferromagnets. *International Journal of Modern Physics B*, 5(01n02):219–249, 1991.

- [109] Subir Sachdev. Kagome and triangular lattice heisenberg antiferromagnets: Ordering from quantum fluctuations and quantum-disordered ground states with unconfined bosonic spinons. *Physical Review B*, 45(21):12377, 1992.
- [110] Fa Wang. Schwinger boson mean field theories of spin liquid states on a honeycomb lattice: Projective symmetry group analysis and critical field theory. *Physical Review B*, 82(2):024419, 2010.
- [111] Xiao-Gang Wen. Mean-field theory of spin-liquid states with finite energy gap and topological orders. *Physical Review B*, 44(6):2664, 1991.
- [112] Claudius Gros. Physics of projected wavefunctions. *Annals of Physics*, 189(1):53–88, 1989.
- [113] Tiamhock Tay and Olexei I Motrunich. Variational study of j_1 - j_2 heisenberg model on kagome lattice using projected schwinger-boson wave functions. *Physical Review B*, 84(2):020404, 2011.
- [114] V. Pasquier and F. D. M. Haldane. A dipole interpretation of the $\nu = 1/2$ state. *Nuclear Physics B*, 516(3):719–726, 1998.
- [115] Nicholas Read. Lowest-Landau-level theory of the quantum Hall effect: The fermi-liquid-like state of bosons at filling factor one. *Physical Review B*, 58(24):16262, 1998.
- [116] Ganpathy Murthy and R Shankar. Hamiltonian theory of fractionally filled Chern bands. *Physical Review B*, 86(19):195146, 2012.
- [117] Chong Wang, Xiao-Wei Zhang, Xiaoyu Liu, Yuchi He, Xiaodong Xu, Ying Ran, Ting Cao, and Di Xiao. Fractional Chern insulator in twisted bilayer MoTe₂. *arXiv preprint arXiv:2304.11864*, 2023.
- [118] Ajit C Balram, Arkadiusz Wójs, and Jainendra K Jain. State counting for excited bands of the fractional quantum hall effect: Exclusion rules for bound excitons. *Physical Review B*, 88(20):205312, 2013.
- [119] Rajiv K Kamilla, Xiao-Guang Wu, and Jainendra K Jain. Composite fermion theory of collective excitations in fractional quantum Hall effect. *Physical Review Letters*, 76(8):1332, 1996.
- [120] F. D. M. Haldane and E. H. Rezayi. Periodic Laughlin-Jastrow wave functions for the fractional quantized Hall effect. *Physical Review B*, 31(4):2529, 1985.
- [121] Xiao-Liang Qi. Generic wave-function description of fractional quantum anomalous Hall states and fractional topological insulators. *Physical review letters*, 107(12):126803, 2011.
- [122] Yang-Le Wu, Nicolas Regnault, and B Andrei Bernevig. Bloch model wave functions and pseudopotentials for all fractional Chern insulators. *Physical review letters*, 110(10):106802, 2013.
- [123] Chao-Ming Jian and Xiao-Liang Qi. Crystal-symmetry preserving wannier states for fractional Chern insulators. *Physical Review B*, 88(16):165134, 2013.
- [124] Chen Fang, Matthew J Gilbert, and B Andrei Bernevig. Bulk topological invariants in noninteracting point group symmetric insulators. *Physical Review B*, 86(11):115112, 2012.

- [125] Xie Chen. Symmetry fractionalization in two dimensional topological phases. *Reviews in Physics*, 2:3–18, 2017.
- [126] Meng Cheng, Michael Zaletel, Maissam Barkeshli, Ashvin Vishwanath, and Parsa Bonderson. Translational symmetry and microscopic constraints on symmetry-enriched topological phases: A view from the surface. *Physical Review X*, 6(4):041068, 2016.
- [127] Israel M Gelfand, Mikhail M Kapranov, Andrei V Zelevinsky, Israel M Gelfand, Mikhail M Kapranov, and Andrei V Zelevinsky. *Hyperdeterminants*. Springer, 1994.
- [128] Christopher J Hillar and Lek-Heng Lim. Most tensor problems are np-hard. *Journal of the ACM (JACM)*, 60(6):1–39, 2013.
- [129] Alexander I Barvinok. New algorithms for linear k-matroid intersection and matroid k-parity problems. *Mathematical Programming*, 69:449–470, 1995.
- [130] Songyang Pu, Ying-Hai Wu, and Jainendra K Jain. Composite fermions on a torus. *Physical Review B*, 96(19):195302, 2017.
- [131] Mikael Fremling. Coherent state wave functions on the torus. *arXiv preprint arXiv:1401.6834*, 2014.
- [132] Yuan-Ming Lu and Ying Ran. Symmetry-protected fractional Chern insulators and fractional topological insulators. *Physical Review B*, 85(16):165134, 2012.
- [133] Ajit C Balram and Songyang Pu. Positions of the magnetoroton minima in the fractional quantum Hall effect. *The European Physical Journal B*, 90:1–9, 2017.
- [134] Gregory Moore and Nicholas Read. Nonabelions in the fractional quantum Hall effect. *Nuclear Physics B*, 360(2-3):362–396, 1991.
- [135] Sung-Sik Lee, Shinsei Ryu, Chetan Nayak, and Matthew P. A. Fisher. Particle-hole symmetry and the $\nu = 5/2$ quantum Hall state. *Physical Review Letters*, 99(23):236807, 2007.
- [136] Michael Levin, Bertrand I Halperin, and Bernd Rosenow. Particle-hole symmetry and the Pfaffian state. *Physical Review Letters*, 99(23):236806, 2007.
- [137] Dam Thanh Son. Is the composite fermion a dirac particle? *Physical Review X*, 5(3):031027, 2015.
- [138] Nicholas Read and Dmitry Green. Paired states of fermions in two dimensions with breaking of parity and time-reversal symmetries and the fractional quantum Hall effect. *Physical Review B*, 61(15):10267, 2000.
- [139] Ammar Aboud and Jean-Gabriel Luque. Hyperpfaffians. *arXiv preprint arXiv:1608.05659*, 2016.
- [140] Ana Lopez and Eduardo Fradkin. Fractional quantum Hall effect and Chern-Simons gauge theories. *Physical Review B*, 44(10):5246, 1991.

- [141] Shou-Cheng Zhang. The Chern-Simons-Landau-Ginzburg theory of the fractional quantum Hall effect. *International Journal of Modern Physics B*, 6(01):25–58, 1992.
- [142] Andrey Gromov, Gil Young Cho, Yizhi You, Alexander G Abanov, and Eduardo Fradkin. Framing anomaly in the effective theory of the fractional quantum Hall effect. *Physical Review Letters*, 114(1):016805, 2015.
- [143] Andrey Gromov and Dam Thanh Son. Bimetric theory of fractional quantum Hall states. *Physical Review X*, 7(4):041032, 2017.
- [144] Michael Geracie, Dam Thanh Son, Chaolun Wu, and Shao-Feng Wu. Spacetime symmetries of the quantum Hall effect. *Physical Review D*, 91(4):045030, 2015.
- [145] Ramanjit Sohal, Luiz H Santos, and Eduardo Fradkin. Chern-Simons composite fermion theory of fractional Chern insulators. *Physical Review B*, 97(12):125131, 2018.
- [146] Xiao-Gang Wen. Projective construction of non-abelian quantum Hall liquids. *Physical Review B*, 60(12):8827, 1999.
- [147] Maissam Barkeshli and Xiao-Gang Wen. Effective field theory and projective construction for Z_k parafermion fractional quantum Hall states. *Physical Review B*, 81(15):155302, 2010.
- [148] Zhihuan Dong and T Senthil. Noncommutative field theory and composite fermi liquids in some quantum Hall systems. *Physical Review B*, 102(20):205126, 2020.
- [149] Bertrand I Halperin, Patrick A Lee, and Nicholas Read. Theory of the half-filled Landau level. *Physical Review B*, 47(12):7312, 1993.
- [150] Junren Shi. Quantum mechanics of composite fermions. *arXiv preprint arXiv:2309.00299*, 2023.
- [151] Myungchul Oh, Kevin P Nuckolls, Dillon Wong, Ryan L Lee, Xiaomeng Liu, Kenji Watanabe, Takashi Taniguchi, and Ali Yazdani. Evidence for unconventional superconductivity in twisted bilayer graphene. *Nature*, 600(7888):240–245, 2021.
- [152] Hyunjin Kim, Youngjoon Choi, Cyprian Lewandowski, Alex Thomson, Yiran Zhang, Robert Polski, Kenji Watanabe, Takashi Taniguchi, Jason Alicea, and Stevan Nadj-Perge. Evidence for unconventional superconductivity in twisted trilayer graphene. *Nature*, 606(7914):494–500, 2022.
- [153] Ethan Lake, Adarsh S Patri, and T Senthil. Pairing symmetry of twisted bilayer graphene: a phenomenological synthesis. *arXiv preprint arXiv:2204.12579*, 2022.
- [154] K Krishana, NP Ong, Q Li, GD Gu, and N Koshizuka. Plateaus observed in the field profile of thermal conductivity in the superconductor $\text{Bi}_2\text{Sr}_2\text{CaCu}_2\text{O}_8$. *Science*, 277(5322):83–85, 1997.
- [155] May Chiao, RW Hill, Christian Lupien, Louis Taillefer, P Lambert, R Gagnon, and P Fournier. Low-energy quasiparticles in cuprate superconductors: A quantitative analysis. *Physical Review B*, 62(5):3554, 2000.

- [156] Mike Sutherland, DG Hawthorn, RW Hill, F Ronning, S Wakimoto, H Zhang, Cyril Proust, Etienne Boaknin, C Lupien, Louis Taillefer, et al. Thermal conductivity across the phase diagram of cuprates: Low-energy quasiparticles and doping dependence of the superconducting gap. *Physical Review B*, 67(17):174520, 2003.
- [157] Adam C Durst, Ashvin Vishwanath, and Patrick A Lee. Weak-field thermal Hall conductivity in the mixed state of d-wave superconductors. *Physical Review Letters*, 90(18):187002, 2003.
- [158] Y Zhang, NP Ong, PW Anderson, DA Bonn, R Liang, and WN Hardy. Giant enhancement of the thermal Hall conductivity κ_{xy} in the superconductor $\text{YBa}_2\text{Cu}_3\text{O}_7$. *Physical Review Letters*, 86(5):890, 2001.
- [159] Vladimir Cvetkovic and Oskar Vafek. Berry phases and the intrinsic thermal Hall effect in high-temperature cuprate superconductors. *Nature Communications*, 6(1):1–7, 2015.
- [160] Mitali Banerjee, Moty Heiblum, Vladimir Umansky, Dima E Feldman, Yuval Oreg, and Ady Stern. Observation of half-integer thermal hall conductance. *Nature*, 559(7713):205–210, 2018.
- [161] T Yokoi, S Ma, Y Kasahara, S Kasahara, T Shibauchi, N Kurita, H Tanaka, J Nasu, Y Motome, C Hickey, et al. Half-integer quantized anomalous thermal hall effect in the kitaev material candidate α -rucl3. *Science*, 373(6554):568–572, 2021.
- [162] Z-X Shen, DS Dessau, BO Wells, DM King, WE Spicer, AJ Arko, D Marshall, LW Lombardo, A Kapitulnik, Pa Dickinson, et al. Anomalously large gap anisotropy in the a-b plane of $\text{Bi}_2\text{Sr}_2\text{CaCu}_2\text{O}_{8+\delta}$. *Physical Review Letters*, 70(10):1553, 1993.
- [163] H Ding, MR Norman, JC Campuzano, M Randeria, AF Bellman, T Yokoya, T Takahashi, T Mochiku, and K Kadowaki. Angle-resolved photoemission spectroscopy study of the superconducting gap anisotropy in $\text{Bi}_2\text{Sr}_2\text{CaCu}_2\text{O}_{8+x}$. *Physical Review B*, 54(14):R9678, 1996.
- [164] Y Zhang, JJ Lee, RG Moore, W Li, M Yi, M Hashimoto, DH Lu, TP Devereaux, D-H Lee, and Z-X Shen. Superconducting gap anisotropy in monolayer fese thin film. *Physical Review Letters*, 117(11):117001, 2016.
- [165] T Hanaguri, Y Kohsaka, JC Davis, C Lupien, I Yamada, M Azuma, M Takano, K Ohishi, M Ono, and H Takagi. Quasiparticle interference and superconducting gap in $\text{Ca}_{2-x}\text{Na}_x\text{CuO}_2\text{Cl}_2$. *Nature Physics*, 3(12):865–871, 2007.
- [166] Peter O Sprau, Andrey Kostin, Andreas Kreisel, Anna E Böhmer, Valentin Taufour, Paul C Canfield, Shantanu Mukherjee, Peter J Hirschfeld, Brian Møller Andersen, and JC Séamus Davis. Discovery of orbital-selective cooper pairing in fese. *Science*, 357(6346):75–80, 2017.
- [167] Inti Sodemann and Liang Fu. Quantum nonlinear Hall effect induced by berry curvature dipole in time-reversal invariant materials. *Physical Review Letters*, 115(21):216806, 2015.

- [168] Qiong Ma, Su-Yang Xu, Huitao Shen, David MacNeill, Valla Fatemi, Tay-Rong Chang, Andrés M Mier Valdivia, Sanfeng Wu, Zongzheng Du, Chuang-Han Hsu, et al. Observation of the nonlinear hall effect under time-reversal-symmetric conditions. *Nature*, 565(7739):337–342, 2019.
- [169] See Supplemental Material for detailed derivations on both intraband and interband contribution of SATHE. Discussion on the nodal origin of the interband contribution and the Fermi surface reconstruction of twisted-bilayer FeSe are also covered.
- [170] Philip JD Crowley and Liang Fu. Supercurrent-induced resonant optical response. *Physical Review B*, 106(21):214526, 2022.
- [171] Tao Qin, Qian Niu, and Junren Shi. Energy magnetization and the thermal Hall effect. *Physical Review Letters*, 107(23):236601, 2011.
- [172] Hiroaki Sumiyoshi and Satoshi Fujimoto. Quantum thermal Hall effect in a time-reversal-symmetry-broken topological superconductor in two dimensions: approach from bulk calculations. *Journal of the Physical Society of Japan*, 82(2):023602, 2013.
- [173] Oleg V Dolgov, Igor I Mazin, David Parker, and Alexander A Golubov. Interband superconductivity: contrasts between Bardeen-Cooper-Schrieffer and Eliashberg theories. *Physical Review B*, 79(6):060502, 2009.
- [174] Xue-Yang Song, Ya-Hui Zhang, and Ashvin Vishwanath. Doping a moiré mott insulator: A t - J model study of twisted cuprates. *Physical Review B*, 105(20):L201102, 2022.
- [175] Xiaodong Hu and Ying Ran. Engineering chiral topological superconductivity in twisted ising superconductors. *Physical Review B*, 106(12):125136, 2022.
- [176] V Brouet, M Fuglsang Jensen, Ping-Hui Lin, A Taleb-Ibrahimi, P Le Fèvre, F Bertran, Chia-Hui Lin, Wei Ku, A Forget, and D Colson. Impact of the two fe unit cell on the electronic structure measured by arpes in iron pnictides. *Physical Review B*, 86(7):075123, 2012.
- [177] SV Borisenko, DV Evtushinsky, Z-H Liu, I Morozov, R Kappenberger, S Wurmehl, B Büchner, AN Yaresko, TK Kim, M Hoesch, et al. Direct observation of spin-orbit coupling in iron-based superconductors. *Nature Physics*, 12(4):311–317, 2016.
- [178] Ming Yi, ZK Liu, Yan Zhang, Rong Yu, J-X Zhu, JJ Lee, RG Moore, FT Schmitt, Wei Li, SC Riggs, et al. Observation of universal strong orbital-dependent correlation effects in iron chalcogenides. *Nature Communications*, 6(1):1–7, 2015.
- [179] DF Agterberg, Tatsuya Shishidou, Joseph O’Halloran, PMR Brydon, and Michael Weinert. Resilient nodeless d-wave superconductivity in monolayer fese. *Physical Review Letters*, 119(26):267001, 2017.
- [180] Ying Ran, Fa Wang, Hui Zhai, Ashvin Vishwanath, and Dung-Hai Lee. Nodal spin density wave and band topology of the feas-based materials. *Physical Review B*, 79(1):014505, 2009.

- [181] Amit Kanigel, U Chatterjee, M Randeria, MR Norman, S Souma, M Shi, ZZ Li, H Raffy, and JC Campuzano. Protected nodes and the collapse of fermi arcs in high- T_c cuprate superconductors. *Physical Review Letters*, 99(15):157001, 2007.
- [182] Takeshi Kondo, W Malaeb, Y Ishida, T Sasagawa, H Sakamoto, Tsunehiro Takeuchi, T Tohyama, and S Shin. Point nodes persisting far beyond T_c in Bi2212. *Nature Communications*, 6(1):1–8, 2015.
- [183] C Kendziora, RJ Kelley, and M Onellion. Superconducting gap anisotropy vs doping level in high- T_c cuprates. *Physical Review Letters*, 77(4):727, 1996.
- [184] H Anzai, A Ino, M Arita, H Namatame, M Taniguchi, M Ishikado, K Fujita, S Ishida, and S Uchida. Relation between the nodal and antinodal gap and critical temperature in superconducting Bi2212. *Nature Communications*, 4(1):1–7, 2013.
- [185] M Eschrig and MR Norman. Effect of the magnetic resonance on the electronic spectra of high- T_c superconductors. *Physical Review B*, 67(14):144503, 2003.
- [186] RS Markiewicz, S Sahrakorpi, M Lindroos, Hsin Lin, and A Bansil. One-band tight-binding model parametrization of the high- T_c cuprates including the effect of k_z dispersion. *Physical Review B*, 72(5):054519, 2005.
- [187] Chao-Sheng Lian, Chen Si, and Wenhui Duan. Unveiling charge-density wave, superconductivity, and their competitive nature in two-dimensional nbse2. *Nano letters*, 18(5):2924–2929, 2018.
- [188] Minhao He, Pasqual Rivera, Dinh Van Tuan, Nathan P Wilson, Min Yang, Takashi Taniguchi, Kenji Watanabe, Jiaqiang Yan, David G Mandrus, Hongyi Yu, et al. Valley phonons and exciton complexes in a monolayer semiconductor. *Nature communications*, 11(1):1–7, 2020.
- [189] Aaron M Jones, Hongyi Yu, Nirmal J Ghimire, Sanfeng Wu, Grant Aivazian, Jason S Ross, Bo Zhao, Jiaqiang Yan, David G Mandrus, Di Xiao, et al. Optical generation of excitonic valley coherence in monolayer wse 2. *Nature nanotechnology*, 8(9):634–638, 2013.
- [190] Pasqual Rivera, Kyle L Seyler, Hongyi Yu, John R Schaibley, Jiaqiang Yan, David G Mandrus, Wang Yao, and Xiaodong Xu. Valley-polarized exciton dynamics in a 2d semiconductor heterostructure. *Science*, 351(6274):688–691, 2016.
- [191] Weijie Li, Xin Lu, Jiatian Wu, and Ajit Srivastava. Optical control of the valley zeeman effect through many-exciton interactions. *Nature Nanotechnology*, 16(2):148–152, 2021.
- [192] Davide Costanzo, Sanghyun Jo, Helmuth Berger, and Alberto F Morpurgo. Gate-induced superconductivity in atomically thin mos 2 crystals. *Nature nanotechnology*, 11(4):339–344, 2016.
- [193] Rusen Yan, Guru Khalsa, Brian T Schaefer, Alexander Jarjour, Sergei Rouvimov, Katja C Nowack, Huili G Xing, and Debdeep Jena. Thickness dependence of superconductivity in ultrathin nbs2. *Applied Physics Express*, 12(2):023008, 2019.

- [194] Chang-woo Cho, Jian Lyu, Cheuk Yin Ng, James Jun He, Kwan To Lo, Dmitriy Chareev, Tarob A. Abdel-Baset, Mahmoud Abdel-Hafiez, and Rolf Lortz. Evidence for the fuldeâ€“ferrellâ€“larkinâ€“ovchinnikov state in bulk nbs2. *Nature Communications*, 12(1):3676, Jun 2021.
- [195] Sergio C. de la Barrera, Michael R. Sinko, Devashish P. Gopalan, Nikhil Sivadas, Kyle L. Seyler, Kenji Watanabe, Takashi Taniguchi, Adam W. Tsen, Xiaodong Xu, Di Xiao, and Benjamin M. Hunt. Tuning ising superconductivity with layer and spinâ€“orbit coupling in two-dimensional transition-metal dichalcogenides. *Nature Communications*, 9(1):1427, Apr 2018.
- [196] Lijun Li, Xiaoyu Deng, Zhen Wang, Yu Liu, Milinda Abeykoon, Eric Dooryhee, Aleksandra Tomic, Yanan Huang, John B. Warren, Emil S. Bozin, Simon J. L. Billinge, Yuping Sun, Yimei Zhu, Gabriel Kotliar, and Cedomir Petrovic. Superconducting order from disorder in 2h-tase2â”xsx. *npj Quantum Materials*, 2(1):11, Feb 2017.
- [197] Chao-Sheng Lian, Christoph Heil, Xiaoyu Liu, Chen Si, Feliciano Giustino, and Wenhui Duan. Coexistence of superconductivity with enhanced charge density wave order in the two-dimensional limit of tase2. *The Journal of Physical Chemistry Letters*, 10(14):4076–4081, 2019.
- [198] Xinghan Cai, Tiancheng Song, Nathan P Wilson, Genevieve Clark, Minhao He, Xiaoou Zhang, Takashi Taniguchi, Kenji Watanabe, Wang Yao, Di Xiao, et al. Atomically thin crcl3: an in-plane layered anti-ferromagnetic insulator. *Nano letters*, 19(6):3993–3998, 2019.
- [199] Grant Aivazian, Zhirui Gong, Aaron M Jones, Rui-Lin Chu, Jiaqiang Yan, David G Mandrus, Chuanwei Zhang, David Cobden, Wang Yao, and Xiaodong Xu. Magnetic control of valley pseudospin in monolayer wse2. *Nature Physics*, 11(2):148–152, 2015.
- [200] Michael A McGuire, Genevieve Clark, KC Santosh, W Michael Chance, Gerald E Jellison Jr, Valentino R Cooper, Xiaodong Xu, and Brian C Sales. Magnetic behavior and spin-lattice coupling in cleavable van der waals layered crcl 3 crystals. *Physical Review Materials*, 1(1):014001, 2017.
- [201] Linfeng Ai, Enze Zhang, Jinshan Yang, Xiaoyi Xie, Yunkun Yang, Zehao Jia, Yuda Zhang, Shanshan Liu, Zihan Li, Pengliang Leng, et al. Van der waals ferromagnetic josephson junctions. *Nature communications*, 12(1):1–9, 2021.
- [202] H Ildzuchi, F Pientka, K-F Huang, K Harada, Ö GüL, YJ Shin, LT Nguyen, NH Jo, D Shindo, RJ Cava, et al. Van der waals heterostructure magnetic josephson junction. *arXiv preprint arXiv:2012.14969*, 2020.
- [203] Hongyuan Li, Shaowei Li, Mit H Naik, Jingxu Xie, Xinyu Li, Jiayin Wang, Emma Regan, Danqing Wang, Wenyu Zhao, Sihan Zhao, et al. Imaging moiré flat bands in three-dimensional reconstructed wse2/ws2 superlattices. *Nature materials*, 20(7):945–950, 2021.

- [204] Mattia Angeli and Allan H MacDonald. Γ valley transition metal dichalcogenide moiré bands. *Proceedings of the National Academy of Sciences*, 118(10):e2021826118, 2021.
- [205] Xue-Yang Song, Ya-Hui Zhang, and Ashvin Vishwanath. Doping a moiré mott insulator: A tj model study of twisted cuprates. *arXiv preprint arXiv:2109.08142*, 2021.
- [206] SY Zhao, Nicola Poccia, Xiaomeng Cui, Pavel A Volkov, Hyobin Yoo, Rebecca Engelke, Yuval Ronen, Ruidan Zhong, Genda Gu, Stephan Plugge, et al. Emergent interfacial superconductivity between twisted cuprate superconductors. *arXiv preprint arXiv:2108.13455*, 2021.
- [207] Pavel A Volkov, Justin H Wilson, and JH Pixley. Magic angles and current-induced topology in twisted nodal superconductors. *arXiv preprint arXiv:2012.07860*, 2020.
- [208] Pavel A Volkov, Shu Yang Frank Zhao, Nicola Poccia, Xiaomeng Cui, Philip Kim, and JH Pixley. Josephson effects in twisted nodal superconductors. *arXiv preprint arXiv:2108.13456*, 2021.
- [209] Daniel Shaffer, Jian Kang, FJ Burnell, and Rafael M Fernandes. Crystalline nodal topological superconductivity and bogolyubov fermi surfaces in monolayer nbse 2. *Physical Review B*, 101(22):224503, 2020.
- [210] Wen-Yu He, Benjamin T Zhou, James J He, Noah FQ Yuan, Ting Zhang, and Kam Tuen Law. Magnetic field driven nodal topological superconductivity in monolayer transition metal dichalcogenides. *Communications Physics*, 1(1):1–7, 2018.
- [211] Xiaoxiang Xi, Zefang Wang, Weiwei Zhao, Ju-Hyun Park, Kam Tuen Law, Helmuth Berger, László Forró, Jie Shan, and Kin Fai Mak. Ising pairing in superconducting NbSe₂ atomic layers. *Nature Physics*, 12(2):139–143, 2016.
- [212] Ying Xing, Kun Zhao, Pujia Shan, Feipeng Zheng, Yangwei Zhang, Hailong Fu, Yi Liu, Mingliang Tian, Chuanying Xi, Haiwen Liu, et al. Ising superconductivity and quantum phase transition in macro-size monolayer nbse2. *Nano letters*, 17(11):6802–6807, 2017.
- [213] Efrén Navarro-Moratalla, Joshua O Island, Samuel Manas-Valero, Elena Pinilla-Cienfuegos, Andres Castellanos-Gomez, Jorge Quereda, Gabino Rubio-Bollinger, Luca Chirolli, Jose Angel Silva-Guillén, Nicolás Agraït, et al. Enhanced superconductivity in atomically thin TaS₂. *Nature Communications*, 7(1):1–7, 2016.
- [214] Lede Xian, Dante M Kennes, Nicolas Tancogne-Dejean, Massimo Altarelli, and Angel Rubio. Multiflat bands and strong correlations in twisted bilayer boron nitride: Doping-induced correlated insulator and superconductor. *Nano letters*, 19(8):4934–4940, 2019.
- [215] Xiaobo Lu, Ruixiang Fei, Linghan Zhu, and Li Yang. Meron-like topological spin defects in monolayer crcl3. *Nature communications*, 11(1):1–8, 2020.

- [216] Fang Zhang, Hui Zhang, Wenbo Mi, and Xiaocha Wang. Electronic structure, magnetic anisotropy and dzyaloshinskii-moriya interaction in janus cr₂i₃x₃ (x= br, cl) bilayers. *Physical Chemistry Chemical Physics*, 22(16):8647–8657, 2020.
- [217] Huei-Ru Fuh, Ching-Ray Chang, Yin-Kuo Wang, Richard FL Evans, Roy W Chantrell, and Horng-Tay Jeng. Newtype single-layer magnetic semiconductor in transition-metal dichalcogenides vx₂ (x= s, se and te). *Scientific reports*, 6(1):1–11, 2016.
- [218] Wen Zhang, Lei Zhang, Ping Kwan Johnny Wong, Jiaren Yuan, Giovanni Vinai, Piero Torelli, Gerrit van der Laan, Yuan Ping Feng, and Andrew TS Wee. Magnetic transition in monolayer vse₂ via interface hybridization. *ACS nano*, 13(8):8997–9004, 2019.
- [219] Shawulienu Kezilebieke, Md Nurul Huda, Paul Dreher, Ilkka Manninen, Yifan Zhou, Jani Sainio, Rhodri Mansell, Miguel M Ugeda, Sebastiaan van Dijken, Hannu-Pekka Komsa, et al. Electronic and magnetic characterization of epitaxial vse₂ monolayers on superconducting nbse₂. *Communications Physics*, 3(1):1–8, 2020.
- [220] Faluke Aikebaier, Tero T Heikkilä, and JL Lado. Controlling magnetism through ising superconductivity in magnetic van der waals heterostructures. *Physical Review B*, 105(5):054506, 2022.
- [221] Ding Zhong, Kyle L Seyler, Xiayu Linpeng, Ran Cheng, Nikhil Sivadas, Bevin Huang, Emma Schmidgall, Takashi Taniguchi, Kenji Watanabe, Michael A McGuire, et al. Van der waals engineering of ferromagnetic semiconductor heterostructures for spin and valleytronics. *Science advances*, 3(5):e1603113, 2017.
- [222] Ding Zhong, Kyle L Seyler, Xiayu Linpeng, Nathan P Wilson, Takashi Taniguchi, Kenji Watanabe, Michael A McGuire, Kai-Mei C Fu, Di Xiao, Wang Yao, et al. Layer-resolved magnetic proximity effect in van der waals heterostructures. *Nature Nanotechnology*, 15(3):187–191, 2020.
- [223] Kyle L Seyler, Ding Zhong, Bevin Huang, Xiayu Linpeng, Nathan P Wilson, Takashi Taniguchi, Kenji Watanabe, Wang Yao, Di Xiao, Michael A McGuire, et al. Valley manipulation by optically tuning the magnetic proximity effect in wse₂/cri₃ heterostructures. *Nano letters*, 18(6):3823–3828, 2018.
- [224] Klaus Zollner, Paulo E Faria Junior, and Jaroslav Fabian. Proximity exchange effects in mose 2 and wse 2 heterostructures with cri 3: Twist angle, layer, and gate dependence. *Physical Review B*, 100(8):085128, 2019.
- [225] Livio Ciociaro, Martin Kroner, Kenji Watanabe, Takashi Taniguchi, and Atac Imamoglu. Observation of magnetic proximity effect using resonant optical spectroscopy of an electrically tunable mose 2/crbr 3 heterostructure. *Physical Review Letters*, 124(19):197401, 2020.
- [226] Jie Pan, Chenguang Guo, Changsheng Song, Xiaofang Lai, Hui Li, Wei Zhao, Hui Zhang, Gang Mu, Kejun Bu, Tianquan Lin, et al. Enhanced superconductivity in restacked tas₂ nanosheets. *Journal of the American Chemical Society*, 139(13):4623–4626, 2017.

- [227] Miguel M Ugeda, Aaron J Bradley, Yi Zhang, Seita Onishi, Yi Chen, Wei Ruan, Claudia Ojeda-Aristizabal, Hyejin Ryu, Mark T Edmonds, Hsin-Zon Tsai, et al. Characterization of collective ground states in single-layer nbse2. *Nature Physics*, 12(1):92–97, 2016.
- [228] Xiaoxiang Xi, Liang Zhao, Zefang Wang, Helmuth Berger, László Forró, Jie Shan, and Kin Fai Mak. Strongly enhanced charge-density-wave order in monolayer nbse 2. *Nature nanotechnology*, 10(9):765–769, 2015.
- [229] Yuki Nakata, Katsuaki Sugawara, Satoru Ichinokura, Yoshinori Okada, Taro Hitosugi, Takashi Koretsune, Keiji Ueno, Shuji Hasegawa, Takashi Takahashi, and Takafumi Sato. Anisotropic band splitting in monolayer nbse2: implications for superconductivity and charge density wave. *npj 2D Materials and Applications*, 2(1):1–6, 2018.
- [230] Yafang Yang, Shiang Fang, Valla Fatemi, Jonathan Ruhman, Efrén Navarro-Moratalla, Kenji Watanabe, Takashi Taniguchi, Efthimios Kaxiras, and Pablo Jarillo-Herrero. Enhanced superconductivity upon weakening of charge density wave transport in 2 h-tas 2 in the two-dimensional limit. *Physical Review B*, 98(3):035203, 2018.
- [231] Paolo Giannozzi, Stefano Baroni, Nicola Bonini, Matteo Calandra, Roberto Car, Carlo Cavazzoni, Davide Ceresoli, Guido L Chiarotti, Matteo Cococcioni, Ismaila Dabo, et al. Quantum espresso: a modular and open-source software project for quantum simulations of materials. *Journal of physics: Condensed matter*, 21(39):395502, 2009.
- [232] Paolo Giannozzi, Oliviero Andreussi, Thomas Brumme, Oana Bunau, M Buongiorno Nardelli, Matteo Calandra, Roberto Car, Carlo Cavazzoni, Davide Ceresoli, Matteo Cococcioni, et al. Advanced capabilities for materials modelling with quantum espresso. *Journal of physics: Condensed matter*, 29(46):465901, 2017.
- [233] Giovanni Pizzi, Valerio Vitale, Ryotaro Arita, Stefan Blügel, Frank Freimuth, Guillaume Géranton, Marco Gibertini, Dominik Gresch, Charles Johnson, Takashi Koretsune, et al. Wannier90 as a community code: new features and applications. *Journal of Physics: Condensed Matter*, 32(16):165902, 2020.
- [234] Alexandre Tkatchenko and Matthias Scheffler. Accurate molecular van der waals interactions from ground-state electron density and free-atom reference data. *Physical review letters*, 102(7):073005, 2009.
- [235] Kristian Berland, Debajit Chakraborty, and T Thonhauser. van der waals density functional with corrected c 6 coefficients. *Physical Review B*, 99(19):195418, 2019.
- [236] Kyuho Lee, Éamonn D Murray, Lingzhu Kong, Bengt I Lundqvist, and David C Langreth. Higher-accuracy van der waals density functional. *Physical Review B*, 82(8):081101, 2010.
- [237] Valentino R Cooper. Van der waals density functional: An appropriate exchange functional. *Physical Review B*, 81(16):161104, 2010.

- [238] B Andrei Bernevig. *Topological insulators and topological superconductors*. Princeton university press, 2013.
- [239] Gonçalo Catarina, Bruno Amorim, Eduardo V Castro, João MVP Lopes, and Nuno MR Peres. Twisted bilayer graphene: low-energy physics, electronic and optical properties. *Handbook of Graphene*, 3:177–232, 2019.
- [240] Patrick Ledwith, Eslam Khalaf, and Ashvin Vishwanath. Lecture notes on magic angle tbg. 2021.